Multivalent Glycoconjugates to Modulate Carbohydrate-protein Interactions (CPIs)

A Thesis submitted in partial fulfilment of the requirements of the degree
of Doctor of Philosophy

By

Sivakoti Sangabathuni

ID: 20113133

Indian Institute of Science Education and Research, Pune

Research Supervisor
Dr. Raghavendra Kikkeri
Associate Professor
Indian Institute of Science Education and Research, Pune

Dedicated to

My Family and Teachers

CERTIFICATE

This is to certify that the work incorporated in this entitled **“Multivalent Glycoconjugates to Modulate Carbohydrate-protein Interactions (CPIs)”** submitted by Sivakoti Sangabathuni carried out by candidate at Indian Institute of Science Education and Research (IISER), Pune, under my supervision. The work presented here or any part of it has not been included in any other thesis submitted previously for the award of any degree or diploma form any other university or institution.

Date: 26/04/2017

Dr. Raghavendra V. Kikkeri
(Research Supervisor)
Associate Professor
IISER, Pune - 411008
India.

Declaration

I hereby declare that the thesis entitled **"Multivalent Glycoconjugates to Modulate Carbohydrate-protein Interactions (CPIs)"** submitted for Doctor of Philosophy in chemistry at Indian Institute of Science Education and Research (IISER), Pune, has not been submitted by me to any other university or institution. This work presented here was carried out at the, Indian Institute of Science Education and Research, Pune, India under the supervision of Dr. Raghavendra V. Kikkeri.

Date: 26/04/2017

Sivakoti Sangabathuni
ID-20113133
Senior Research Fellow
Department of Chemistry
IISER, Pune- 411008
India.

Acknowledgments

The past six years has become one of the most important and memorable chapters in my life. This, in many ways, is the beginning, not the end, of my journey. Looking back, there are so many people that deserve my heartfelt gratitude. First, of all I would like to express my heartfelt sincere profound thanks to my supervisor Dr. Raghavendra V. Kikkeri in bringing me in field of glycobiology and pursuing good knowledge of interdisciplinary research. As a Ph.D student it gives me a great pleasure to express my deep sense of gratitude to my research supervisor for all his advice, guidance, support and encouragement in chemistry and its relevance in biological systems. His energy and tireless enthusiasm and passion for science have been an inspiration for me in the past six years and will always be in me years to come. I cannot think of a better advisor who can give me such freedom to pursue science and foster me to become independent thinker.

I thank our Director, Prof. K. N. Ganesh for giving excellent research platform, financial support and facilities that I have been fortunate with during my research here Indian Institute of Science Education and Research, Pune. Besides I gained many novel ideas and enthuse regarding how to become a great researcher at initial stage. A special vote of thanks would be for Dr. Hosahudya N. Gopi and Dr. C. V. Ramana for their valuable suggestion during research advisory committee (RAC) meeting. I am also thankful for CSIR, India for my 5 year research fellowship. I am thankful to all the chemistry faculties in IISER-Pune for their support. Also my work wouldn't be possible without help from our collaborators Dr. Anjan Banerjee, IIT Bombay, Dr. Ido braslavasky, The Hebrew University of Jerusalem, Israel. I also thank to all administrative staff of our department.

The research becomes interesting and fruitful due to wonderful lab mates around me. I am fortunate to have an excellent blend of talented and hardworking lab mates who can resonate in any occasion in their own different way, in addition being supportive and helpful. My special thanks to Dr. Raghavendra, Dr. Preeti, Dr. Rohan, Dr. Harikrishna, Madhuri, Phani, Catherin, Chetan, Balamurugan, Suraj, Prashant, Akhil, Sandhya, Amol and Keerthana for their generous support and their active participation in group tour and joyful moments. I also experienced the cheerful company of neighbouring group participants from Rajendra, Narasimha and Ashok and sharing my hard and struggles and thoughts in IISER. And I also acknowledge my friends Dr. Rammohan, Vara Prasad, P. Srinu, Dattu, Hanu,

Balaji, Joshi and Dr. M. Suresh for their constant encouragement and support from the starting day of my Ph.D.

This thesis remains incomplete without mentioning the motivation blessings and love of my family. There are no better words to express my heartfelt gratitude for their unconditional love, gracious understanding and life time support.

Finally, I pray to almighty god 'Siva' and goddess 'Durga' whose blessings made me able to complete the research work and submit this thesis successfully for the Ph. D degree.

Sivakoti Sangabathuni

Contents

Chapter 1

Introduction to Multivalent Glycoprobes to Study Carbohydrate-protein Interactions (CPIs)

Chapter 2

Assessing the Effect of Different Shapes of Glyco-goldnanoparticles on Bacterial Adhesion and Infections

---

Chapter 3

Glyco-goldnanoaprticle shapes Enhance Carbohydrate-Protein Interactions in Mammalian Cells

---

Chapter 4

Mapping the Glyco-goldnanoparticles of Different Shapes Toxicity, Bio-distribution and Sequestration in Adult Zebrafish

---

Chapter 5

Self-Assembly of Collagen Glycopeptides to Profile Cell Migration and In Vivo Wound Healing.

Abbreviations

ABTS = 2,2’-Azino-bis(3-ethylbenzthiazoline-6-sulfonic acid)

Ac = Acetyl

$AgNO_3$ = Silver nitrate

AIBN = Azobisisobutyronitrile

ASGPR = Asialoglycoprotein receptor

AuNPs = Goldnanoparticles

BDAC = Benzyldimethylhexadecylammonium chloride

$BF_3.Et_2O$ = Boron trifluoride diethyl etherate

BSA = Bovine serum albumin

CA = Contrast agents

CAM = Ceric ammonium molybdate

CD = Circular dichroism

ConA = Concanavalin A

CPI = Carbohydrate-protein interaction

CRP = Collagen related peptides

CT = Computerized tomography

CTAB = Cetyltrimethylammonium bromide

DAPI = 4’,6-Diamidino-2-phenylindole dihydrochloride

DCM = Dichloromethane

DC-SIGN = Dendritic cell-specific intercellular adhesion molecule-3-grabbing non-integrin

DER = Dow epoxy resin

DFM = Dark field microscopy

DIPEA = Diisopropylethylamine

DMEM = Dulbecco’s modified eagle medium

DMF = *N,N’*-dimethylformamide

DMSO = Dimethyl sulfoxide

DOTA = Tetraazacyclododecane-1,4,7,10-tetraacetic acid

DTPA = Diethylenetriaminepentaacetic acid

E.coli = Escherichia coli

EDC = 1-Ethyl-3(3-Dimethylaminopropyl)carbodiimide

ELISA = Enzyme-linked immunosorbent assay

eq. = equivalents

et al = and others (*et alii*)

EtOAc = Ethylacetate

FACS = Fluorescence-activated cell sorting

FBS = Fetal bovine serum

FDG = 2-^{18}F-2-deoxy-d-glucose

FE-SEM = Field emission scanning electron microscopy

FITC = Fluorescene isothio cyanate

FSNP = Fluroscein doped silica nanoparticles

GAGs = Glycosaminoglycans

Gal = Galactose

GCC = Glyco collagen peptide complex

GLUT1 = Glucose transporters

GSA = Galactosylated serum albumin

$HAuCl_4$ = Chloroauric acid

HCA = Heiracheal cluster analysis

HEPES = (4-(2-hydroxyethyl)-1-piperazineethanesulfonic acid)

HIV = Human immunodeficiency virus

HOBt = Hydroxybenzotriazole

HPLC = High performance liquid chromatography

HRMS = High resolution mass spectrometry

HRP = Horseradish peroxidase

Hz = Hertz

IC_{50} = Inhibitory concentration

ICP-MS = Inductively coupled plasma mass spectrometry

IgG = Immunoglobulin G

ILT = Intraluminal thread

ITC = Isothermal titration calorimetry

LD = Lethal dose

LRET = Luminescence resonance energy transfer

MALDI = Matrix-assisted laser desorption ionization

Man = Mannose

MCAO = Middle cerebral artery occlusion

Me = Methyl

MeOH = Methanol

Me-β-CD = Methyl- β-Cyclodextrin

MGD = Metallo glyco dendrimer

MMP = Matrix metallo protein

MRI = Magnetic resonance imaging

MTT = Methylthiazolyldiphenyl-tetrazolium bromide

mV = millivolt

Mw = Molecular weight

Na_2SO_4 = Sodium sulfate

$NaBH_4$ = Sodium borohydride

NaH = Sodium hydride

NaN_3 = Sodium azide

NaOH = Sodium hydroxide

nm = Nanometer

NMR = Nuclear magnetic resonance

NOE = Nuclear overhauser effect

OD = Optical density

OsO_4 = Osmium tetroxide

PBS = Phosphate buffer saline

PCA = Principal compound analysis

PEG = Polyethylene glycol

PET = Petroleum

PET = Photo-induced electron transfer

PET = Positron emission tomography

PIM = Phosphatidylinositol mannose

PL = Poly L- Lysine

PNA = Peanut agglutinin

PPM = Parts per million

Py = Pyridine

QD = Quantum dots

RCA = Ricinus communis agglutinin

RT = Room temperature

SEM = Standard error of the mean

SERS = Surface enhance raman spectroscopy

SPECT = Single-photon emission computed tomography

SWV = Square wave voltametric

TC = Tricarbonyl

TEM = Transmission electron microscopy

TFA = Trifluoroacetic acid

THF = Tetrahydrofuran

TLC = Thin layer chromatography

TMB = Tetramethyl benzidine

TOF = Time of flight

µm = Micrometer

Publications

1. **S. Sangabathuni**, R. V. Murthy, P. M. Chaudhary, B. Subramani, S. Toraskar and R. Kikkeri, "Mapping the glyco-gold nanoparticles of different shapes toxicity, bio-distribution and sequestration in adult zebrafish", (*Just accepted in* *Sci. Rep. (2017)*).
2. **S. Sangabathuni**, R. V. Murthy, P. M. Chaudhary, M. Surve, A. Banerjee and R. Kikkeri, "Glyco-gold nanoparticle shapes enhance carbohydrate-protein interactions in mammalian cells", *Nanoscale*, 2016, **8**, 12729.
3. P. M. Chaudhary,[#] **S. Sangabathuni**,[#] R. V. Murthy, A. Paul, H. V. Thulasiram and R. Kikkeri, "Assessing the effects of different shapes of glyco-gold nanoparticles on bacterial adhesion and infections", *Chem. Commun*., 2015, **51**, 15669. ([#] = equal contribution).
4. H. Bavireddi,[#] R. V. Murthy,[#] M. Gade, **S. Sangabathuni**, P. M. Chaudhary, C. Alex, B. Lepenis and R. Kikkeri, "Deciphering carbohydrate-protein interactions using homologous supramolecular chiral Ru(II)- glyconanoclusters", *Nanoscale*, 2016, **47**, 19696. ([#] = equal contribution).
5. H. Bavireddi, R. V. Murthy, M. Gade, **S. Sangabathuni** and R. Kikkeri, "Supramolecular metalloglycodendrimers selectively modulate lectin binding and delivery of Ru(II) complexes into mammalian cells", *Org. Biomol. Chem*., 2016, **14**, 10816.
6. M. Gade, P. Khandelwal, **S. Sangabathuni**, H. Bavireddi, R. V. Murthy, P. Poddar and R. Kikkeri, "Immobilization of multivalent glycoprobes on gold surfaces for sensing proteins and macrophages", *Analyst*, 2016, **141**, 2250.
7. R. V. Murthy, P. Bharate, M. Gade, **S. Sangabathuni** and R. Kikkeri, "Effect of transition metals on polysilaic acid structure and functions", *ChemMedChem*., 2016, **7**, 667.
8. P. M. Chaudhary, M. Gade, R. A. Yellin, **S. Sangabathuni** and R. Kikkeri, "Targeting label free carbohydrate-protein interactions for biosensor design", *Anal. Metods*, 2016, **8**, 3410.
9. **S. Sangabathuni**, R. V. Murthy, M. Gade, H. Bavireddi, S. Toraskar, M. V. Sonar, K. N. Ganesh and R. Kikkeri. "Convergent synthesis of glyco-collagen peptides to identify the marker for wound healing", (*Submitted…*).
10. **S. Sangabathuni**, C. K. Phanendhra and R. Kikkeri, "Synthesis of proline based cyclic and linear glyco-peptides and its lectin and bacterial binding studies", (*Manuscript under preparation…*).

Abstract of Thesis

Carbohydrate-protein interactions (CPIs) are one of the most important and major events on cell surfaces. Basic components involved in the interaction are the cell surface glycans, which demonstrate a sensitive and selective *cis*/*trans* binding with protein counterparts. However, due to weak CPIs, nature facilitates multivalency to target specific proteins. Recently, extensive efforts have been directed toward mimicking these bio-events by replicating the multivalent scaffolds. Significant progress has been achieved in this regard using multivalent glycoprobes. However, other important issues regarding the preparation of multivalent carbohydrates are related to the size, shape, orientation, and local concentration of the sugars with respect to external stimuli. In the following chapters, we have investigated the role of different shapes in carbohydrate-mediated interactions.

Chapter 1 summarizes different multivalent scaffolds and their major applications in targeting carbohydrate-protein interactions. We highlighted the current efforts made in the synthesis of glycodendrimers, glycopeptides, metallo-glycodendrimers, glyconanoparticles, and supramolecular complexes and the role of spatial arrangements, chirality, and symmetry of these multivalent probes in carbohydrate-protein interactions. Finally, we discuss shape-dependent biological interactions that have been reported in literature.

Chapter 2 describes the synthesis of glyco-gold nanoparticles of three different shapes and their applications in bacterial aggregations and infection. More specifically, we have compared the behavior of nanospheres, nanorods and nanostars with mannose and galactose conjugations. The mechanism of aggregation revealed that the large number of surface interaction of rod shaped mannose-AuNPs with *E.coli* ORN 178 compared with spherical and star-shaped AuNPs. Moreover, such sensitive binding can be used for effective inhibition of bacterial infection of cells.

Chapter 3 deals with the shape dependent uptake of glyco-gold nanoparticles (G-AuNPs) by different cancer cell lines. *In vitro* experiments once again showed that rod-AuNPs exhibited the highest uptake than that of the star and spherical counterparts. Further investigation of the mechanism of uptake clearly demonstrated clathrin mediated endocytosis of the specific G-AuNPs. Overall, these results revealed the benefits of different shapes in carbohydrate-mediated interactions.

Chapter 4 reports a systematic evaluation of the toxicity, biodistribution of fluorescently tagged mannose -AuNPs of three different shapes (sphere, rod, and star) in the adult zebrafish model, which could accelerate and provide preliminary results for further experiments in the higher order animal system. ICP-MS analysis and confocal images of various zebrafish organs revealed that shape and different carbohydrates on AuNPs show noticeable different in the rate of biodistribution and clearance of G-AuNPs. Among the different shapes, rod-AuNPs exhibited the fast uptake, while, star-AuNPs displayed prolong sequestration, demonstrating its potential therapeutic efficacy in drug delivery. These findings provide new insight into the use of the zebrafish as a potential *in vivo* system to study glyco-materials.

Chapter 1

Inroduction to Multivalent Glycoprobes to Study Carbohydrate-protein Interactions (CPIs)

1.1 Introduction

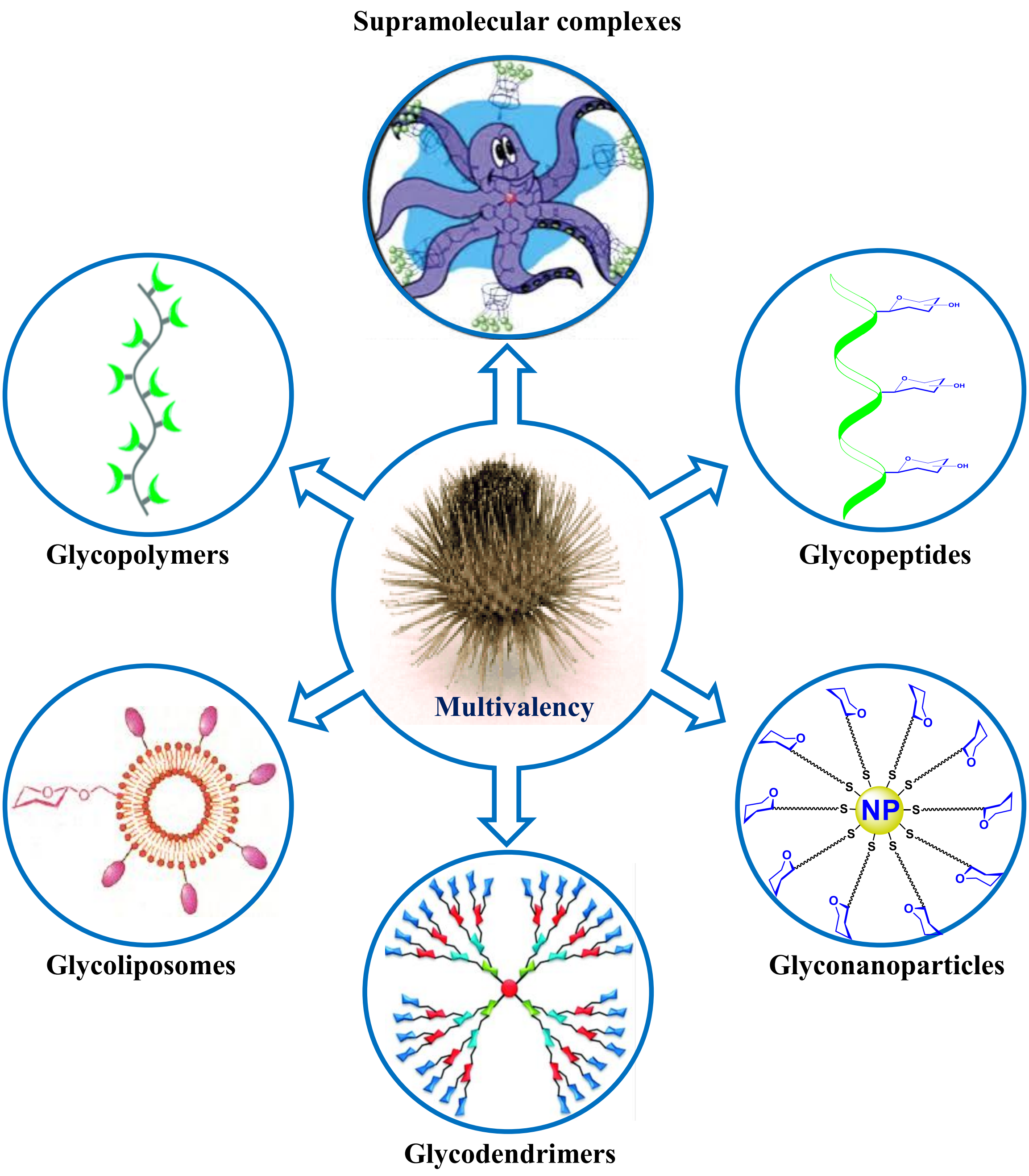

Figure 1. Types of multivalent glycoclusters.

Mimicking the cell surface glycocalyx with multivalent glycoconjugates are one of the intense investigations due to their fascinating biological properties.[1] In contrast to weak and non-specific binding that occur between monovalent carbohydrates and proteins, the multivalent display of carbohydrates at the surface of a molecular scaffold is indeed currently used to enhance avidity and selectivity toward specific lectin.[2-3] This process is also called as the c*luster-glycoside effect* [4-5] However, the significance of the size, the valency and the geometry of scaffolds are important parameters to design a high affinity ligands.[6-7] For this reason a large variety of multivalent scafolds have been developed to inhibit and detect infectious agents or to stimulate immunity against cancers or pathogens.[8-11] Linear multivalent scaffolds such as peptides,[12] oligonucleotides,[13] polymers,[14] nanotubes,[15] etc, cyclic scaffolds such as, cyclodextrins,[16] calixarenes,[17] glycophanes,[18] aromatics,[19] etc, dendritic scaffolds such as fullerenes,[20] quantum dots,[21] metal nanoparticles,[22] etc. have been extensively used to construct multivalent glycostructures (Fig 1). The chapter 1 gives an overview of the recent advances on the synthesis of multivalent glycoclusters and their recognition properties toward specific carbohydrates-binding proteins, namely lectins.

1.2 Glycodendrimers

Multivlent structures have been constructed from protein, lipids and polymers displayed a serious limitation to characterize the structure of these neoglyconjugates. Because of this reason, methodologies to obtain structurally well-defined multivalent glycoconjugate systems have become an important area of research activity in recent years. Dendrimers represent a new class of highly branched, homogeneous multivalent glycoconjugates and incorporation of dendritic synthetic is an interesting proposition to generate multivalent glyconjugates.[23-26] The first example of glycodendrimers was reported with lysyl-lysine multivalent scaffolds. Roy et al. and Jayaraman et al. utilitized this scaffold to synthesize multivalent carbohydrate ligands.[27-28]

Dendrimers are well defined highly branched complexes that emanate from a central multifunctional core unit and terminated with multiple reactive groups at their peripheries for further conjugation of bioactive molecules including saccharides. Dendrimers can be synthesized in a step-wise process with many reactive groups around their peripheries in a controlled manner, which provides homogenous and very low polydispersities structures.

Glycodendrimers were classified as: (1) carbohydrate-coated; (2) carbohydrate-centered; and (3) carbohydrate-based glycodendrimers (Fig 2). Many research groups have contributed to design and synthesize of these glycodendrimers. Key coupling reactions such as amide and thiourea coupling, glycosylation and photochemical cycloaddition reaction were

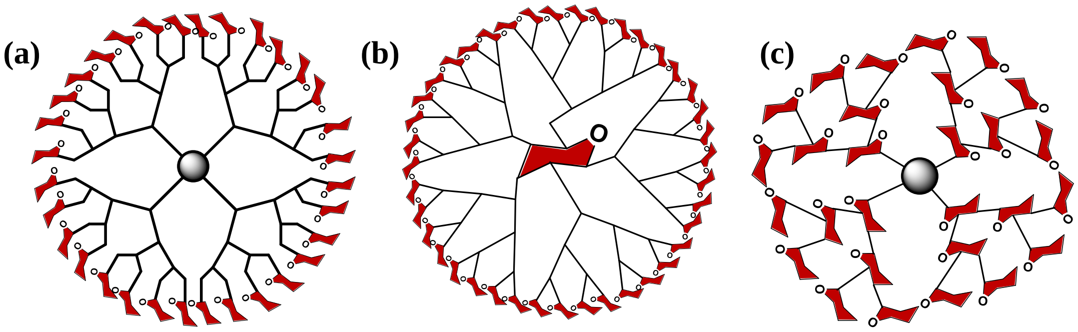

Figure 2. Different types of glycodendrimers (a) carbohydrate coated peripheral functional groups; (b) carbohydrate at the centre and pheripheral; (c) carbohydrate-based dendrimers.

employed to generated glycodendrimers. The binding affinity of multivalent system can be explained by two different mechanisms. Pohl and Kiessling et al. reported molecular level statistical effect in which multivalency displayed a localized concentration of the sugar at the receptor binding site and enhance the binding affinity. In the second mechanism, the multivalent ligand cross-linked binding sited either in adjacent receptors or in a single multivalent receptor and enhances the binding avidity.

There are two methods generally accepted for the synthesis of multivalent glycodendrimers: the convergent approach and the divergent approach. A convergent synthesis is essentially the polyvalent construction from the 'outside-in' toward a suitable core. Here, synthesis of ligand carrying carbohydrates followed by dendron integration. A divergent approach corresponds to opposite building from the 'inside-out' starting with a multi-functional core. A suitable glycodendrimers was constructed followed by encapsulation of carbohydrate at the final modification step. Both approaches result in glycoclusters having 3-dimensional topology similar to cell surface glycans topology and play an important role in elucidating carbohydrate-protein interactions. However, the divergent method is considered to be more suitable for generation of glycodendrimers, as it is more straightforward to control the clusterization and multivalency (Fig 3).

1.2.1 Carbohydrate-coated dendrimers: One of the most well studied carbohydrate coated dendimers are from polyamidoamine (PAMAM) dendrimers[29] and poly(propylene imine) dendrimers (Fig 4).[30] Both types of dendrimers have tertiary amine-based skeletons, displaying primary amines around their periphery to which carbohydrate scaffolds are incorporated by urea, thiourea and amide bonds chemistry.

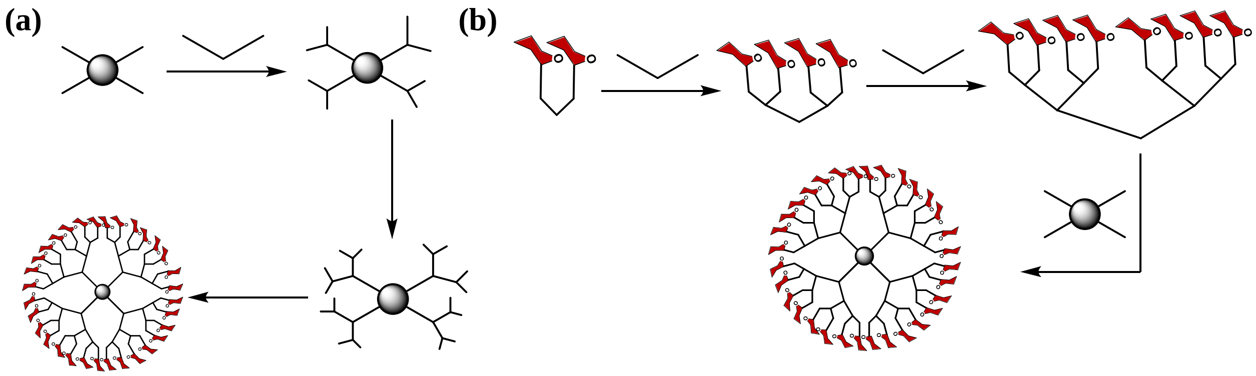

Figure 3. Synthetic strategy of glycodendrimer (a) Convergent and (b) Divergent synthesis.

1.2.2 Carbohydrate-centered dendrimers: Monosaccharides are multiple hydroxyl terminals and they have found and used as a core for glycoclusture synthesis.[31-32] Lindhorst et al. was first synthesized carbohydrate centered dendrimers to which linkers are attached to hydroxyl group of sugar.[33] Using this strategy Kitov et al. conjugated Gb3 trisaccharide with all hydroxyl groups of *β*-D-glucose sugar which results in pentameric arrangement of Gb3 sugar in starfish morphology. This starfish multivalent ligand showed millionfold increase in affinity towards the pentameric Verotoxin B-subunit compare to monovalent Gb3 ligand (Fig 5).[34]

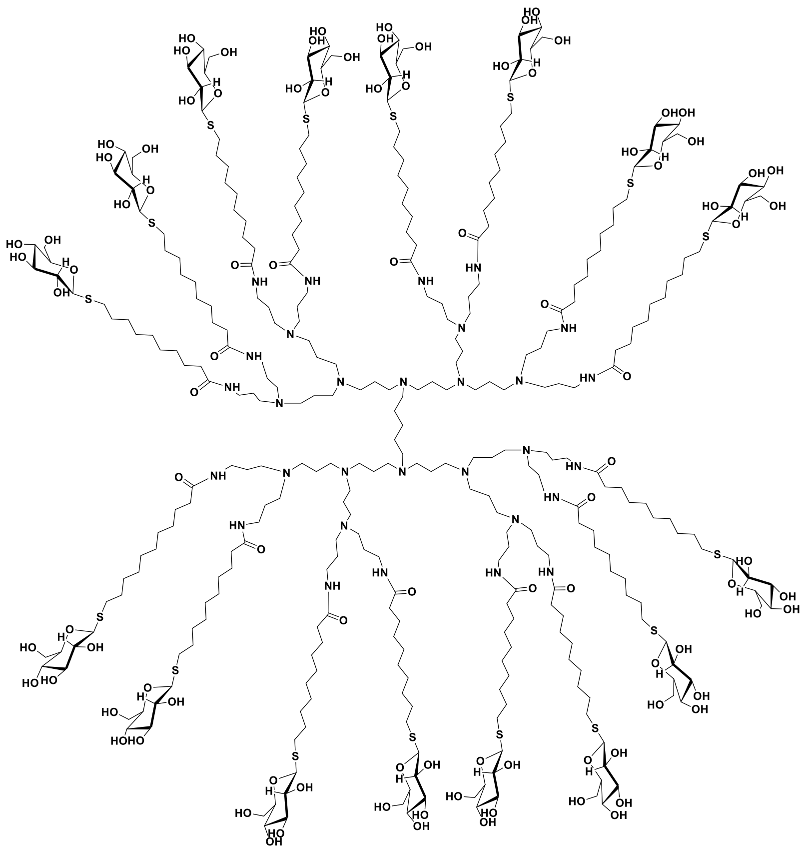

Figure 4. β-D-Glucose coated Poly(propylene imine) glycodendrimers.

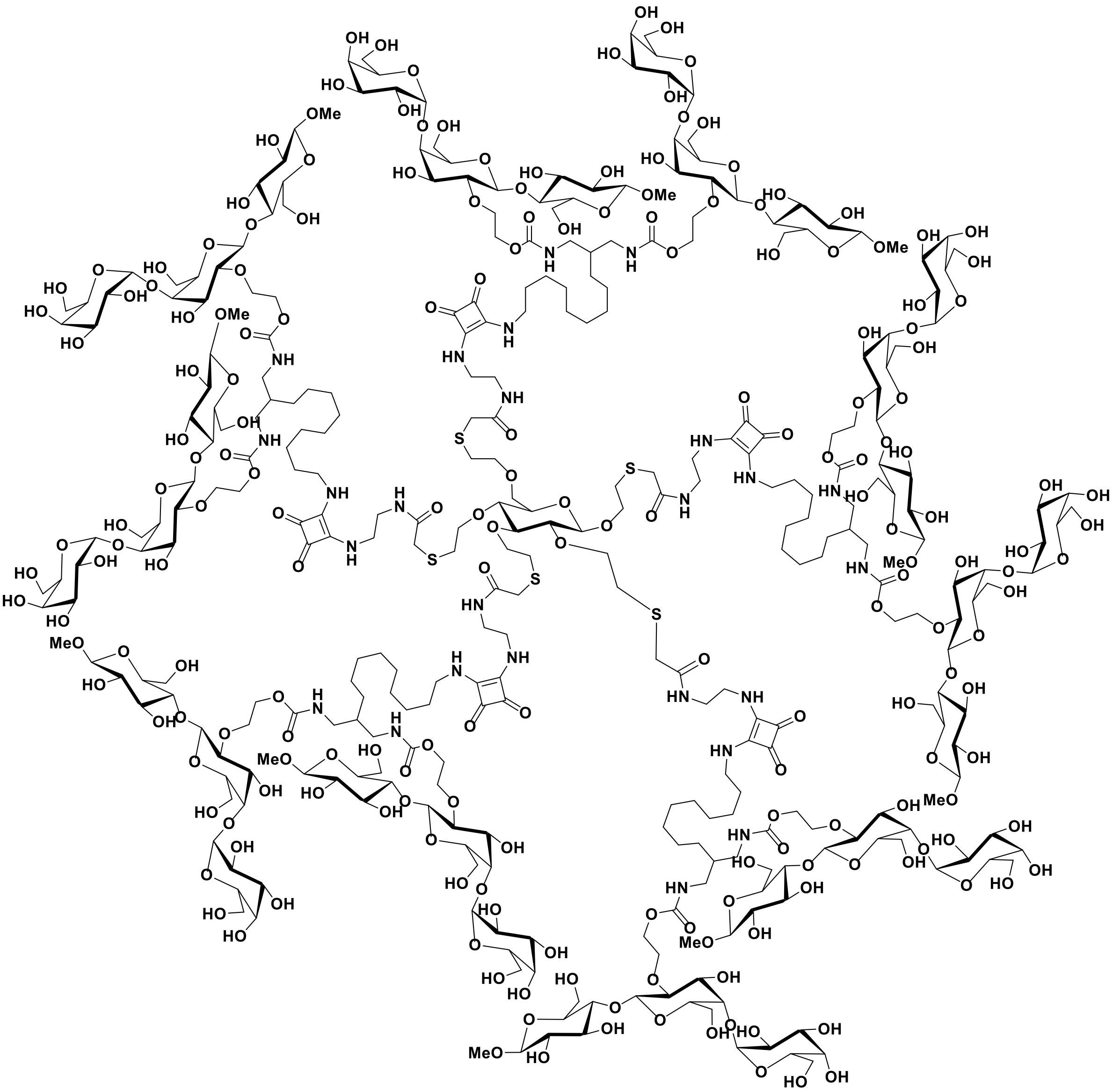

Figure 5. STARFISH compound of two copies of the Gb3 oligisccharide conjugated to the β-D-glucose sugar.

Another example of carbohydrate-centred dendrimer is cyclodextrin, Cyclodextrins (CDs) are find to be interesting cores for dendrimers synthesis, as they would allow combination of both multivalent structures with the ability to complex small hydrophobic molecules within the cavity of the CD moiety. Stodaart et al. has been developed a mild and efficient method for achieving CD per-substitution, which involves the radical photoaddition of glycosyl thiols onto allyl ether substituted β-CDs results in multivalency glycocluster.[35] Using this method seven sugar residues can be attached to either the primary or secondary faces of the β-CDs in good yield (Fig 6).

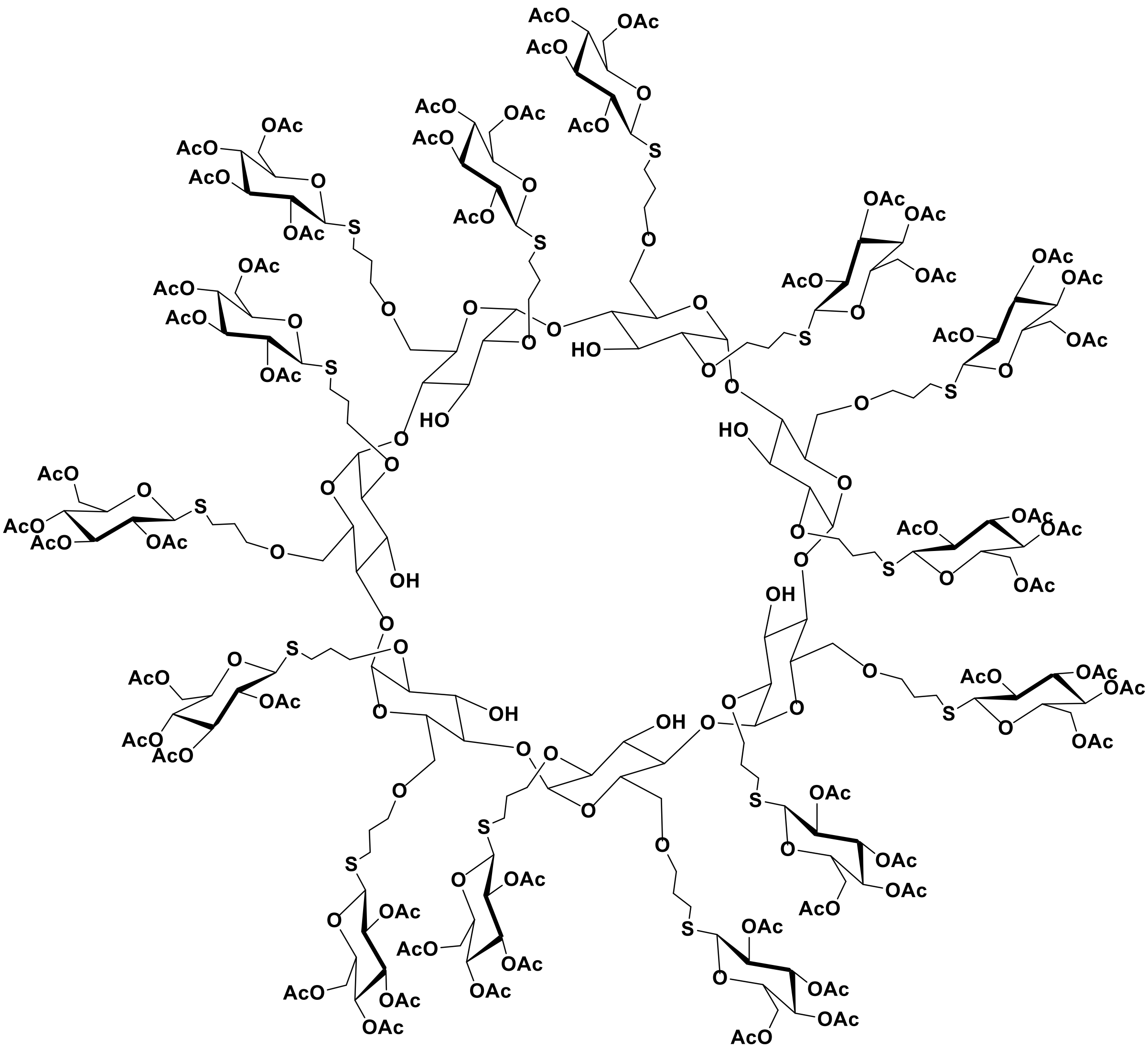

Figure 6. Radical photoaddition of peracetylated β-glucose onto the primary and secondary hydroxyl group of the β-CD.

1.3 Metallo-glycodendrimers

1.3.1 What makes metallo-glycodendrimers special?: Metal complexes have a very broad range of optical, magnetic, or redox properties that could be, in principle, exploited for the development of specific lectin-carbohydrate biosensors. A metal center can be envisaged as a structural locus that organizes chelators in specific geometries or clustures to propagate specific sugar mediated lectin binding. The relative ease of synthesis of metal complexes can allow the generation of small libraries of related compounds. Moreover, variations can be introduced by modifying the ligands or metal center to tune the multivalency and structural arrangements of the glyco-clusters. These variations render metal complexes advantageous over their organic counterparts, where analogous geometrical changes are often more difficult to introduce. Finally, metal complexes allow one of the best methods to study the influence of internal or external chirality and orientation of the sugar clusters with respect to external stimuli.

1.3.2 Glycodendrimers with transition metals: Iron complexes are one of the earliest examples of metalloglycodendrimers to be evaluated for the importance of chirality during specific carbohydrate protein interactions. Sasaki et al. showed the synthesis of the sugar substituted bipyridine ligands, which subsequently form Δ and ^ sugar Fe(III) complexes to study specific carbohydrate-lectin interactions.[36] Metallo-glycodendrimers focused on Cu(II), Fe(II), Ir(II), Rh(II) and Ru(II) were also reported.[37-42] Among these metals, ferrocene and Ru(II) complexes were most attractive metallo-glycodendrimers for their robustness and photophysical properties.[43] Ru(II) complexes exhibit a low excited triple metal-to-ligand charge transfer state (^{3}MLCT) and the room temperature ^{3}MLCT lifetimes were up to 1μs, high-emission quantum yields and strong oxidazing and reducing capabilities.[44-45] Ru(II) dendrimers were extensively used as photo-catalysts, as reactions in intermolecular and intramolecular energy and electron-transfer process.[46] The synthesis of Ru(II)-glycodendrimers were started from 2,2'-bipyridine (bpy) functionalization at 4 and 4' positions, so that a variety of dendritic wedges could be appended to build glycodendrimers contained on $[Ru(bpy)_3]^{2+}$ core. Both convergent and divergent method was applied to synthesize Ru(II)-glycodendrimers bearing various number of carbohydrates. In the convergent method, ligands carrying sugar dendrons were synthesized separately and then united with Ru(II) ion to get octahedral symmetric metallo-glycodendrimers.[47] A straight forward Huisgen [3+2] cyclo-addition, host-guest strategy were applied in divergent method to synthesize a library of metalloglycodendrimers (Fig 7).[48]

The luminescent Ru(II) and Ir(II) complexes of mannose or galactose glycodendrimers have been utilized to address biochemical and biomedical questions.[49-50] In this context, carbohydrate-protein interactions were studied by using fluorescent turbidity assay and microarray techniques. Seeberger et al. have shown that the density of sugar around the metal complex directly influence the binding affinity and photo-physical properties of the complexes. This alteration in photo-physical properties is due to better shielding of Ru(II) core by the topology of the hydrophilic core of the sugar.[49] Based on optical properties of Ru(II) complexes, lectin biosensors were developed on microarray plates. ConcanavalinA (ConA) lectin was immobilized on a microarrays prior to incubation with mannose or galactose Ru(II) complexes. Upon fluorescence scanning of rinsed slides, strong fluorescent signals were observed on slides that were incubated with mannose complexes and ConA could be detected at as low as 0.125 mg/mL (620 nM). To probe the versatility of the Ru(II)-glycodendrimers as a potential lectin biosensor, photo-induced electron transfer (PET) between Ru(II)-glycodendrimers and methyl viologen dication (MV^{2+}) was applied to detect ConA at 25–28 nM (Fig 8c).[51] The redox properties of Ru(II) complexes were also exploited to develop electrochemical biosensors. ConA was immobilized on a self-assembled monolayer gold surface prior to incubation with Ru(II) complexes.[52] The chip was transferred to a cyclic voltameter cell to record square wave voltametric (SWV) signal of Ru(II) complex. Based on the electrochemical signals, lectin-metalloglycodendrimer interaction was established and ConA was sensed at a lowest limit of 2.5 nM, which was comparable to other sugar sensor models. A reusable sugar sensor, based on the displacement of the redox glyco-probes by preferential lectin binding carbohydrates was also developed. Using this method biologically important sugars such as glucose, phosphatidylinositol mannose (PIM) glycans were detected at a detection limit of

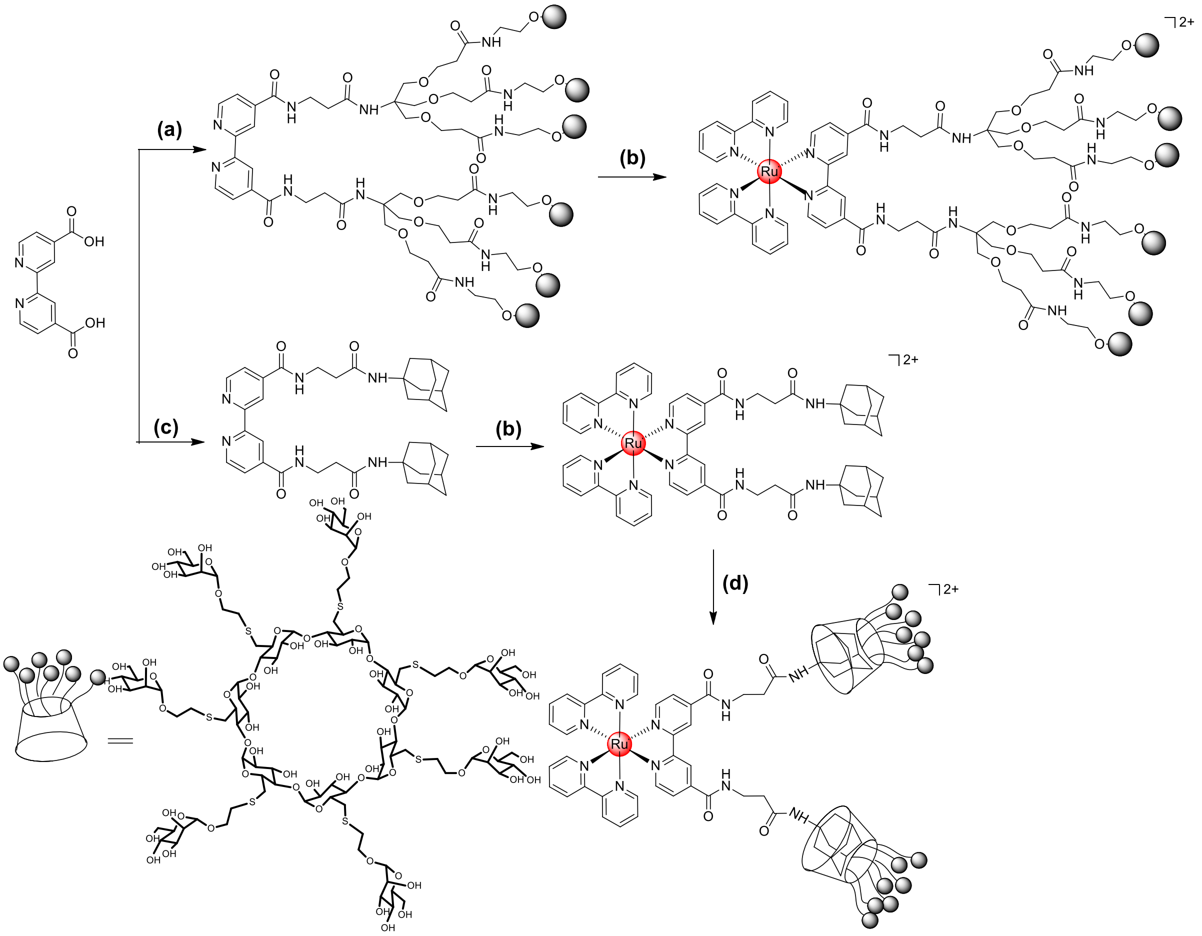

Figure 7. Assembly of metallo-glycodendrimers using convergent method and host-guest method: (a) $SOCl_2$, mantripod-amine linker, TEA, RT, 12 h; (b) $Ru(bipy)_2Cl_2$, EtOH, 80°C, 4 h; (c) $SOCl_2$, man tripod-amine linker, TEA, RT, 12 h; (d) CD-Man, H_2O.

7.0 and 0.6 μM concentrations. The reproducibility of the above chip was established by exposing the gold chips to boronic acid substituted merrified resin to regenerate the lectin surface for the next measurement (Fig 8a).

More recently, Seeberger et al. have extended the synthesis of metalloglycodendrimers by using host-guest concept. Fluorescent Ru(II) complexes were functionalized with 14, 28 or 42 mannopyranosyl units using adamantine-cyclodextrin based host-guest chemistry. These systems proved to be very well suited to probe the structural arrangement of glycodendrimer for efficient binding to immobilized ConA lectin by surface plasmon resonance (SPR). Additionally, the optical properties of Ru(II)-glycodendrimers allowed direct imaging of their association with *E. coli* (stain ORN178), having mannose binding FimH lectin in the pili, by confocal microscopic imaging (Fig 8d).[48]

Kikkeri et al. focused on this area to development of metalloglycodendrimers that can be used to increase the local concentration of essential elements to amplify the growth and other functions in living species. A catechol coupled Fe(III) glycodendrimers have been prepared using self-assembly process for targeting a specific stain of *E. coli* (ORN 178) and showed that the interaction of Fe(III)-glycodendrimers and FimH receptor mediated iron delivery, inducing iron mediated growth promotion, by growth promotion assay and LB plate assay (Fig 8b).[37] These results have confirmed that transition metallo-glycodendrimers can be use in biosensors and imaging studies.

1.3.3 Complexes with lanthanide metals: Among lanthanides, Gd(III) complexes are the most studied and popular choice for functionlization with carbohydrates to obtain Gd(III) based glycodendrimers. Lanthanide ions specially Gd(III)-glycoconjugates have been extensively used in Magnetic Resonance Imaging(MRI), which is a diagnostic modality based on the enhancement of contrast given by paramagnetic contrast agents (CAs). Gd(III) complexes demonstrated to be the most suitable paramagnetic CAs for MRI, due to the high paramagnetism of the Gd(III) ion ($4f^7$) and to its slow electron spin relaxation.[53-54] Andre et al. have successfully synthesized a new class of DOTA (1,4,7,10-tetrakis(carboxymethyl)-1,4,7,10-tetraazacyclododecane) monoamide- linked glycoconjugates (glucose, lactose and

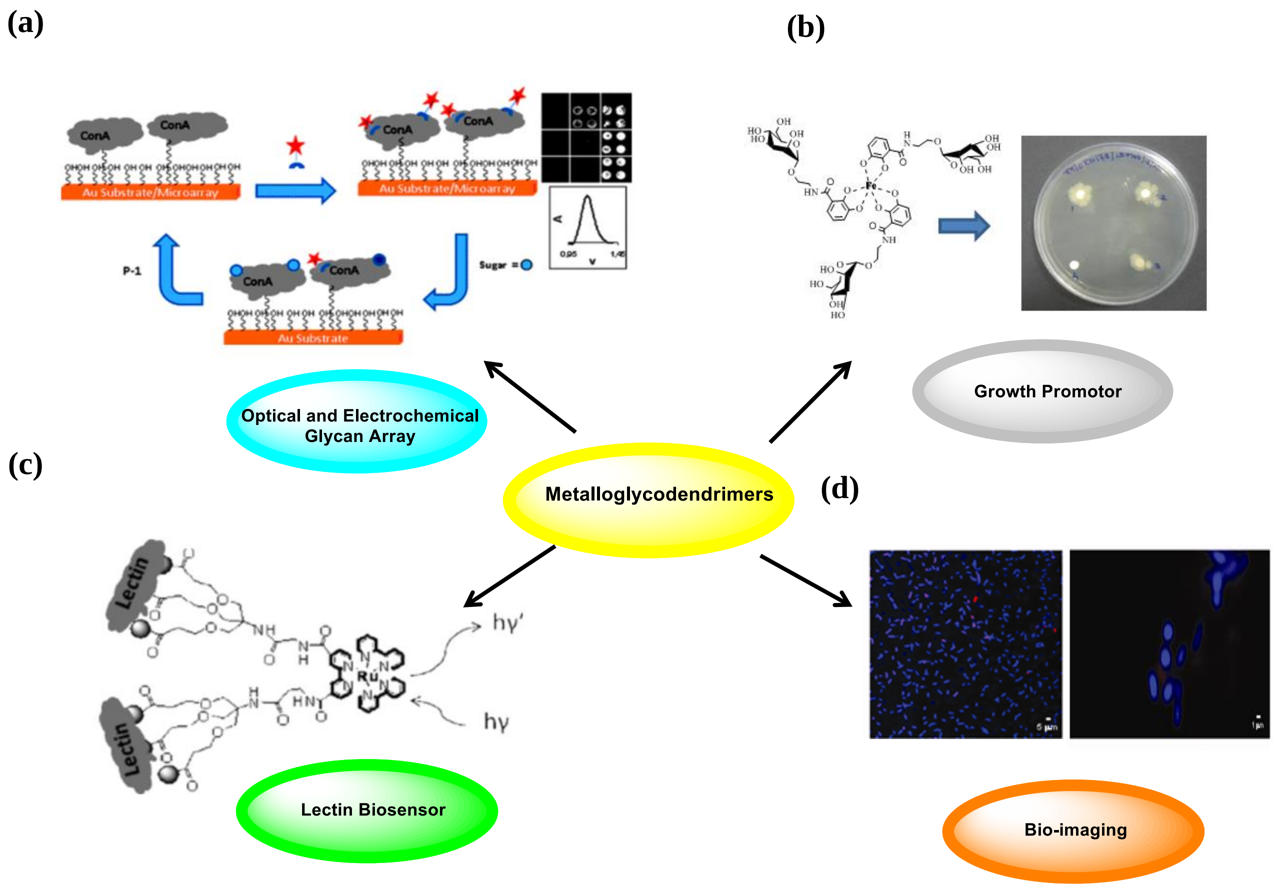

Figure 8. Applications of metallo-glycodendrimers**.**

galactose) of different valencies (mono, di and tetra) and their lanthanide ions complexes such as Gd(III), Eu(III) and Sm(III) ions. The authors also studied the interaction of Gd(III)-glycoconjugates *in vitro* with the model lectin Ricinus communis agglutinin (RCA) through relaxometric measurements. Their results could open the way for the study of Gd(III)-glycoconjugates as potential candidates for lectin-mediated molecular imaging agents.[55] Similar kind of work has been carried out by Fulton et al. where they have synthesized glycoconjugates of Gd(III) complexes with enhanced relaxivity as sharp contrast agents for MRI.[56] Vera et al. have also developed Gd-DTPA conjugate of polylysine (PL) derivatized with galactosyl groups (Gd-DTPA-gal-PL) as potential contrast agents for liver MRI by targeting the hepatocyte ASGPR (asyaloglycoprotein receptor) and tested in cells and mice.[57] Gd(III)-based glycodendrimers have also been shown to be useful for *in vitro* and *in vivo* (X. laevis embryos) visualisation and localisation of gene expression by MRI (Fig 9a).[58-59]

The fluorescent and relaxometric properties of Eu(III) and Gd(III) complexes respectively with bound sugars (galactose, glucose) were used to gain mechanistic insights into their water binding behavior.[60] Very recently Rodrigues et al. have reported the synthesis of a luminescent Tb^{3+}-DOTA complex bearing an α-D-mannose residue and the related study of binding affinity with concanavalin A (ConA) labelled with rhodamine-B-isothiocyanate (RITC-ConA). Luminescence spectroscopy and dynamic studies showed the changes in emission spectra that can be ascribed to a luminescence resonance energy transfer (LRET) from Tb(III) complex (donor) to RITC-ConA (acceptor).The binding constant value between the two species was found to be one order of magnitude larger than those previously reported for similar types of recognition (Fig 9b).[61] These results confirmed that the possibility to generate lanthanide-glycodendrimers, which can be used in MRI imaging studies.

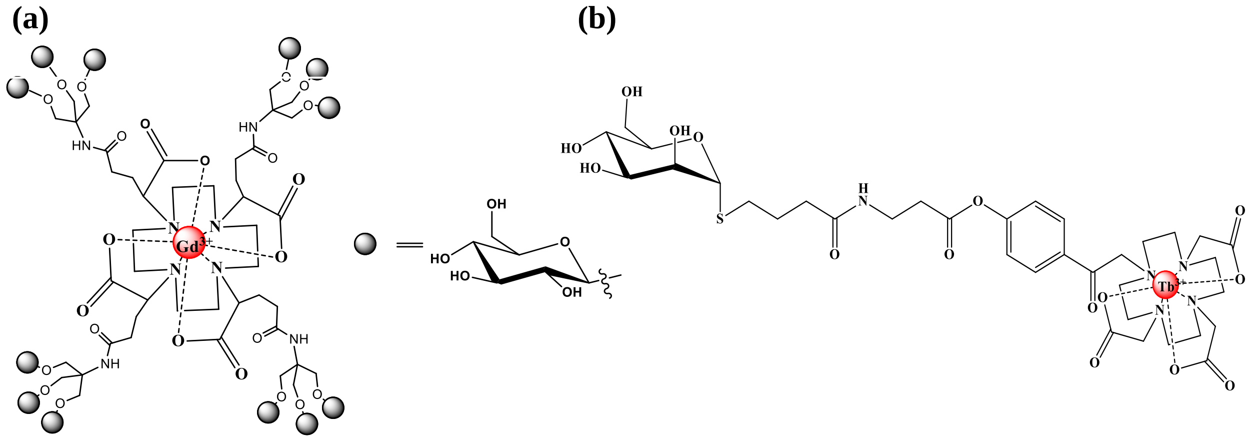

Figure 9. (a) Gd(III) based glycodendrimer; (b) Tb(III) based glycodendrimer.

1.3.4 Metal complexes with radioactive properties: Due to the rapid development of imaging techniques like single-photon emission computed tomography (SPECT) or positron emission tomography (PET) and coupled procedures like PET/computed tomography (CT), radioactive-labeled biomolecules are being increasingly used for the visualization of certain cell types and tissues. Glycoclusters conjugated with radioactive metal complexes are gradually becoming important tools for *in vivo* cell and tissue imaging. Among this ^{99m}Tc(I) based glycoconjugates are the most widely used and extensively studied.[62-63] Most of the synthesized complexes are glucose-based aiming to take advantage of the over expression of glucose transporters (GLUT1). Schubiger et al. tested the cellular uptake of the ^{99m}Tc(I) complexes bound to the C-2, C-3 or C-6 position of glucose by oxygen, in colon carcinoma cells HT29.[64] ^{99m}Tc-DTPA-GSA, a conjugate of galactosylated serum albumin (GSA) with ^{99m}Tc-DTPA (DTPA=3,6,9 tris(carboxymethyl)-3,6,9-triazaundecan- 1,11-dioic acid) (Fig 10a), has been shown to be useful in SPECT (single photon emission computed tomography) hepatic imaging to assess ASGPR in mice[65] and used clinically in humans.[66-67] The targeting of the ASGPR has been demonstrated both in a cell line and mice with a ^{111}In-radiolabelled galactopyranosyl conjugate of DOTA (1,4,7,10-tetrakis(carboxymethyl)- 1,4,7,10-tetraazacyclododecane).[68] So far, ^{99m}Tc-/^{188}Re-DTPA (diethylenetriamine pentaacetic acid) complexes are the most promising candidates to act as functional imaging agents which are derived from 2-*N*-2-deoxy-D-glucosamine. These derivatives were phosphorylated by hexokinase exhibiting cellular uptake probably by a multifunctional glucose transport system and reveal higher tumor-to-tissue ratios than observed for other tracers in *in vivo* experiments in small animal tumour models.[69-70] Another radiolabelled metal complex of 2-^{18}F-2-deoxy-D-glucose (FDG) is used as a sugar-based tracer to monitor glucose transporter (GLUT1) activity by PET/CT, and to image tumor cell metabolism (Fig 10b).[71] Despite all these results, only few *in-vivo* experiments are reported with radioactive metallo-glycodendrimers. Therefore, the final goal should lie in the development of stable and facile method to synthesize radioactive glycodendrimers.

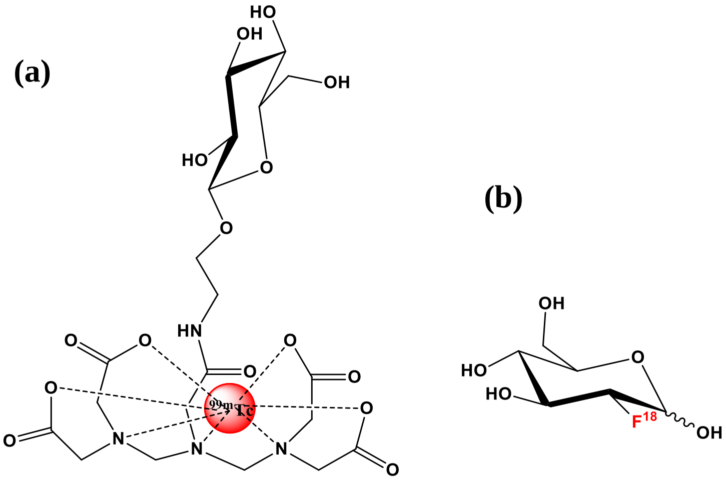

Figure 10. (a) Radiolabelled ^{99}Tc glycodendrimer; (b) 2-[^{18}F]-fluoro-2-deoxy-D-glucose (FDG).

1.4 Glycopeptides

Glycoproteins are polymer network of sugar conjugated peptides. It has been mainly classified into 3 types, *N*-linked glycopeptide, *O*-linked glycopeptide, and *C*-linked glycopeptides. The synthetic mimics of the cell surface glycocalyx by glycopeptides are being the object of intense research investigations due to their fascinating biological applications. Unlike synthetic glycopolymer systems, which were formed from rational considerations about multiplicity, nature prefers to design a customized glycopeptides with defined spatial orientation of the carbohydrate moieties, enabling the specific carbohydrate-protein interactions. The advantage of applying peptides backbone is that a variety of analytical methods can be incorporated for structural characterization, thus, not only the distance between the ligands but also the secondary structure of the glycopeptide can be controlled.

The advantages of peptide-backbone-based scaffold structures compare to other polymeric structures are that they are monodisperse, easy to synthesize with variable length by chemical solid phase peptide synthesis and established orthogonal protecting-group strategies. Furthermore, side-chain functionalities of amino acids can be easy to modify with different substitution. Synthetic glycopeptides scaffolds are classified based on its secondary structures into (1) disordered, (2) helical and (3) cyclic system (Fig 11).[72]

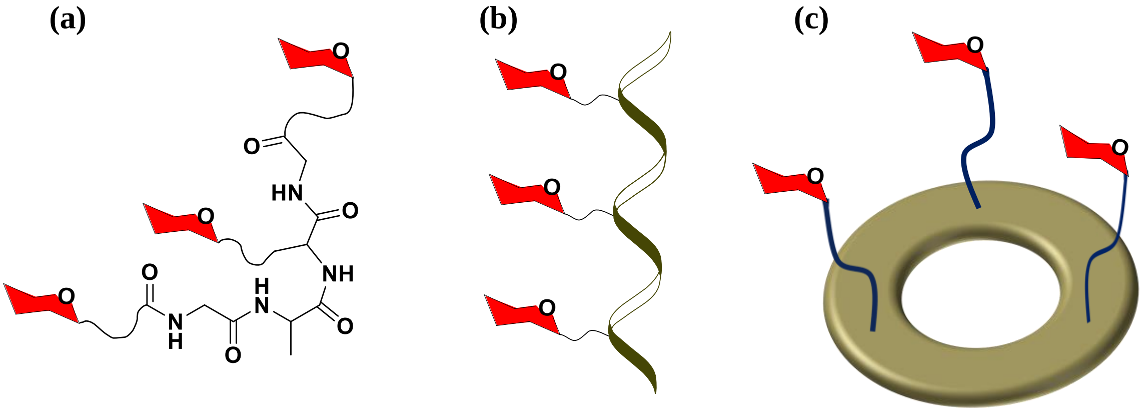

Figure 11. Peptide based multivalent scaffolds. a) Disordered or linear peptide structure; (b) Helical structure; c) Cyclic structure. (Sugar molecules are covalently conjugated to the amino acid side chains).

Linear glycopeptides carrying functional groups are extensively used to synthesize glycopeptides. The best known example is poly-l-glutamic acid (PGA), to which the carbohydrate scaffold are introduced in the carboxyl side chains through amide coupling reactions. The resultant glycopeptides are having flexible structure to interact with lectins. In addition, low toxicity, immunogenicity, biodegradability and water solubility of the glycopeptides enhance its biological signficiance. The conjugation of Ganglioside with PGA showed the picomolar inhibition acitivity of trimeric hemagglutinin of the influenza virus.[73]

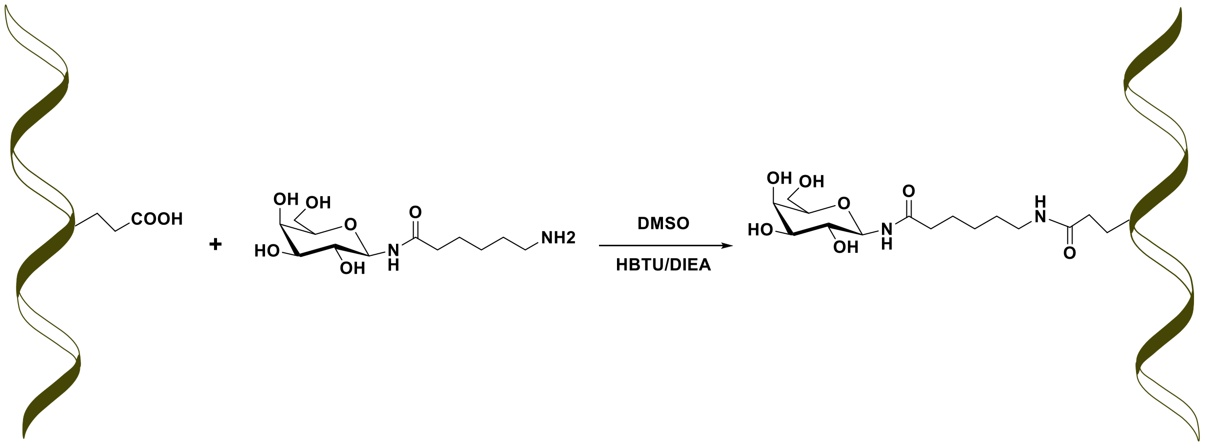

Figure 12. Glycosylation of α-helical polypeptide with N-(ε-aminocaproyl)-β-D-galactosylamine.

Kiick et al. reported alanine-rich helical peptide backbone to inhibit cholera toxin. The sugar scaffold were conjugated to glutamate side and incorporated into hexyl amino spaces so that the sugar scaffolds were maintain different distances and influence the binding affinity. Circular diachorism (CD) spectroscopic measurement of the peptide before glycosylation and after showed no such significant difference, indicating that glycopeotides exhibited similar helical confirmation after glycosylation and thermal stability (Fig 12).[74]

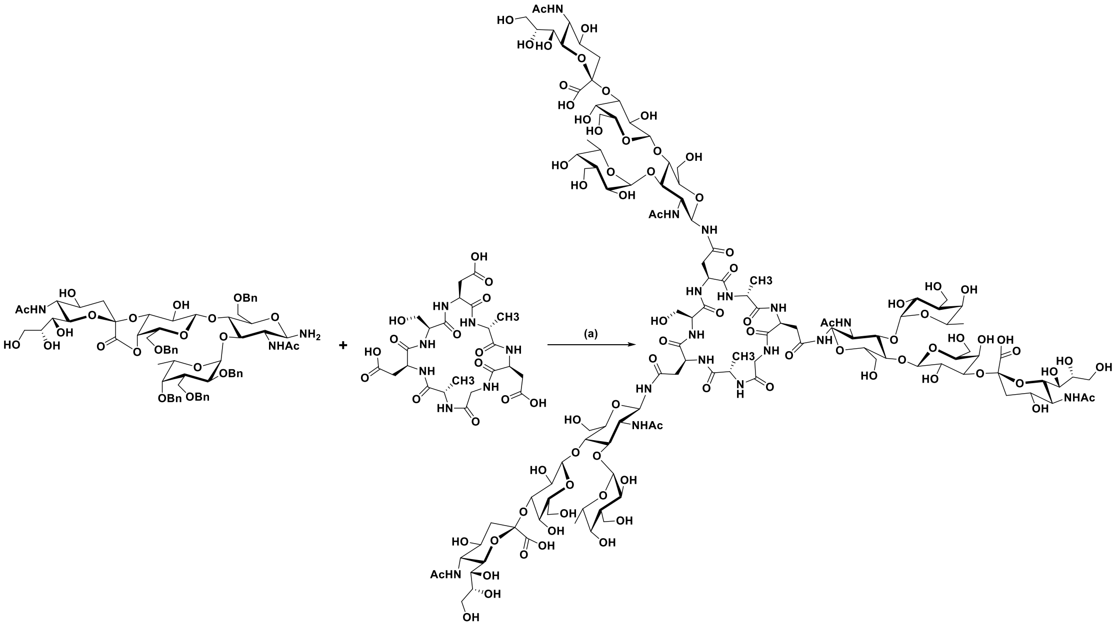

Figure 13. C3-symmetry arrangement of sialyl lewis^x conjugated glycodendrimers (a) HATU (3 eq), DIPEA (3 eq), in DMF.

Cyclopeptides enable the distance between the ligands to be controlled. Furthermore, they are adapted by nature and, therefore, biocompatible, which means they have low toxicity and immunogenicity in addition to being water-soluble and biodegradable, their resistance against proteolysis. This ensures both versatility and modularity which has tremendously facilitated the synthetic access to glycostructures with optimized valence, linker, and geometry.

Kunz et al. utilized cyclopeptide scaffold to target E-selectin by using sialyl lewisx lingad. To an aspartic acid unit contacting cyclic heptapeptides were conjugated with sialis lewisx ligand and demonstrated the E-selectin binding affinity. The cyclic peptides showed nearly strong inhibition of (IC_{50} of 0.35-0.6 mM) E-selectin mediated cell-adhesion compared to linker peptide (Fig 13).[75]

1.5 Glyconanoparticles

Despite knowing that carbohydrates are first line of contact for any biological interactions on cell surfaces, the glycomic research was not immediately obvious, mainly due to the extreme complexity and variability of the glycans structure and weak chemical tools used for their interactions studies. Nanomaterials can provide a formidable platform for multivalent ligand presentation through its large surface to volume ratio, increasing the avidity by several orders of magnitude. Nanomaterials (1–100 nm size) (Fig 14) often show unique catalytic, photonic, electronic or magnetic properties but not seen in the bulk material. The bioconjugation on nanomaterials can results new hybrid materials with synergistic properties and multiple applications in sensing, cargo delivery or catalysis.[76]

1.5.1 Glyco-Quantumdots: Quantum dots (QDs) are spherical semiconductor nanoparticles with a diameter of 2-10 nm. Changes in the particle size of quantum dots sowed drastic differences in their characteristics such as optical absorption, excitation energies. QDs are constituted with highly toxic substrates, such as cadmium and selenium and shows native inability to disperse within biological compatible solutions. However, fuctionalization of QDs with different glycans confer biological activity to QDs and along with that it improves their solubility and stability in water. The most difficult challenging task of glyco-QDs is the synthesis of glycoconjugates with reduced toxicity and nonspecific interactions. Two categories of glycomaterials based on the source of carbohydrates immobilized on QD surfaces can be found. Naturally isolated glycolipids, glycoproteins, proteoglycans and lipopolysaccharides have been directly conjugated on QDs using self-assembly or synthetic conjugation techniques.

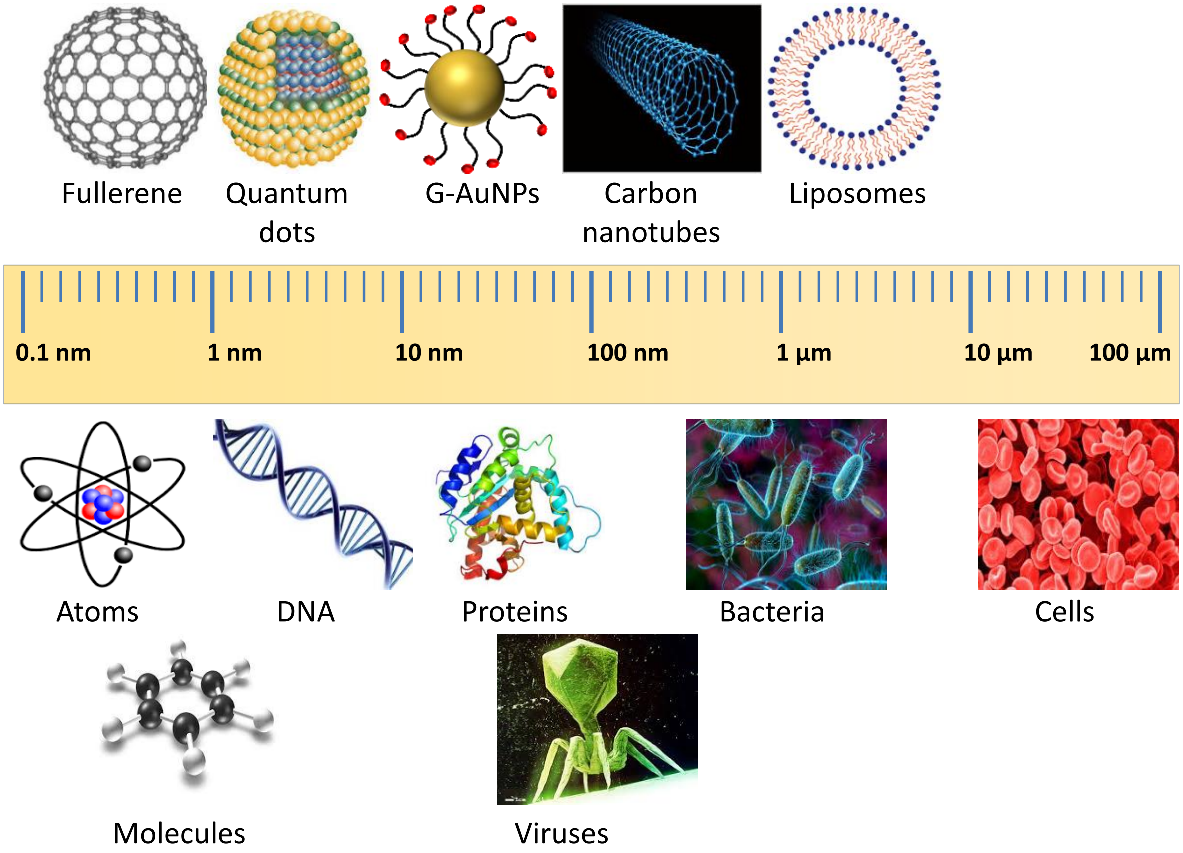

Figure 14. Schematic representation of Glyconanoparticles.

Seeberger et al. reported a simple and convenient method to prepare different glucose, galactose and mannose-capped PEGylated QDs, that can be used for *in-vitro* and *in-vivo* applications. CdSe/ZnS core glyconanospheres were prepared by ligand exchange with tri-*n*-octyl phosphine/tri-*n*octyl phosphine oxide (TOP/TOPO)-capped QDs with thioctic acid conjugated PEG2000-amine.[77] The terminal amine was further reacted sugar scaffolds such as galactose, mannose with acid terminal to synthesize glyco-QDs. Furthermore, they have shown that QDs capped with D-galactose are preferentially taken up via asialoglycoprotein receptor (ASGPR)-mediated endocytosis *in* V*itro*. The uptake of Gal-capped QDs can be partially inhibited by knockdown of ASGPR1. Moreover, in the mouse model, QDs capped with D-mannose and D-galactosamine sequester specifically in the liver.

1.5.2 Glyco-ironnanoparticles: Magnetic resonance imaging (MRI) is one of the most important non-invasive, biomedical imaging techniques and capable of providing both anatomic and physiological information in three dimensions. Contrast agents like iron nanoparticles and gadolinium complexes with high magnetic susceptibility and paramagnetic natures enhance the sensitivity for the detection of inflamed or diseased tissues considerably. By functionalization of iron nanoparticles with biomolecules imaging of specific tissue or disease site can be enhanced.

Recently, Davis et al. and Seeberger et al. synthesized biocompatible selectin specific carbohydrate ligand conjugated glyco-iron nanoparticles to image the ischemic strokes.[78-79] It has been reported that, brain injury induces up-regulation of the carbohydrate-binding trans-membrane proteins, CD62E (E-selectin) and CD62P (P-selectin), present at the sites of inflammation in brain, thereby offering the opportunity to act as an ideal diagnostic marker. Iron nanoparticles were coated with Sialyl Lewis^x (SiaLe^x) –a targeting vector for CD62 followed by intravenous injection in the tail vein to visualize inflammation in the brain. In this work, selectin expression on activated endothelium in the brain was induced by microinjection of interleukin-1 (IL-1) into the left striatum of the rat. Since the artificial inflammation was used, it is unclear if one can extrapolate to the particular disease (i.e. ischemic stroke). To address this issue, Seeberger et al. used intraluminal thread (ILT) techniques to develop ischemic stroke mouse model. This involved the insertion of an occluding device into the internal carotid of the mice. The thread was removed from a mouse model of middle cerebral artery occlusion (MCAO) after 60 mins. Depending on the length of occlusion, the severity of the reduction in blood flow, and the collateral supply resulting impacts was located either in cortical and subcortical regions.

1.5.3 Glyco-goldnanoparticles: Gold nanoparticles have unique physical properties. They shift their surface plasmon peak between the dispersed and aggregated state, which can be observed by the naked eye, which can be used to develop calorimetric sensors.[76,80-81] Specific bioconjugation of gold nanoparticles via thio chemistry results useful biosensors In addition, there is also a significant effort in using gold for in vivo biomedical imaging and delivery purposes. Gold nanoparticles have another unique property; they enhance the Raman signals of adsorbed dye molecules on their surface. This signal enhancement, which is referred to as Surface Enhanced Raman Scattering (SERS) results in picomolar detection sensitivity of analytes.

Turchi et al. reported microwave irradiation method to synthesize glyco goldnanoparticles. These nanoparticles were used in calorimetric detection of specific carbohydrate-protein interactions.[82] The interaction strength of Au glyconanoparticles with Concanavalin A (ConA) was found to be as follows: maltose > mannose > glucose > lactose > N-linked mannose-5 glycan (Man5). Iyer et al. developed glycolipids conjugated gold nanoparticles for the selective inhibition of shiga toxin.[83] Penadés et al. reported that ten different multifunctional gold glyconanoparticles incorporating sialylTn and Lewisyl antigens, T-cell helper peptides and glucose in well-defined average proportions and with different density were synthesized in a one-step procedure.[84] The method allows the tailoring of complex bio-functional nanoclusters incorporating a set of different ligands in a controlled way and it complements the dynamic place-exchange reaction. Yan et al. reported a new type of glyconanoparticle microarray to study glycan-lectin interactions.[85] The glyco-nanoparticle microarrays were fabricated using the means of photocoupling chemistry, where the printed glyconanoparticles were covalently immobilized on the substrates with high efficiency. The glyconanoparticle microarrays, when probed with fluorescein doped silica nanoparticles (FSNP)-labeled lectin, gave higher signals as compared to fluorescein isothiocyanate (FITC)-labeled lectin or carbohydrate microarrays.

1.6 Factors influence in carbohydrate protein intraction

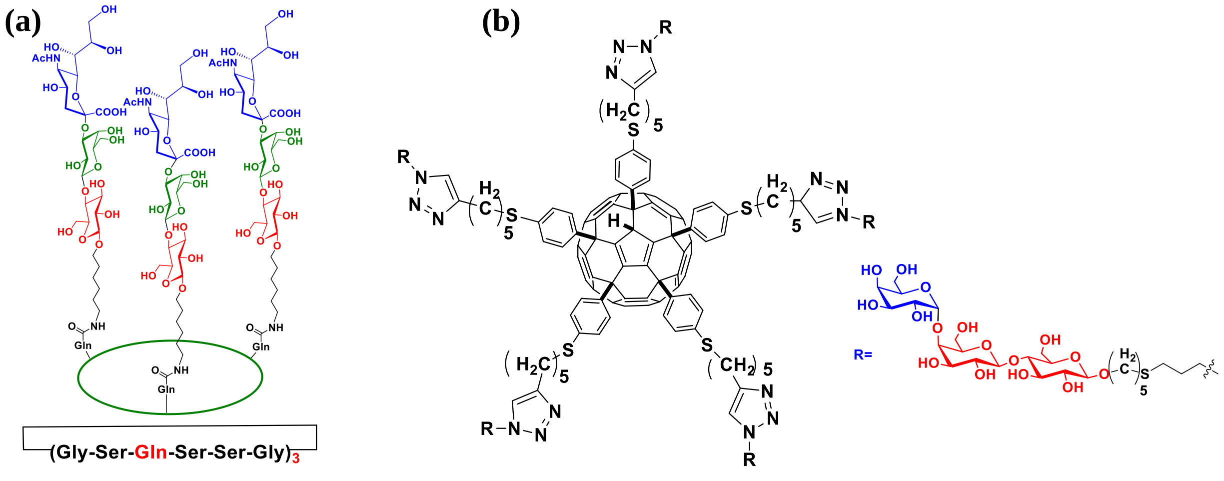

Figure 15. (a) C3-symmetrical ganglioside GM3 trisaccharide; (b) C5-symmetrical arrangement of Gb3 trisacchride.

1.6.1 Symmetry: One of the important considerations for designing multivalent probes is symmetry of the multivalent probes**.** For instance, C5-symmetrical glycoconjugates that orient five Gb3 trisaccharide can neutralize the pentameric Shiga toxin via a specific and multivalent interaction. Similarly, a multivalent C3-symmetrical ganglioside GM3 trisaccharide is a potent inhibitor of hemagglutin protein of influenza virus. Seeberger et al. reported the synthesis of fullerene C5-symmetric of Gb3 trisaccharide and demonstrated it potential application to inhibit the shiga toxin more selectively compare to linear polymers.[86,34] Nishimura et al. reported the synthesis of C3 symmetrical cyclic glycopeptide (GM3) to target influenza virus (Fig 15).[87]

1.6.2 Chirality: Chirality in the dendrimers can also induce defined spatial arrangements.[88-90] Studying how the particular chirality at the glycodendrimer translates its information to the final CPIs is crucial, because usually just one enantiomer of the molecule is biologically active, while the other one may exhibit side effects. Owing to the critical role of chirality in biological interactions, glycoclusters and hydrogels carrying different enantiomers of amino acids and carbohydrates have been synthesized to alter lectin binding affinity and cellular recognition.[91-94] In order to rationalize the enantiomeric effect on carbohydrate–protein interactions, it is essential to examine chirality at different positions of the glycodendrimers, their spatial arrangement, and lectin and cellular interactions. Designing glycodendrimers with multiple chiral centers, For instance Kikkeri et al. synthesized Ru(II) glycodendrimers via the host–guest strategy. Previously, the Seeberger laboratory had introduced the host–guest strategy to synthesize racemic Ru(II)- glycodendrimers by mixing the Ru(II)-adamantyl dendrimers and sugar appended β-cyclodextrins. They provide stereogenic centers at their core (Δ & Λ), C3-symmetry and also optical and electrochemical properties for direct detection of their specific recognition.[51,52] The effect of chirality was further rationalized by incorporating additional chiral centers close to the mannose units on β-CD derivatives to modulate the binding affinity. Overall, we synthesized two distinct series of MGDs. The first group of supramolecular complexes containing racemic Ru(II)- adamantyl derivative (Ru-1) decorated with β-CD (C-A) or mannosylated β-CD derivatives (C-B to C-D) resulted in MGDs (M-1A to M-1D). The second group of molecules bearing chiral Ru(II)- adamantyl derivatives (Ru-2 and Ru-3) hosted β-CD derivatives resulted in MGDs (M-2A to M-2D or M-3A to M-3D) (Fig 16a). The stability, enantiopurity, spatial arrangement of sugars and topology of the complexes were characterized. A lectin inhibition assay of the MGDs was performed using selected C-type lectins. Finally, the optical properties of the Ru(II) complexes were exploited to track cell uptake in vitro and in vivo.[95]

The ligand for the Ru(II) complexes, 4,4′-bipyridine, was linked to L, D or DL-alanine adamantyl molecules via amide bonds. Metal complexes were prepared by refluxing stoichiometric amount of the ligands with $RuCl_3$ in ethanol and the structures and stereochemistry of the products were corroborated by circular dichroism.

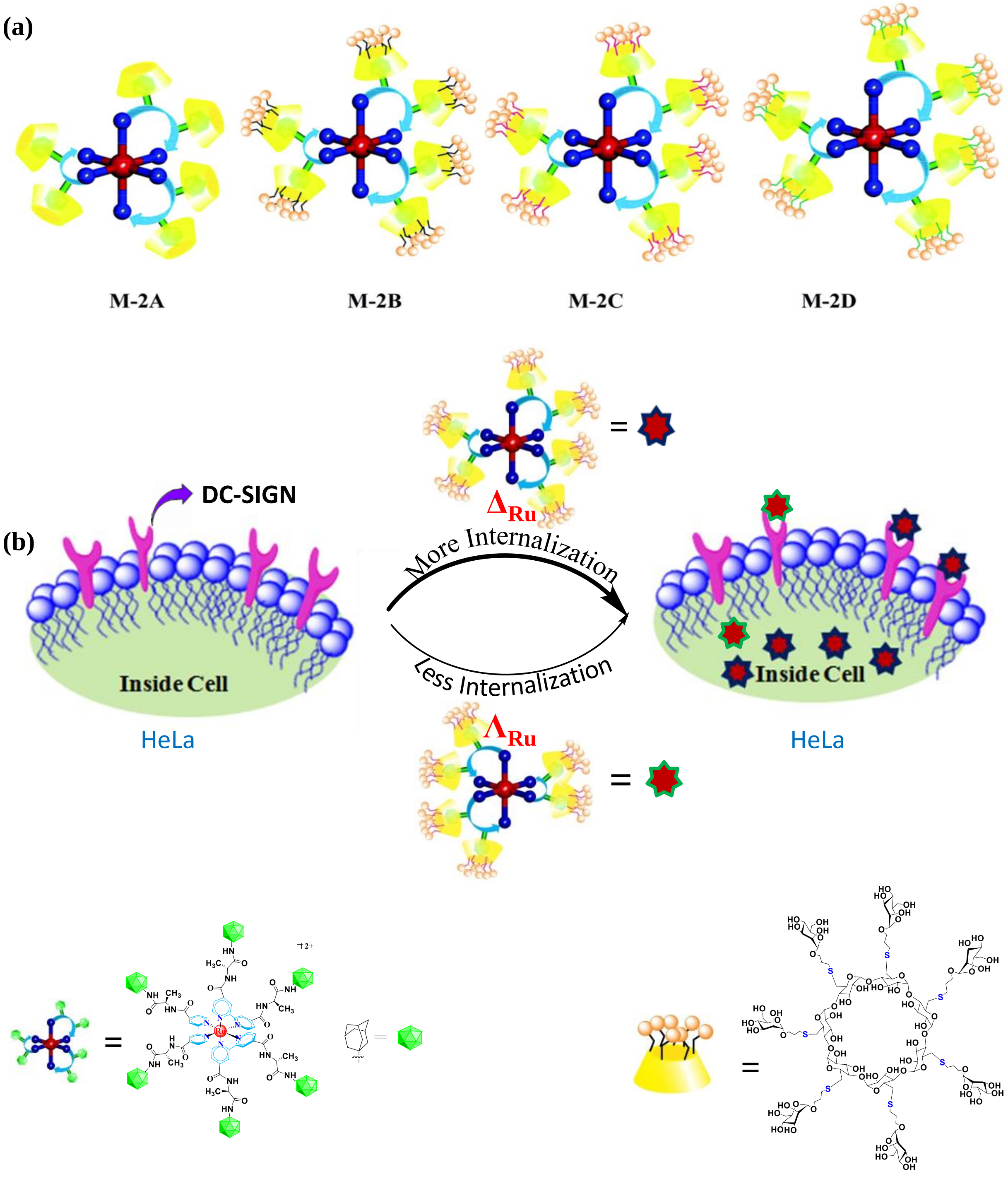

Figure 16. (a) Chiral metallo-glycodendrimers; (b) Internaliszation of Ru(II) complexes in HeLa cells.

Ru(II) complexes were prepared by attaching glycodendrimers via chiral linkers and studied their binding with C-type lectin receptor-Fc fusion proteins, further cell migration experiments showed that Δ-Ru(II) complexes were more internalise into the cell compare to the Λ-Ru(II) (Fig 16b). The interrelationship between carbohydrate–protein interactions and the spatial arrangement of carbohydrates generated by multiple chiral centers in a glycodendrimer were examined. Our results highlight the fact that small changes in the chirality of the compounds had a major impact on selected CPIs.

1.7 References

1) O. Renaudet and R. Roy, *Chem. Soc. Rev.*, 2013, **42**, 4515-4517.
2) M. Mammen, S. K. Choi and G. M. Whitesides, *Angew. Chem. Int. Ed. Engl.*, 1998, **37**, 2755-2794.
3) L. L. Kiessling, J. E. Gestwicki and L. E. Strong, *Angew. Chem. Int. Ed. Engl.*, 2006, **45**, 2348-2368.
4) J. J. Lundquist and E. J. Toone, *Chem. Rev.*, 2002, **102**, 555-578.
5) Y. C. Lee and R. T. Lee, *Acc. Chem. Res.*, 1995, **28**, 321-327.
6) D. Deniaud, K. Julienne and S. G. Gouin, *Org Biomol Chem*, 2011, **9**, 966-979.
7) R. J. Pieters, *Org Biomol Chem*, 2009, **7**, 2013-2025.
8) Y. M. Chabre and R. Roy, *Adv. Carbohydr. Chem. Biochem.*, 2010, **63**, 165-396.
9) A. Bernardi, J. Jimenez-Barbero, A. Casnati, C. De Castro, T. Darbre, F. Fieschi, J. Finne, H. Funken, K. E. Jaeger, M. Lahmann, T. K. Lindhorst, M. Marradi, P. Messner, A. Molinaro, P. V. Murphy, C. Nativi, S. Oscarson, S. Penades, F. Peri, R. J. Pieters, O. Renaudet, J. L. Reymond, B. Richichi, J. Rojo, F. Sansone, C. Schaffer, W. B. Turnbull, T. Velasco-Torrijos, S. Vidal, S. Vincent, T. Wennekes, H. Zuilhof and A. Imberty, *Chem. Soc. Rev.*, 2013, **42**, 4709-4727.
10) T. R. Branson and W. B. Turnbull, *Chem. Soc. Rev.*, 2013, **42**, 4613-4622.
11) F. Peri, *Chem. Soc. Rev.*, 2013, **42**, 4543-4556.
12) M. C. Galan, P. Dumy and O. Renaudet, *Chem. Soc. Rev.*, 2013, **42**, 4599-4612.
13) N. Spinelli, E. Defrancq and F. Morvan, *Chem. Soc. Rev.*, 2013, **42**, 4557-4573.
14) V. Ladmiral, E. Melia and D. M. Haddleton, *Eur. Polym. J.*, 2004, **40**, 431-449.
15) Y. Chen, A. Star and S. Vidal, *Chem. Soc. Rev.*, 2013, **42**, 4532-4542.
16) A. Martinez, C. Ortiz Mellet and J. M. Garcia Fernandez, *Chem. Soc. Rev.*, 2013, **42**, 4746-4773.
17) F. Sansone and A. Casnati, *Chem. Soc. Rev.*, 2013, **42**, 4623-4639.
18) P. V. Murphy, S. Andre and H. J. Gabius, *Molecules*, 2013, **18**, 4026-4053.
19) Y. M. Chabre and R. Roy, *Chem. Soc. Rev.*, 2013, **42**, 4657-4708.

20) P. Compain, C. Decroocq, J. Iehl, M. Holler, D. Hazelard, T. Mena Barragan, C. Ortiz Mellet and J. F. Nierengarten, *Angew. Chem. Int. Ed. Engl.*, 2010, **49**, 5753-5756.

21) R. Kikkeri, P. Laurino, A. Odedra and P. H. Seeberger, *Angew. Chem. Int. Ed. Engl.*, 2010, **49**, 2054-2057.

22) M. Marradi, F. Chiodo, I. Garcia and S. Penades, *Chem. Soc. Rev.*, 2013, **42**, 4728-4745.

23) O. A. Matthews, A. N. Shipway and J. F. Stoddart, *Prog. Polym. Sci.*, 1998, **23**, 1-56.

24) Y. Kim and S. C. Zimmerman, *Curr. Opin. Chem. Biol.*, 1998, **2**, 733-742.

25) A. W. Bosman, H. M. Janssen and E. W. Meijer, *Chem. Rev.*, 1999, **99**, 1665-1688.

26) M. Fischer and F. Vogtle, *Angew Chem Int Edit*, 1999, **38**, 885-905.

27) R. Roy, *Polymer News*, 1996, **21**, 226-232.

28) N. Jayaraman, S. A. Nepogodiev and J. F. Stoddart, *Chemistry-a European Journal*, 1997, **3**, 1193-1199.

29) D. A. Tomalia, H. Baker, J. Dewald, M. Hall, G. Kallos, S. Martin, J. Roeck, J. Ryder and P. Smith, *Polym. J.*, 1985, **17**, 117-132.

30) E. M. M. De Brabander-van den Berg and E. W. Meijer, *Angew. Chem. Int. Ed. Engl.*, 1993, **32**, 1308-1311.

31) S. Hanessian, C. Hoornaert, A. G. Pernet and A. M. Nadzan, *Carbohydrate Res*., 1985, **137**, C14-C-16.

32) C. Kieburg, M. Dubber and T. K. Lindhorst, *Synlett*., 1997, 1447-1449.

33) M. Dubber and T. K. Lindhorst, *Chem. Commun*., 1998, 1265-1266.

34) P.I. Kitov, J. M. Sadowska, G. Mulvey, G. D. Armstrong, H. Ling, N. S. Pannu, R. J. Read and D. R. Bundle, *Nature*, 2000, **403**, 669-672.

35) D. A. Fulton and J. F. Stoddart, *Org. Lett.*, 2000, **2**, 1113-1116.

36) S. Sakai, Y. Shigemasa and T. Sasaki, *Tetrahedron Lett*., 1997, **38**, 8145-8148.

37) R. Yadav and R. Kikkeri, *Chem. Commun*., 2012, **48**, 1704-1706.

38) M. Gottschaldt, D. Koth, D. Müller, I. Klette, S. Rau, H. Görls, B. Schäfer, R. P. Baum and S. Yano, *Chem. Eur. J.*, 2007,**13**, 10273-10280.

39) R. Roy and J. M. Kim, *Tetrahedron*, 2003, **59**, 3881-3893.

40) E. C. Constable, B. Kariuki and A. Mahmood, *Polyhedron*, 2003, **22**, 687-698.

41) S. Kojima, T. Hasegawa, T. Yonemura, K. Sasaki, K. Yamamoto, Y. Makimura, T. Takahashi, T. Suzuki, Y. Suzuki and K. Kobayashi, *Chem. Commun*., 2003, **11**, 1250-1251.

42) T. Hasegawa, T. Yonemura, K. Matsuura and K. Kobayashi, *Bioconjugate Chem*., 2003, **14**, 728-737.

43) S. Top, A. Vessières, G. Leclercq, J. Quivy, J. Tang, J. Vaissermann, M. Huché and G. Jaouen, *Chem. Eur. J.*. 2003, **9**, 5223-5236.

44) F. Vögtle, M. Plevoets, M. Nieger, G. C. Azzellini, A. Credi, L. De Cola, V. De Marchis, M. Venturi and V. Balzani, *J. Am. Chem. Soc.*, 1999, **121**, 6290-6298.

45) J. Wang, Y.-Q. Fang, L. Bourget-Merle, M. I. Polson, S. Garry, A. Juris, F. Loiseau and S. Campagna, *Chem. Eur. J.*, 2006, **12**, 8539-8548.

46) Y. Z. Hu, S. Tsukiji, S. Shinkai, S. Oishi and I. Hamachi, Chemistry, 2000, **6**, 1907-1916.

47) R. Kikkeri, X. Liu, A. Adibekian Y. H. Tsai and P. H..Seeberger, *Chem Commun.*, 2010, **46**, 2197-2199.

48) D. Grünstein, M. Maglinao, R. Kikkeri, M. Collot, K. Barylyuk, B. Lepenies, F. Kamena, R . Zenobi and P. H. Seeberger, *J. Am. Chem. Soc.*, 2011, **133**, 13957-13966.

49) R. Kikeri, L. H. Hossain and P. H. Seeberger, *Chem. Commun.*, 2008, **18**, 2127-2129.

50) M. Gottschaldt, U. S. Schubert, S. Rau, S. Yano, J. G. Vos, T. Kroll, J. Clement and I. Hilger, *ChemBioChem.*, 2010, **11**, 649-652.

51) R. Kikkeri, D. Grunstein and P. H. Seeberger, *J. Am. Chem. Soc.*, 2010, **132**, 10230-10232.

52) R. Kikkeri, I. Garcia-Rubio and P. H. Seeberger, *Chem. Commun*., 2009, **2**, 235-237.

53) P. Caravan, J. J. Ellison, T. J. McMurry and R. B. Lauffer, *Chem. Rev.*, 1999, **99**, 2293-2352.

54) E. Toth, L. Helm and A. E. Merbach, *Top. Curr. Chem.*, 2002, **221**, 61-101.

55) J. P. André, C.F. G. C. Geraldes, J. A. Martins, A.E. Merbach, M. I. M. Prata, A.C. Santos, J.J.P. de Lima and Iva Tóth, *Chem. Eur. J.*, 2004, **10**, 5804-5816.

56) D. A. Fulton, E. M. Elemento, S. Aime, L. Chaabane, M. Botta and D. Parker, *Chem. Commun*., 2006, **10**, 1064-1066.

57) D. R. Vera, R. Stadalnik and K. Krohn, *J. Nucl. Med.*, 1985, **26**, 1157-1167.

58) R. A. Moats, S. E. Fraser and T. J. Meade, *Angew. Chem. Int. Ed.*, 1997, 36, 726-728.

59) A. Y. Louie, M. M. Hüber, E. T. Ahrens, U. Rothbächer, R. Moats, R. E. Jacobs, S. E. Fraser and T. J. Meade, *Nat. Biotechnol.*, 2000, **18**, 321-325.

60) L. M. Urbanczyk-Pearson, F. J. Femia, J. Smith, G. Parigi, J. A. Duimstra, A. L. Eckermann, C. Luchinat and T. *J.* Meade, *Inorg. Chem.*, 2008, **47**, 56-68.

61) Emma Martín Rodríguez, Nicoleta Bogdan, John A. Capobianco, Simonetta Orlandi, Marco Cavazzini, Chiara Scalerab, and Silvio Quici, *Dalton Trans.*, 2013, 42, 9453-9461.

62) C. L. Ferreira, S. R. Bayly, D. E. Green, T. Storr, C. A. Barta, J. Steele, M. J. Adam and C. Orvig, *Bioconjugate Chem.*, 2006, **17**, 1321-1329.

63) T. Storr, C. L. Fischer, Y. Mikata, S. Yano, M. J. Adam and C. Orvig, *Dalton Trans.*, 2005, **4**, 654-655.

64) R. Schibli, C. Dumas, J. Petrig, L. Spadola, L. Scapozza, E. Garcia- Garayoa and P. A. Schubiger, *Bioconjugate Chem.*, 2005, **16**, 105-112.

65) S. D. Colquhoum, C. A. Conelly and D. R. Vera, *J. Nucl. Med.*, 2001, **42**, 110-116.

66) K. Miki, K. Kubota, Y. Inoue, D. R. Vera and M. Makuuchi, *J. Nucl. Med.*, 2001, **42**, 733-737.

67) N. Shuke, H. O. Kizaki, S. Kino, J. Sato, Y. Ishikawa, C. L. Zhao, S. Kineya, N. Watabane, K. Yokoama and T. Aburano, *J. Nucl. Med.*, 2003, **44**, 475-482.

68) M. M. Alauddin, A. Y. Louie, A. Shahinian, T. J. Meade and P. S. Conti, *Nucl. Med. Biol.*, 2003, **30**, 261-265.

69) Y. Chen, Q. Xiong, X. Yang, Z. Huang and L. He, *Cancer Biother. Radiopharm*., 2007, **22**, 400-402.

70) Y. Chen, Q. Xiong, X. Yang, Z. Huang, Y. Zhao and L. He, *Cancer Biother. Radiopharm*., 2007, **22**, 403-405.

71) C. Plathow and W. A. Weber, *J. Nucl. Med*., 2008, **49**, 43S-63S.

72) C. Fasting, C. A. Schalley, M. Weber, O. Seitz, S. Hecht, B. Koksch, J. Dernedde, C. Graf, E. W. Knapp and R. Haag, *Angew. Chem. Int. Ed. Engl.*, 2012, **51**, 10472-10498.

73) H. Kamitakahara, T. Suzuki, N. Nishigori, Y. Suzuki, O. Kanie and C. H. Wong, *Angew Chem Int Edit*, 1998, **37**, 1524-1528.

74) S. Liu and K. L. Kiick, *Macromolecules*, 2008, **41**, 764-772.

75) U. Sprengard, M. Schudok, W. Schmidt, G. Kretzschmar and H. Kunz, *Angewandte Chemie International Edition in English*, 1996, **35**, 321-324.

76) N. C. Reichardt, M. Martin-Lomas and S. Penades, *Chem. Soc. Rev.*, 2013, **42**, 4358-4376.

77) R. Kikkeri, B. Lepenies, A. Adibekian, P. Laurino and P. H. Seeberger, *J. Am. Chem. Soc.*, 2009, **131**, 2110-2112.

78) S. I. van Kasteren, S. J. Campbell, S. Serres, D. C. Anthony, N. R. Sibson and B. G. Davis, *Proc Natl Acad Sci U S A*, 2009, **106**, 18-23.

79) T. D. Farr, C. H. Lai, D. Grunstein, G. Orts-Gil, C. C. Wang, P. Boehm-Sturm, P. H. Seeberger and C. Harms, *Nano Lett.*, 2014, **14**, 2130-2134.

80) M. Marradi, F. Chiodo, I. Garcia and S. Penades, *Chem. Soc. Rev.*, 2013, **42**, 4728-4745.

81) Y. C. Yeh, B. Creran and V. M. Rotello, *Nanoscale*, 2012, **4**, 1871-1880.

82) Y. J. Chuang, X. Zhou, Z. Pan and C. A. Turchi, *Biochem. Biophys. Res. Commun.*, 2009, **39**, 4771-4773

83) A. A. Kulkarni, C. Fuller, H. Korman, A. A. Weiss and S. S. Iyer, *Bioconjug. Chem.*, 2010, **21**, 1486-1493.

84) R. Ojeda, J. L. de Paz, A. G. Barrientos, M. Martin-Lomas and S. Penades, *Carbohydr. Res.*, 2007, **342**, 448-459.

85) Q. Tong, X. Wang, H. Wang, T. Kubo and M. Yan, *Anal. Chem.*, 2012, **84**, 3049-3052.

86) H. Isobe, K. Cho, N. Solin, D. B. Werz, P. H. Seeberger and E. Nakamura, *Org. Lett.*, 2007, **9**, 4611-4614.

87) T. Ohta, N. Miura, N. Fujitani, F. Nakajima, K. Niikura, R. Sadamoto, C. T. Guo, T. Suzuki, Y. Suzuki, K. Monde and S. Nishimura, *Angew. Chem. Int. Ed. Engl.*, 2003, **42**, 5186-5189.

88) D. Seebach, P. B. Rheiner, G. Greiveldinger, T. Butz and H. Sellner, *Top. Curr. Chem.*, 1998, **197**, 125-164.

89) M. Liu, L. Zhang and T. Wang, *Chem. Rev.*, 2015, **115**, 7304-7397.

90) E. C. Constable, *Chem. Soc. Rev.*, 2013, **42**, 1637-1651.

91) N. S. Kehr, *Biomacromolecules*, 2016, **17**, 1117-1122.

92) N. S. Kehr, H. J. Galla, K. Riehemann and H. Fuchs, *Rsc Adv*, 2015, **5**, 5704-5710.

93) D. Schwefel, C. Maierhofer, J. G. Beck, S. Seeberger, K. Diederichs, H. M. Moller, W. Welte and V. Wittmann, *J. Am. Chem. Soc.*, 2010, **132**, 8704-8719.

94) V. Wittmann and S. Seeberger, *Angew Chem Int Edit*, 2000, **39**, 4348-4352.

95) H. Bavireddi,$^{\#}$ R. V. Murthy,$^{\#}$ M. Gade, **S. Sangabathuni**, P. M. Chaudhary, C. Alex, B. Lepenis and R. Kikkeri, *Nanoscale*, 2016, **47**, 19696-19702.

Chapter 2

Assessing the Effect of Different Shapes of Glyco-gold nanoparticles on Bacterial Adhesion and Infections

2.1 Introduction

Carbohydrate-protein interactions (CPIs) are one of the most important and major events on cell surfaces.[1] Basic components involved in the interaction are the cell surface glycans, which demonstrate a sensitive and selective *cis*/*trans* binding with protein counterparts. However, due to weak CPIs, nature facilitates multivalency to target specific proteins. Recently, extensive efforts have been directed toward mimicking these bio-events by replicating the multivalent scaffolds.[2] However, to fully understand CPIs, it is important to quantify binding affinity with different size, shape, orientation, and local concentration of the sugars.[3] Varieties of synthetic multivalent templates such as cyclodextrin,[4] calixarenes,[5] polymers,[6] dendrimers,[7] supramolecular complexes[8] have been extensively used to decorate sugars in particular topology to target CPIs. These synthetic templates offer controllability and reproducibility, but the drawbacks include production methods that sometimes require complex synthetic conditions. Another class of templates for multivalent glyco-probes are nanoparticles (NPs), such as gold, silver, iron and CdSe NPs.[9] These templates are more rigid and easy to synthesize in large quantities in different sizes, shapes and orientations and can also be easily decorated chemically and biologically.[11]

Among these NPs, AuNPs are more attractive for their different shapes (rod, sphere, star, cubic and spindle), surface resonance band and ease of characterization by UV-visible and transmission electron microscopy (TEM).[10] Moreover, they are less toxic compared to quantum dots. Penadés and co-workers used AuNPs to decorate more than one sugars to target HIV, bacteria, modulation of immune responses, and CPIs.[11] Similarly, enormous effort have been expended by the group of Lin, Wu, Tseng and others to develop gold nanodots and nanoclusters for the sensitive and selective detection of *E.coli*.[12] However, in all these studies, the shape of AuNPs were kept constant to validate the binding with bacteria, cells or organs, limiting the assessment of the role of different shapes of nanoparticles involved in specific CPIs. The latter is a fundamental importance for understanding the CPIs and developing new biomaterials. Various targeting units, such as antibodies, peptides, and aptamers have been functionalized on different shapes of AuNPs to enhance their specificity for tumors, immune responses and biosensing processes.[13] However, a systematic investigation of shape dependent CPIs with the same volume and sugar density and its potential applications have not been reported. Herein, we report the use of glyco-AuNps in bacterial recognition and inhibiting bacterial infection. Three different shapes (rod, sphere and star) of gold nanoparticles coated with mannose and galactose sugar substrates and PEG were used to quantify the binding affinity with *E. coli*. To profile the potential applications of the shape dependent CPIs, inhibition of *E. coli* infection of HeLa cells was quantified.

2.2 Results & Discussions

2.2.1 Synthesis of Glyco-goldnanoparticles (G-AuNPs): The monovalent mannose and galactose modified linkers (**10** and **11**) were synthesized by using the slightly modified procedure from the protocol reported in the literature.[14] Briefly, the conjugation of triethylene glycol with 11-bromoundec-1-ene, followed by glycosylation with per-acetylated mannose or galactose yielded compound **6** or **7**. These compounds were further treated with thioacetic acid in the presence of azo-isobutyronitrile (AIBN), followed by deacetylation with NaOMe to yield compound **10** or **11**. (Scheme 1). Rod AuNPs coated with cetyltrimethylammonium bromide (CTAB) were synthesized *via* a seeding growth method as reported previously (Scheme 2).[15] Synthesis of star shaped AuNPs was carried out by biocompatible surfactant free method[16] and spherical shaped AuNPs by reducing chloroauric acid with sodium citrate.[17] Finally, sugar encapsulation of AuNPs was carried out by ligand exchange process.

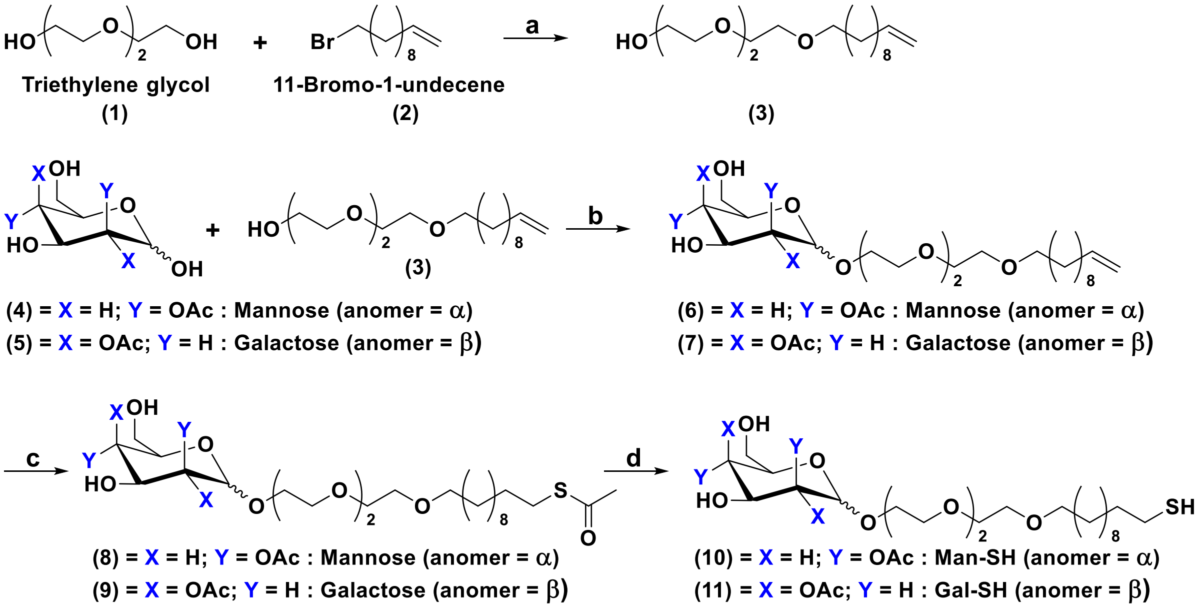

Scheme 1. Synthesis of mannose and galactose modified linker: (a) 60 % NaH, THF, (0°C to RT), 12 h; (b) $BF_3.Et_2O$, DCM, (0°C to RT); (c) Thioaceticacid, AIBN, 1-4 dioxane, 60°C; (d) NaOMe, MeOH, RT.

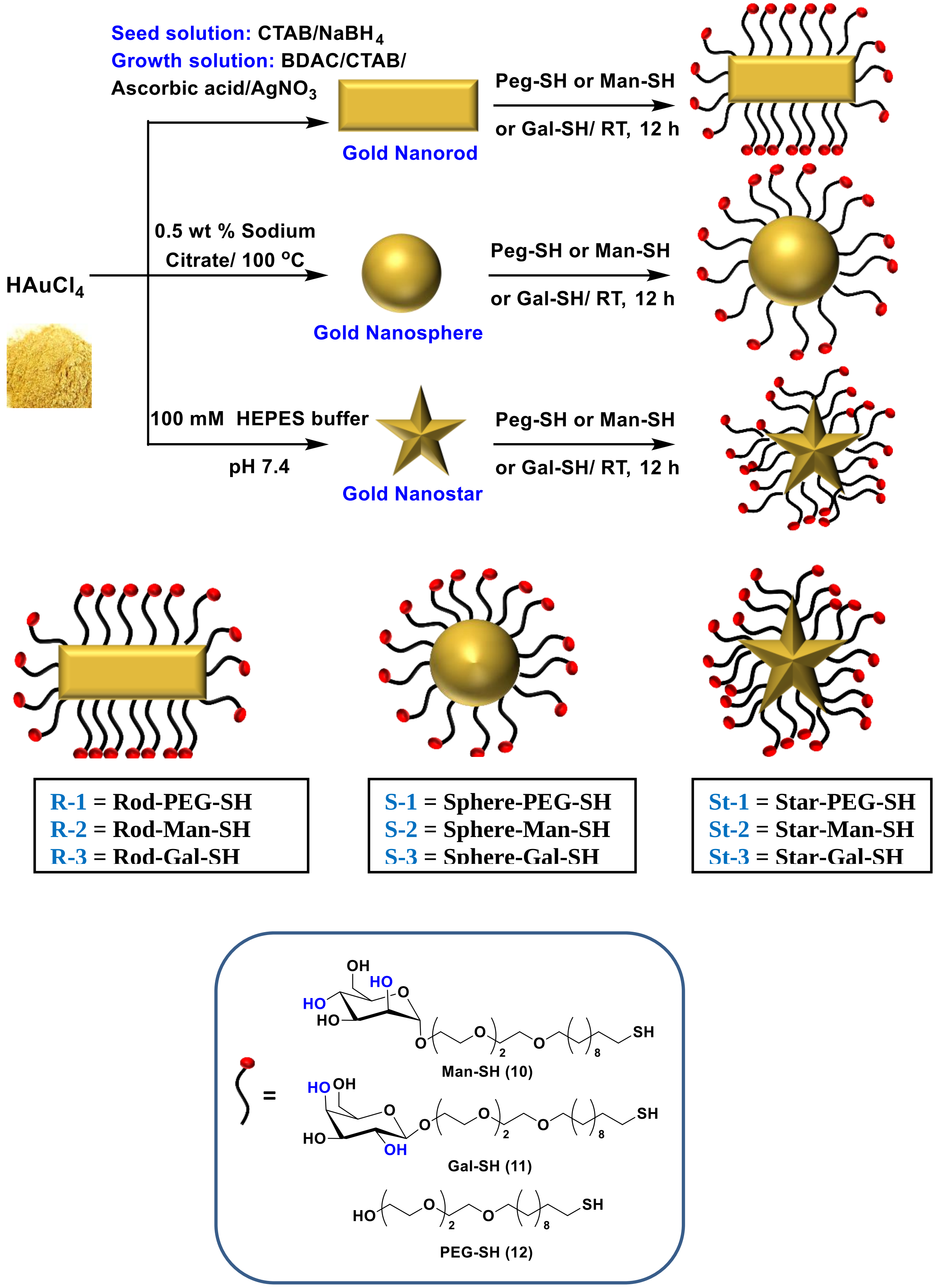

Scheme 2. Synthesis of gold nanoparticles and glyco-goldnanoparticles (G-AuNPs).

2.2.2 Characterization of G-AuNPs: The physical characteristics of AuNP complexes are presented in Table 1. The shape and size of the synthesized AuNPs were confirmed by scanning electron microscopy (SEM) transmission electron microscopy (TEM) and UV-vis absorption (Fig 1 & 2). Spherical AuNPs (18.5 ± 2.5), nano-rods (45.6 ±3.5 × 11.2 ± 0.5) and nano-star (40.6 ± 3.1 × 17 ± 0.9) of equal volume were used as model particles in this study. AuNPs functionalized with sugar and PEG was confirmed by changes of Zeta (ζ) potential (Table 1). After sugar ligation, the ζ-potentials for rod AuNPs changed from 34 to 10 mV, indicating the effective ligand changes of CTAB surfactant by the sugar substrates. At the same time, sphere and star AuNPs showed only a slight change in the negative potential (sphere: -24 to -17 mV; star: -29 to -23 mV). This may be due to the displacement of negatively charged citrate and HEPES surfactant by sugar scaffolds respectively.

The number of sugar molecules on AuNPs was quantified by using a phenol-sulfuric acid method (Table 2). As expected almost equal concentration of sugar scaffolds confirmed. Experiments were performed using two *E. coli* strains to validate the shape dependent bacterial adhesion. The choice of bacterial strains was based on their ability to recognize specific sugar substrates. In this study, we choose FimH-mannose interactions based on ORN 178 contain FimH receptors and ORN 208 is a mutant, having no FimH receptors.[4a] Fluorescence imaging clearly showed aggregation of bacteria due to specific CPIs.

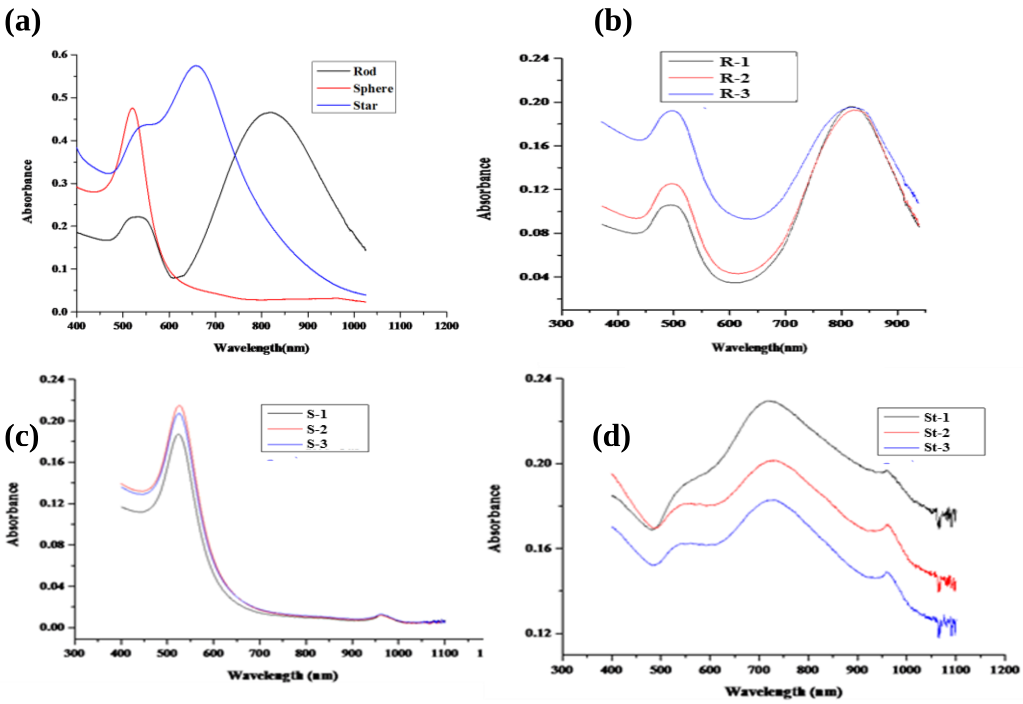

Figure 1. UV-Visible spectroscopy of (a) gold nanoparticles (AuNPs); (b) rod G-AuNPs; (c) sphere G-AuNPs; (d) star G-AuNPs.

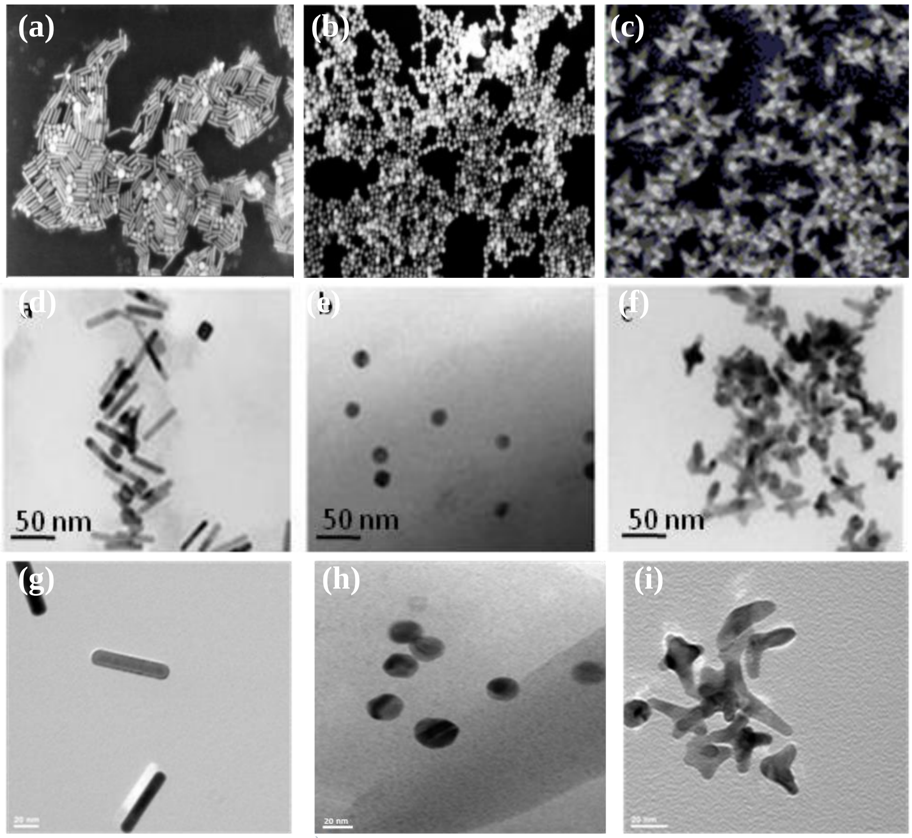

Figure 2. SEM images of AuNPs (a) rod; (b) sphere; (c) Star; and TEM images of AuNPs (d) rod; (e) sphere; (f) star; TEM images of G-AuNPs after mannose modification (g) R-2; (h) S-2; (i). St-2.

2.2.3 Study of Bacterial Aggregation with G-AuNPs : Our first experiment was to establish the binding selectivity. In this experiment, we incubated different shapes and sugar conjugated AuNPs with ORN 178 and ORN 208 for 1 h in PBS solution. After that cells were centrifuged and the aggregates formed by the bacteria were imaged and quantified. As expected, the maximum number of aggregation was observed with mannose coated AuNPs compared to galactose and PEG counterparts (Fig 3i). On the contrary, no aggregation formation was seen in ORN 208 in any of AuNPs (Fig 3ii). Thus, the difference in specific *vs* nonspecific binding was highly dependent on the sugar scaffold compared to the shape of the AuNPs. Although all three different shapes of AuNPs contained same amount of sugar, they apparently differ in three important physical properties such as: (1) contact area of the NPs with respect to external stimuli; (2) rotational volume availability and; (3) aspect ratio. Thus, we hypothesize that specific shape might induce sensitive bacterial adhesion and; (3) aspect ratio. Thus, we hypothesize that specific shape might induce sensitive bacterial adhesion.

Table 1. Physical characteristics of AuNPs and G-AuNPs.

Particle	**Diameter(s) (nm)**	**λ_{max} (nm)**	**ζ-potentials (mV)**
Rod	45.6 ± 3.5 × 11.3 ± 0.5	798	34.4± 0.3
Sphere	18.5 ± 2.5	525	-24± 0.2
Star	40.6 ± 3.1 × 17.1 ± 0.9	715	-29± 1.4
Man-rod	45.9 ± 3.2 × 11.5 ± 1.7	799	10.7± 0.5
Gal-rod	45.2 ± 2.2 × 11.8 ± 0.7	802	17.3± 0.8
PEG-rod	45.9 ± 3.1 × 11.3 ± 1.5	798	30.1 ± 0.6
Man-sphere	20.5 ± 1.3	520	-21.3± 0.5
Gal-sphere	20.5 ± 1.2	525	-17.5± 0.3
PEG-sphere	19.2 ± 1.8	525	-15.3± 0.2
Man-star	44.2 ± 0.2 × 18.2 ± 0.9	725	-22.4± 1.1
Gal-star	42.9 ± 0.2 × 18.2 ± 0.7	725	-23.8± 1.3
PEG-star	44.6 ± 0.2 × 17.4 ± 0.9	725	-16.2± 1.6

Table 2. Quantification of sugars on AuNPs

S.No	**Nanoparticles**	**Concentration (mg/mL)**	**S.No**	**Nanoparticles**	**Concentration (mg/mL)**
1	Rod-Man	1.45 ± 0.21	**4**	Sphere-Gal	1.72 ± 0.25
2	Rod-Gal	1.62 ± 0.17	**5**	Star-Man	1.72 ± 0.09
3	Sphere-Man	1.79 ± 0.11	**6**	Star-Gal	1.43 ± 0.12

To demonstrate the shape dependent bacterial adhesion, experiments were performed using different concentrations of rod, sphere and star shaped Man-AuNPs (Fig 4i). The dose-response bar graph of different shapes is presented in figure 4ii. Two groups of interactions could be identified in terms of their aggregation. The first group, composed of sphere and star shape AuNPs, gave a detection limit of 17 ± 2 μg/ml and 14 ± 2 μg/ml respectively with known number of ORN 178 *E.coli* stain. The second group, composed of rod-shaped AuNPs, gave a detection limit of 0.03 ± 0.01 μg/ml at the same conditions.

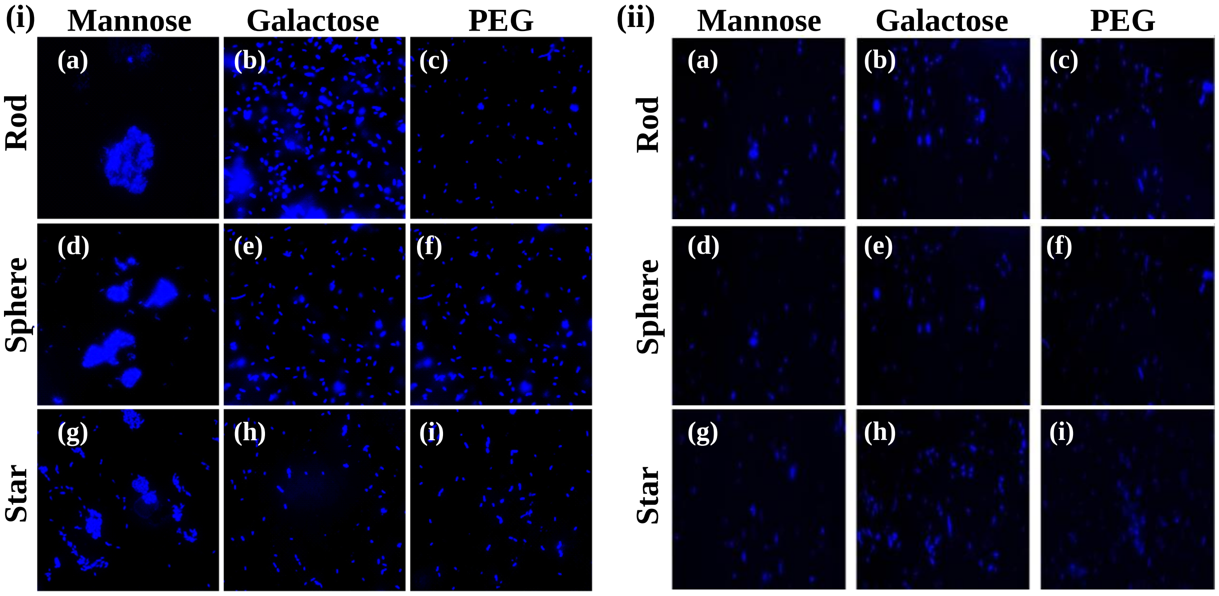

Figure 3. (i) *E. coli* strain ORN178 aggregation using G-AuNPs**;** (ii) *E. coli* strain ORN208 aggregation using G-AuNPs;

The observed ~80-fold difference in the detection of bacteria by rod AuNPs could be attributed to several factors: 1) aspect ratio, which could increase specific attachment of particles on bacterial cell surfaces; 2) the surface effective availability for AuNPs binding; 3) self-assembly of NPs to amplify the specific interaction. To further validate the above results, SEM images were done at the lowest concentration (0.8 μg/ml) of AuNPs treated bacteria (Fig 5a-f). As expected, the relative amount of mannose rod AuNPs involved in effective CPIs is higher than sphere and star counterparts. This might be because of the large number of rod AuNPs interaction with *E.coli* surface compared to star or spherical counterparts(Fig 5a,d).[18] On close examination of the rod shaped AuNPs, we observed head-to-head self-assembly of on the surface of the bacteria (Fig 5d). In contrast, star and spherical AuNPs under the same conditions resulted mono-dispersed and very few aggregations, indicating that

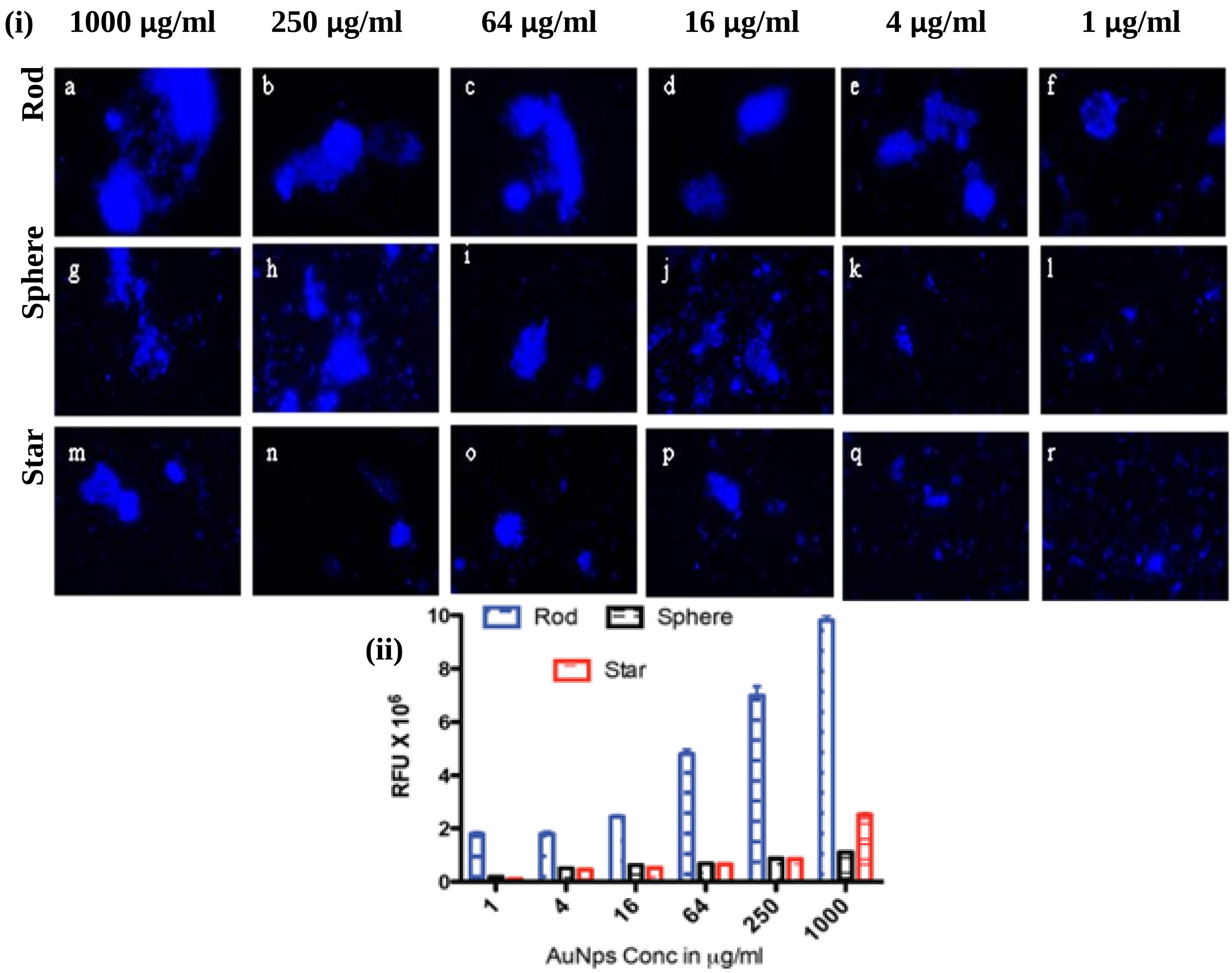

Figure 4.(i) *E. coli* ORN178 aggregation by various concentrations of mannose modified G-AuNPs; (ii) Quantification of bacterial aggregation in the presence of different shapes of G-AuNPs functionalized with mannose. Data represent the mean of ± SEM (n =3).

the aspect ratio of AuNPs is crucial for self-assembly and to improve the sensitive interactions, we also quantified the number of nanoparticles adhered on a specific µm^2 area of the bacteria (Fig 5g). The binding density of rod AuNPs was found nearly 2.5 fold higher than that of star and spherical shaped AuNPs. This confirmed that the rod AuNPs occupied more surface area on bacteria than that of star and sphere AuNPs, which directly modulate the binding affinity. All these results correlate to mathematical model and flow chemistry experiment proposed by Kohlar et al.[19] Finally, we quantified the number of AuNPs actively bound on the surface of the bacteria. We observed that spherical AuNPs occupied nearly 10 and 4 fold less surface area of the bacteria compare to rod and star AuNPs, indicating that rod AuNPs exhibit higher avidity toward the bacteria (Fig 5h).

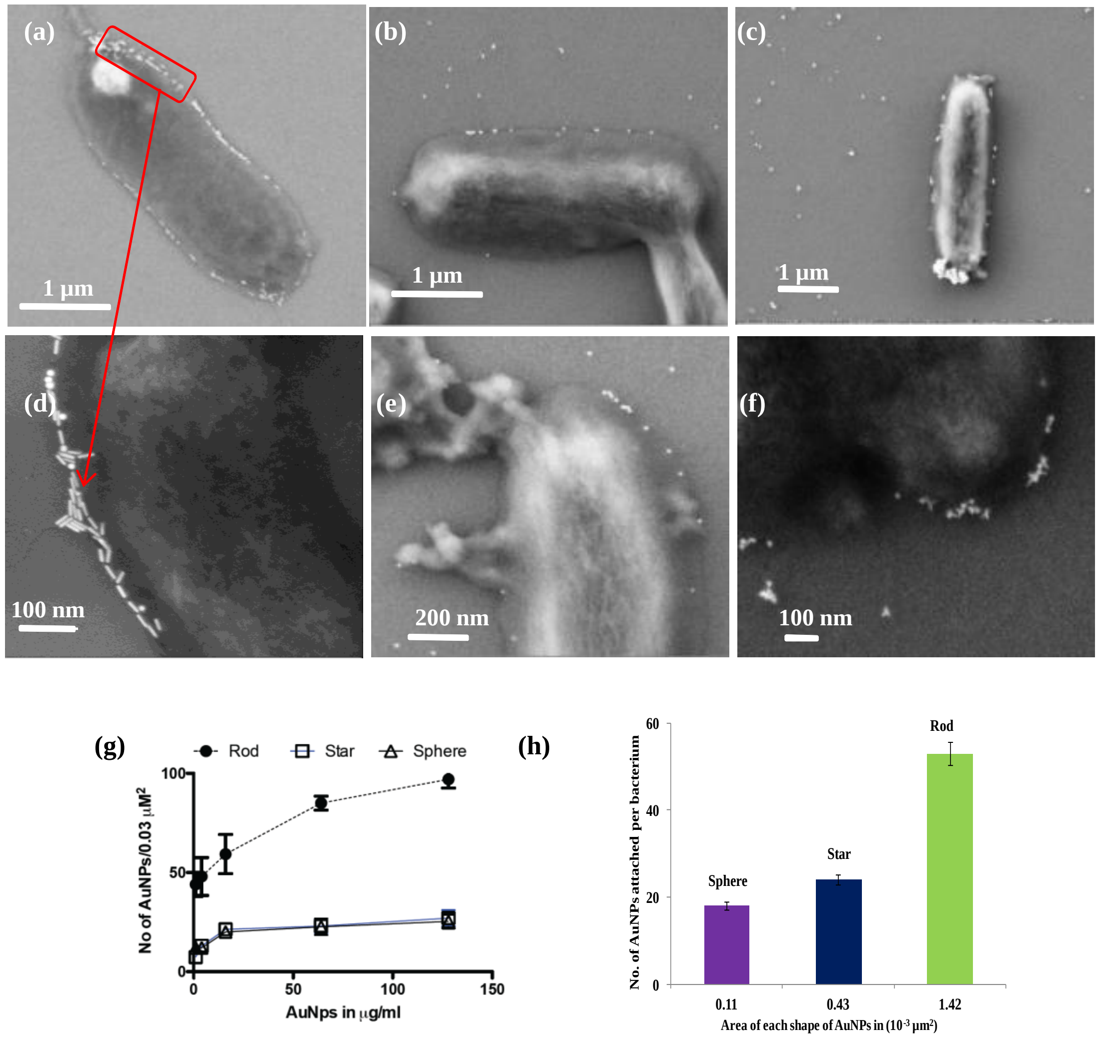

Figure 5. (a-f) SEM images of mannose functionalized G-AuNPs with *E. coli* ORN 178 stain: (a), (d) Rod; (b), (e) Sphere; (c), (f) Star; (g) Quantification of attachment of Man-AuNPs on the surface of bacteria. Data represent the mean number of nanoparticles on the surfaces of bacteria (n =10); (h) Mannose functionalized G-AuNPs bound to the surface of bacteria according to the surface availability; Conc of G-AuNPs = 0.8 µg/ml (n=5). (Note: While quantifying the bound G-AuNPs and area, the surface of the bacteria was assumed as flat surface).

2.2.4 Study of Inhibition of Bacterial Infection with G-AuNPs: To demonstrate potential applications of shape dependent CPIs, HeLa cells, which have been known to express high mannose on the cell surface[20,] were infected with a known amount of DAPI stained ORN 178 *E. coli*. We examined infection caused by the bacteria in the presence three different shapes and five different concentrations (12, 25, 50, 100 and 200 µg/ml) of mannose-AuNPs. After 1 h of incubation, both bound and unbound bacteria were separated and quantified by

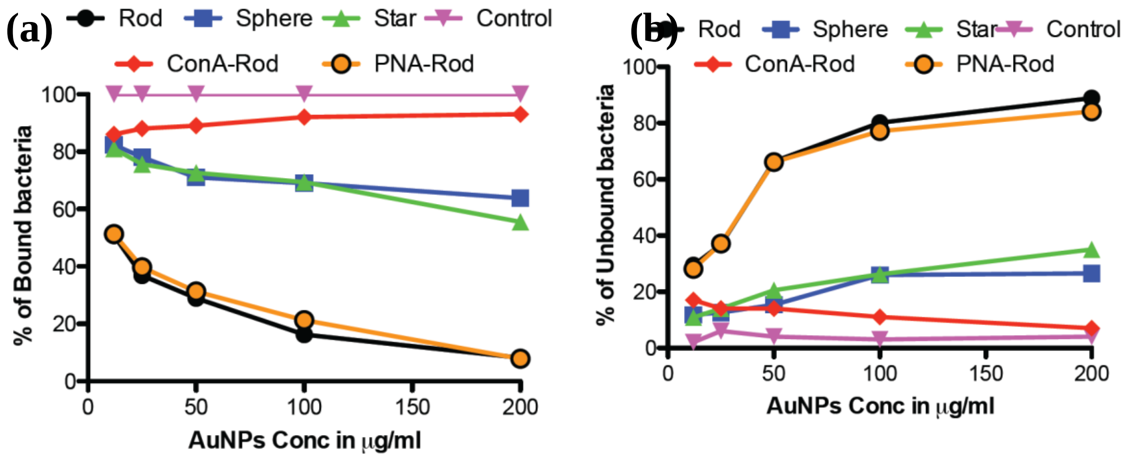

Figure 6. Inhibition of *E. coli* infection of HeLa cells: (a) percentage of bound bacteria; (b) percentage of unbound bacteria. Quantification was done with respect to the DAPI fluorescence intensity, which corresponds to the concentration of the bacteria taken for the above experiment (control). Fluorescence intensity was calculated from the average of three independent experiments.

measuring the fluorescence intensity of DAPI. Results obtained from different shapes showed that the percentage of inhibition (unbound bacteria) caused by rod AuNPs was approximately six-fold more than that of the star and spherical AuNPs (Fig 6). To confirm that the inhibition effect of mannose-rod AuNPs is indeed anchored by specific CPIs, ConA and PNA (10 µl of 0.1 mg/ml) were added to mannose-AuNPs before mixing with bacteria and HeLa cells. Due to specific CPIs between mannose-ConA most of the cells got infected, whereas in the presence of PNA lectin, which is specific to galactose sugars showed effective inhibition of cell-bacterial interactions. These results confirmed that the shape of the AuNPs and specific CPIs fine tune the inhibition properties.

2.3 Conclusions

In summary, we have demonstrated that shape is one of the factor in establishing sensitive carbohydrate-protein interactions. Data from the bacterial adhesion and HeLa cells infection studies showed that the rod-shaped AuNPs functionalized with mannose had substantial sensitivity compared to that of star-shaped and spherical shaped AuNPs. Factors such as self-assembly and effective surface contact are critical for sensitive adhesion. In a more general perspective, blockage of *E.coli* infection by rod mannose-AuNPs may open opportunities to develop efficient medicines for urinary or digestive tract infections.

2.4 Experimental Sections

2.4.1 General Information: All chemicals were reagent grade and unless otherwise noted were used as supplied. TLC was performed on Merck silica gel 60 F254 plates (0.25 mm) and visualized by UV or by dipping the plate in CAM/ninhydrin solution and heating. Column chromatography was carried on Fluka Kieselgel 60, mesh 230–400. ^{1}H and ^{13}C NMR spectra were recorded on Jeol 400 MHz. Chemical shifts (δ) are reported in ppm, coupling constants (J) in Hz. Residual solvents, for $CDCl_3$ - δ_H, 7.26 and δ_C 77.3, for CD_3OH - δ_H 3.31, and δ_C 49.0, D_2O - δ_H, 4.75, are used as internal references.

2.4.2 Synthesis of 10 and 11

2-(2-(2-(undec-10-en-1-yloxy)ethoxy)ethoxy)ethan-1-ol (3): Triethylene glycol **1** (1.00 g, 6.66mmol) was dissolved in THF in a round bottom flask to which 11-Bromo-1-undecene **2** (0.776 g, 3.33 mmol) was added in the presence of 60% NaH (0.080 g, 3.33 mmol) and stirred it for 12 h at 0°C to RT. The solvent was removed under reduced pressure. The residue was dissolved in EtOAc (10 ml) and washed with water (3× 10 ml). The organic layer was dried over Na_2SO_4, filtered, and evaporated under reduced pressure. The crude was then purified by column chromatography (silica gel, EtOAc / PET ether 1:1) and dried under reduced pressure to give the product **3** as a colorless oil (44% yield). ^{1}H NMR (400 MHz, $CDCl_3$): δ 5.87-5.77 (m, 1H), 5.02-4.92 (m, 2H), 3.75-3.58 (m, 12H), 3.46 (t, J = 6.41 Hz, 2H), 2.07-2.01 (m, 2H), 1.62-1.55 (m, 2H), 1.36-1.26 (m, 12H).^{13}C NMR (100 MHz, $CDCl_3$): δ 139.13, 114.02, 72.47, 71.50, 70.51, 70.23, 69.91, 61.60, 33.72, 29.46, 29.44, 29.37, 29.34, 29.02, 28.83, 25.96. HRMS (ESI) m/z: calc'd for $C_{17}H_{34}NaO_4$, 325.2355; Found, 325.2354.

Undec-1-en-11-yltri(ethy1eneglycol)-2,3,4,6-penta-O-acetyl-α-D-mannopyranoside (6): A solution of peracylated mannose **4** (0.22 g, 0.56 mmol) and PEG linker **3** (0.34 g, 1.12 mmol) in DCM (7 ml) was cooled to 0 °C. Boron trifluoride diethyl etherate (0.2 ml, 2.24 mmol) was added slowly and the solution was stirred for 12 h at 0 °C. Triethylamine (1.5 ml) was added, the solution was allowed to warm to RT and the solvent was removed under reduced pressure. The residue was dissolved in EtOAc (10 ml) and washed with water (3× 10 ml). The organic layer was dried over Na_2SO_4, filtered, and evaporated under reduced pressure. The crude was the purified by column chromatography (silica gel, EtOAc / DCM 3:7 to 1:1) and dried under reduced pressure to give the product **6** as a colorless oil (65%

yield). ^{1}H NMR (400 MHz, $CDCl_3$): *δ* 5.85-5.78 (m, 1H); 5.38-5.28 (m, 1H), 5.32-5.27 (m, 1H); 5.02-4.92 (m, 1H); 4.85 (d, *J* = 1.7 Hz, 1H, anomeric-H), 4.32-4.28 (m, 1H); 4.14-4.08 (m, 1H); 3.84-3.79 (m, 1H); 3.67-3.59 (m, 12H); 3.45 (t, *J* = 6.41 Hz, 2H); 2.16 (s, 3H); 2.11 (s, 3H); 2.05 (s, 3H), 2.0 (s, 3H); 1.64-1.58 (bm, 4H); 1.37-1.26 (m, 14H). ^{13}C NMR (100 MHz, $CDCl_3$): *δ* 170.66, 166.99, 169.84, 169.70, 139.19, 114.06, 97.6 (anomeric-C), 71.49, 70.56, 69.99, 69.52, 69.03, 68.68, 68.31, 67.32, 66.07, 62.34, 33.76, 29.64, 29.57, 29.49, 29.42, 29.38, 29.07, 28.87, 20.74, 20.68. HRMS (ESI) m/z: calc'd for $C_{31}H_{52}NaO_{13}$, 655.3306; Found, 655.3311.

[1-[Methylcarbonyl)thio]undec-11-yl-tri(ethyleneglycol)-2,3,4,6-O-acetyl-α-D-mannopyranoside (8). Undec-1-en-11-yltri(ethy1eneglycol)-2,3,4,6-penta-O-acetyl-α-D-mannopyranoside **6** (0.15 g, 0.24 mmol) and AIBN (0.31 g, 1.92 mmol) were dissolved in dioxane (7 ml). Thioacetic acid (0.439 ml, 6.24 mmol) was added and the reaction mixture was stirred for 12 h at 60°C. The solvent was removed and the crude product was purified by flash column chromatography (silica gel, pet ether /EtOAc 1:1 to 1:9). The product was dried under high vacuum to give **8** as yellowish oil (44% yield). ^{1}H NMR (400 MHz, $CDCl_3$): *δ* 5.38-5.28 (m, 2H), 5.25 (dd, *J*= 1.7, 3.2 Hz, 1H); 4.85 (d, J = 1.7 Hz, 1H, anomeric-H); 4.29 (dd, *J* = 5.40, 7.33 Hz, 1H); 4.08-4.05 (m, 1H); 3.85-3.78 (m, 1H); 3.69-3.57 (m, 12H); 3.44 (t, *J* = 7.33 Hz, 2H); 2.86 (t, *J* = 7.33 Hz, 2H), 2.32 (S, 3H); 2.16 (s, 3H); 2.11(S, 3H); 2.04(S, 3H), 1.99 (S, 3H); 1.59-1.54 (m, 4H), 1.29-1.25(m, 14H). ^{13}C NMR (100 MHz, $CDCl_3$): 196.12, 170.69, 170.02, 169.88, 169.73, 97.67 (anomeric-C), 71.52, 70.69, 70.60, 70.56, 69.99, 69.93, 69.52, 69.05, 68.33, 67.34, 66.09, 62.35, 29.66, 29.58,29.53, 29.45, 29.12, 29.08, 28.77, 20.89, 20.75, 20.69. HRMS (ESI) m/z: calcd for $C_{33}H_{56}NaO_{14}S$, 731.3288; Found 731.3310.

1-Mercaptoundec-11-yl)triethyleneglycol-α-D-mannopyranoside (10). Sodium methoxide (3 mg, 0.08 mmol) was added to a solution of **8** (0.1 g, 0.14 mmole) in MeOH (5 mL) and the solution was stirred at rt for 2 h. The reaction mixture was neutralized with Resin Amberlite H^+ IR 120, filtered and the solid was washed with MeOH (20 mL). The solvent was removed and the product was dried under high *vacuo* to give product **10** as yellowish oil (94% yield). ^{1}H NMR (400 MHz, CD_3OD): δ 4.77 (d, J = 1.7 Hz, 1H, anomeric-H); 3.82-3.78 (m, 3H), 3.68-3.44 (m, 15H); 3.44 (t, J = 6.41 Hz, 2H); 2.65 (t, J = 7.33 Hz, 2H); 1.58-1.53 (m, 4H); 1.31-1.26 (bm, 14H).^{13}C NMR (100 MHz, CD_3OD): 101.90 (anomeric-C), 74.76, 72.70, 72.26, 71.74, 71.56, 71.31, 68.74, 67.92, 63.08, 30.88, 30.81, 30.75, 30.46, 30.36, 29.59, 27.36; HRMS (ESI) m/z: calc'd for $C_{23}H_{46}NaO_9S$, 521.2760; Found 521.2747.

Undec-1-en-11-yl-tri(ethy1eneglycol)-2,3,4,6-penta-O-acetyl-β-D-galactopyrannoside (7). Boron trifluoride diethyl etherate (0.18 ml, 2.04 mmol) was added slowly to a solution of peracylated galactose **5** (0.20 g, 0.51 mmol) and PEG linker **3** (0.30 g, 1.02 mmol) in DCM (7 ml) at 0 °C and the solution was stirred for 2 hours. The reaction was quenched with triethyl amine (2 ml) and allowed to warm to RT. The solvent was removed under reduced pressure; the residue was dissolved in EtOAc (10 ml) and washed with water (3×10 ml). The organic layer was dried with Na_2SO_4, filtered and the solvent was removed under reduced pressure. The crude was purified by column chromatography (silica gel, EtOAc / DCM 3:7 to 1:1). The product **7** was obtained as colorless oil (60% yield). ^{1}H NMR (400 MHz, $CDCl_3$): δ 5.86-5.76 (m, 1H); 5.43-5.37 (m, 1H); 5.23-5.19 (m, 1H); 5.03-4.91 (m, 1H); 4.56 (d, *J* = 7.9 Hz, 1H, anomeric-H) 4.23-4.11(m, 2H); 3.98-3.89 (m, 1H); 3.80-3.72 (m, 2H); 3.67-3.57 (m, 12H); 3.44 (t, *J* = 6.87 2H); 2.15-1.99 (m, 12H); 1.61-1.54 (m, 2H), 1.39-1.26(m, 14H). ^{13}C NMR (100 MHz, $CDCl_3$): δ 170.40, 170.28, 170.17, 169.49, 139.21, 114.08, 101.34 (anomeric-C), 71.53, 70.89, 70.69, 70.59, 70.26, 70.01, 69.06, 68.76, 67.03, 61.27, 33.78, 29.58, 29.51, 29.43, 29.40, 29.09, 28.89, 26.04, 20.81, 20.76, 20.67, 20.58. HRMS (ESI) m/z: calc'd for $C_{31}H_{52}NaO_{13,}$ 655.3306; Found 655.3305.

[1-[Methylcarbonyl)thio]undec-11-yl-tri(ethyleneglycol)-2,3,4,6-O-acetyl-β-D-galactopyrannoside (9). Compound **7** (0.12 g, 0.19 mmol) and AIBN (0.25 g, 1.52 mmol) were dissolved in dioxane (7 ml), thioacetic acid (0.35 ml, 4.94 mmol) was added and the solution was stirred for 12 h at 60 °C. The solvent was removed and the crude was purified by flash column chromatography (silica gel, pet ether /EtOAc 1:1 to 1:9). The solvent was removed and the residue was dried to **9** as yellowish oil (40% yield. ^{1}H NMR (400 MHz, $CDCl_3$): δ 5.37 (d, J = 6.87, 1H); 5.21-5.18 (m, 1H), 5.02-4.99 (m, 1H); 4.59 (d, *J* = 7.9 Hz, 1H, anomeric-H), 4.20-4.10 (m, 1H); 3.97-3.89 (m, 1H); 3.78-3.72 (m, 1H); 3.65-3.56 (m, 12H); 3.43 (t, 2H, J = 6.87); 2.85 (t, 2H J = 7.33); 2.31 (s, 3H); 2.14-1.97 (m, 12H); 1.57-1.52 (m, 4H), 1.32-1.24(m, 14H). ^{13}C NMR (100 MHz, $CDCl_3$): 196.06, 170.36, 170.25, 170.13, 169.47, 101.31(anomeric-C), 71.49, 70.87, 70.85, 70.57, 70.23, 69.98, 69.02, 68.76, 67.02, 61.26, 30.59, 29.63, 29.55, 29.44, 29.09, 28.75, 26.01, 20.68, 20.59. HRMS (ESI) m/z: calc'd for $C_{33}H_{56}NaO_{14}S$, 731.3288; Found 731.3284.

(1-Mercaptoundec-11-yl)triethylene glycol-β-D-galactopyrannoside (11). Sodium methoxide (2 mg, 0.01 mmol) was added to a solution of compound **9** (0.09 g, 0.13 mmole) in MeOH (4 mL) and the reaction was stirred at rt for 2 h. The solution was neutralized with Resin Amberlite H^+ IR 120, filtered, and washed with MeOH (20 mL). The solvent was removed and the product was dried under high *vacuum* to give product **11** as yellowish oil. ^{1}H NMR (400 MHz, CD_3OD): δ 4.23(d, J = 7.33, 1H, anomeric-H); 4.01-3.94 (m, 2H), 3.82-3.80 (bm, 1H); 3.68-3.53 (m, 15H); 3.45 (t, *J* = 6.41 Hz, 1H); 2.65 (t, J = 6.87 Hz, 1H); 2.46 (t, J = 7.33 Hz, 2H); 1.58-1.53 (m, 4H); 1.31-1.26 (bm, 14H).^{13}C NMR (100 MHz, CD_3OD): 103.42 (anomeric-C), 75.42, 75.35, 73.53, 71.21, 21.08, 70.31, 70.11, 70.02, 69.68, 69.09, 68.83, 61.53, 33.92, 29.67, 29.42, 29.34, 29.16, 29.08, 28.98, 25.87, 23.67. HRMS (ESI) m/z: calc'd for $C_{23}H_{46}NaO_9S$, 521.2760; Found 521.2759.

2.4.3 Synthesis of rod, sphere, star shape nanoparticles:

Synthesis of Star AuNPs: Star shaped AuNPs were synthesized by reducing Au (III) chlorate in HEPES buffer pH 7.4. The Star AuNPs were prepared by mixing 5 µL of 40 mM $HAuCl_4$ (Sigma-Aldrich) with 1 mL of 100 mM 2-[4-(2-hydroxyethyl) piperazine-1-yl]ethanesulfonic (HEPES) buffer. After centrifugation at 12000 rpm, the Au nanostars were re-dispersed in deionized water.

Synthesis of Sphere AuNPs: The sphere AuNPs were synthesized by mixing 1 mL of 0.5 wt% sodium citrate with 19 mL of 0.2 mM $HAuCl_4$ aqueous solution at 100 °C till solution turns pale red. After centrifugation at 13,200 rpm, the Au nanospheres were re-dispersed in deionized water.

Synthesis of Rod AuNPs: Rod gold nanoparticles (AuNPs) coated with cetyltrimethylammonium bromide (CTAB) were synthesized *via* seeding growth method as reported previously.[1]

Seed solution: 5 mL, 0.20 M CTAB solution was mixed with 5 ml of 0.5 mM $HAuCl_4$. To the stirred solution, 0.60 ml of ice-cold 0.010 M $NaBH_4$ was added; this will form a brownish yellow solution. After 2 min of the vigorous stirring solution was stored at 25 °C.

Growth Solution: First 5 mL of 0.15 M BDAC and 0.2 M of CTAB were mixed and dissolved mixture by sonication at 40 °C for 20 min. To this solution was added 200 µl of 4 mM of $AgNO_3$ followed by addition of 5.0 mL of 1 mM of $HAuCl_4$ solution, and after gentle mixing of the solution 70 µl of 0.0778 M ascorbic acid was added. The growth process will start with addition 12-μl of seed solution and it completes in 1 h. After centrifugation at 7,000 rpm, the nanorods were re-dispersed in deionized water.

2.4.4 Synthesis of sugar conjugated AuNPs: 0.5 ml of 1 mM thiol PEG linker/thiol mannose linker/thiol galactose linker was added to 0.5 ml of the AuNPs solution. After incubation at room temperature for 12 h, the modified Au nanoparticles were separated by centrifugation and re-dispersed in deionized water.

2.4.5 Zeta potential studies: We used the zeta-potential analyzer to measure the surface potential of AuNPs. The electrostatic potential on the particle surface is called the zeta potential. In the measurement, we applied unit field strength (1 Volt per metre) to the AuNP solution.

2.4.6 Phenol-Sulfuric acid Assay: The concentration of mannose/ galactose sugars on AuNPs were determined by the phenol-sulfuric acid method. 100 µL sugar functionalized-AuNPs was mixed with concentrated sulfuric acid (750 µL, 100%) and aqueous phenol solution (5% w/v, 100 µL) in the test tube and heated to 80°C. After 5 min, solution was cooled to room temperature and the absorbance coefficient at 490 nm was measured. AuNPs as such in sulfuric acid was used as a control. The sugar concentration was estimated by comparing the absorption of the sample with a standard curve.

2.4.7 Bacterial Aggregation Assay: Bacterial Strains growth: The mutants *E. coli* ORN178 and ORN208 were provided by Prof. Orndorff (College of Veterinary Medicine, Raleigh, NC United States). The bacterial cultures were grown overnight at 37°C until they reached an approximate OD_{600} of 1.0.

For aggregation assay 2 ml aliquot of bacteria of approximate OD_{600} of 1.0 was centrifuge to obtain a bacterial pellet. The resulting pellet was washed twice with PBS buffer and resuspended in 1 ml PBS and adjust the concentration to 10^8 bacteria in 1 ml. 100 µl of bacterial PBS solution was mixed with different shapes and different sugar coated AuNPs (1000 µg/ml) and incubated at room temperature for 1 h with gentle shaking. Then, nanoparticles-bacteria conjugated was incubated with organic dye 4',6-diamidino-2-phenylindole dihydrochloride, (DAPI) at dilution of 1/1000 for another 15 mins. Bacteria were then centrifuged at 4000 rpm and the pellet washed with 100 µL of PBS for 2 times. Pellet was again dissolved in PBS and fixed with 4% (w/v) paraformaldehyde for 15 min. A drop of fixed solution was mounted on microscopic slides and imaged. The relative fluorescent intensity of bacteria aggregates was calculated by measuring the fluorescent intensity of 50 random aggregations using imagej software.[3]

Concentration dependent studies: 10 µl of different concentration of mannose-AuNPs (1 to 1000 µg/ml) were incubated with ORN 178 (10^8 concentration) for 1 h, followed by above protocol to image the bacteria aggregations.

2.4.8 SEM Imaging of G-AuNPs and Bacterial Aggregation: 100 µl of bacterial suspension with 10^8 concentration of ORN 178 and 0.8 µg/ml of different shapes of mannose-AuNps) was washed with PBS. Then bacterial pellet was dehydrated in ethanol gradient (10, 30, 70, 95, and 100%) and fixed with 4% glutaraldehyde for 2h. These bacteria were placed on small piece of silicon wafer and drying under vaccume in desicator. Before imaging samples were coated with gold (Polaron SC 502 sputter coater). SEM images were performed in FE-SEM instrument.

Quantification of the attachment of AuNPs on the surface of ORN 178 stain: Approximately 100 µl of bacterial suspension with 10^8 concentration of ORN 178 and different concentration of three different shapes of AuNPs (0.8, 4, 16, 64, 128 µg/ml) were added and after 1 h washed with PBS. The bacteril pellet was dehydrates as described above and places a drop of it was place on silicon wafe. SEM images were collected and using imageJ software the number of nanoparticles in a specific area was quantified.

2.4.9 Inhibition of Bacterial Binding to HeLa Cell Line: 10^4 HeLa cells were seeded per well into a 96-well plate and incubated for 24 h at 37 °C in CO_2 atmosphere. Cells were washed three times with PBS before adding bacteria. DAPI stained ORN 178 bacteria 0.25 × 10^8 cells/ml) and 100 µl of (15 to 250 µg/ml) different concentrations of mannose-AuNPs or ConA or PNA (0.1 mg/ml) pretreated mannose-AuNPs (15 to 250 µg/ml) were added together. After 60 min of incubation, cells were washed with PBS in order to eliminate non-adherent bacteria. PBS solutions were centrifuge and 100 µl of concentration solution was used in fluorescent plate reading to quantify the amount of bacteria. In parallel, attached bacteria were released with Triton X100 0.1% in PBS and transferred to a 96 well plate and DAPI fluorescence was measured in fluorescent plate reader.

2.5. References

1. M. Cohen and A. Varki, *Int. Rev. Cell. Mol. Biol.,* 2014, **308,** 75-125.
2. C. R. Bertozzi and L. L. Kiessling, *Science*, 2001, **291**, 2357-2364.
3. H. Lis and N. Sharon, *Chem. Rev.*, 1998, **98**, 637-674.
4. Y. M. Chabre and R. Roy; *Chem. Soc. Rev*., 2013, **42**, 4657-4708.

5. M. Gingras, Y. M. Chabre, M. Roy and R. Roy, *Chem. Soc. Rev.*, 2013, **42**, 4823-4841.

6. P. Bojarová, R. R. Rosencrantz, L. Elling, V. Křen. *Chem. Soc. Rev.*, 2013, **42**, 4774-4797.

7. R. J. Pieters, *Org. Biomol. Chem.,* 2009, **7**, 2013-2025.

8. M. Gade, A. Paul, C. Alex, D. Choudhury, H. V. Thulasiram and R. Kikkeri, *Chem. Commun.*, 2015, **51**, 6346-6349.

9. S. venwetswinkel, A. N. Volkov, Y. G. Sterckx, A. Garcia-Pino, L. Buts, W. F. Vranken, J. Bouckaert, R. Roy, L. Wyns, N. A. van Nuland, *J. Med. Chem*., 2014, **57**, 1416-1427.

10. L. Baldini, A. Casnati, F. Sansone, and R. Ungaro, *Chem. Soc. Rev*., 2007, **36**, 254-266.

11. J. D. Badjić, A. Nelson, S. J. Cantrill, W. B. Turnbull and J. F. Stoddart, *Acc. Chem. Res*., 2005, **38**, 723-732.

12. L. L. Kiessling and J. C. Grim, *Chem. Soc. Rev*., 2013, **42**, 4476-4491.

13. L. R. Prost, J. C. Grim, M. Tonelli and L. L. Kiessling, *ACS. Chem. Biol*., 2012, **7**, 1603-1608.

14. R. Kikkeri, D. Grünstein and P. H. Seeberger, *J. Am. Chem. Soc.,* 2010, **132**, 10230-10232.

15. R. Yadav, R. Kikkeri, *Chem. Commun*., 2012, **48**, 1704-1706.

16. Y. Kim, S. Shin, T. Kim, D. Lee, C. Seok and M. Lee, *Angew. Chem. Int. Ed. Engl*., 2013, **52**, 6426-6429.

17. D. Grünstein, M. Maglinao, R. Kikkeri, M. Collot, K. Barylyuk, B. Lepenies, F. Kamena, R. Zenobi and P. H. Seeberger, *J. Am. Chem. Soc*., 2011, **133,** 13957-13966.

18. N. C. Reichardt, M. Martín-Lomas and S. Penadés, *Chem. Soc. Rev.*, 2013, **42**, 4358-4376.

19. M. Marradi, F. Chiodo, I. García and S. Penadés, *Chem. Soc. Rev*., 2013, **7**, 4728-4745.

20. K. Turcheniuk, C-H. Hage, J. Spadavecchia, A. Y. Serrano, I. Larroulet, A. Pesquera, A. Zurutuza, M. G. Pisfil, L. Héliot, J. Boukaert, R. Boukherroub and S. Szunerits, *J. Mater. Chem. B.,* 2015, **3**, 375-386.

21. S. Eustis and M. A. El-Sayed, *Chem. Soc. Rev.,* 2006, **35,** 209-217.

22. S. H. Radwan and H. M. Azzazy, *Expert Rev Mol Diagn.,* 2009, **9**, 511-524.

23. F. Chiodo, M. Marradi, J. Park, A. F. J. Ram, S. Penadés, I. van Die and B. Tefsen, *ACS Chem. Biol.*, 2014, **9**, 383-389.

24. D. Arosio, F. Chiodo, J. J. Reina, M. Marelli, S. Penadés, Y. van Kooyk, J. J. Garcia-Vallejo and A. Bernardi, *Bioconjugate Chem.*, 2014, **25**, 2244-2251.

25. I. García, A. Sánchez-Iglesias, M. Henriksen-Lacey, M. Grzelczak, S. Penadés and L. M. Liz-Marzán, *J. Am. Chem. Soc.*, 2015, **137**, 3686-3692.

26. F. Chiodo, M. Marradi, B. Tefsen, H. Snippe, I. van Die and S. Penadés, *Plos. One*, 2013, **8**, e73027.

27. C. C. Lin, Y. C. Yeh, C. Y. Yang, C. L. Chen, G. F. Chen, C. C. Chen and Y. C. Wu, *J. Am. Chem. Soc.*, 2002, **124**, 3508-3509.

28. Y. T Tseng, H. T. Chang, C. T. Chen, C. H. Chen and C. C. Huang, *Biosens. Bioelectron*., 2011, **27**, 95-100.

29. P. H. Chan, B. Ghosh, H. Z. Lai, H. L. Peng, K. K. T. Mong and Y. C. chen, *PLOS One.*, 2013, **8**, e58064;

30. C. C. Huang, C. T. Chen, Y. C. Shiang, Z. H. Lin and H. T. Chang, *Anal. Chem.*, 2009, **81**, 875-882.

31. J. Wang, G. Zhu, M. You, E. Song, M. I. Shukoor, K. Zhang, M. B. altman, Y. Chen, Z. Zhu, C. Z. Huang, W. Tan, *ACS Nano*,. 2012, **6**, 5070-5077;

32. X. yang, X. Liu, Z. Liu, F. Pu, J. Ren, X. Qu. *Adv. Mater*., 2012, **24**, 2890-2895;

33. L. A. Dykman and N. G. Khlebtson, *Chem. Rev.*, 2014, **114**, 1258-1288;

34. K. Niikura, T. Matsunga, T. Suzuki, S. Kobayashi, H. Yamaguchi, Y. Orba, A. Kawaguchi, H. Hasegawa, K. Kajino, T. Ninomiya, K. Ijiro and H. Sawa, *ACSNano.*, 2013, **7**, 3926-3938.

35. G. Bellapadrona, A. B. Tesler, D. Grünstein, L. H. Hossain, R. Kikkeri, P. H. Seeberger, A. Vaskevich and I. Rubinstein, *Anal. Chem*., 2012, **84**, 232-240.

36. B. Nikoobakht and M. A. El-Sayed, *Chem. Mater.*, 2003, **15**, 1957-1962.

37. J. Xie, J. Y. Lee, and D. I. C. Wang, *Chem. Mater.*, 2007, **19**, 2823-2830.

38. E. C. Cho, Y. Liu, and Y. Xia, *Angew. Chem. Int. Ed.*, 2010, **49**, 1976-1980.

39. W. Li, P. Zhang, M. Dai, J. He, T. Babu, Y.-L. Xu, R. Deng, R. Liang, M.-H. Lu, Z. Nie and J. Zhu, *Macromolecules.* 2013, **46**, 2241-2248.

40. P. Kolhar, A. C. Anselmo, V. Gupta, K. Pant, B. Prabhakarpandian, E. Ruoslahti and S. Mitragotri, *Proc. Natl. Acad. Sci. USA.*, 2013, **110**, 10753-10758.

41. P. M. Chaudhary, R. V. Murthy, R. Yadav and R. Kikkeri, *Chem. Commun.*, 2015, **51**, 8112-8115.

2.6. Appendix I: Characterization Data of Synthesized Compounds

Designation	Description	Page
Compound 3	^{1}H, ^{13}C, HRMS	47-48
Compound 6	^{1}H, ^{13}C, HRMS	48-49
Compound 8	^{1}H, ^{13}C, HRMS	50-51
Compound 10	^{1}H, ^{13}C, HRMS	51-52
Compound 7	^{1}H, ^{13}C, HRMS	53-54
Compound 9	^{1}H, ^{13}C, HRMS	54-55
Compound 11	^{1}H, ^{13}C, HRMS	56-57

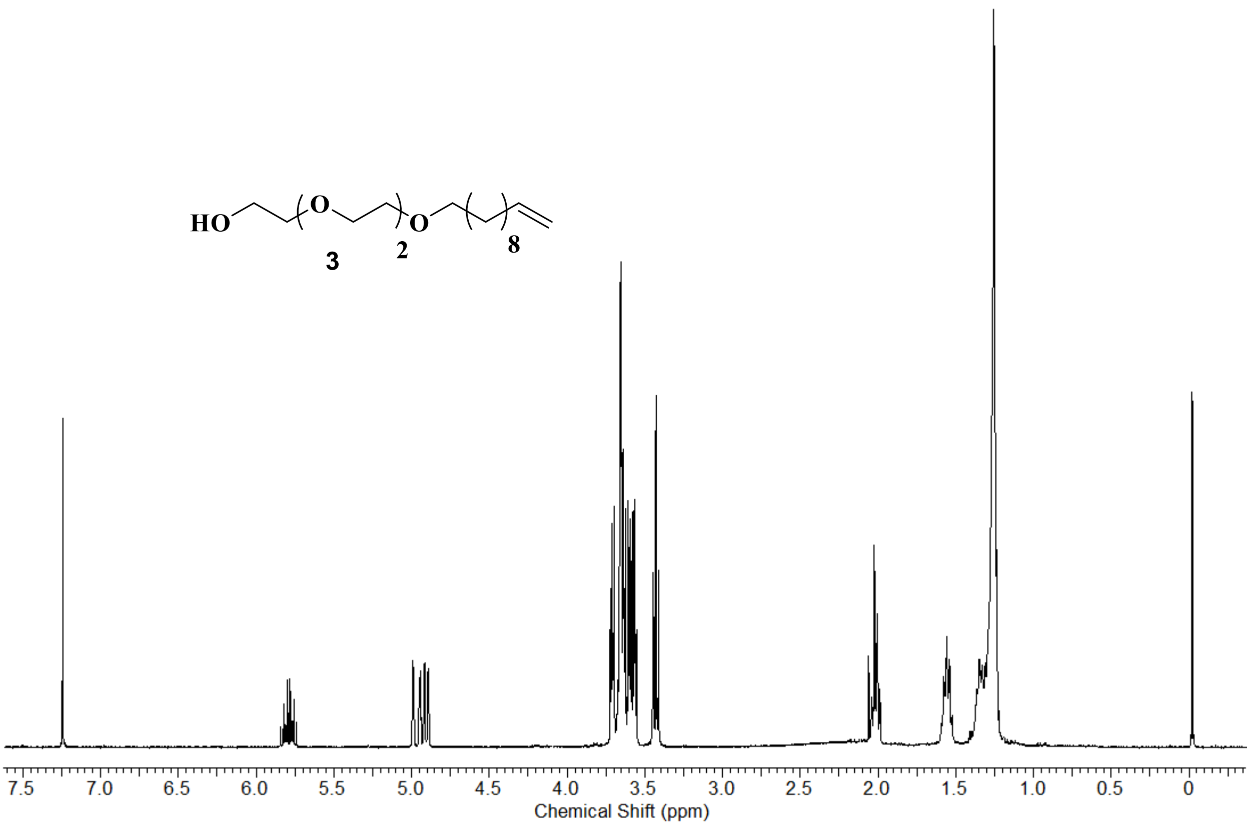
HO
O
O
3
2
8
7.5
7.0
6.5
6.0
5.5
5.0
4.5
4.0
3.5
3.0
2.5
2.0
1.5
1.0
0.5
0
Chemical Shift (ppm)

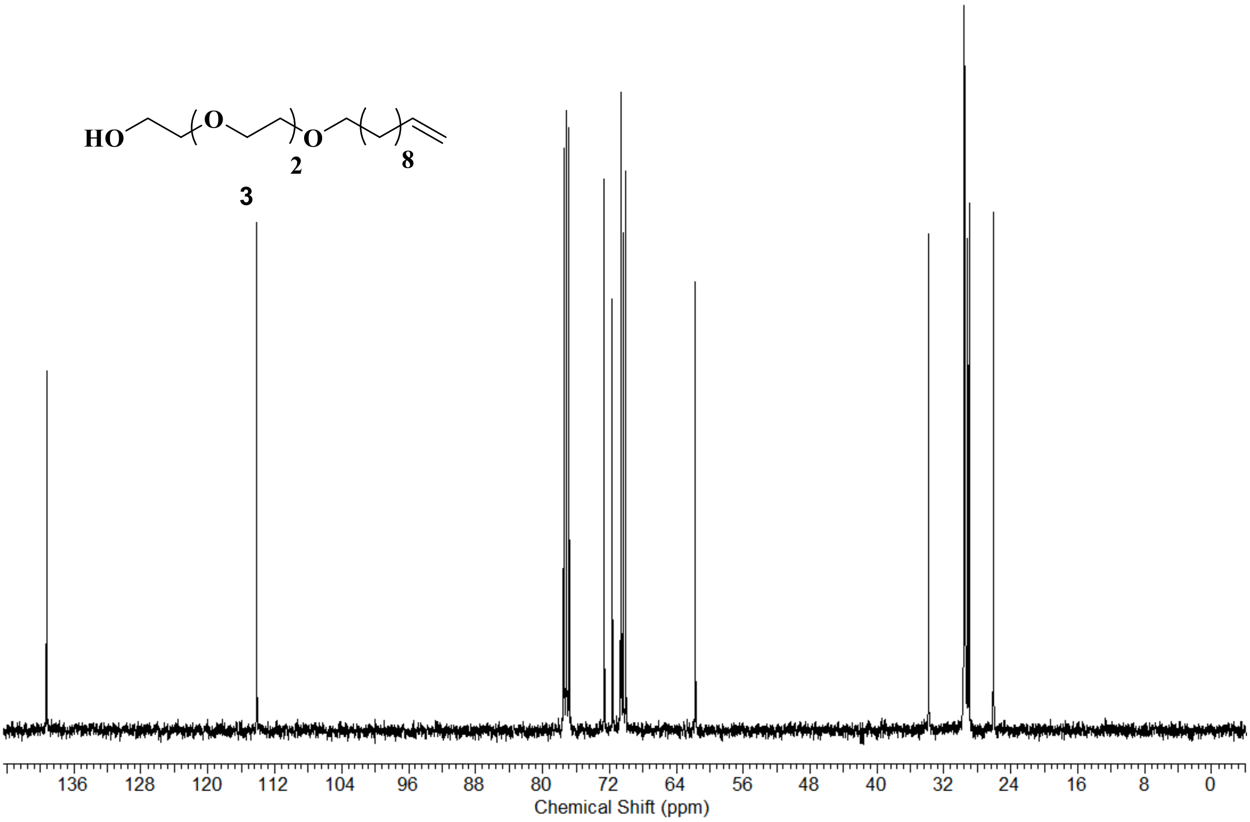
HO
O
O
2
8
3
136
128
120
112
104
96
88
80
72
64
56
48
40
32
24
16
8
0
Chemical Shift (ppm)

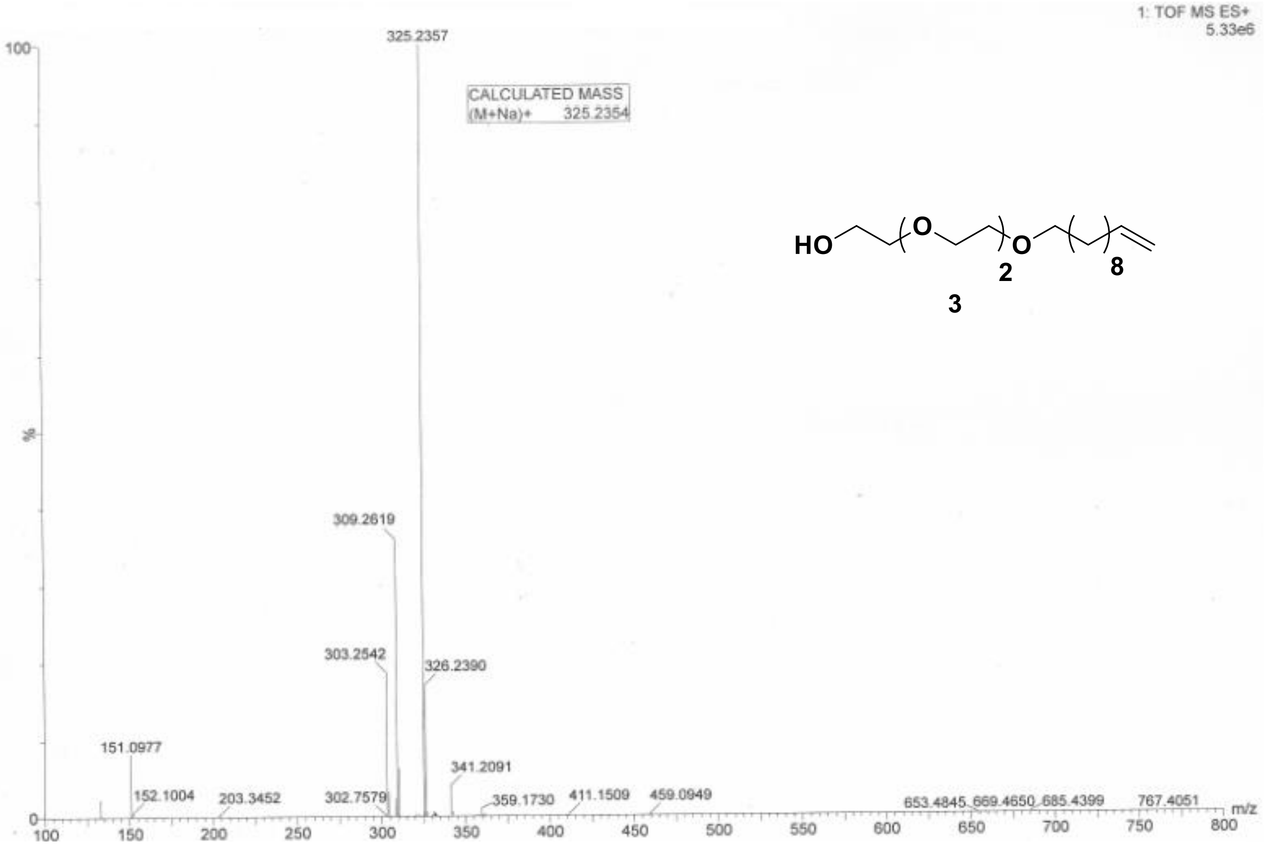
1: TOF MS ES+
5.33e6
100
%
0
325.2357
CALCULATED MASS
(M+Na)+ 325.2354
309.2619
303.2542
326.2390
151.0977
152.1004
203.3452
302.7579
341.2091
359.1730
411.1509
459.0949
653.4845
669.4650
685.4399
767.4051
m/z
100
150
200
250
300
350
400
450
500
550
600
650
700
750
800
HO
O
O
2
8
3

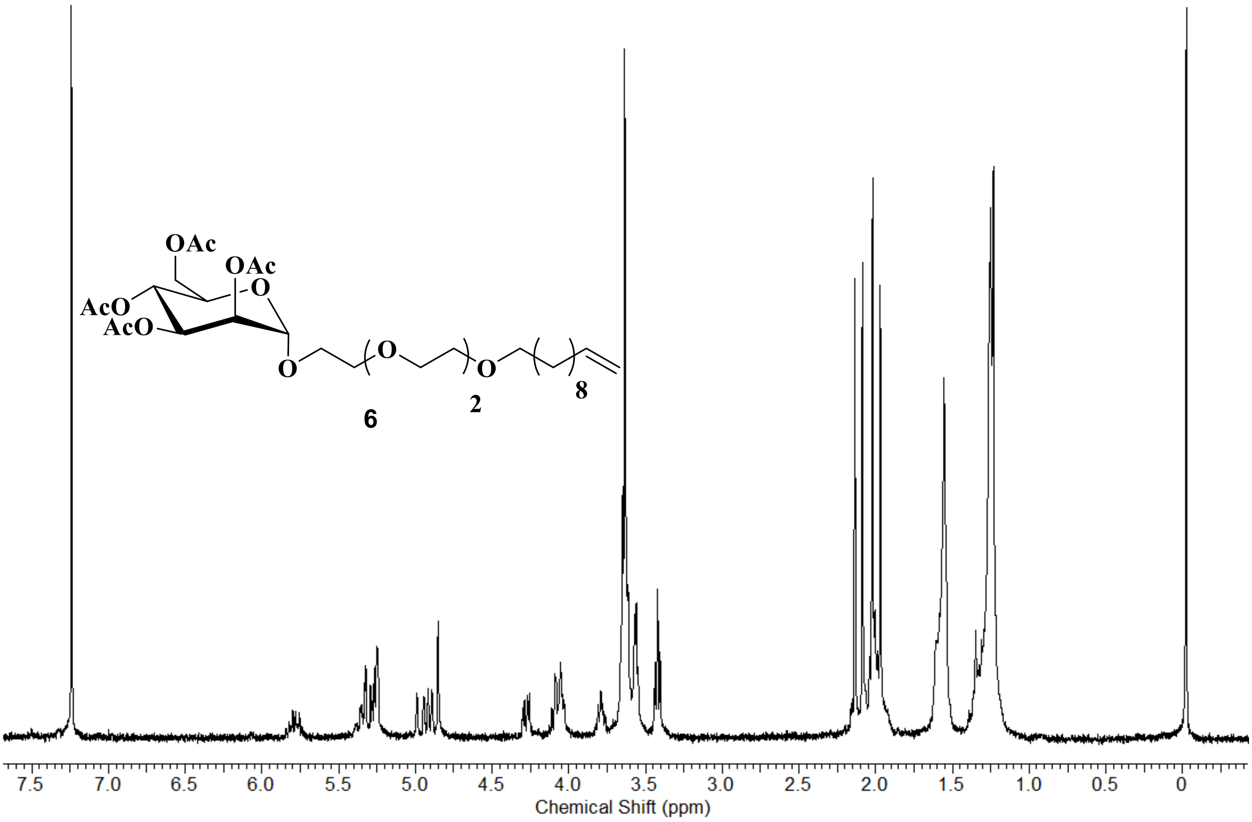
OAc
OAc
O
AcO
AcO
O
O
O
2
8
6
7.5
7.0
6.5
6.0
5.5
5.0
4.5
4.0
3.5
3.0
2.5
2.0
1.5
1.0
0.5
0
Chemical Shift (ppm)

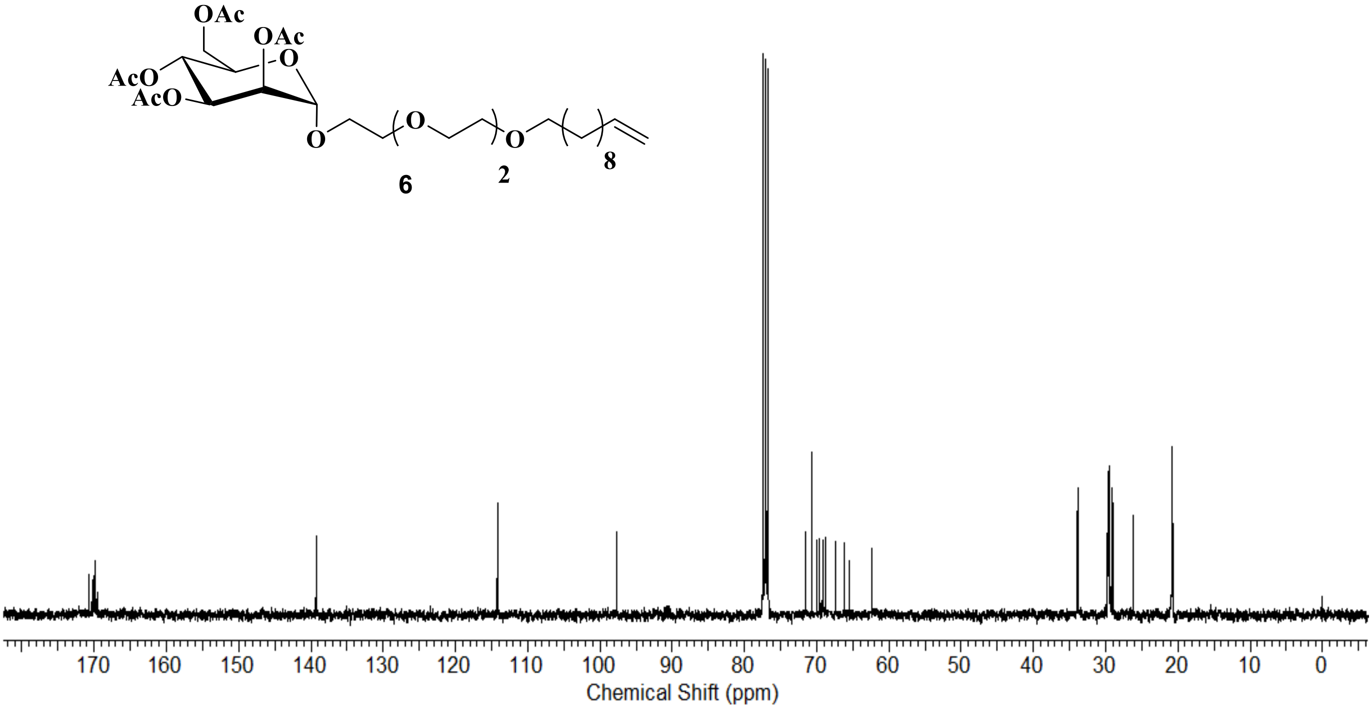
OAc
OAc
O
AcO
AcO
O
O
2
O
8
6
170
160
150
140
130
120
110
100
90
80
70
60
50
40
30
20
10
0
Chemical Shift (ppm)

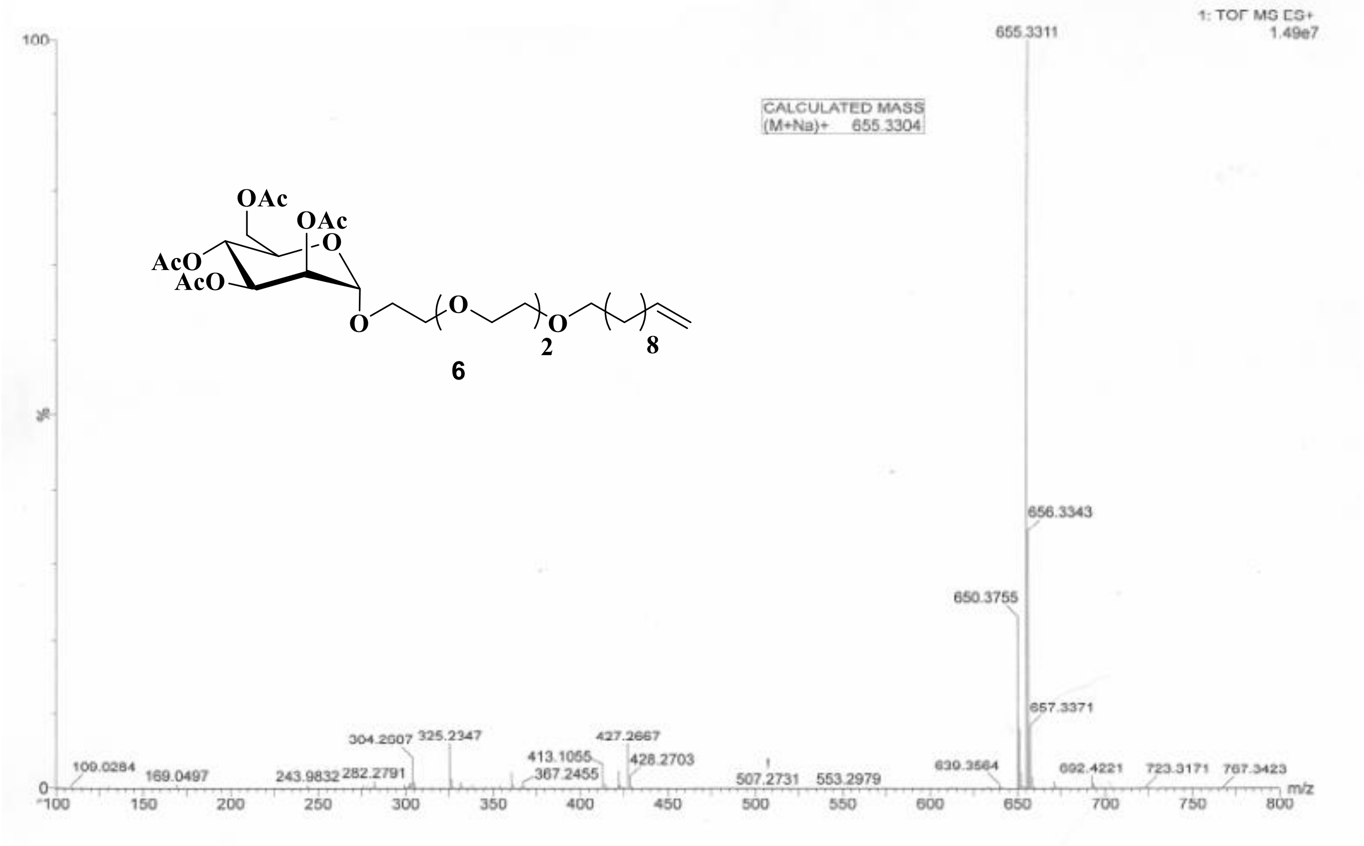
1: TOF MS ES+
1.49e7
655.3311
CALCULATED MASS
(M+Na)+ 655.3304
OAc
OAc
O
AcO
AcO
O
O
2
O
8
6
%
100
0
656.3343
650.3755
657.3371
109.0284
169.0497
243.9832
282.2791
304.2607
325.2347
413.1055
367.2455
427.2667
428.2703
507.2731
553.2979
639.3564
692.4221
723.3171
767.3423
m/z
100
150
200
250
300
350
400
450
500
550
600
650
700
750
800

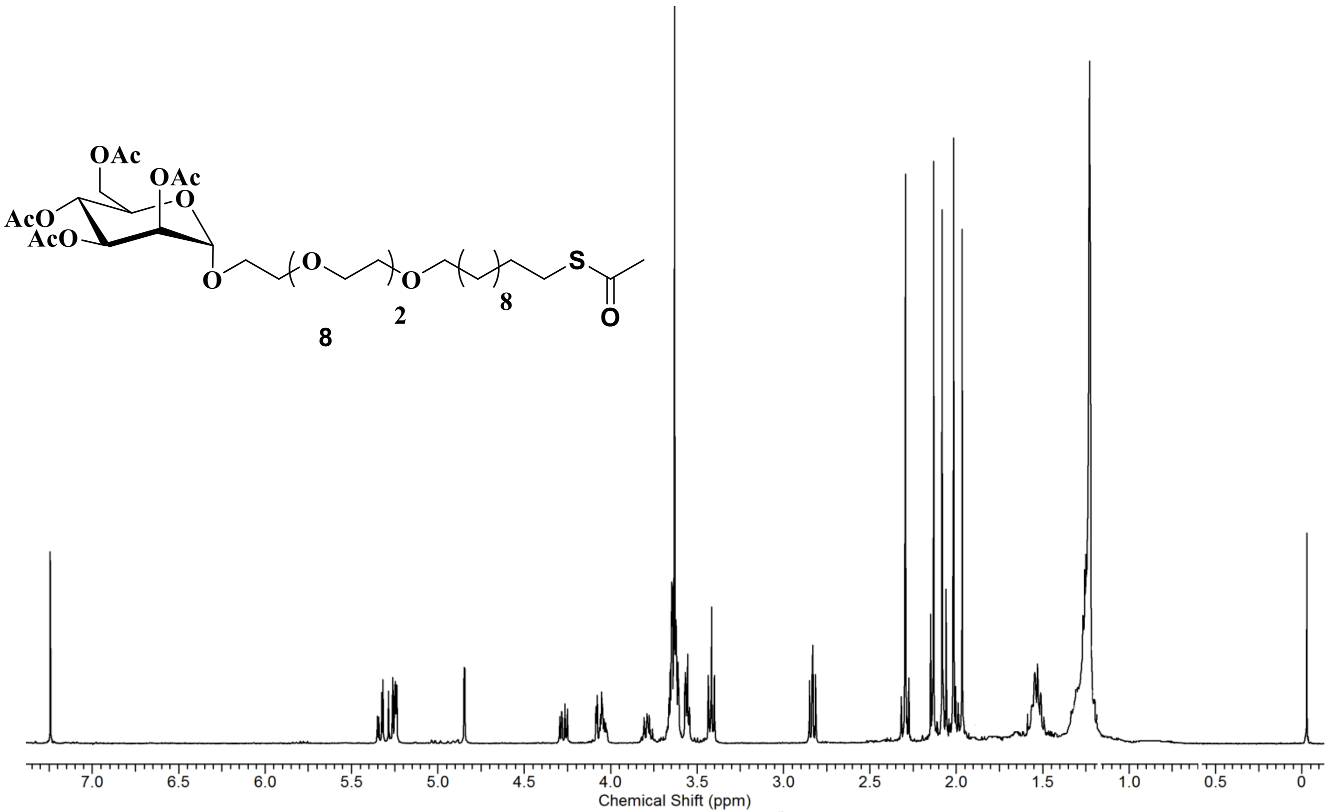
OAc
OAc
AcO
AcO
O
O
O
O
S
O
2
8
8
7.0
6.5
6.0
5.5
5.0
4.5
4.0
3.5
3.0
2.5
2.0
1.5
1.0
0.5
0
Chemical Shift (ppm)

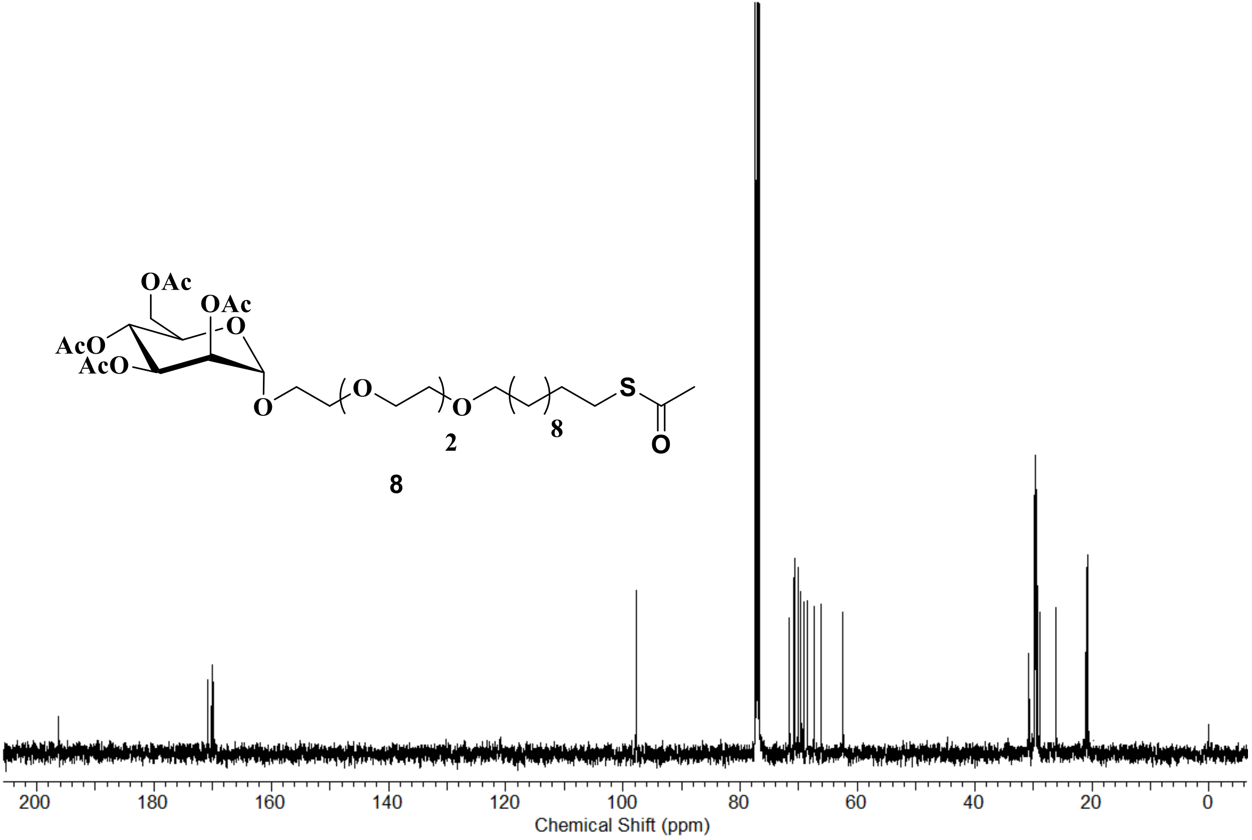
OAc
OAc
AcO
AcO
O
O
O
O
S
O
2
8
8
200
180
160
140
120
100
80
60
40
20
0
Chemical Shift (ppm)

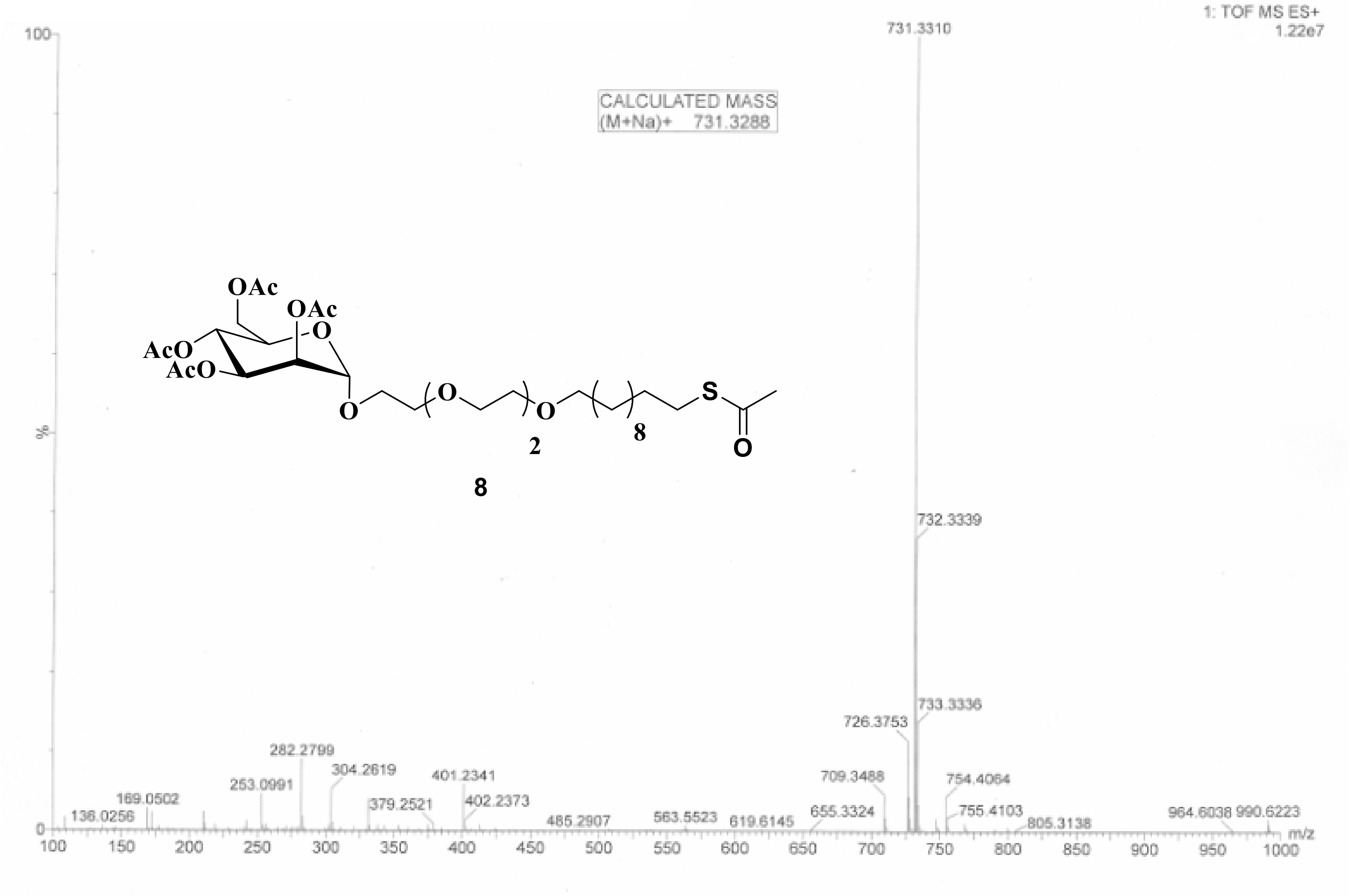
1: TOF MS ES+
1.22e7
CALCULATED MASS
(M+Na)+ 731.3288
731.3310
732.3339
733.3336
726.3753
709.3488
754.4064
755.4103
805.3138
964.6038
990.6223
655.3324
619.6145
563.5523
485.2907
402.2373
401.2341
379.2521
304.2619
282.2799
253.0991
169.0502
136.0256
100
%
0
m/z
100 150 200 250 300 350 400 450 500 550 600 650 700 750 800 850 900 950 1000
OAc
OAc
O
AcO
AcO
O
O
O
S
O
2
8

8

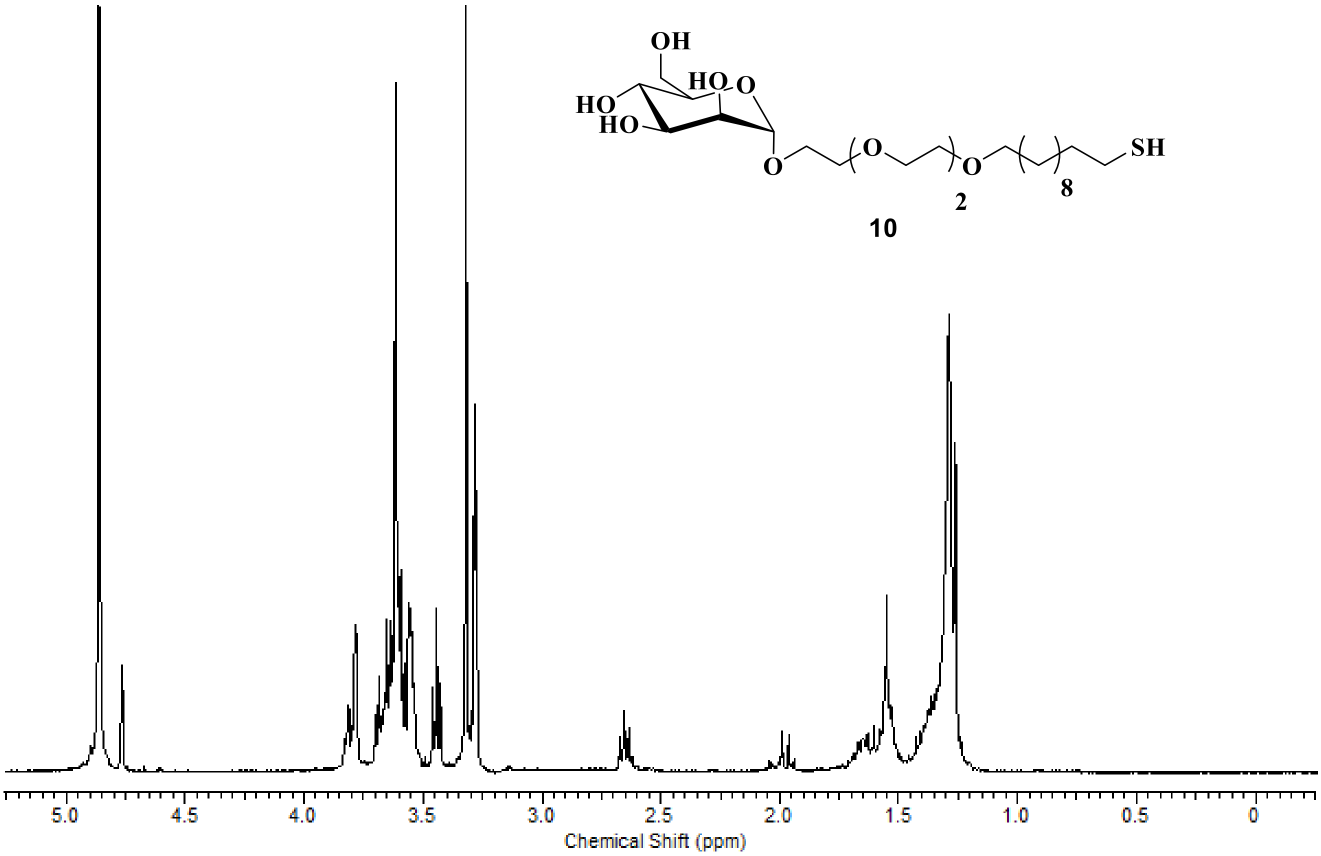
OH
HO
O
HO
HO
O
O
O
SH
2
8
5.0 4.5 4.0 3.5 3.0 2.5 2.0 1.5 1.0 0.5 0
Chemical Shift (ppm)

10

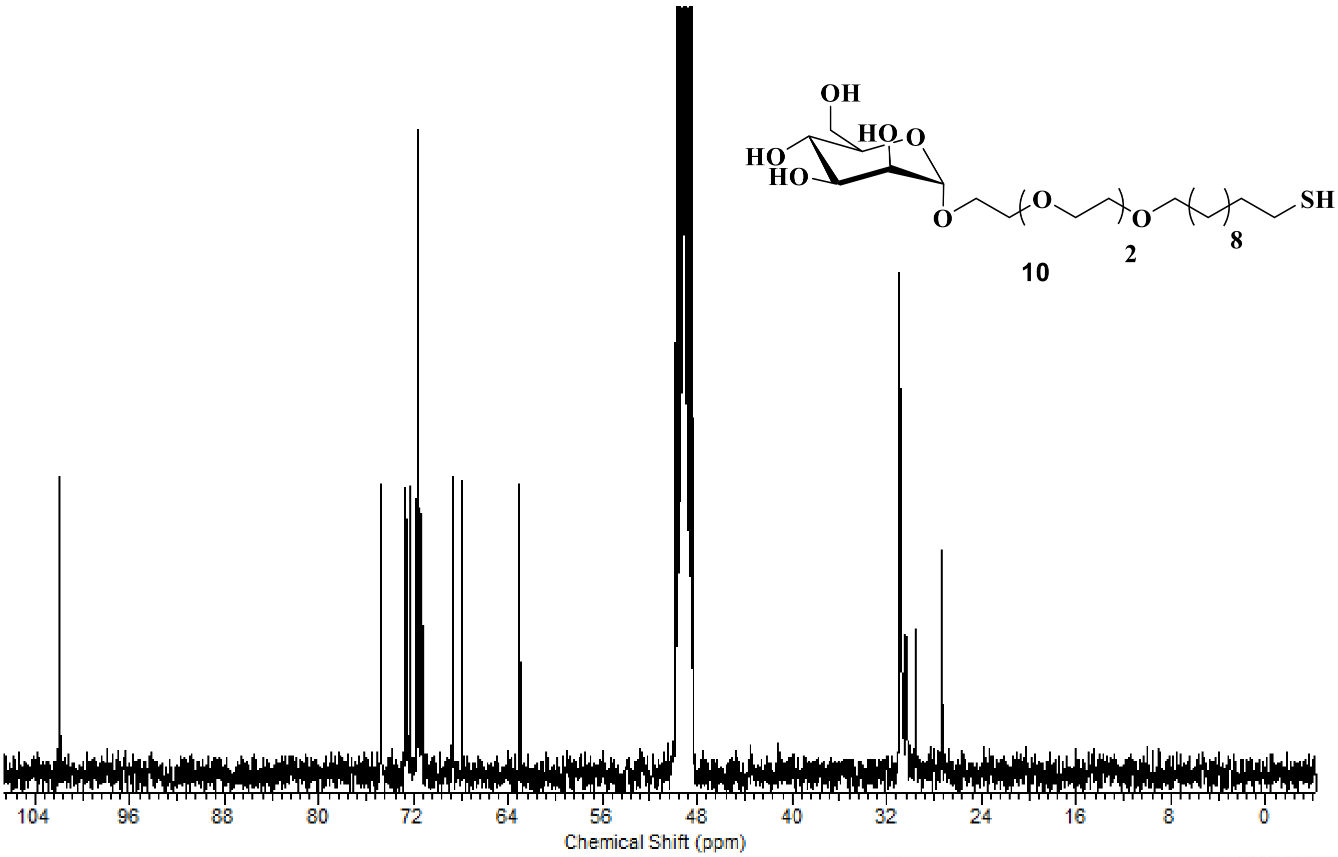
OH
HO
O
HO
HO
O
O
O
SH
2
8
10
104
96
88
80
72
64
56
48
40
32
24
16
8
0
Chemical Shift (ppm)

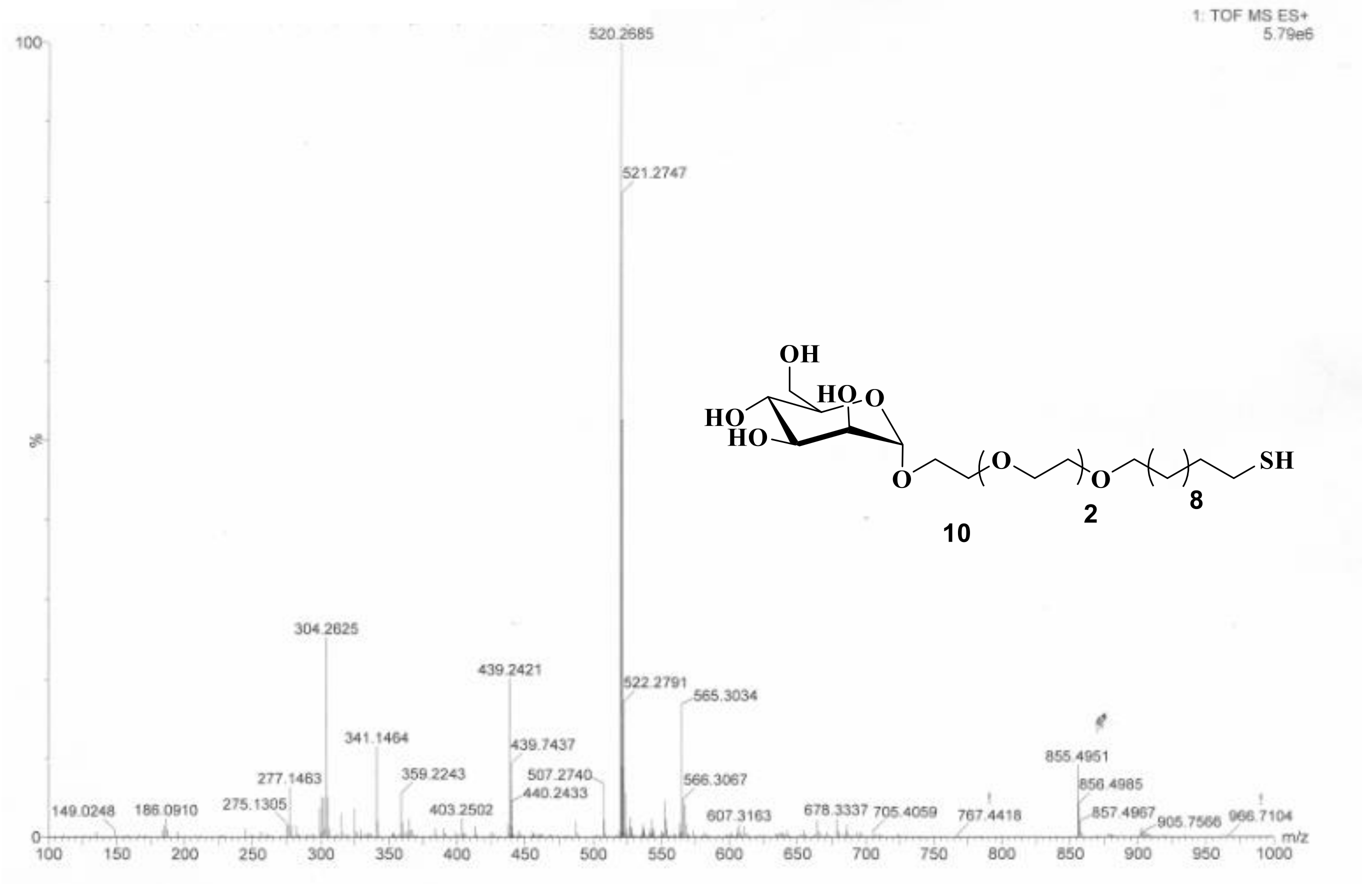
1: TOF MS ES+
5.79e6
100
%
0
520.2685
521.2747
304.2625
439.2421
522.2791
565.3034
341.1464
439.7437
855.4951
277.1463
359.2243
507.2740
566.3067
856.4985
440.2433
149.0248
186.0910
275.1305
403.2502
607.3163
678.3337
705.4059
767.4418
857.4967
905.7566
966.7104
m/z
100
150
200
250
300
350
400
450
500
550
600
650
700
750
800
850
900
950
1000
OH
HO
O
HO
HO
O
O
O
SH
2
8
10

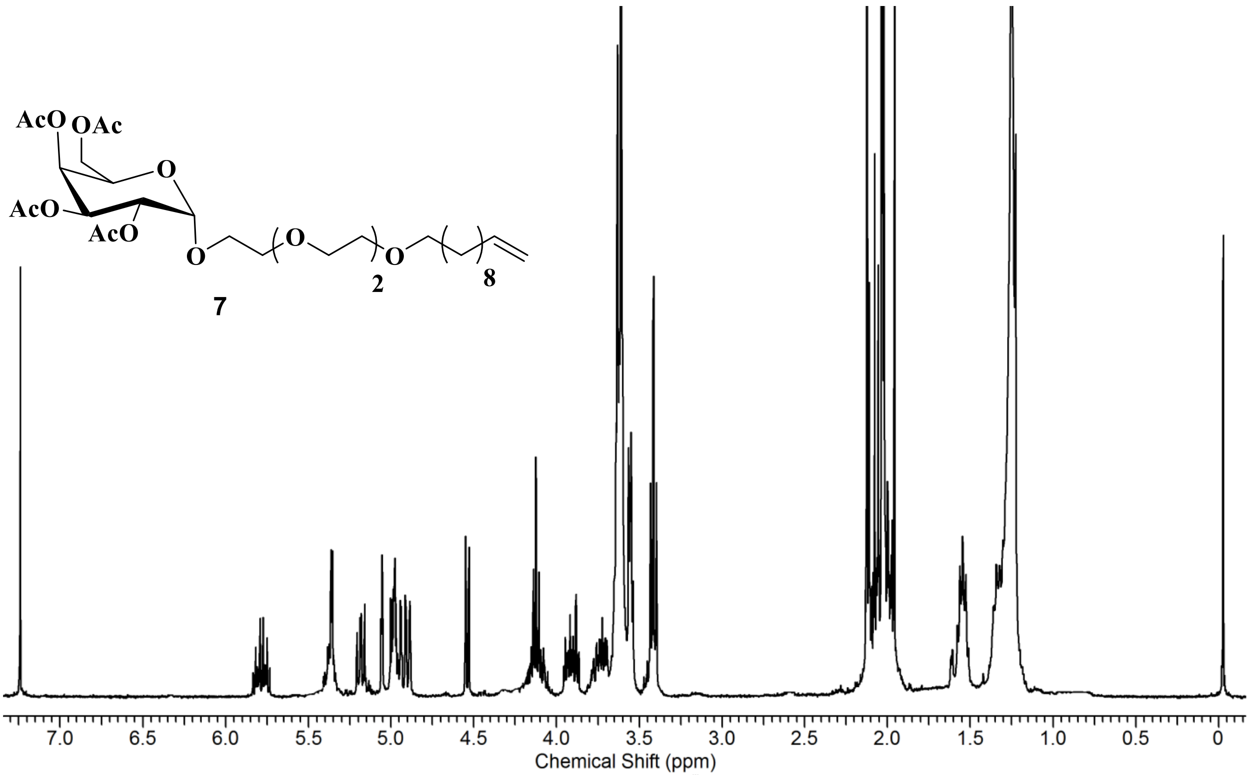
AcO
OAc
O
AcO
AcO
O
O
2
O
8
7
7.0
6.5
6.0
5.5
5.0
4.5
4.0
3.5
3.0
2.5
2.0
1.5
1.0
0.5
0
Chemical Shift (ppm)

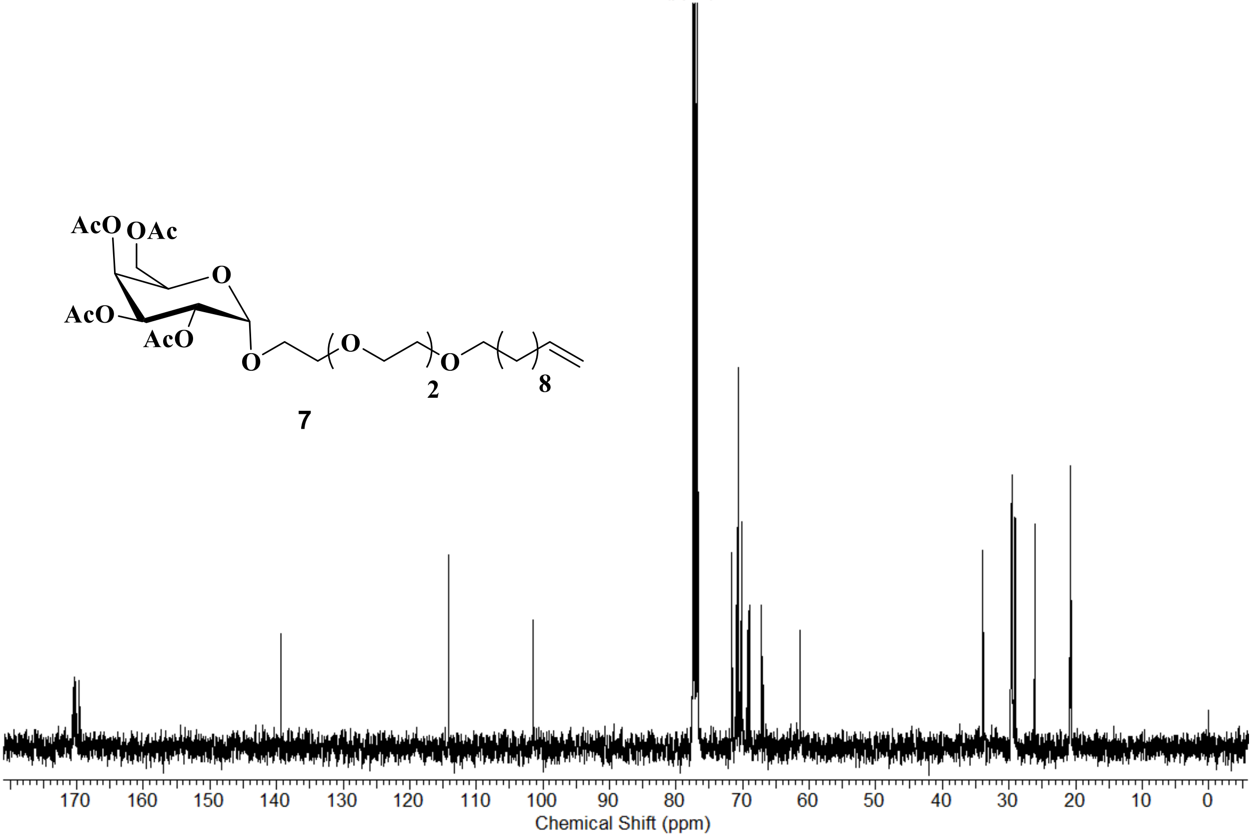
AcO
OAc
O
AcO
AcO
O
O
2
O
8
7
170
160
150
140
130
120
110
100
90
80
70
60
50
40
30
20
10
0
Chemical Shift (ppm)

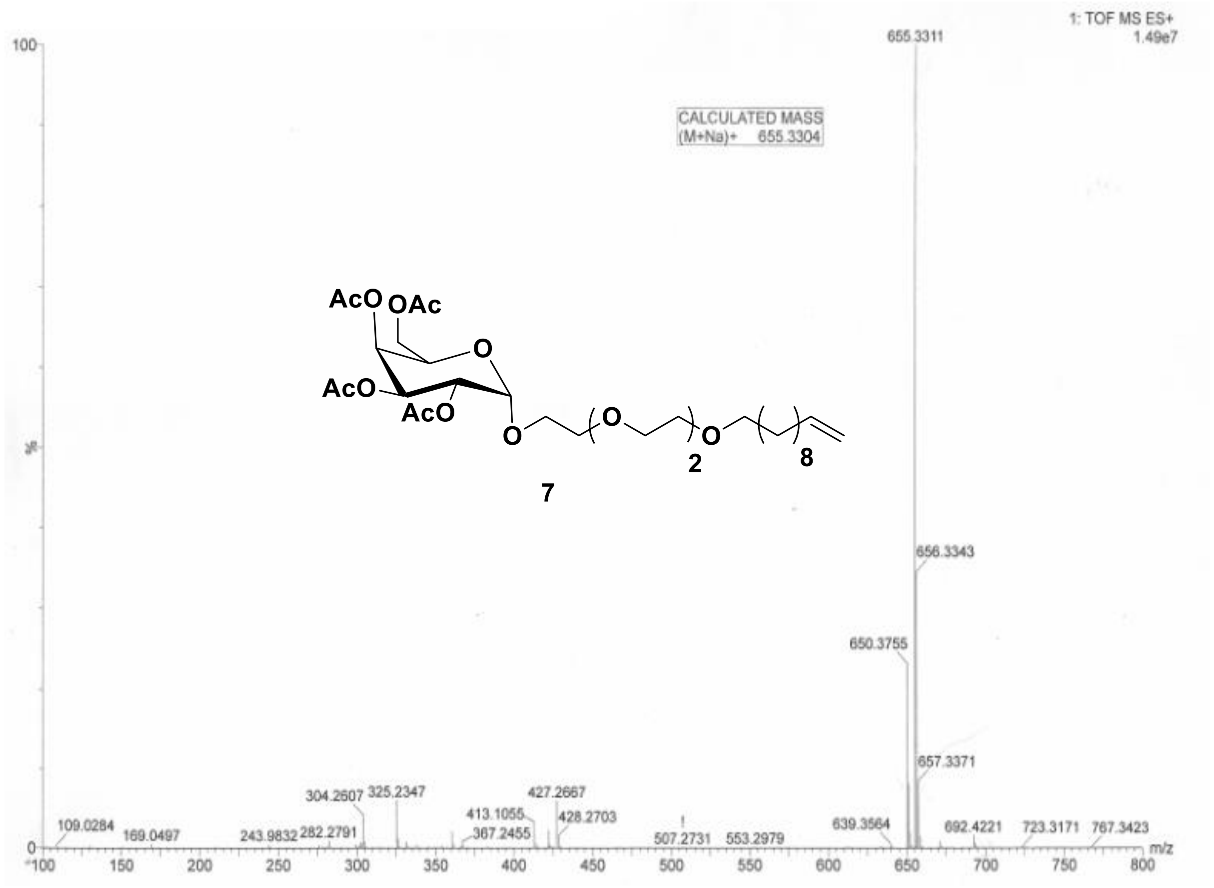
1: TOF MS ES+
1.49e7
655.3311
CALCULATED MASS
(M+Na)+ 655.3304
AcO
OAc
O
AcO
AcO
O
O
O
2
8
656.3343
650.3755
657.3371
109.0284
169.0497
243.9832
282.2791
304.2607
325.2347
413.1055
367.2455
427.2667
428.2703
507.2731
553.2979
639.3564
692.4221
723.3171
767.3423
100
%
0
100
150
200
250
300
350
400
450
500
550
600
650
700
750
800
m/z

7

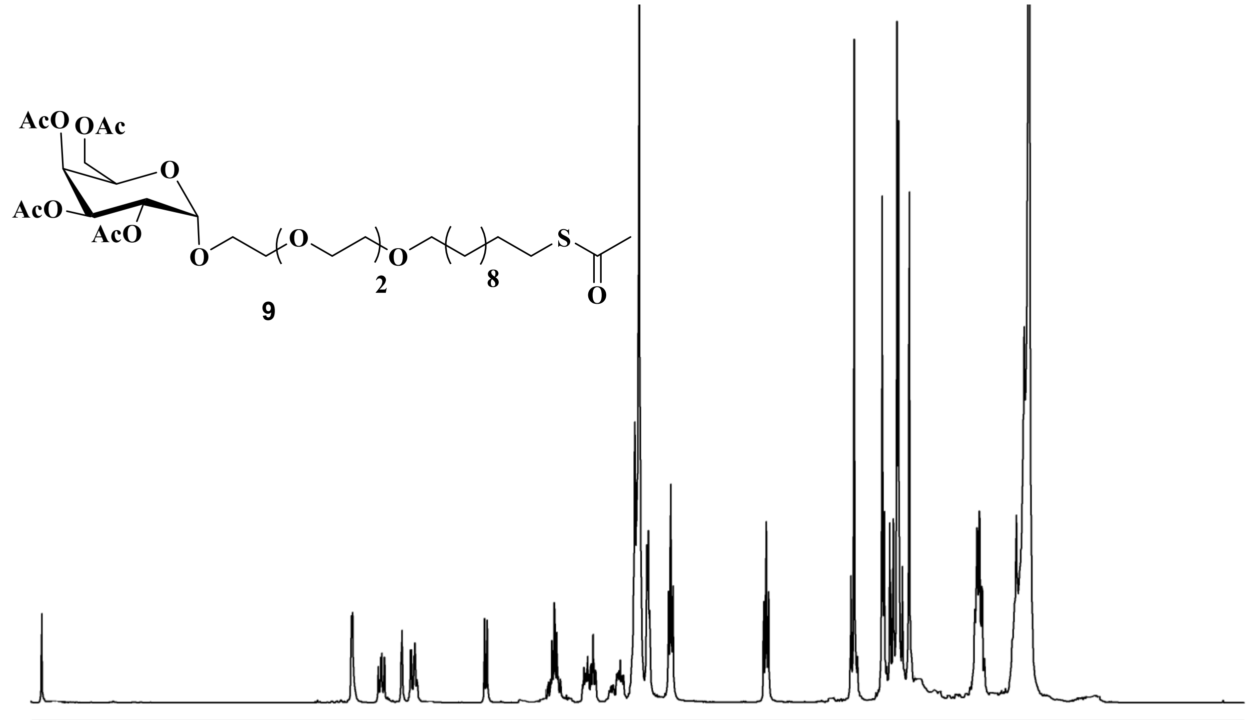
AcO
OAc
O
AcO
AcO
O
O
O
2
8
S
O
7.0
6.5
6.0
5.5
5.0
4.5
4.0
3.5
3.0
2.5
2.0
1.5
1.0
0.5
0
Chemical Shift (ppm)

9

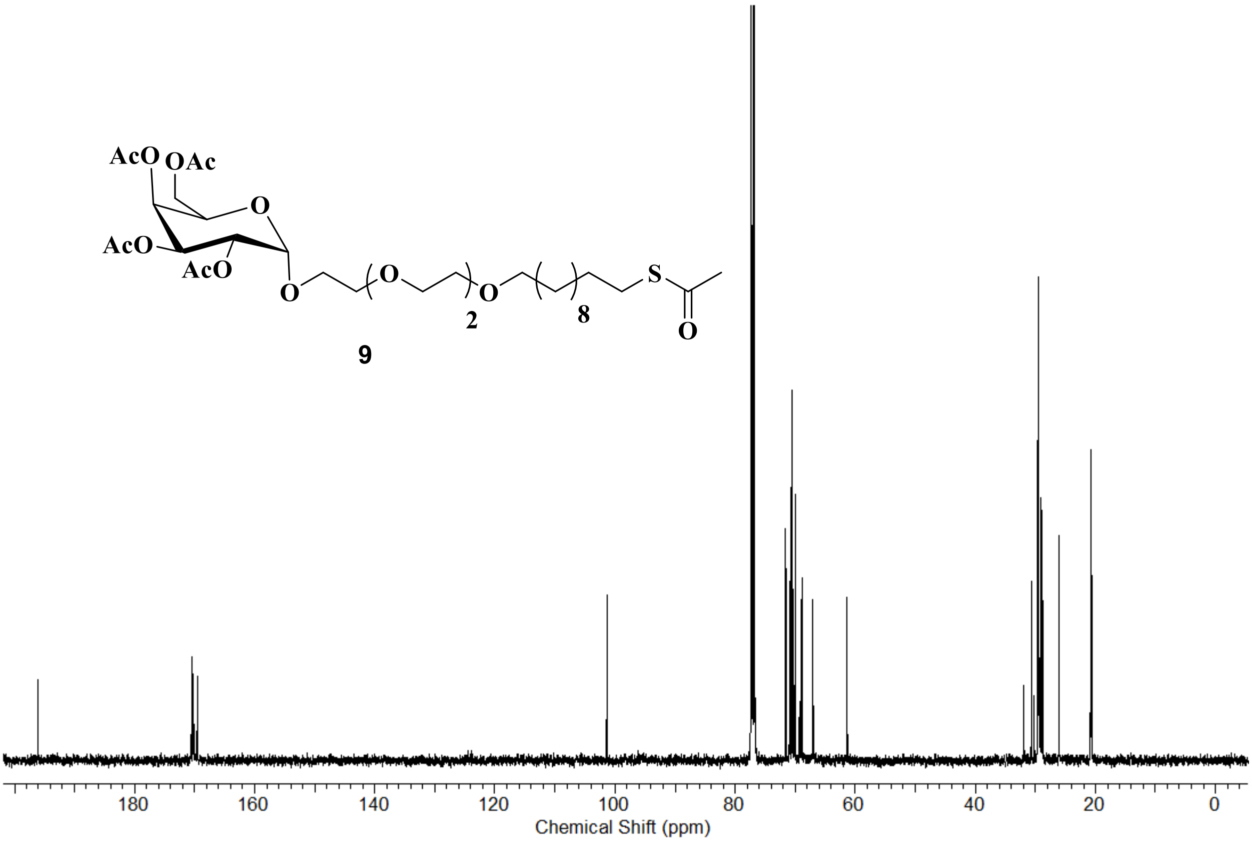

AcO
OAc
O
AcO
AcO
O
O
O
2
8
S
O
9
180
160
140
120
100
80
60
40
20
0
Chemical Shift (ppm)

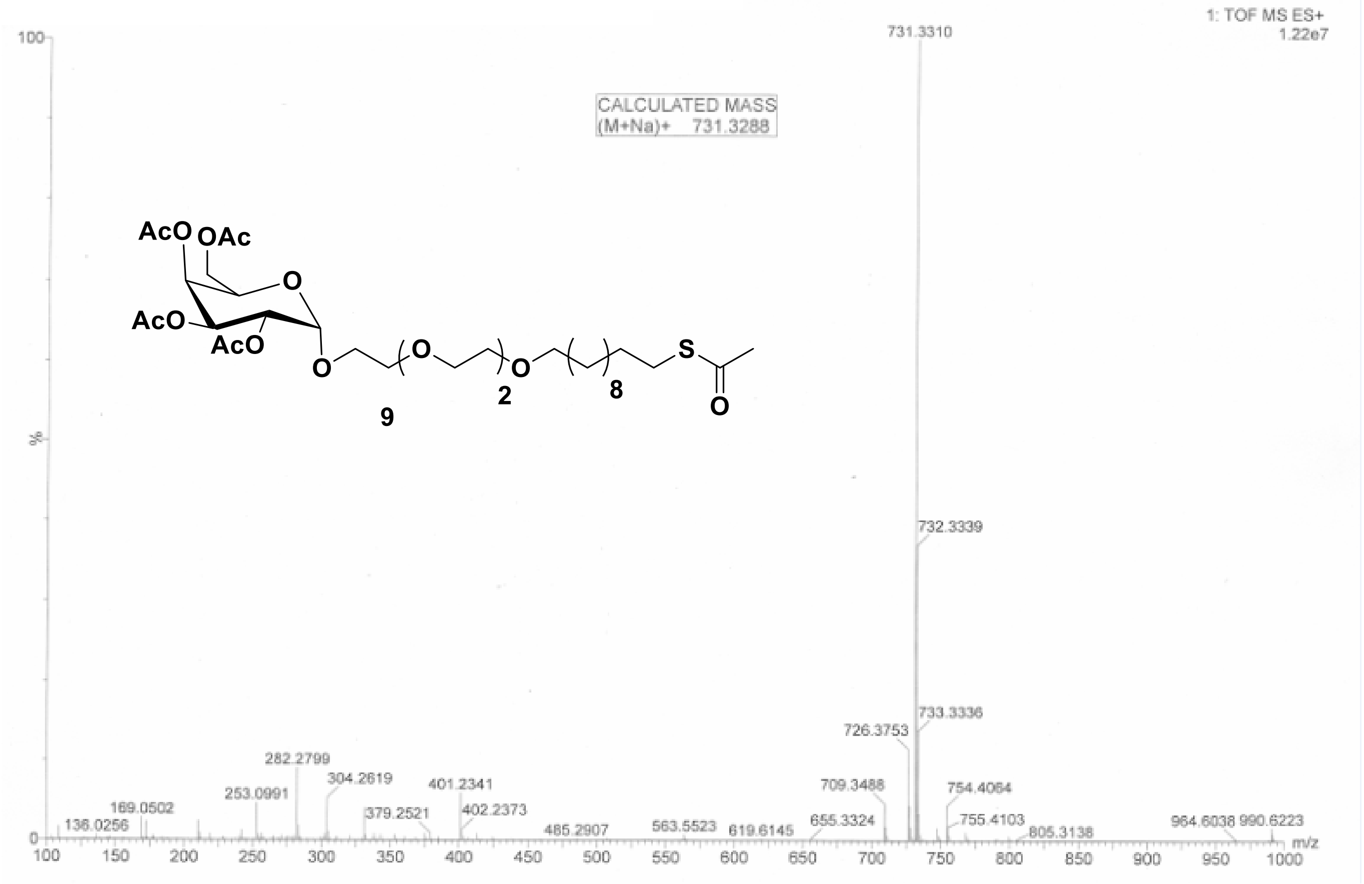

1: TOF MS ES+
1.22e7
100
%
0
731.3310
CALCULATED MASS
(M+Na)+ 731.3288
AcO
OAc
O
AcO
AcO
O
O
O
2
8
S
O
9
732.3339
733.3336
726.3753
709.3488
754.4064
755.4103
805.3138
964.6038
990.6223
282.2799
304.2619
253.0991
401.2341
402.2373
379.2521
169.0502
136.0256
485.2907
563.5523
619.6145
655.3324
m/z
100
150
200
250
300
350
400
450
500
550
600
650
700
750
800
850
900
950
1000

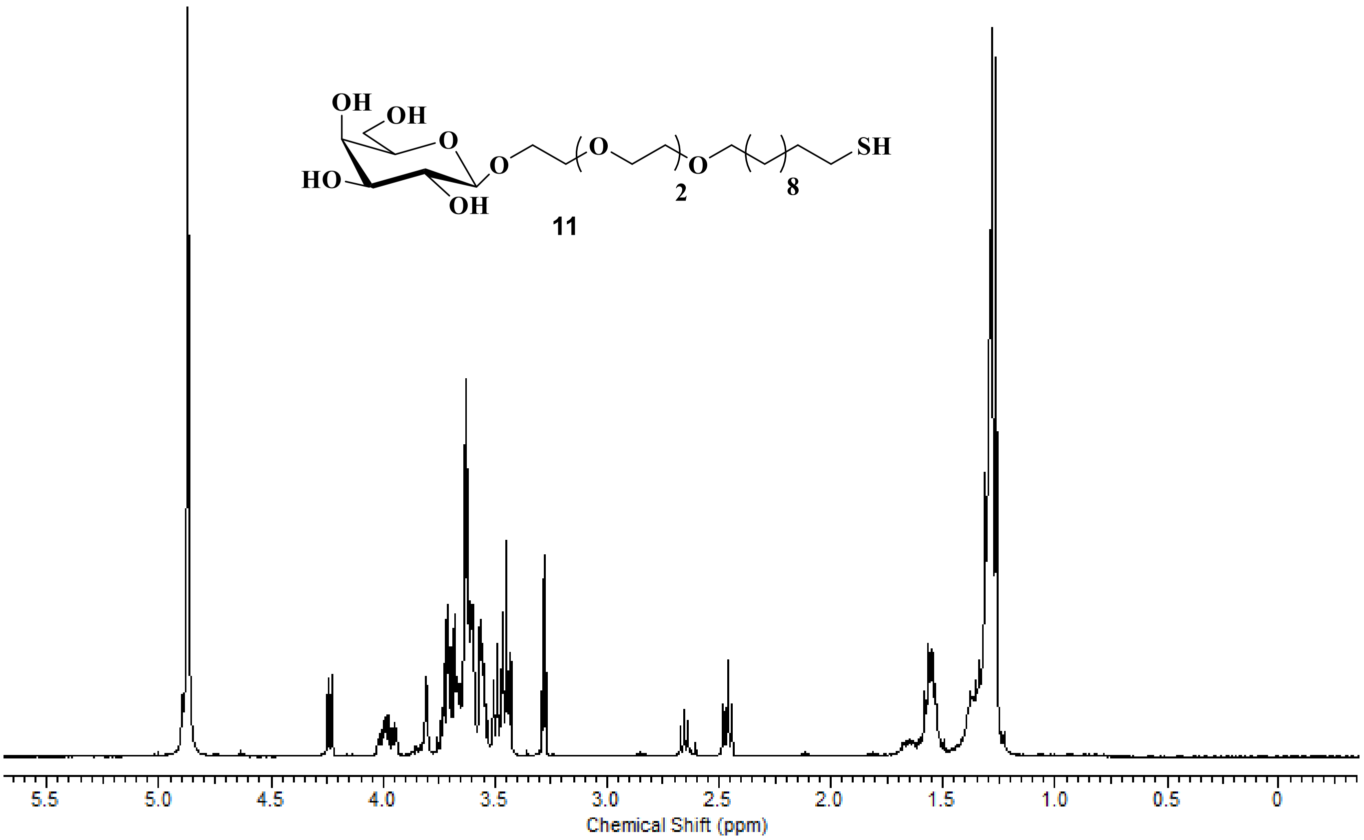
OH
OH
O
HO
OH
O
O
O
2
8
SH
5.5
5.0
4.5
4.0
3.5
3.0
2.5
2.0
1.5
1.0
0.5
0
Chemical Shift (ppm)

11

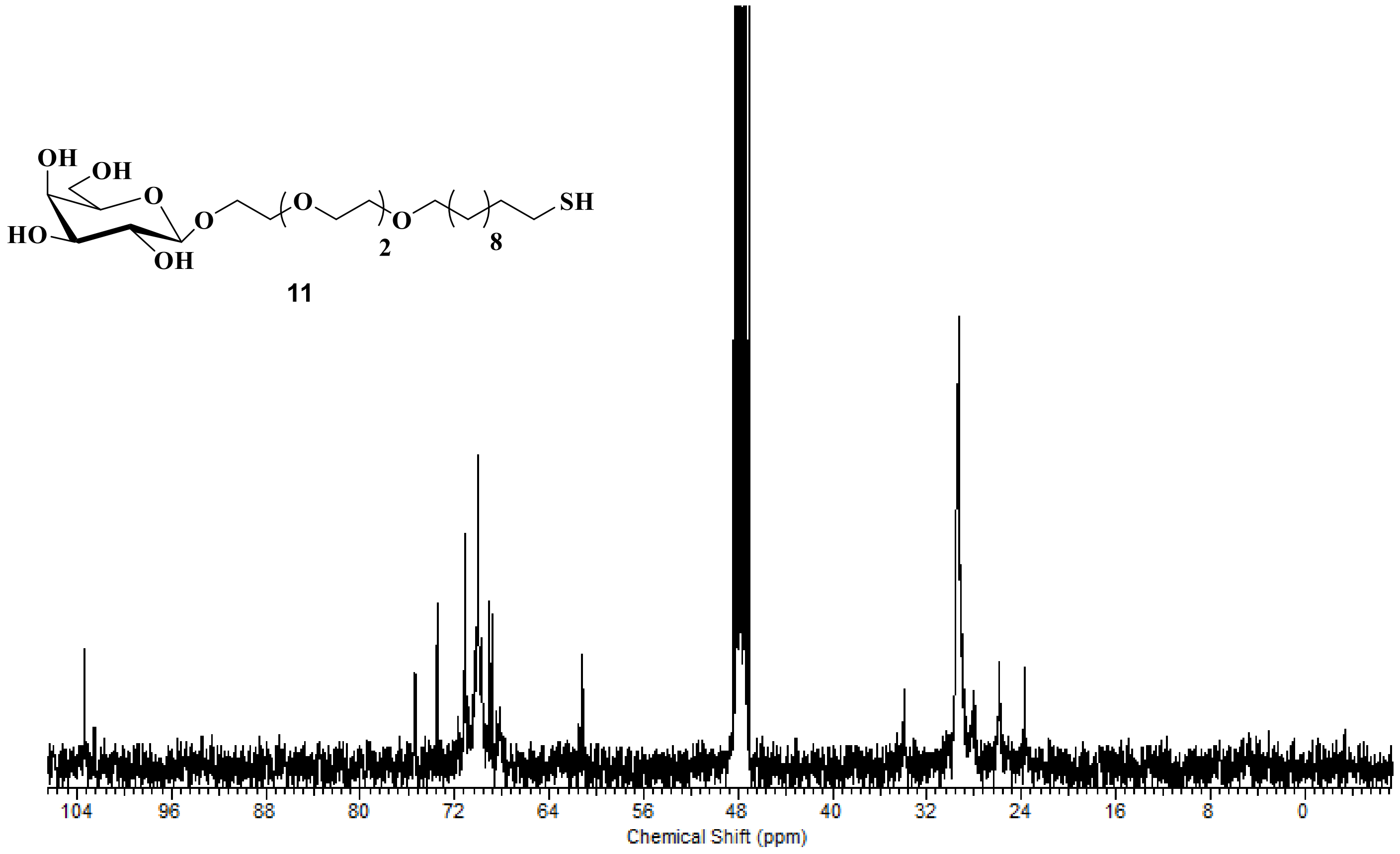
OH
OH
O
HO
OH
O
O
O
2
8
SH
104
96
88
80
72
64
56
48
40
32
24
16
8
0
Chemical Shift (ppm)

11

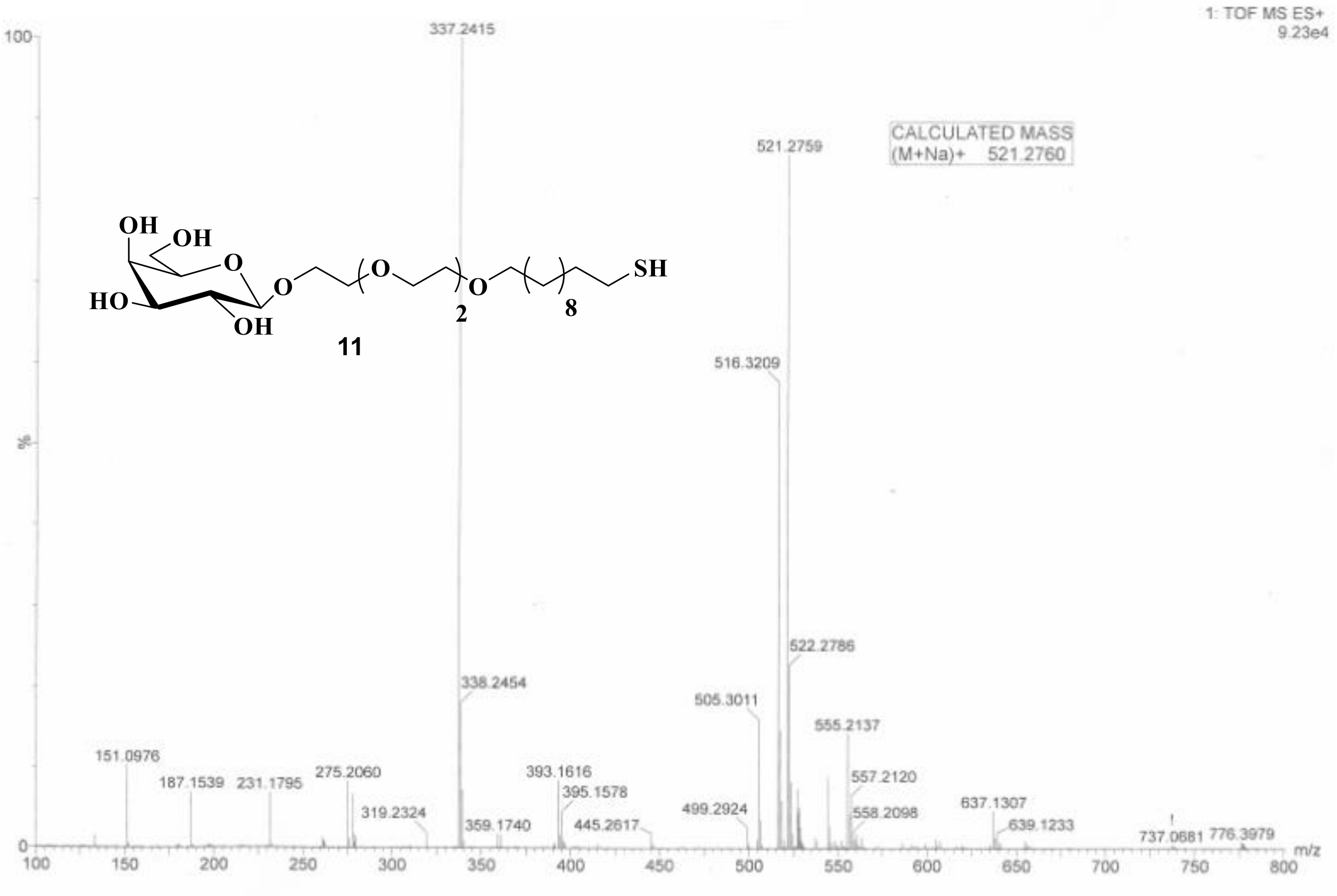
1: TOF MS ES+
9.23e4
100
%
0
337.2415
521.2759
CALCULATED MASS
(M+Na)+ 521.2760
516.3209
522.2786
338.2454
505.3011
555.2137
151.0976
187.1539
231.1795
275.2060
393.1616
395.1578
557.2120
319.2324
499.2924
637.1307
558.2098
359.1740
445.2617
639.1233
737.0681
776.3979
100
150
200
250
300
350
400
450
500
550
600
650
700
750
800
m/z
OH
OH
O
HO
OH
O
O
O
SH
2
8
11

Chapter 3

Glyco-gold nanoparticle shapes enhance carbohydrate-protein interactions in mammalian cells.

3.1 Introduction

Carbohydrates are the most abundant class of biomolecules on cell surfaces which are critically important for the cellular behaviour and functions and are considered to be the first line of interaction between different pathogens, toxic materials, and between different cells.[1-2] Hence, carbohydrates are of central importance in the development of the next-generation biomarkers. However, the avidity of the monovalent carbohydrate-protein interactions is usually weak. Glyco-nanotechnology has provided multivalent scaffolds to increase the avidity of carbohydrate-mediated interactions and also has offered additional optical and electrochemical properties to develop biosensors and imaging tools.[3-5] In addition to the multivalency, the investigation showed that the size, orientation and density of the sugars on multivalent scaffolds can fine tune specific carbohydrate-protein interactions (CPI).[6-12] For example, Kiessling et al. have shown the importance of multivalent ligand architectures in CPI.[13] Penadés et al. developed a protocol to synthesize AuNPs with the hybrid-sugar system to explore its applications in blood brain barrier permeability, anti-HIV pro-drugs carrier.[14-16] Galan et al. developed glyco-quantum dots with defined glycan density and the nature of the oligosaccharide structures to tune the cell uptake and intracellular localization.[17] Seeberger et al. have shown the orientation and spatial arrangements of sugars that influence the relative activity.[18-19] Also, recent studies have demonstrated that the different shapes of the nanoparticles influenced the cellular uptake, biodistribution, and immune response.[20] High molecular stimulation *in vitro* and *in vivo* studies reported that elongated shapes have enhanced translocation rate over spherical ones and might have contributed to the structural evolution of pathogens such as bacteria and virus from spherical to rod-like morphologies. Among the existing shape dependent nanoparticles to date, gold nanoparticles have been at the forefront of nanotechnology research.[21-27] Questions regarding the shape dependent *in vitro* uptake and *in vivo* distribution have been thoroughly investigated by conjugating ligands such as antibodies, peptides, and aptamers to alter both the cytokine response, sequestration of NPs in different organs and clearance.[28-31] However, deciphering the shape dependent carbohydrate-mediated interactions undoubtedly assist in understand the origin of cell surface carbohydrates behaviour on endothelial, epithelial and neural cells which exhibit different shapes. To the best of our knowledge, no attempt has been made to study the shape-dependent CPI in *in vitro* models. Herein, we synthesized 3 different shapes of G-AuNPs and interpreted their roles in carbohydrate-mediated lectin binding and cellular uptake. Finally, we also studied the mechanism of cellular uptake of G-AuNPs using different pathway inhibitors. Our screening deciphers the role of shape in designing the next generation phenotypic specific drug delivery probes.

3.2 Results & Discussion

3.2.1 Synthesis & Lectin Binding Affinity of The G-AuNPs: PEG linker (1) and sugar ligands (2-3) (Fig 1) were covalently conjugated to AuNPs using previously reported ligand exchange processes[32] and formed G-AuNPs were characterized by UV, SEM and TEM (Fig 2) To demonstrate the sensitive and selective binding between G-AuNPs and lectins, we performed ELISA plate inhibition assay using ConA, DC-SIGN and PNA lectins with G-AuNPs. Briefly, mannose-BSA and galactose-BSA, as reference ligands, were immobilized on a 96-well plate and treated with HRP-conjugated ConA or PNA lectins (1 mg/ml), in the presence of G-AuNPs, at different concentrations.

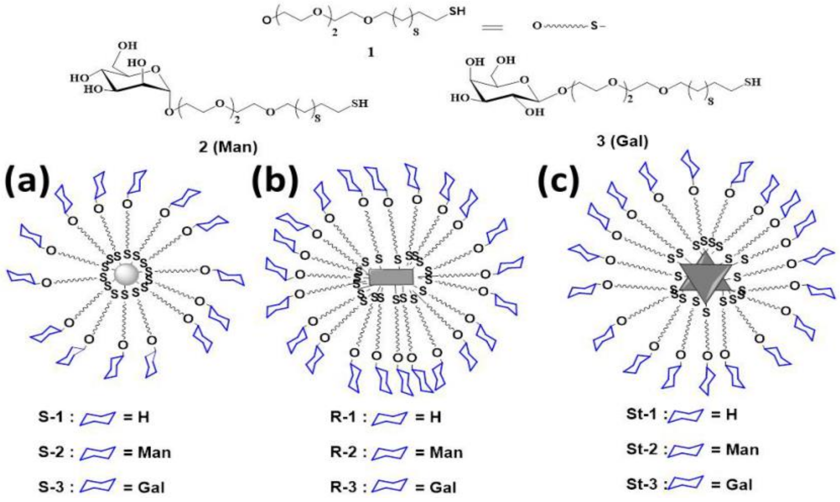

Figure 1. Structure of the sugar conjugated AuNPS (a) sphere; (b) rod; (c) star.

In case of DC-SIGN, lectin treatment was followed by HRP anti-IgG. After incubation, HRP was catalyzed and logarithmic curve for inhibition of lectin binding was plotted and IC_{50} values were determined (Fig 3(ii)). Table 1 summarizes the IC_{50} values of G-AuNPs. Mannose conjugated AuNPs exhibited substantial inhibition of ConA and DC-SIGN lectins, while galactose or PEG-conjugated G-AuNPs showed no affinity at all. Among three different shapes, rod-AuNPs exhibited nearly 3-fold more potent inhibition than spherical and star-shaped AuNPs. To demonstrate the possible selectivity of the binding, we performed inhibition assay with PNA lectin. As expected, mannose-conjugated AuNPs did not bind at all, while a significant inhibition was seen with galactose-coated AuNPs. Among the different

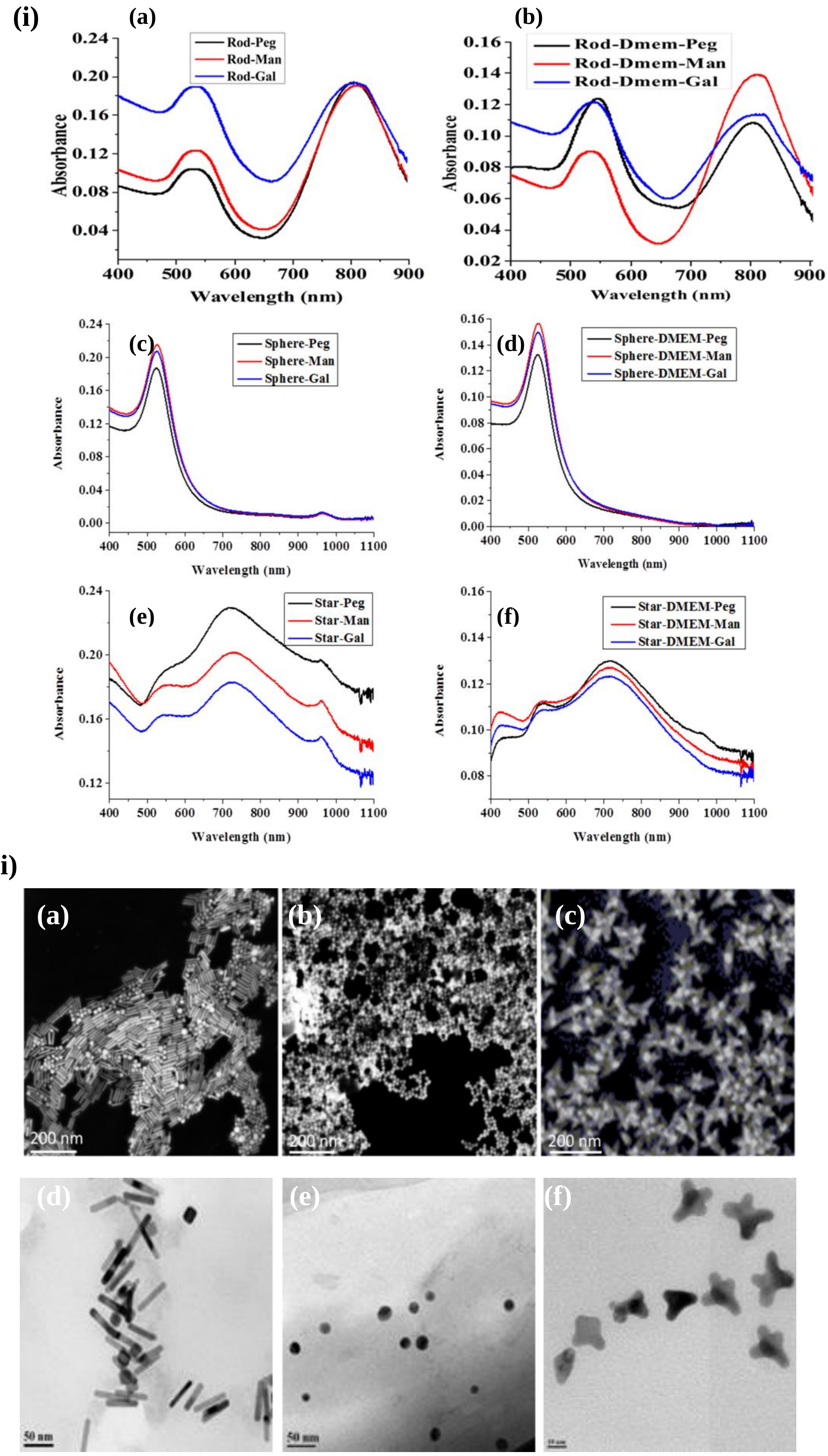

Figure 2. (i) UV-Visible spectra of rod, sphere and star shaped G-AuNPs in water (a, c, e) and DMEM medium without phenol red (b, d, f); (ii) SEM images of (a) rod (R-2); (b) sphere (S-2); and (c) star (St-2) shaped G-AuNPs; TEM images of (d) rod (R-2); (e) sphere (S-2); and (f) star (St-2) shaped G-AuNPs.

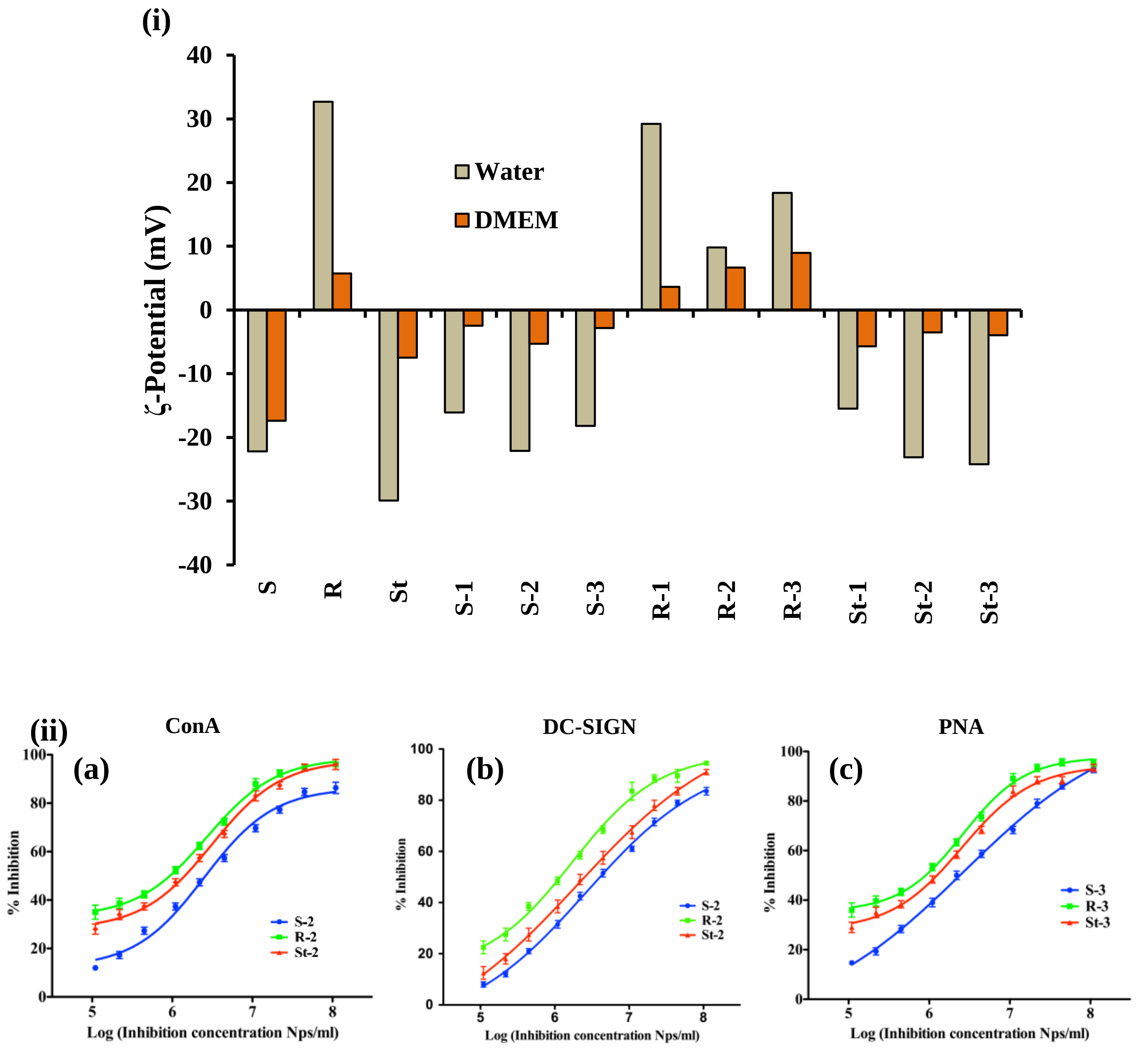

Figure 3. (i) Zetapotential of G-AuNPs in water (brown) and DMEM (red) respectively; (ii) Inhibition assay of G-AuNPs with (a) ConA; (b) DC-SIGN; and (C) PNA.

Table 1. IC_{50} values of G-AuNPs for inhibition of lectins

G-AuNPs	ConA (Nps/ml)	DC-SIGN	PNA
S-2	2.6×10^6	4.3×10^6	-
R-2	9.5×10^5	1.1×10^6	-
St-2	1.4×10^6	2.7×10^6	-
S-3	-	-	2.5×10^6
R-3	-	-	8.7×10^5
St-3	-	-	1.3×10^6

shapes of AuNPs, rod-AuNPs once again demonstrated much more inhibition sensitivity compared to spherical and star counterparts. Overall, these results showed that the aspect ratio and surface to volume ratio of the rod-AuNPs influence the strong binding affinity with lectins.

3.2.2 Cellular cytotoxicity and uptake studies: The difference in the binding affinity of G-AuNps was further assessed in an *in vitro* model. As the proteins present in the biological media can destabilize the NPs structures and functions, we first assessed the stability of the AuNPs in DMEM medium containing 10% FBS. The incubation of each AuNPs in biological medium showed no significant shift in the UV-visible profile after 24 h, which confirmed the stability of the shape and the size of the AuNPs (Fig 2(i)). In contrast, the zeta-potential of the G-AuNPs varied quite significantly, indicating that the nanoparticles were surrounded by a soft layer of serum proteins and which modulated the charge distribution on the G-AuNPs (Fig 3(i)). These results demonstrated that G-AuNPs retained their shape and stability in biological medium. All these results correlate to Chan et al. results.[25]

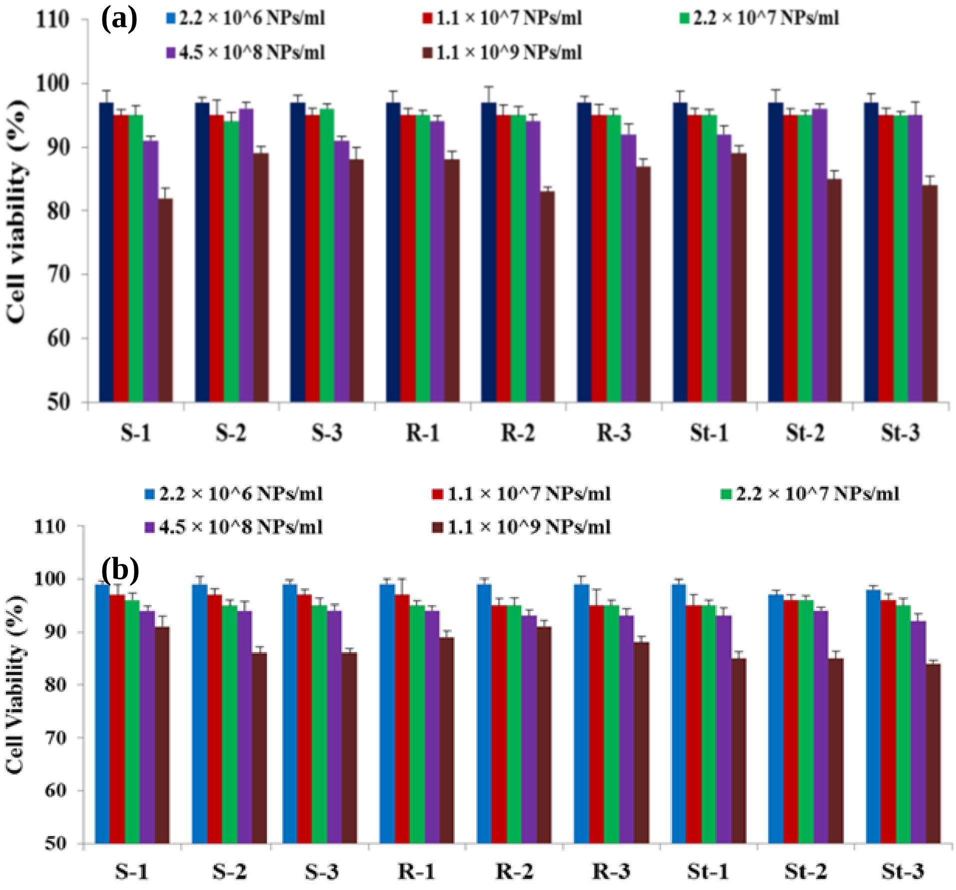

Figure 4. MTT assay showing the cell viability of sphere, rod and star G-AuNPs at 37 ºC for 48 h incubation with (a) NIH 3T3 cells; (b) HeLa cells.

After confirming the stability of the G-AuNPs, we investigated the uptake kinetics and mechanism using DC-SIGNtransfected and knockdown HeLa (human cervical cancer cells), HepG2 (hepatocellular liver carcinoma) and MDA-MB-231 (human breast cancer) cells.[33-39] To assess the relative toxicity of the G-AuNPscell viability was evaluated using MTT assay in HeLa (cancer) and NIH-3T3 (normal) cell lines, incubated with different concentrations ($2.2 \times 10^6 - 1.1 \times 10^9$ NPs per ml) of PEGylated and G-AuNPs. It can be seen that both the HeLa and NIH-3T3 (Fig 4) cells did not show any significant cytotoxicity up to 4.5×10^8 NPs per ml even after 48 h. Hence, we set the above concentration as an ideal condition for further *in vitro* studies.

We then addressed the cellular internalization of G-AuNPs by measuring the gold concentration inside the cells. DC-SIGN-transfected HeLa cells were incubated with PEGylated and G-AuNPs for 4 h, 24 h, and 48 h respectively, followed by washing to remove unbound AuNPs. The cell pellets were dissolved in *aqua regia* solution and the gold concentration was quantified by inductively coupled plasma mass spectrometry (ICP-MS). The mannose-AuNPs exhibited the highest number of uptake compared to galactose or PEGylated-AuNPs in transfected HeLa cells. Among the different shapes of mannose-AuNPs, **R-2** showed approximately 3-fold increase in the number of NPs uptakes compared to **S-2** and **St-2** after 4 h incubation and this trend continued for next 24 h and 48 h (Fig 5a-c). The probable reason for the highest number of rod-AuNPs uptake may be attributed to the fact that rod nanoparticles exhibited (1) aspect ratio, which could increase adhesion of particle to the cell surfaces, (2) high contact area of rod-AuNP with respect to external stimuli and (3) self-assembly of rod-AuPs. To confirm the selectivity, we also studied the nanoparticles uptake profile with DC-SIGN knockdown HeLa cells. ICP-MS clearly revealed the significant decrease in the mannose-AuNPs uptake, revealing the selective uptake of the AuNPs via receptors (Fig 5d-f).[33-35] Further, we performed the uptake kinetics with MDA-MB-231, which has both mannose and galactose receptors.[36] ICP-MS results clearly revealed that the rod-AuNPs uptake is dominated compared to that of two other shapes and we could see the uptake of both the mannose and the galactose-AuNPs (Fig 5g-i). However, the number of mannose-AuNPs uptake was relatively higher than that of galactose-AuNPs, which indicated that the mannose receptors on the cell surfaces are more active than the galactose receptors. Finally, the above experiment was further confirmed with HepG2 cells, which has asialoglycan galactose receptors.[37-39]

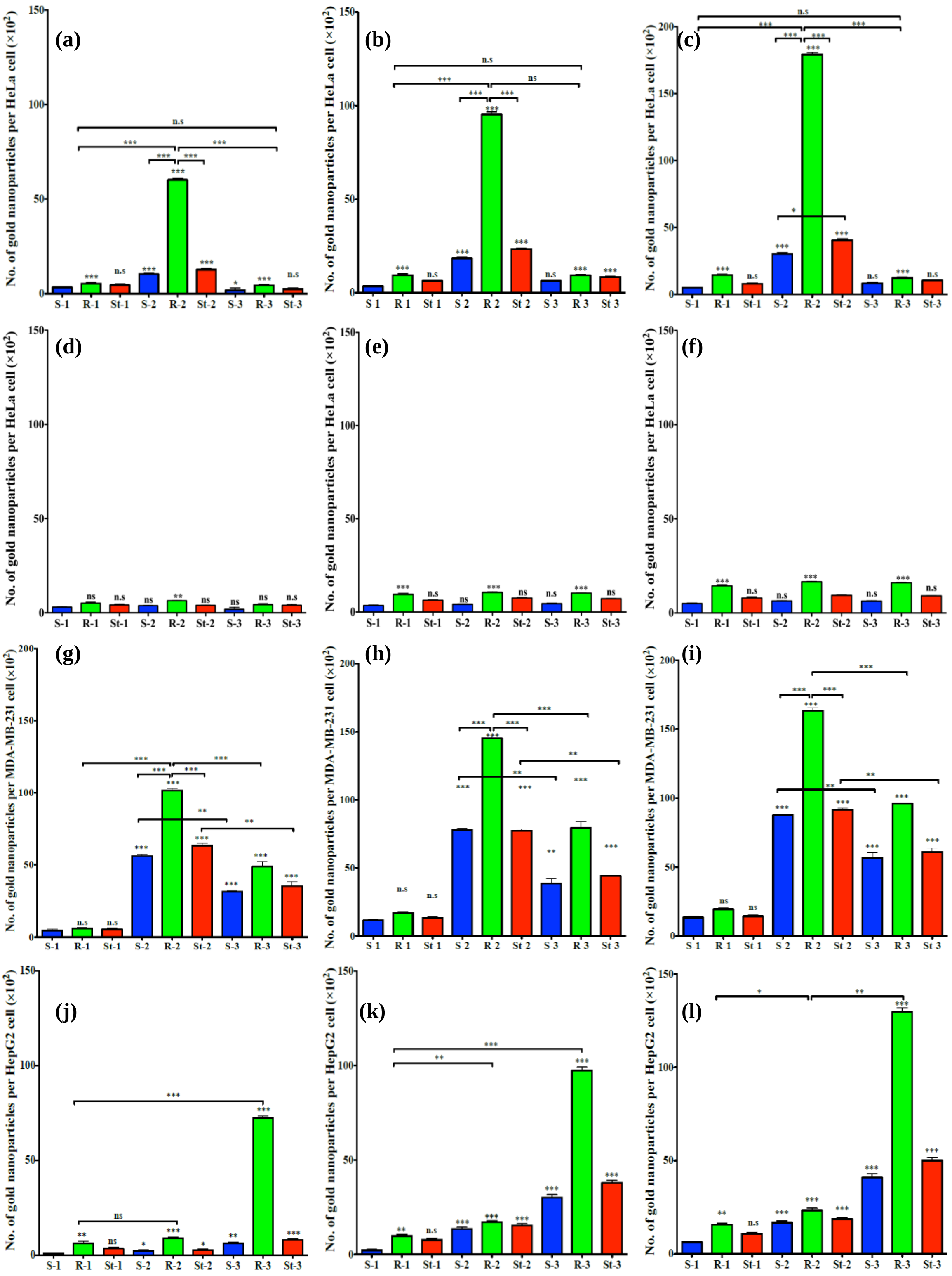

Figure 5. Statistical analysis of ICP-MS data of HeLa (DC-SIGN transfected), HeLa (DC-SIGN knockdown), MDA-MB-231 and HepG2 at different time intervals. (a) HeLa-4h; (b) HeLa-24 h; (c) HeLa-48 h; DC-SIGN knockdown of (d) HeLa-4h; (e) HeLa-24 h; (f) HeLa-48 h (g) MDA-MB-231-4 h; (h) MDA-MB-231-24 h; (i) MDA-MB-231-48 h; (j) HepG2-4h; (k) HepG2-24h; (l) HepG2-48h. Data are presented as mean ±SEM for three independent experiments (***P<0.001, **P<0.01 *P<0.05 and n.s = not significant).

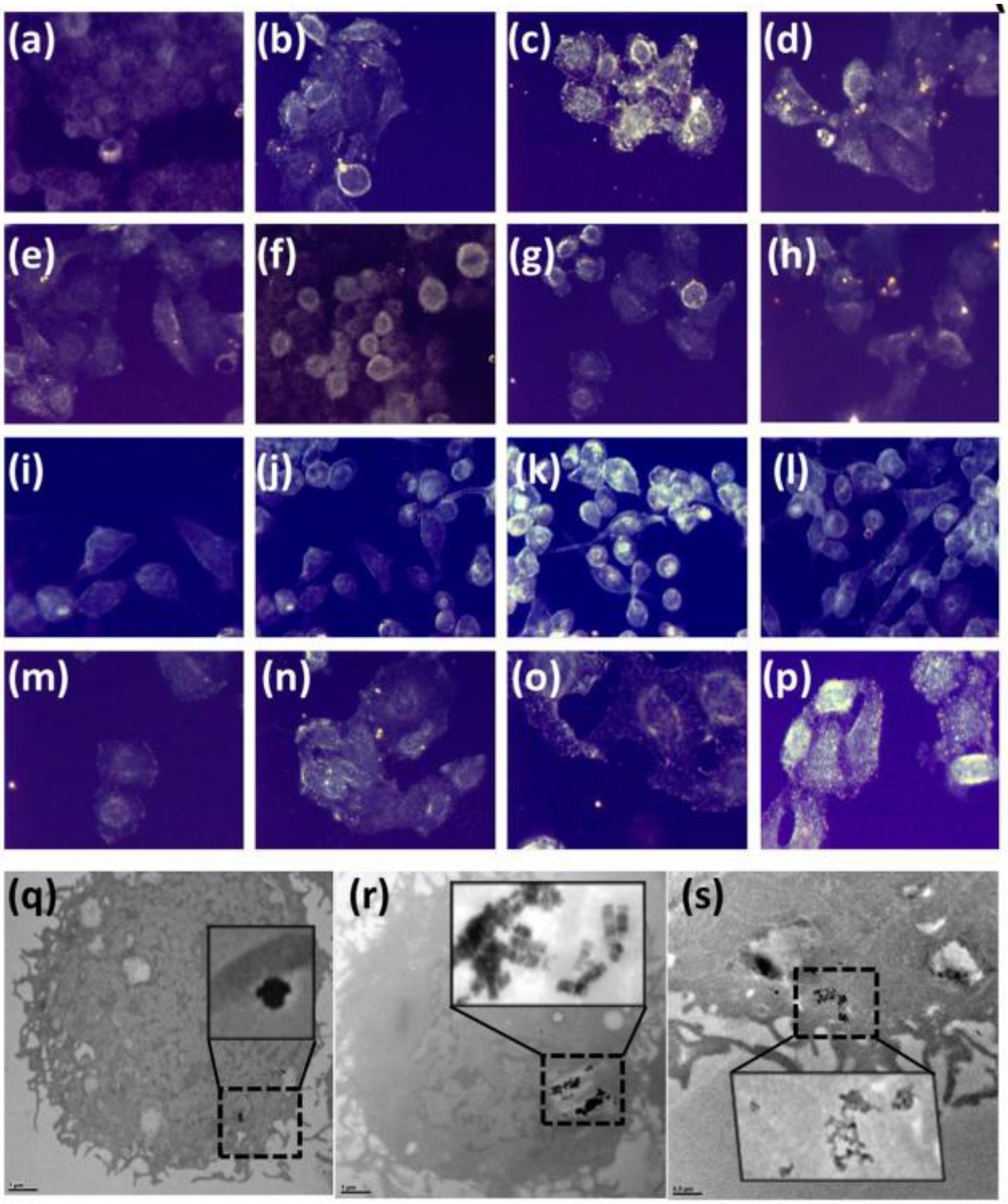

Figure 6. Dark field microscopic images of rod shape nanoparticles incubated with HeLa (DC-SIGN transfected), (a) HeLa-control; (b) HeLa, R-1; (c) HeLa, R-2; (d) HeLa, R-3; HeLa (DC-SIGN knockdown), (e) HeLa-control; (f) HeLa, R-1; (g) HeLa, R-2; (h) HeLa, R-3; MDA-MB-231 MDA-MB-231-control; (j) MDA-MB-231, R-1; (k) MDA-MB-231, R-2; (l) MDA-MB-231, R-3; and HepG2 cells. (i) (m) HepG2-control; (n) HepG2, R-1; (o) HepG2, R-2; (p) HepG2, R-3; for 24 h at 37°C; TEM images of HeLa cells (DC-SIGN transfected) contain (q) S-2; (r) R-2; (s) St-2 after 24 h at 37°C.

As expected, rod-AuNPs (**R-3**) was taken up much higher than other AuNPs **(**Fig 5j-l). After 24 h and 48 h, the concentration of these AuNPs decreased. These results strongly suggest that nano-rods can induce specific fast uptake via carbohydrate receptors on the cell surfaces.

To validate the results with different cell lines with G-AuNPs, a more conventional dark field microscopic (DFM) imaging study was performed.[40] Figure 6i displays DFM images of DC-SIGN transfected HeLa, knockdown HeLa, MDA-MB-231 and HepG2 cells after 24 h incubation. In transfected HeLa cells, the bright spots from mannose-AuNPs (**S-2, R-2, St-2**) were observed close to the cell surfaces and in the cytoplasmic regions and the relative intensity of these bright spots was higher than PEG and galactose counterparts. Similar results were observed with the cell line MDA-MB-231 and HepG2 with respect to the carbohydrate receptors. Finally, the transmission electron microscopic (TEM) images of transfected HeLa cells were collected to confirm AuNPs sequestration. TEM images displayed a significant number of **R-2** sequestration in the cytoplasmic region compared to **S-2** and **St-2** (Fig 6q-s). Moreover, we observed that the nano-rods were aligned parallelly and/or perpendicularly to each other. Overall, these results clearly showed that the shapes of the AuNPs indeed modulate the CPI.

3.2.3 Cellular Internalization pathway of R-2 in HeLa cells: To prove the mechanism of endocytosis, we utilized different known inhibitors for dynamin, clathrin and caveolae pathways to analyze the mechanism of internalization in DC-SIGN transfected HeLa cells.[41-42] ICP-MS was used to analyze the data, which quantifies gold concentration during the uptake of G-AuNPs in a cell (Fig 7). To evaluate the energy-dependent endocytosis, we incubated the cells with NaN_3 for 30 mins to deplete ATP, followed by the addition of **R-2** NPs for 4 h. We observed a strong decrease in gold concentration during cellular uptake of **R-2**, confirming the active endocytic pathway of internalization in HeLa cells. We next established dynamin-dependent uptake. The addition of dynasore hydrate resulted in blocking dynamin function inhibiting the internalization of **R-2**, indicating that the internalization follows the conventional trend of clathrin or caveolae pathway. Further, we studied the effect of methyl-β-cyclodextrin (Me-β-CD), which inhibit caveolae-mediate endocytosis and chlorpromazine (inhibitor for clathrin-mediated endocytosis). As shown in figure 7a, cells that were pre-treated with clathrin inhibitor showed a significant reduction in internalization, whereas, Me-β-CD pre-treatment showed negligible inhibition effect. These results validated that the **R-2** internalize *via* energy-dependent, clathrin-mediated endocytosis. Finally, we studied the uptake of **R-2** in the presence of Man-9-glycan that blocks the DC-SIGN receptor. The high mannose pre-treatment of cells dramatically reduce uptake of **R-2**. Altogether this clearly proves that **R-2** uptake depends on the DC-SIGN receptor on clathrin-mediated endocytosis. A similar experiment with HepG2 cells also revealed the clathrin-mediated endocytosis (Fig 7b).

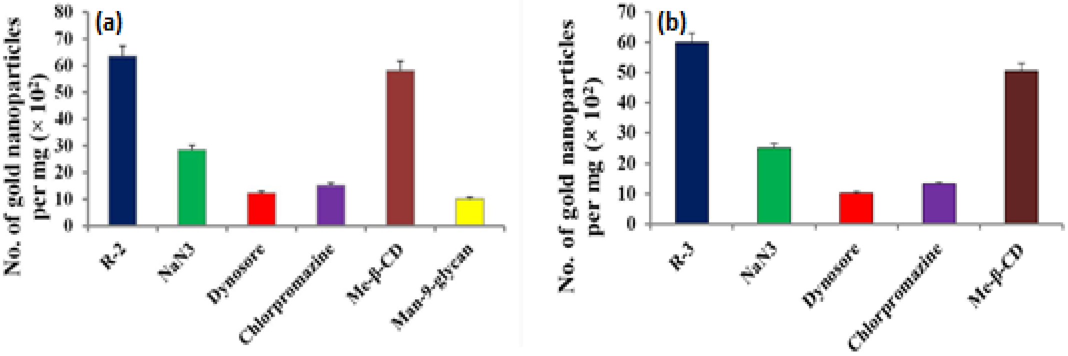

Figure 7. Statistical analysis of ICP-MS data in presence and absence of inhibitors incubation in (a) HeLa (DC-SIGN transfected) cells; (b) HepG2 cells after 4 h. Data are presented as mean ±SEM for three independent experiments.

3.3 Conclusions

A library of different shapes of glyco-AuNPs was synthesized and we used them as a tool to characterize the cellular uptake. ELISA plate lectin inhibition assay revealed that selectivity and sensitivity of the binding depended not only on the sugar composition but also was influenced by the shape of the AuNPs. *In vitro* experiments further supported the high affinity of rod-AuNPs compared to spherical and star counterparts. The mechanistic insight clearly demonstrated the clathrin-mediated mannose-dependent endocytosis. We anticipate that this shape-dependent enhancement of cellular uptake offers a new dimension to synthesize multivalent glyco-probes for diagnostic and therapeutic applications.[43-44]

3.4 Experimental Section

3.4.1 General Information: All chemicals were reagent grade and used as supplied except where noted. Analytical thin layer chromatography (TLC) was performed on Merck silica gel 60 F254 plates (0.25 mmol). Compounds were visualized by UV irradiation or dipping the plate in CAM/ninhydrin solution followed by heating. Column chromatography was carried out using force flow of the indicated solvent on Fluka Kieselgel 60 (230–400 mesh). ^{1}H and

^{13}C NMR spectra were recorded on Jeol 400 MHz, with cryo probe using residual solvents signals as an internal reference ($CDCl_3$ δ_H, 7.26 ppm, δ_C 77.3 ppm and CD_3OD δ_H 3.31 ppm, δ_C 49.0 ppm). The chemical shifts (δ) are reported in ppm and coupling constants (*J*) in Hz. UV-visible measurements were performed with Evolution 300 UV-visible spectrophotometer (Thermo Fisher Scientific, USA). Fluorescence spectra were recorded in FluoroMax-4 spectrofluorimeter (Horiba Scientific, U.S.A.). DC-SIGN transfected and Knockdown HeLa was obtained from UCSD cell bank. MDA-MB-231 and HepG2 cell lines were purchased from NCCS, Pune.

3.4.2 Inhibition Assay: 96-well ELISA plates were immobilized with mannose, galactose-BSA (1 mg/ml) as reference ligand and incubated with horesradish peroxide (HRP) labeled ConA or PNA (0.5 mg/ml) or DC-SIGN in the presence of different shapes of G-AuNPs (5.69 X 10^5 -10^8) in varying concentrations. After incubation for 2 h, the plates were washed and remaining labeled lectin bound to the reference ligand was quantified by a HRP-catalysed color reaction using 2, 2’-azinobis(3-ethyl-benzo-thiazoline-6-sulfonic acid) diammonium salt (ABTS) as substrate. In case of DC-SIGN and anti-IgG-HRP was added to quantify the binding of lectin. Logerthemic curve for inhibition of lectin binding to immobilized Mannose or galactose are drawn. From these curves the concentration that reduce the binding of labeled lectin to the microtiter plates by 50% (IC_{50} values) were determined as a meassure of potency of the synthesized inhibitors.

3.4.3 MTT Assay: The cell viability was assessed by MTT (3-(4, 5-dimethylthiazol-2-yl)-2,5-diphenyltetrazolium bromide) assay in HeLa and NIH-3T3 cells. The NIH-3T3 and HeLa cells in monolayers were cultured in DMEM with 10% FBS medium in 100 mm cell culture dishes. Cells were trypsinized and plated at a density of 10,000 cells per well in a 96 well plate and once the cells got adhered; they were treated with varying concentration of G-AuNPs (number of nanoparticles) and incubated for 48 h. The medium was replaced and 10 µl of MTT was added to each well and incubated for 4 h at 37 °C. Formazan crystals were dissolved in 100 µl of DMSO and absorbance at 570 nm was recorded using microplate reader.

3.4.4 Preparation of Cell samples for ICP-MS analysis: For the quantitative analysis of gold (Au) contents in the cellular uptake study, HeLa, MDA-MB-231 and NIH-3T3 cells (10^4 cells per plate) were incubated with the rod, sphere and star G-AuNPs (5×10^8 nanoparticles) for 4h, 24h and 48h at 37 ºC. The medium was removed and cells were washed with PBS (3 times) before trypsinizing, centrifuged and the cell pellets were digested at 85 °C with 200 µl of fresh *aqua regia* for 4 h. Then each digested sample was diluted to 6 ml with Millipore water. The concentration of gold, determined by ICP-MS (Thermo-Fisher Scientific, Germany), was converted into the number of AuNP per cell.

3.4.5 Dark field images of cell lines: Cellular uptake of AuNPs was examined using dark field microscopic images. HeLa, MDA-MB-231 and NIH-3T3 cells (10^4 cells per plate) were seed into 6 well plate with cover slip at the bottom and allowed to grow for 24 h in DMEM medium containing 10% FBS. Then cells were treated with AuNPs (5×10^8 nanoparticles) and incubated at 37 °C for 24 h. Later, cells were washed 3 times with PBS and fixed with 4% paraformaldehyde at 37 °C for 15 min. The coverslips were then placed on the slide and fixed it with mounting media and dark field images were collected by exciting the cells with white light.

3.4.6 TEM images of cells containing nanoparticles: The uptake of different shapes of AuNPs by HeLa cells was assessed by transmission electron microscopy. HeLa cells (10^4) were seeded in 6-well plates at 37 °C for 4 h. Cells were treated with different shapes of AuNPs (5×10^8 nanoparticles) for 24 h at 37 ºC, followed by trypsinization. The pellet was fixed with 2.5% of glutaraldehyde in PBS for 4 h. The fixed cells were washed with PBS, further treated with 1% osmium tetroxide in water, then again washed with Millipore water for 2 times. The pellet was stained with 2% uranyl acetate in water for 1 h in dark after that the cells were again washed with water further dehydrated in ethanol (50%, 75%, 95% and 100%). The cell pellet was made into blocks by using Epon resin kit (DER 332, DER 732) by heating at 60 °C for 48 h. Sections of 70–90 nm thickness were cut on an ultramicrotome (RMC MTX) using a diamond knife. The sections were deposited on carbon-film copper grids and lead citrate treatment at room temperature for 3 min prior to TEM.

3.4.7 Cellular uptake mechanism: For all these experiments, DC-SIGN transfected HeLa cells were grown in 8-well chamber and treated with the specific inhibitor for 30 mins followed by **R-2** (5×10^8 NPs per ml) for 4 h at 37 °C. For energy dependent study, cells were incubated for 30 mins with NaN_3 (50 mM). For dynamin-mediated (clathrin and caveolae-mediated uptake) cells were treated with dynasore Hydrate (50 µM). For clathrin mediated uptake studies chlorpromazine (25 µM) were added. For caveolae mediated uptake, cells were treated with methylated-β-cyclodextrin (10 mM). For mannose-dependent uptake, cells were treated with high mannose glycans (1µg) for 30 mins. After 4 h of **R-2** treatment, cells were washed to remove unbound materials; ICP-MS of these samples were done as reported in respective sections. Similarly, we performed same experiments for HepG2 by incubating with **R-3**.

3.4.8 Zeta potential studies: We used a zeta-potential analyzer to measure the surface potential of AuNPs. The electrostatic potential on the particle surface is called the zeta potential. In the measurement, we applied unit field strength (1 Volt per metre) to the AuNP solution. We measured zetapotential of different shapes of AuNPs in water. In case of DMEM medium, We incubated all AuNps in DMEM medium for 24 h and purified by centrifugation and measured zetapotential.

3.4.9 Phenol-sulfuric acid method to quantify sugars on AuNPs: The concentration of mannose/ galactose sugars on AuNPs was determined by the phenol-sulfuric acid method. 100 μL sugar functionalized-AuNPs were were added to concentrated sulfuric acid (750 μL, 100%) and aqueous phenol solution (5% w/v, 100 μL) in the test tube and heated to 80°C. After 5 min, solution was cooled to room temperature and the absorbance coefficient at 490 nm was measured. AuNPs as such in sulfuric acid was used as a control. The sugar concentration was estimated by comparing the absorption of the sample with a standard curve.

3.5 References

1. M. Cohen and A. Varki, *Int. Rev. Cell Mol. Biol.*, 2014, **308**, 75-125.
2. C. R. Bertozzi and L. L. Kiessling, *Science*, 2001, **291**, 2357-2364.
3. N. C. Reichardt, M. Martín-Lomas and S. Penadés, *Chem. Soc. Rev.*, 2013, **42**, 4358-4376.
4. M. Marradi, F. Chiodo, I. García and S. Penadés, *Chem. Soc. Rev.*, 2013, **42,** 4728-4745.
5. B. Kang, T. Opatz, K. Landfester and F. R. Wurm, *Chem. Soc. Rev.*, 2015, **44,** 8301-8325.
6. R. J. Pieters, *Org. Biomol. Chem.*, 2009, **7,** 2013-2025.
7. T. R. Branson and W. B. Turnbull, *Chem. Soc. Rev*., 2013, **42,** 4613-4622.

8. S. Zhang, Q. Xiao, S. E. Sherman, A. Muncan, A. D. Ramos Vicente, Z. Wang, D. A. Hammer, D. Williams, Y. Chen, D. J. Pochan, S. Vértesy, S. André, M. L. Klein, H. J. Gabius and V. Percec, *J. Am. Chem. Soc.*, 2015, **137,** 13334-13344.

9. E. M. Munoz, J. Correa, R. Riguera and E. Fernandez-Megia, *J. Am. Chem. Soc.*, 2013, **135,** 5966-5969

10. B. D. Polizzotti and K. L. Kiick, *Biomacromolecules,* 2006, **7,** 483-490.

11. R. Roy and T. C. Shiao, *Chem. Soc. Rev.*, 2015, **44,** 3924-3941.

12. C. Fasting, C. A. Schalley, M. Weber, O. Seitz, S. Hecht, B. Koksch, J. Dernedde, C. Graf, E. W. Knapp and R. Haag, *Angew. Chem. Int. Ed.*, 2012, **51,** 10472-10498.

13. J. E. Gestwicki, C. W. Cairo, L. E. Strong, K. A. Oetjen and L. L. Kiessling, *J. Am. Chem. Soc.,* 2002, **124,** 14922-14933.

14. F. Chiodo, M. Marradi, J. Park, A. F. Ram, S. Penadés, I. van Die and B. Tefsen, *ACS Chem. Biol.,* 2014, **9,** 383-389.

15. Garcia, A. Sánchez-Iqlesias, M. Henriksen-Lacey, M. Grzelczak, S. Penadés and L. M. Liz-marzán, *J. Am. Chem. Soc.*, 2015, **137,** 3686-3692.

16. F. Chiodo, M. Marradi, B. Tefsen, H. Snippe, I. Van Die and S. Penadés, *PLoS. One,* 2013, **8,** e73027.

17. D. Benito-Alifonso, S. Tremel, B. Hou, H. Lockyear, J. Mantell, D. J. Fermin, P. Verkade, M. Berry and M. C. Galan, *Angew. Chem. Int. Ed.*, 2014, **53,** 810-814.

18. D. Grünstein, M. Maglinao, R. Kikkeri, M. Collot, K. Barylyuk, B. Lepenies, F. Kamena, R. Zenobi and P. H. Seeberger, *J. Am. Chem. Soc.*, 2011, **133,** 13957-13966.

19. D. Ponader, P. Maffre, J. Aretz, D. Pussak, N. M. Ninnemann, S. Schmidt, P. H. Seeberger, C. Rademacher, G. U. Nienhaus and L. Hartmann, *J. Am. Chem. Soc.,* 2014, **136**, 2008-2016.

20. L. A. Dykman and N. G. Khlebtsov, *Chem. Rev.,* 2014, **114,** 1258-1288.

21. F. Tian, M. J. Clift, A. Casey, P. Del Pino, B. Pelaz, J. Conde, H. J. Byrne, B. Rothen-Rutishauser, G. Estrada, J. M. de la Fuente and T. Stoeger, *Nanomedicine,* 2015, **10,** 2643-2657.

22. S. H. Cha, J. Hong, M. McGuffie, B. Yeom, J. S. VanEpps and N. A. Kotov, *ACS Nano.*, 2015, **9,** 9097-9105.

23. K. C. Black, Y. Wang, H. P. Luehmann, X. Cai, W. Xing, B. Pang, Y. Zhao, C. S. Cutler, L. V. Wang, Y. Liu and Y. Xia, *ACS Nano.*, 2014, **8,** 4385-4394.

24. H. Herd, N. Daum, A. T. Jones, H. Huwer, H. Ghandehari and C. M. Lehr, *ACS Nano.*, 2013, **7,** 1961-1973.

25. B. D. Chithrani, A. A. Ghazani and W. C. Chan, *Nano Letters*., 2006, **6,** 662-668.

26. B. D. Chithrani and W. C. Chan, *Nano Letters*., 2007, **7,** 1542-1550.

27. S. Nangia and R. Sureshkumar, *Langmuir*, 2012, **28,** 17666-17671.

28. N. M. Schaeublin, L. K. Braydich-Stolle, E. I. Maurer, K. Park, R. I. MacCuspie, A. R. Afrooz, R. A. Vaia, N. B. Saleh and S. M. Hussain, *Langmuir*, 2012, **28,** 3248-3258.

29. J. Wang, G. Zhu, M. You, E. Song, M. I. Shukoor, K. Zhang, M. B. Altman, Y. Chen, Z. Zhu, C. Z. Huang and W. Tan, *ACS Nano*, 2012, **6,** 5070-5077.

30. X. Yang, X. Liu, Z. Liu, F. Pu, J. Ren and X. Qu. *Adv. Mater*., 2012, **24,** 2890-2895.

31. K. Niikura, T. Matsunaga, T. Suzuki, S. Kobayashi, H. Yamaguchi, Y. Orba, A. Kawaguchi, H. Hasegawa, K. Kajino, T. Ninomiya, K. Ijiro and H. Sawa, *ACSNano,* 2013, **7**, 3926-3938.

32. P. M. Chaudhary, S. Sangabathuni, R. V. Murthy, A. Paul, H. V. Thulasiram and R. Kikkeri, *Chem. Commun*., 2015, **51,** 15669-15672.

33. D. Brevet, M. Gary-Bobo, L. Raehm, S. Richeter, O. Hocine, K. Amro, B. Loock, P. Couleaud, C. Frochot, A. Morére, P. Maillard, M. Garcia and J. O. Durand, *Chem. Commun.*, 2009, **28,** 1475-1477.

34. L. Tailleux, O. Schwartz, J. L. Herrmann, E. Pivert, M. Jackson, A. Amara, L. Legres, D. Dreher, L. P. Nicod, J. C. Gluckman, P. H. Lagrange, B. Gicquel and O. Neyrolles, *J. Exp. Med.* 2003, **197**, 121-127.

35. N. Sol-Foulon, A. Moris, C. Nobile, C. Boccaccio, A. Engering, J. P. Abastado, J. M. Heard, Y. Van Kooyk and O. Schwartz, *Immunity*, 2002, **16**, 145-155.

36. Y. Ma, H. Chen, S. Su, T. Wang, C. Zhang, G. Fida, S. Cui, J. Zhao and Y. Gu, *J. Cancer*, 2015**, 6**, 658-670.

37. S. K. Mamidyala, S. Dutta, B. A. Chrunyk, C. Préville, H. Wang, J. M. Withka, A. McColl, T. A. Subashi, S. J. Hawrylik, M. C. Griffor, S. Kim, J. A. Pfefferkon, D. A. Price, E. Menhaji-Klotz, V. Mascitti and M. G. Finn, *J. Am. Chem. Soc*., 2012, **134,** 1978-1981.

38. R. Kikkeri, B. Lepenies, A. Adibekian, P. Laurnio and P. H. Seeberger, *J. Am. Chem. Soc*., 2009, **131,** 2110-2112.

39. G. J. Berndardes, R. Kikkeri, M. Maglinao, P. Laurnio, M. Collot, S. Y. Hong, B. Lepenies and P. H. Seeberger, *Org. Biomol. Chem*. 2010, **8**, 4987-4996.

40. C. M. Treu, O. Lupi, D. A. Bottino and E. Bouskela, *Arch. Dermatol. Res.*, 2011, **303,** 69-78.

41. D. Suresh, A. Zambre, N. Chanda, T. J. Hoffman, C. J. Smith, J. D. Robertson and R. Kannan, *Bioconjug. Chem.*, 2014, **25**, 1565-1579.
42. S. Kumari, S. Mg and S. Mayor, *Cell Res.*, 2010, **20**, 256-275.
43. V. Shanmugam and S. Selvakumar, C. S. Yeh, *Chem. Soc. Rev.*, 2014, **43**, 6254-6287.
44. R. Cao-Milán and L. M. Liz-Marzán, *Expet Opin. Drug. Deliv.*, 2014, **11**, 741-752.

Chapter 4

Mapping the Glyco-Gold Nanoparticles of Different Shapes Toxicity, Bio-distribution and Sequestration in Adult Zebrafish

4.1 Introduction

Carbohydrate on the cell surfaces has been recognized as the first line of contact for pathogens, toxins and cells[1]. Nature has utilized multivalent binding between carbohydrate and proteins to increase the avidity of cell signaling, molecular recognition and inflammations. Hence, mimicking multivalent interactions using synthetic nanoparticles can lead to potential therapeutic models to treat inflammations, imaging, bacterial infections, and cancer[2-5]. Till date, the mouse model has been extensively used as *in vivo* in all these glyconanotechnology research [6-12]. However, owing to a significant amount of sample consumption, and complex biological system, there is a need for an alternative information rich, simple *in vivo* system to reduce quantity of materials consumption and at the same time acquiring useful biological information at inexpensive, before planning the experiment with the complex models. Animals including fish, insects and worms are considered to be the simple model for pre-clinical research and each of these *in vivo* tools has their own merits and demerits. For example, *Caenorhabditis elegans* is widely used to investigate the chemical toxicity due to its sensitivity to oxidative stress[13]. Moreover, they have a short lifespan, transparency, ease of cultivation, and high-level conservation of the vertebrate genome. However, the lack of specific organs (eyes and ears) and specific tissues (bones) limits its applications for further pharmacokinetics studies. Similarly, the invertebrate *Drosophila melanogaster* and Hydra have also received similar attention[14-16]. Drosophila offers various organs similar to human systems including the digestive system, blood vessels and kidney, and high genetic homology with the human genome. However, fruit flies have lack of vital organs such as kidney, liver and spleen. In contrast, zebrafish has been used as a model in developmental biology and wide range of human diseases, including cancer, cardiovascular disorders, neurological diseases, liver diseases and immunological studies[17-20]. Zebrafish is considered to be one of the simple animal models with widely accepted ethical principles and cost of each experiment is expected to be less than a dollar. Currently, zebrafish model was used to study the human diseases, including cancer, cardiovascular disorder, neurological diseases, liver diseases and immunological studies[21-23]. In addition to study the human disease, zebrafish model was also used in nanotechnology research. Li and his coworkers have used zebrafish model to evaluate the neural behavior of silica nanoparticles. Similarly, Zhu et al used fish model to demonstrate the toxicity of gold nanoparticles decorated with positive, negative and neutral charged ligands. Recently, Kovriznych et al has shown that zebrafish model can be used for optimize the toxicity of the different types of nanoparticles.

[24-27] However, the shape dependent gold nanoparticles toxicity, biodistribution and sequestration has not studied well so far in zebrafish model. Herein, we report the potential application of adult zebrafish in glyco-nanomaterial research. As a prototype, we report how different shapes of PEG and mannose capped goldnanoparticles (AuNPs) influence the toxicity, uptake and clearance in the zebrafish model. Previously, it has been shown that shape of the glyco-gold nanoparticles significantly influences carbohydrate-mediated bacterial adhesion and endocytosis in mammalian cells[28]. Hence, deciphering the role of different shapes of gold-nanoparticles in *in vivo* system undoubtedly results in designing better glycoprobes to target or inhibit the carbohydrate-protein interactions (CPI).

4.2 Results & Discussion

4.2.1 Synthesis and characterization of Fluorescein - conjugated glyco-gold nanoparticles: To assess the interplay between the shape and carbohydrate-mediated interactions in the zebrafish model, AuNPs were synthesized by using PEG or mannose and fluorescein linker. The required mannose-linker was synthesized as described in the literature[28]. The fluorescent-linker (1**8**) was synthesized from (**13**), which was obtained by treating with thioacetic acid and azo-isobutyronitrile (AIBN), followed by one-pot de-acetylation and de-esterification to yield compound **15**. Coupling between *tert*-butyl (2-aminoethyl) carbamate and 5-Carboxyfluorescein resulted in compound **17**, which was further deprotected and *in situ* coupling of **15** gave the final fluorescein linker **18**. Hybrid-AuNPs were synthesized by mixing stoichiometric ratio (8:2) of mannose-linker (**10**) and Fluorescein linker (**18**) (Scheme 1 and Fig 1). Unreacted ligands were separated by centrifugation. Similarly, pegylated hybrid AuNPs were also synthesized. The hybrid glyco-AuNPs were characterized by using UV-visible, fluorescence, (Fig. 2) zeta potential, and scanning electron microscopy (SEM) techniques. UV-visible spectra of glyco goldnanoparticles (G-AuNPs) dispalyed characteristic localised surface plasmon resonance (LSPR) peaks at 830 nm and 525 nm for rod-AuNPs, for spherical-AuNPs and 723 nm, for star-AuNPs respectively. Absorbtion peak between 400-500 and emission at 524 nm, provides the evidence for conjugation of fluorescein on AuNPs.corresponds. The sugar and fluorescein conjugation on AuNPs was quantified by phenol-sulfuric acid assay and UV-visible spectroscopy (Table 2). The zeta potentials of nanoparticles were measured in both Dulbecco’s Modified Eagle’s Medium (DMEM) containing 10% fetal bovine serum (FBS) and water. The changes in zeta potentials confirmed displacement of primary surfactants by neutral charged sugar and fluorescein linkers. In DMEM media, the soft layer of fetal bovine serum proteins interacts with carbohydrates moieties[29] and alters the zeta-potential on the AnNPs further (Table 1). SEM images of mannose-AuNPs displayed almost identical size similar to native AuNPs (Fig. 3).

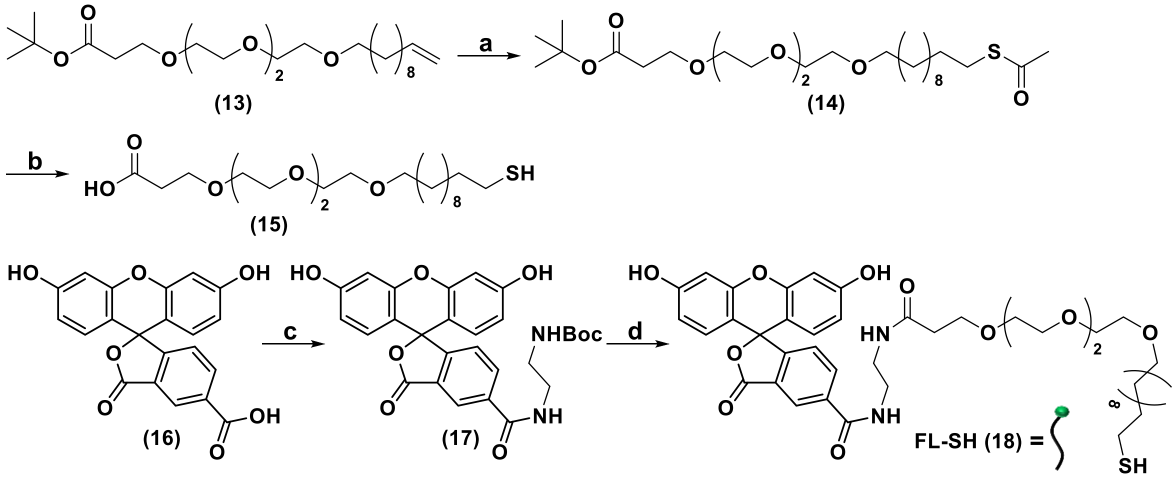

Scheme 1. Synthesis of Fluorescein modified linker: (a) Thioaceticacid, AIBN, 1-4 dioxane, 60°C; (b) (i) NaOMe, MeOH, 2 h, (ii) TFA : DCM (1:1), 2 h; (c) *tert*-butyl (2-aminoethyl)carbamate, EDC, HOBt, Pyridine, 12 h; (d) (i) TFA : DCM (2:8) (ii) **15**, EDCI, HOBt, Pyridine, 12 h.

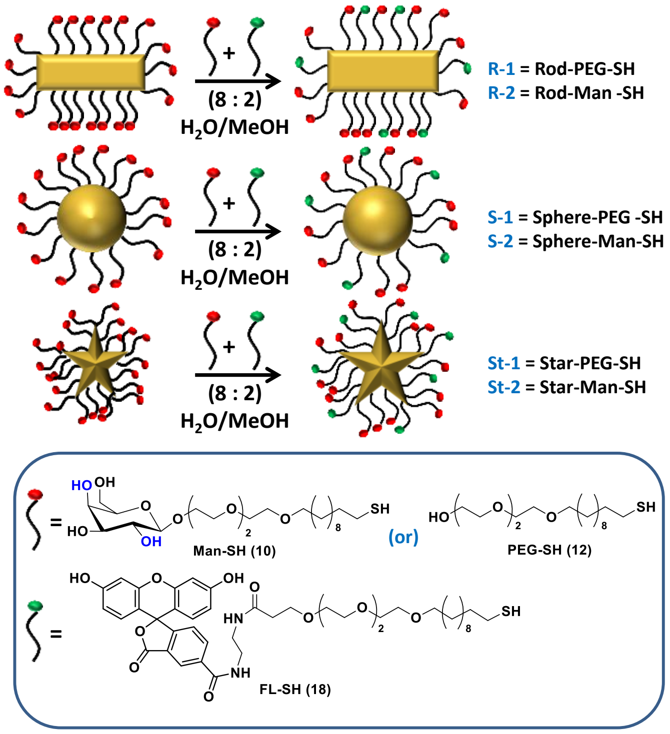

Figure 1. Synthesis of Fluorescence conjugated G-AuNPs: mixing of respective sugar (**10** or **12**) and **18** (8 : 2) ratios in water and methanol mixture (1:1) at RT for 12 h.

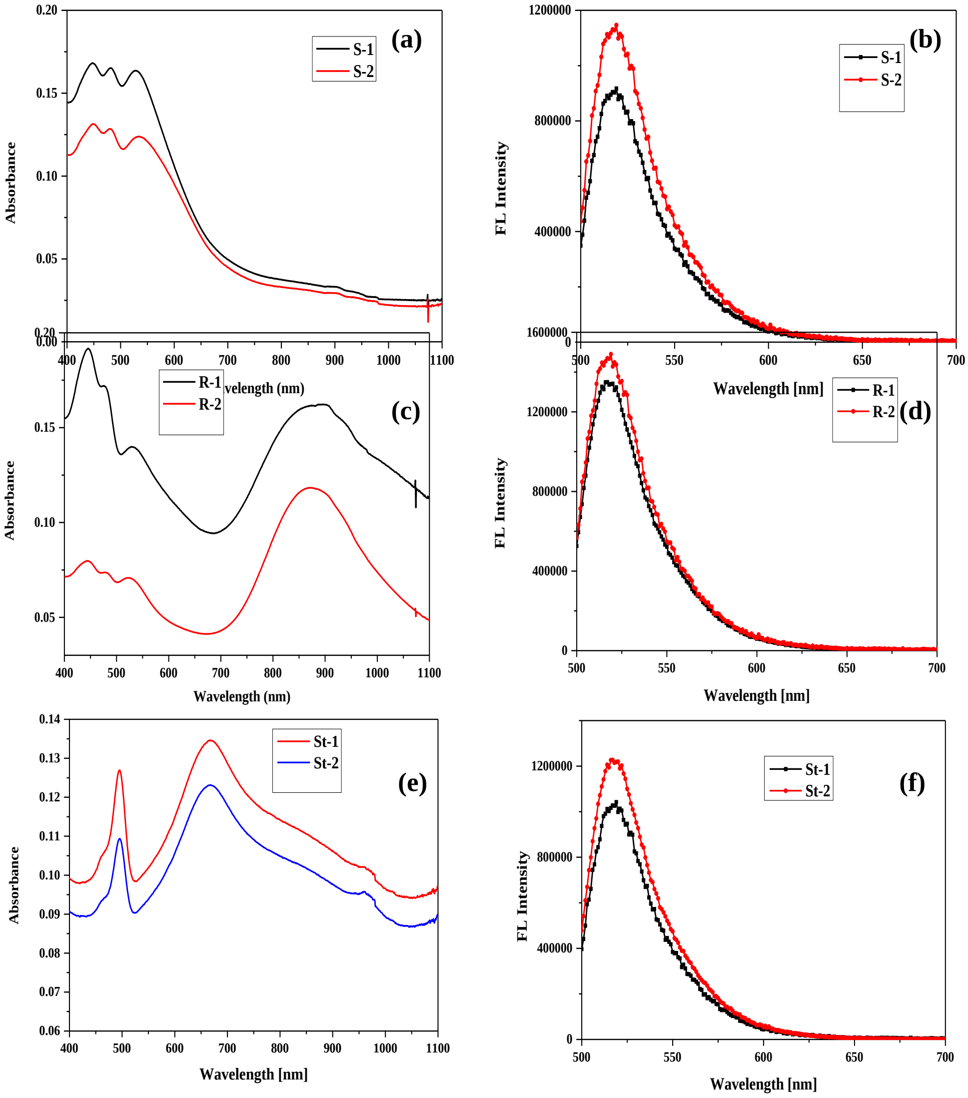

Figure 2. UV-visible spectra of FL conjugated sphere, rod and star G-AuNPs in water (**a, c, e)** and Fluorescene spectra of sphere, rod and star (**b, d, f**) respectively.

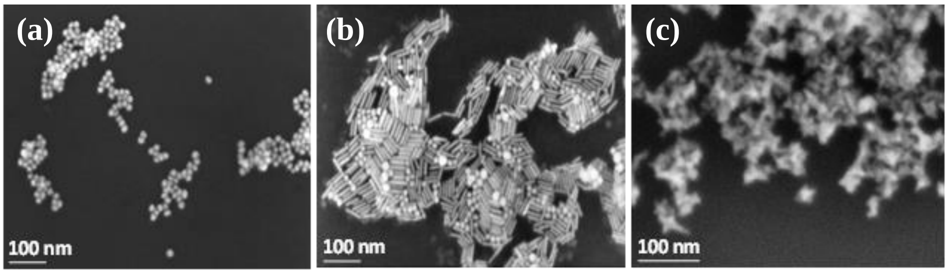

Figure 3. SEM images of (a) S-2; (b) R-2; (c) St-2 G-AuNPs.

Table 1. Physical charecteristics of FL conjugated G-AuNPs.

Particle	Diameter(s) (nm)	λ_{max} (nm)	ζ-potentials (mV)	
			Water	**DMEM**
Rod	47.6 ± 3.0 × 12.3 ± 1.5	820	30.9± 1.3	5.42 ± 0.6
Sphere	16.5 ± 2.0	524	-22± 1.2	-16.8 ± 0.3
Star	42.3 ± 2.5 × 16.1 ± 1.0	714	-27.5± 1.0	-6.9 ± 0.5
R-2	48.8 ± 3.5 × 12.6 ± 1.5	830	9.5± 1.5	6.1 ± 0.7
R-1	46.9 ± 3.0 × 12.0 ± 1.5	825	28.9 ± 1.0	2.9 ± 0.9
S-2	19.5 ± 1.5	525	-20.1± 1.5	-4.9 ± 0.2
S-1	19.0 ± 2.0	524	-13.7± 1.2	-2.1 ± 0.5
St-2	45.5 ± 1.2 × 16.5 ± 2.0	723	-21.1± 1.8	-3.1 ± 0.9
St-1	44.0 ± 1.0 × 16.5 ± 1.0	723	-17.1± 1.2	-5.2 ± 0.8

Table 2. Quantification of sugars and fluorescence functionalised G-AuNPs

S.No	Nanoparticles	FL Concentration (µg/mL)	Sugar Concentration (µg/mL)
1	S-1	25.54 ± 3.4	
2	S-2	36.12 ± 2.74	1.9 ± 0.3
3	R-1	41.4 ± 3.41	
4	R-2	45.5 ± 4.78	1.7 ± 0.12
5	St-1	29.23 ± 1.54	
6	St-2	38.01 ± 2.45	1.7 ± 0.9

4.2.2 Acute toxicity: The nanomaterial toxicity was extensively explored in the zebrafish model by exposing fishes in the nanoparticles containing tank (classical method). Although zebrafish of all life stages are utilized for toxicological studies, we chose to use adult zebrafish for this study due to their ability to absorb particles effectively. Furthermore, the nanoparticles were administration into the zebrafish *via* intraperitoneal injection instead of classical method to reduce the amount of sample consumption and toxicity can be observed with minimum number of fishes[30]. To this end, AuNPs were intraperitoneal injected to the adult zebrafish and followed their mortality. It has been observed that none of the G-AuNps showed toxicity upto 120 h, indicating that G-AuNPs are biocomatible for *in vivo* studies (Fig. 4).

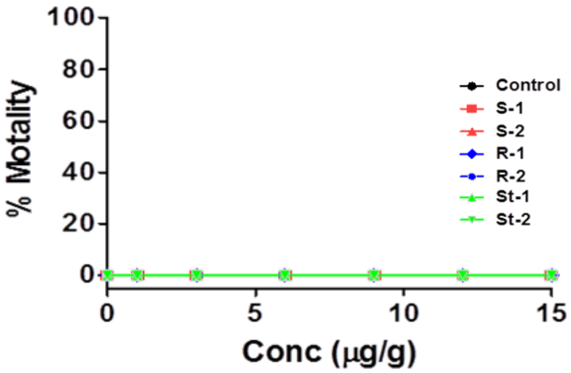

Figure 4. Percentage of motality of zebrafish with respect to concentration in presence of G-AuNPs at 120 h.

4.2.3 Biodistribution and sequestration studies of G-AuNPs in Zebrafish model: Since the AuNPs were non-toxic, it is worth to study their biodistribution and sequestration to target the specific organ using different shapes[31-33] and carbohydrate receptors. To this end, PEGylated and mannose-AuNPs (5 µg/g) of different shapes were intraperitoneally injected into zebrafish (Fig. 5). After 4 h, 24 h and 48 h exposure, fishes were sacrificed and different organs (brain, eye, heart, muscles, swim bladder and digestive system) were dissected. We examined the biodistribution of AuNPs into the various organs by quantifying the gold concentration using inductively coupled plasma mass spectrometry (ICP-MS). Figure 6 shows the organ-specific AuNPs sequestration at different time intervals. Our results demonstrated remarkable sensitivity of the zebrafish towards mannose-AuNPs compared to PEG-AuNPs. Mannose-AuNPs were sequestered in the digestive system, swim bladder and heart, but not in the brain, muscles and the eyes (Fig. 6, 7). However, the intrinsic shape of the AuNPs generated unexpected interrelationship on the number of AuNPs uptake and

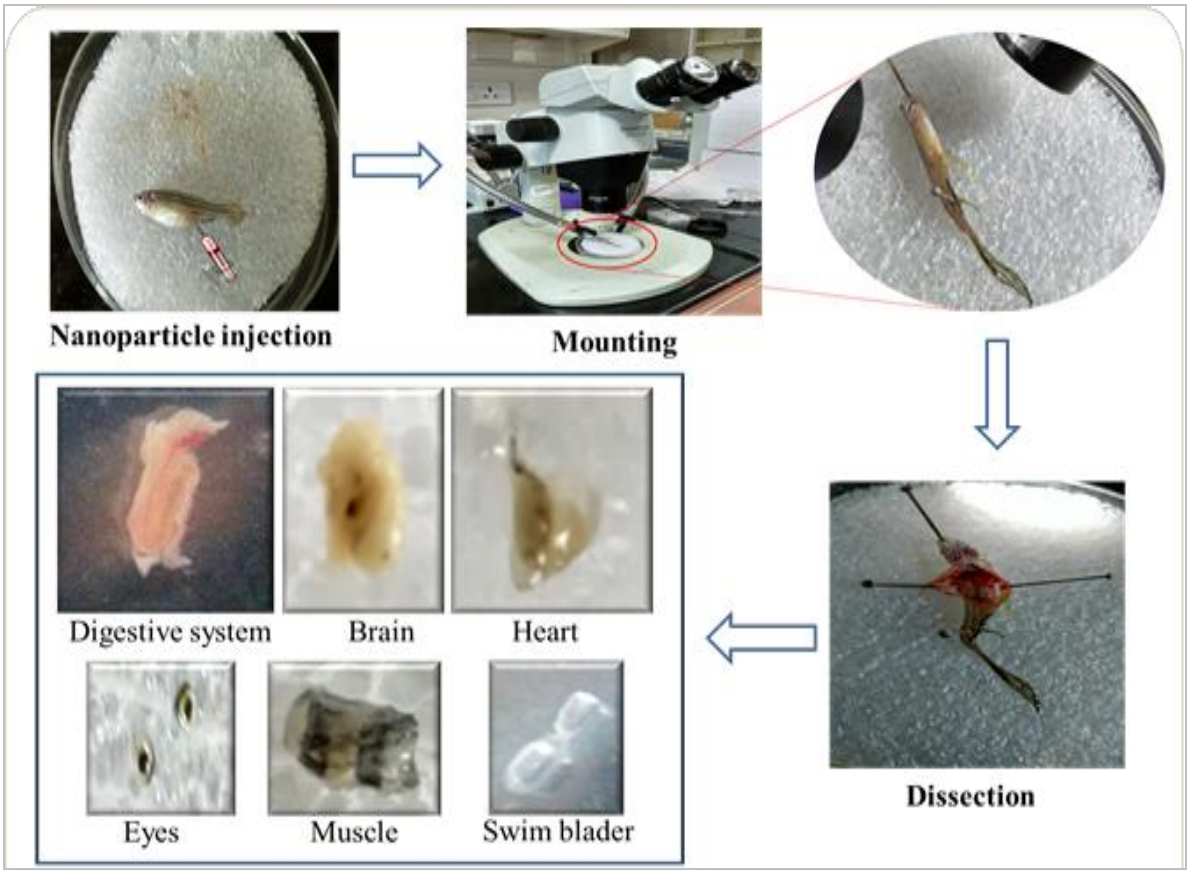

Figure 5. Schematic diagram of injection of G-AuNPs into zebrafish, mounting for dissection and collection of respective organs.

clearance. As illustrated in figure 6(a), the digestive system exhibited maximum mannose AuNPs sequestration after 4 h. However, after 24 h and 48 h a drastic difference in the shape dependent accumulation of nanoparticles was observed. Elongated particles (**R-2**) accumulated in higher number in the initial state and got cleared after 48 h, whereas, the **St-2** was accumulated in steady state and sequestered for extended periods of time as compared to **S-2**. PEGylated-AuNPs had the least sequestration, demonstrating the inter-relationship between shapes and carbohydrate-mediated interactions. The sequestration of mannose-AuNPs further support the presence of sugar receptors, either in the form of dendritic cell-specific intercellular adhesion molecule-3-grabbing non integrin (DC-SIGN) or other C-type lectins. Similar trends were observed in heart, indicating the broad distribution of mannose receptors in the zebrafish model. In the swim bladder, accumulation was higher for mannose nano-rod (**R-2**) after 4 h[34-35]. However, after 24 h and 48 h, clearance of **R-2** and slow sequestration of star- nanoparticles further confirm the therapeutical value of star-AuNPs.

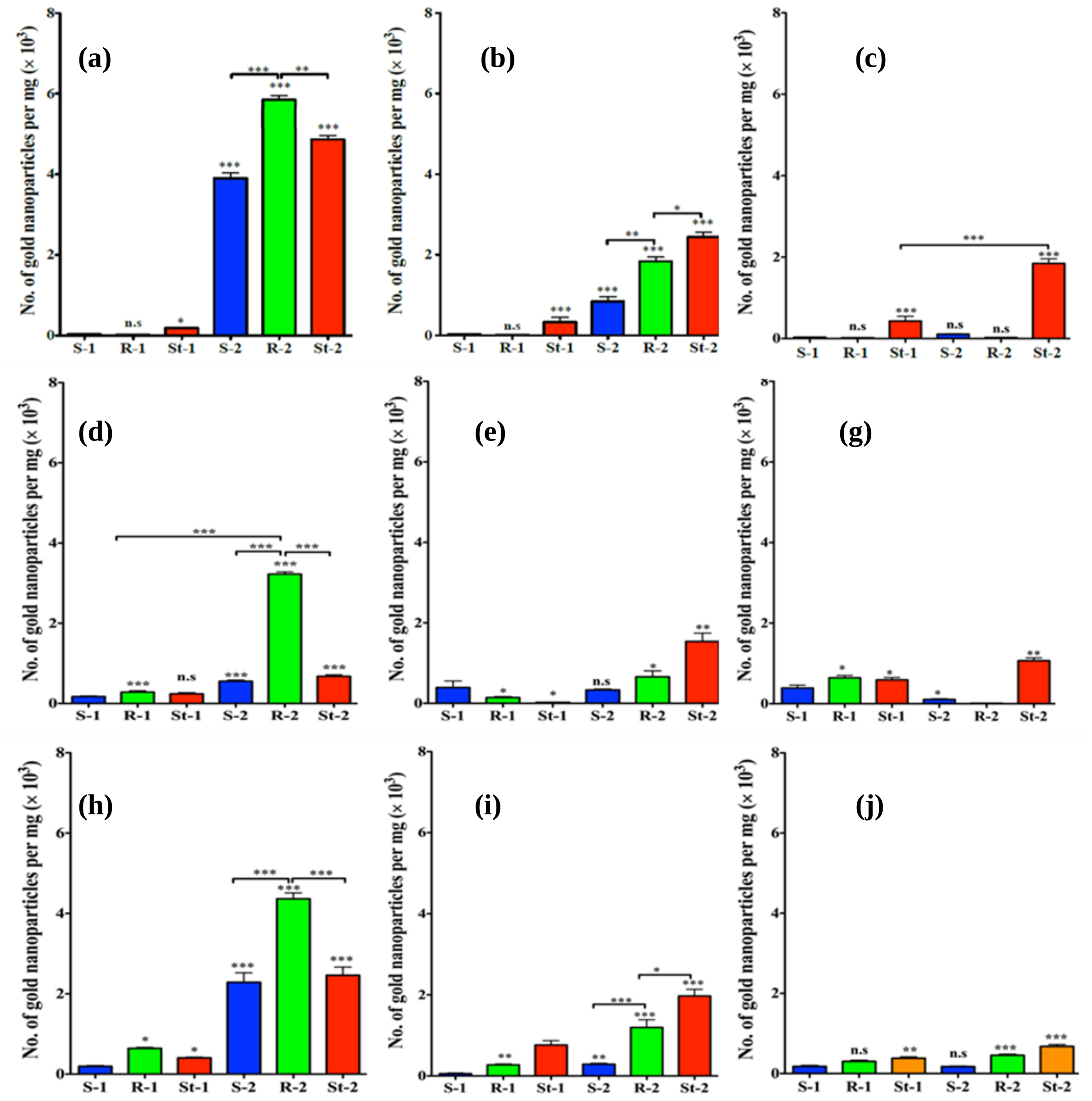

Figure 6. Statistical analysis of ICP-MS data of digestive system, hearth and swimming bladder of zebrafish at different time intervals: (a) digestive system-4 h; (b) digestive systm -24 h; (c) digestive system -48 h; (d) heart-4 h; (e) heart -24 h; (f) heart -48 h; (g) swim bladder-4 h; (h) swim bladder - 24h; (i) swim bladder-48h. Data are presented as mean ± SEM for three independent experiments (***P<0.001, **P<0.01 *P<0.05 and n.s = not significant).

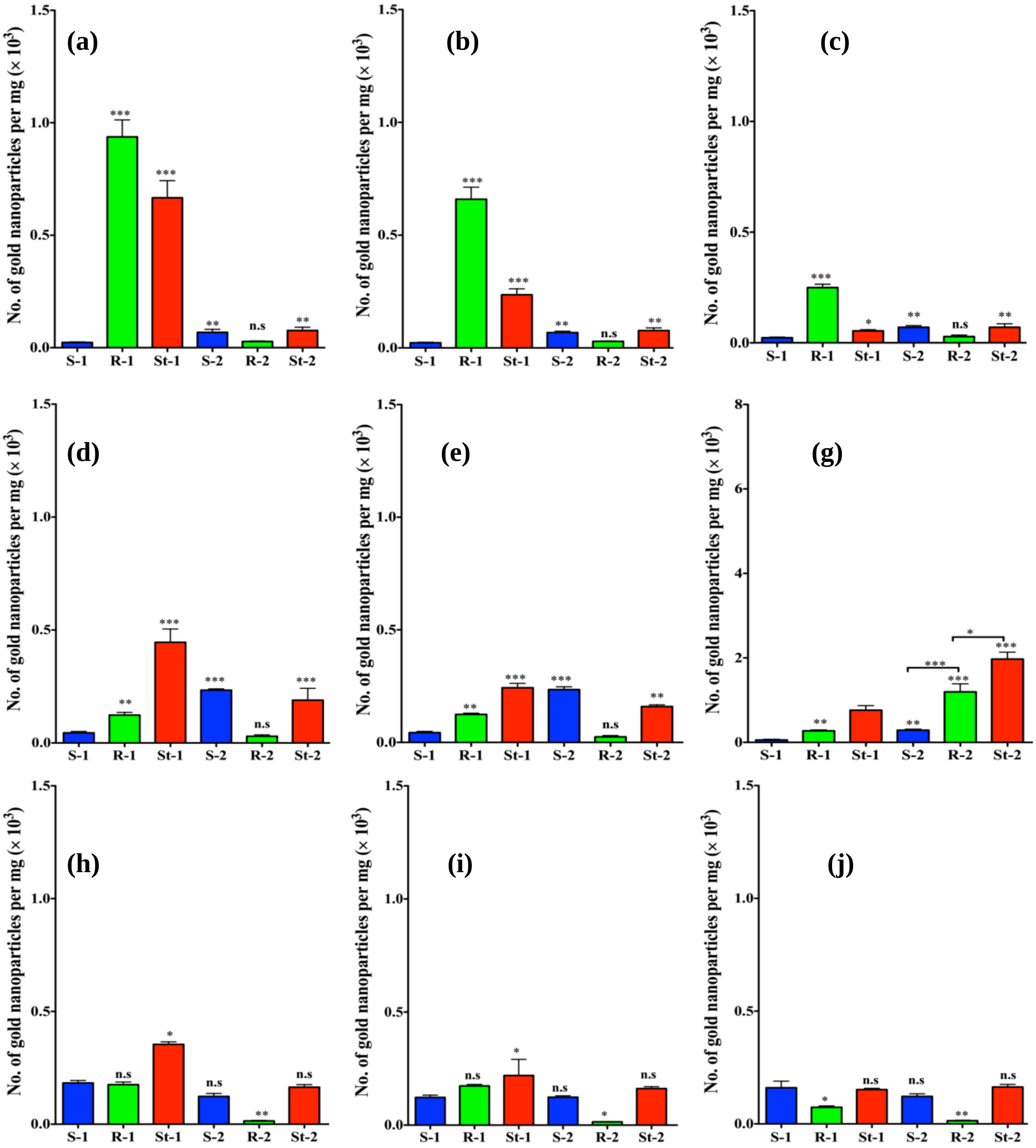

Figure 7. Statistical analysis of ICP-MS data of brain, eye and muscles of zebrafish at different time intervals: (a) brain -4h; (b) brain -24 h; (c) brain-48 h; (d) eye -4 h; (e) eye-24 h; (f) eye-48 h; (g) muscles -4 h; (h) muscles-24 h; (i) muscles-48h. (***P<0.001, **P<0.01 *P<0.05 and n.s = not significant).

The observed differences in the rate of biodistribution and sequestration of different shapes of AuNPs could be attributed to several physical factors associated with the nanoparticles and the chemical compositions as well. The physical factors such as aspect ratio of rod shape nanoparticles induced fast uptake and clearance from the system compared to spherical counter parts. While friction coefficient of nanoparticles (NPs), which is high in the star-shape AuNPs[36] and tumbling motion of NPs underflow invivo system is expected to be influence the sequestration of the star AuNPs. In addition, mannose based interactions could also influence the uptake mechanism. However, these interactions is more precise with higher glycans conjugated AuNPs. Finally, clearance of AuNPs was quantified by gold concentration in the water tank. As illustrated in figure 8, the PEG-AuNPs clearance from the zebrafish system much faster than the mannose-AuNPs counterparts. Further, star-AuNPs slow clearance further illustrates the significance of shapes in the *in vivo* studies.

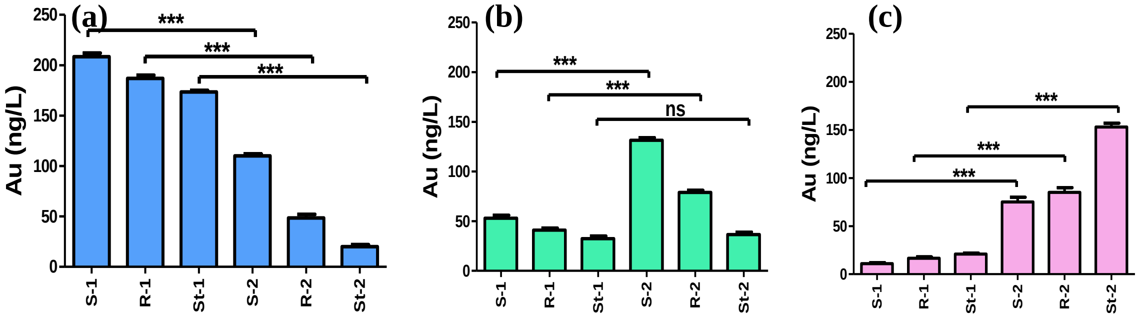

Figure 8. Clearance of Glyco-goldnanoparticles after (a) 4 h; (b) 24 h; (c) 48 h. administration into zebrafish. (***P<0.001, and n.s = not significant).

The accumulation of fluroscence conjugated G-AuNps in digestive system was qualitatively analyzed by confocal imaging of the tissue sections[37]. Figure 9 explicitly describes the relative fluorescent intensity of fluorescein conjugated G-AuNPs after 4 h. As expected, PEGylated nanoparticles were least sequestered in the digestive systems. While, mannose-AuNPs seem to taken up substantial by the digestive system. The time dependent, confocal imaging of **St-2** clearly showed that St-mannose-AuNPs sequestered in the digestive system for a long period (Fig 9) compared to **R-2**. overall, the shape and mannose conjugation on the nanoparticles showed remarkable differences in the biodistribution and sequestration, which could influence the toxicity after several days.

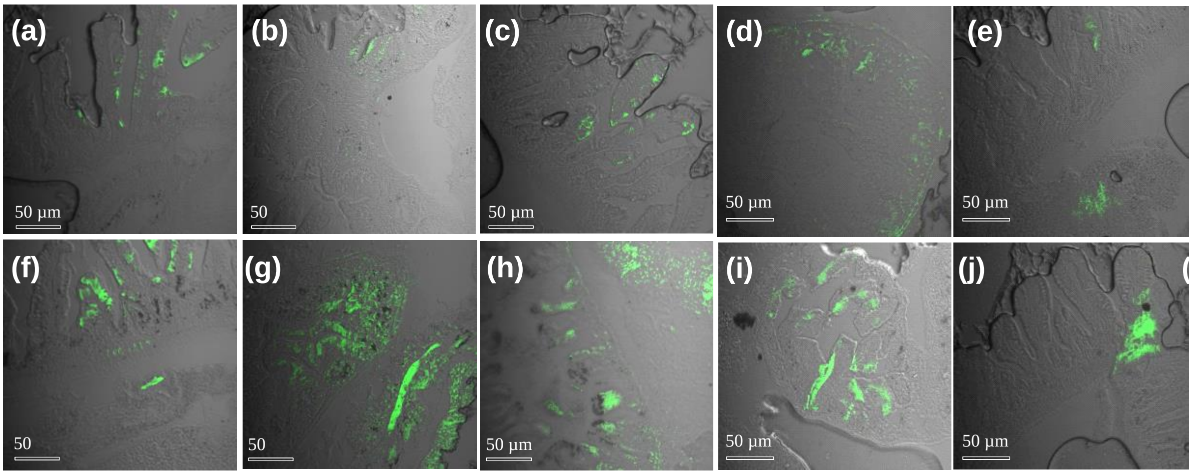

Figure 9. Confocal images of zebrafish digestive system injected with FL conjugated G-AuNPs after 4 h: (a) S-1, 4h; (b) R-1, 4h; (c) St-1, 4h; (d) R-2, 24h; (e) R-2, 48h; (f) S-2, 4h; (g) R-2, 4h; (h) St-2, 4h; (i) St-2, 24h; (j) St-2, 48h.

4.3 Conclusion

Here, we describe successfully constructed bifunctional fluorescent glyco-gold-nanoparticles to probe its *in vivo* efficiency using zebrafish model. The binding interaction between the mannose epitopes of AuNPs and lectins clearly showed the spatial arrangement of sugars on AuNPs influence the selective and sensitive carbohydrate-protein interactions. The intraperitonial injection of these nanoparticles into the adult zebrafish resulted very low toxicity, indicating the potential use of these nanoparticles for drug delivery and imaging studies. Using ICP-MS analysis and confocal imaging, we have demonstrated that the rate of bio-distribution of the AuNPs varies with its shape and mannose conjugation. Rod-AuNPs showed faster uptake and clearance. In contrast, star-AuNPs showed slow and long sequestration compared to other two shapes. Moreover, AuNPs showed remarkable sensitivity towards mannose compared to PEG linker.

4.4 Experimental Section

4.4.1 General Information: All chemicals were reagent grade and used as supplied except where noted. Analytical thin layer chromatography (TLC) was performed on Merck silica gel 60 F254 plates (0.25 mmol). Compounds were visualized by UV irradiation or dipping the plate in CAM/ninhydrin solution followed by heating. Column chromatography was carried out using force flow of the indicated solvent on Fluka Kieselgel 60 (230–400 mesh). ^{1}H and ^{13}C NMR spectra were recorded on Jeol 400 MHz, using residual solvents signals as an internal reference (DMSO d_6 δ_H, 2.5, 3.3 ppm, δ_C 39.5 ppm and CD_3OD δ_H 3.31 ppm, δ_C 49.0 ppm). The chemical shifts (δ) are reported in ppm and coupling constants (*J*) in Hz. UV-visible measurements were performed with Evolution 300 UV-visible spectrophotometer (Thermo Fisher Scientific, USA). Fluorescence spectra were recorded in FluoroMax-4 spectrofluorimeter (Horiba Scientific, U.S.A.).

4.4.2 Synthesis of Fluorescein linker

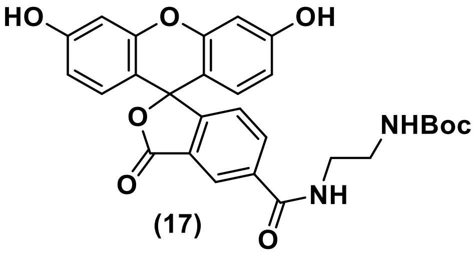

(17)

Synthesis of Compound (17): 5-carboxyl-fluorescein **16** (0.2 g, 0.72 mmol), HOBt (0.08 g, 0.53 mmol) and EDCI (0.153 g, 0.79 mmol) were stirred in dry pyridine at ice cold condition for 15 min. To this solution *tert*-butyl (2-aminoethyl) carbamate (0.127 g, 0.79 mmol), was slowly added. The corresponding reaction mixture was allowed to stir for 12 h. After completion of reaction (monitored by TLC), the crude reaction mixture was concentration and purified by column chromatography with MeOH : DCM (20 : 80) to afford compound **17**. Yield: 0.2 g, (72 %). ^{1}H NMR (400 MHz, DMSO-d^6) δ 10.24 (s, 2H), 8.84-8.68 (m, 1H), 8.25 – 8.07 (m, 1H), 8.02 – 7.96 (m, 1H), 7.72 (d, *J* = 8.4 Hz, 1H), 7.54 (t, *J* = 7.6 Hz, 1H), 7.43-7.37 (m, 1H), 6.98-6.86 (m, 1H), 6.70 (s, 1H), 6.62-6.53 (m, 3H), 3.22 (q, 1H), 3.18-3.13 (m, 2H), 3.05 (q, *J* = 6.2 Hz, 1H), 1.38 (s, 9H). ^{13}C NMR (100 MHz, DMSO-d^6) δ 168.67, 168.52, 165.28, 162.77, 160.08, 156.20, 152.30, 129.70, 129.54, 128.27, 127.68, 126.86, 124.91, 123.82, 119.58, 113.21, 113.14, 110.10, 109.62, 109.58, 102.78, 102.72, 78.16, 78.08, 49.07, 36.25, 28.70, 28.63. HRMS for $C_{28}H_{26}N_2O_8$ $(M+H)^+$ calculated m/z = 519.1767; Found, 519.1767.

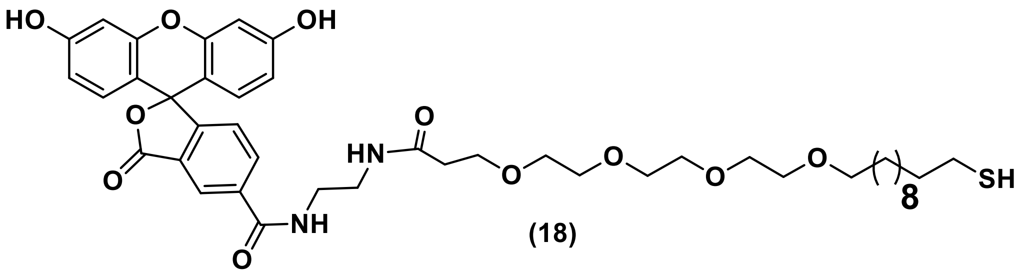

(18)

Synthesis of Compound (18): Compound **17** (0.2 g, 0.38 mmol) was dissolved in 1 ml of TFA : DCM (1 : 1) and allowed to stir for 2 h. After completion of the reaction, the crude mixture was concentrated and directly taken into next step, to this HOBt (0.06 g, 0.38 mmol), EDCI (0.11g, 0.57 mmol) and compound **15** (0.19 g, 0.57 mmol) were added in pyridine. The corresponding reaction mixture was allowed to stir for 12 h. After completion of reaction (monitored by TLC), the crude reaction mixture was concentrated and purified by column chromatography with MeOH : DCM (20 : 80) to afford compound **18**. Yield: 0.08 g (41 %). ^{1}H NMR (400 MHz, CD_3OD) δ 7.89 (d, *J* = 8.3 Hz, 2H), 7.75 (d, *J* = 8.3 Hz, 2H), 7.58 – 7.48 (m, 5H), 3.75 (t, *J* = 6.3 Hz, 2H), 3.68 – 3.57 (m, 12H), 3.47 (t, *J* = 6.6 Hz, 2H), 2.69 (t, *J* = 7.2 Hz, 2H), 2.57 (t, *J* = 6.2 Hz, 2H), 1.70 – 1.66 (m, 2H), 1.57 (t, *J* = 6.9 Hz, 2H), 1.52 – 1.42 (m, 2H), 1.41 – 1.26 (m, 16H). ^{13}C NMR (100 MHz, CD_3OD) δ 173.90, 141.33, 128.19, 127.01, 126.97, 125.86, 117.22, 110.05, 70.98, 70.17, 70.16, 70.08, 70.01, 69.75, 66.42, 38.44, 34.43, 34.35, 29.33, 29.25, 29.22, 29.19, 28.91, 28.82, 28.05, 26.23, 25.82. HRMS for $C_{43}H_{56}N_2O_{11}S$ $(M+Na)^+$ calculated m/z = 831.9738; Found, 832.5280.

4.4.3 Synthesis of fluorescence glyco-gold nanoparticles: Gold nanoparticles of different shapes were synthesized by applying literature procedures[38-40]. 0.5 ml of 1 mM thiol PEG linker (**1**) /thiol mannose linker (**2**) and 0.1 mM of **8** were mixed with 0.5 ml of the AuNPs solution. After incubation at room temperature for 12 h, the modified Au nanostructures were separated by centrifugation and re-dispersed in deionized water.

4.4.4 Zeta potential studies: We used a zeta potential analyzer to measure the surface potential of AuNPs. In the measurement, we applied unit field strength (1 Volt per meter) to the AuNP solution. We measured zeta potential of different shapes of AuNPs in water. In the case of DMEM medium, we incubated all AuNps in DMEM medium (containing 10% FBS) for 24 h and purified by centrifugation and measured zeta potential.

4.4.5 Phenol-sulfuric acid method to quantify sugars on AuNPs: The concentration of mannose sugars on AuNPs were determined by the phenol-sulfuric acid method. 50 µL sugar functionalized-AuNPs were added to concentrated sulfuric acid (130 µL, 100%) and aqueous phenol solution (5% w/v, 30 µL) in the test tube and heated to 90°C. After 5 min, the solution was cooled to room temperature and the absorbance coefficient at 490 nm was measured. AuNPs as such in sulfuric acid was used as a control. The sugar concentration was estimated by comparing the absorption of the sample with a standard curve. The FITC concentration was measured by using absorption coefficient of FITC.

4.4.6 Zebrafish model: Local wild-type zebrafish strain weighing approximately 500-600 mg (2-3 months old) were maintained under standard laboratory conditions at 28 ºC under 14:10 h light/dark cycle conductivity of 350 µS of the water maintained at pH 7.2 – 7.4. The surgical procedures were performed in accordance with Institutional Animal Ethical Committee regulation, set up by CPCSEA, Govt. of India.

4.4.7 Acute toxicity determination: Zebrafishes were anesthetized with 2-phenoxyethanol and -AuNPs were injected. The number of zebrafish in each experimental and control group was 6 in each group.

4.4.8 Sample preparation for ICP-MS analysis: Zebrafish were anesthetized with 2-phenoxyethanol and injected 2 µl contain 5 µg/g nanoparticles of rod, sphere and star shape AuNPs via intraperitoneally using *catheter* implantation tubing attached to a cut 22-G needle tip at one end and another end attached to Hamilton syringe. After 4 h, 24 h and 48 h injection, fishes were sacrificed and organs were collected. Organs were homogenized with 400 µl of *aqua regia* at 95 °C for 4 h. All digested samples were centrifuged at 5000 rpm for 10 min to remove debris. Then each digested samples were diluted to 6 ml with Millipore water. The concentration of Au, determined by ICP-MS (Thermo-Fisher Scientific, Germany), was converted into the number of AuNPs per one mg.

4.4.9 Confocal imaging studies: Zebrafish were anesthetized with 2-phenoxyethanol and injected with 2 µl contain 5 µg/g nanoparticles of FITC conjugated G-AuNPs *via* intraperitoneal injection. After 4 h and 48 h of injection, fishes were sacrificed and digestive system was collected. Organ was fixed with 4% paraformaldehyde and 4% glutaraldehyde followed by dehydration with the gradient increase of ethanol (75%, 95%, 100%) for 30 min each, further with xylene for 1 h and then fixed in paraplast. Blocks were stored in -10 °C for 12 h before proceeding to section. 10 µm thicknesses of sections were cut by using *Leica* microtome instrument and sections were collected on PLL-coated glass plates. The sections were washed with xylene to remove excess of paraplast. After drying, sections were fixed with mounting media. Sequestration of AuNPs in digestive system was analyzed by confocal fluorescence microscopy using CLSM (Zeiss LSM 710) microscope. The excitation wavelength was 450 nm, detection wavelength was 510 nm. 25X objective was used to image digestive system sections

4.4.10 Statistical analysis: Statistical comparisons were done using the student *t* test or one-way ANOVA. The $^{***}P<0.001$ $^{**}P<0.01$ $^{*}p < 0.05$ is considered to be statistical significance.

4.5 References

1. A. Varki, R.D. Cummings, J. D. Esko, H. H. Freeze, P. Stanley, C. R. Bertozzi, G. Hart and M. E. Etzler Essentials of Glycobiology, second ed., Cold Spring Harbor Laboratory Press, New York, 2009.
2. M. Cohen and A. Varki, *International review of cell and molecular biology,* 2014, **308**, 75-125.
3. C. R. Bertozzi and L. L. Kiessling, *Science*, 2001, **291**, 2357-2364.
4. D. Safari, M. Marradi, F. Chiodo, H. A. Th Dekker, Y. Shan, R. Adamo, S. Oscarson, G. T. Rijkers, M. Lahmann, J. P. Kamerling, S. Penades and H. Snippe, *Nanomedicine*, 2012, **7**, 651-662.
5. M. Delbianco, P. Bharate, S. Varela-Aramburu and P. H. Seeberger, *Chem. Rev.*, 2016, **116**, 1693-1752.
6. S. I. van Kasteren, S. J. Campbell, S. Serres, D. C. Anthony, N. R. Sibson and B. G. Davis, *Proc Natl Acad Sci U S A*, 2009, **106**, 18-23.
7. P. Padmanabhan, A. Kumar, S. Kumar, R. K. Chaudhary and B. Gulyas, *Acta Biomater.*, 2016, **41**, 1-16.
8. C. H. Lai, J. Hutter, C. W. Hsu, H. Tanaka, S. Varela-Aramburu, L. De Cola, B. Lepenies and P. H. Seeberger, *Nano Lett.*, 2016, **16**, 807-811.
9. D. C. Kennedy, G. Orts-Gil, C. H. Lai, L. Muller, A. Haase, A. Luch and P. H. Seeberger, *Journal of nanobiotechnology*, 2014, **12**, 59.
10. R. Kikkeri, B. Lepenies, A. Adibekian, P. Laurino and P. H. Seeberger, *J. Am. Chem. Soc.*, 2009, **131**, 2110-2112.
11. A. Barandov, D. Grunstein, I. Apostolova, R. Buchert, M. Roger, W. Brenner, U. Abram and P. H. Seeberger, *ChemBioChem*, 2014, **15**, 986-994.
12. T. Ohyanagi, N. Nagahori, K. Shimawaki, H. Hinou, T. Yamashita, A. Sasaki, T. Jin, T. Iwanaga, M. Kinjo and S. Nishimura, *J. Am. Chem. Soc.*, 2011, **133**, 12507-12517.

13. L. Gonzalez-Moragas, A. Roig and A. Laromaine, *Adv. Colloid Interface Sci.*, 2015, **219**, 10-26.

14. V. Marchesano, A. Ambrosone, J. Bartelmess, F. Strisciante, A. Tino, L. Echegoyen, C. Tortiglione and S. Giordani, *Nanomaterials-Basel*, 2015, **5**, 1331-1350.

15. B. Wang, N. Chen, Y. Wei, J. Li, L. Sun, J. Wu, Q. Huang, C. Liu, C. Fan and H. Song, *Scientific reports*, 2012, **2**, 563.

16. S. Jiang, C. P. Teng, W. C. Puah, M. Wasser, K. Y. Win and M. Y. Han, *Acs Biomater Sci Eng*, 2015, **1**, 1077-1084.

17. C. A. MacRae and R. T. Peterson, *Nat. Rev. Drug Discov.*, 2015, **14**, 721-731.

18. J. W. Lu, Y. J. Ho, Y. J. Yang, H. A. Liao, S. C. Ciou, L. I. Lin and D. L. Ou, *World journal of gastroenterology*, 2015, **21**, 12042-12058.

19. S. George, T. Xia, R. Rallo, Y. Zhao, Z. Ji, S. Lin, X. Wang, H. Zhang, B. France, D. Schoenfeld, R. Damoiseaux, R. Liu, S. Lin, K. A. Bradley, Y. Cohen and A. E. Nel, *ACS nano*, 2011, **5**, 1805-1817.

20. M. Newman, E. Ebrahimie and M. Lardelli, *Frontiers in genetics*, 2014, **5**, 189.

21. Q. Wu, G. Li, S. Deng, L. Ouyang, L. Li, L. Liu, N. Luo, X. Song, G. He, C. Gong and Y. Wei, *Nanoscale*, 2014, **6**, 11940-11952.

22. J. Li, H. H. Ha, L. Guo, D. Coomber and Y. T. Chang, *Chem Commun (Camb)*, 2010, **46**, 2932-2934.

23. S. W. Son, J. H. Kim, S. H. Kim, H. Kim, A. Y. Chung, J. B. Choo, C. H. Oh and H. C. Park, *Skin Res. Technol.*, 2009, **15**, 157-160.

24. A. M. da Rocha, J. R. Ferreira, D. M. Barros, T. C. Pereira, M. R. Bogo, S. Oliveira, V. Geraldo, R. G. Lacerda, A. S. Ferlauto, L. O. Ladeira, M. V. Pinheiro and J. M. Monserrat, *Comparative biochemistry and physiology. Part A, Molecular & integrative physiology*, 2013, **165**, 460-467.

25. X. Li, B. Liu, X. L. Li, Y. X. Li, M. Z. Sun, D. Y. Chen, X. Zhao and X. Z. Feng, *Scientific reports*, 2014, **4**, 3810.

26. Z. J. Zhu, R. Carboni, M. J. Quercio, Jr., B. Yan, O. R. Miranda, D. L. Anderton, K. F. Arcaro, V. M. Rotello and R. W. Vachet, *Small*, 2010, **6**, 2261-2265.

27. J. A. Kovriznych, R. Sotnikova, D. Zeljenkova, E. Rollerova, E. Szabova and S. Wimmerova, *Interdisciplinary toxicology*, 2013, **6**, 67-73.

28. P. M. Chaudhary, S. Sangabathuni, R. V. Murthy, A. Paul, H. V. Thulasiram and R. Kikkeri, *Chem Commun (Camb)*, 2015, **51**, 15669-15672.

29. B. D. Chithrani, A. A. Ghazani and W. C. Chan, *Nano Lett.*, 2006, **6**, 662-668.
30. O. Bar-Ilan, R. M. Albrecht, V. E. Fako and D. Y. Furgeson, *Small*, 2009, **5**, 1897-1910.
31. G. E. Weber, L. Dal Bosco, C. O. Goncalves, A. P. Santos, C. Fantini, C. A. Furtado, G. M. Parfitt, C. Peixoto, L. A. Romano, B. S. Vaz, D. M. Barros, *Toxicol. Appl. Pharmacol.*, **280**, 2014, 484-492.
32. Y. Wang, J. L. Seebald, D. P. Szeto, J. Irudayaraj, *ACS Nano.*, 2010, **4**, 4039-4053.
33. J. Zhang, X. Nie, Y. Ji, Y. Liu, X. Wu, C. Chen, X. Fang, *J. Nanosci. Nanotechnol.*, 2014, **14**, 4124-4138.
34. W. Zheng, Z. Wang, J. E. Collins, R. M. Andrews, D. Stemple and Z. Gong, *PloS one*, 2011, **6**, e24019.
35. F. Zheng, M. Asim, J. Lan, L. Zhao, S. Wei, N. Chen, X. Liu, Y. Zhou and L. Lin, *International journal of molecular sciences*, 2015, **16**, 10997-11012.
36. K. C. Black, Y. Wang, H. P. Luehmann, X. Cai, W. Xing, B. Pang, Y. Zhao, C. S. Cutler, L. V. Wang, Y. Liu and Y. Xia, *ACS nano*, 2014, **8**, 4385-4394.
37. L. M. Skjolding, G. Asmonaite, R. I. Jolck, T. L. Andresen, H. Selck, A. Baun, J. Sturve, *Nanotoxicology*, 2017, **11**, 351-359.
38. B. Nikoobakht and M. A. El-Sayed, *Chem. Mater.*, 2003, **15**, 1957-1962.
39. J. P. Xie, J. Y. Lee and D. I. C. Wang, *Chem. Mater.*, 2007, **19**, 2823-2830.
40. E. C. Cho, Y. Liu and Y. Xia, *Angew. Chem. Int. Ed. Engl.*, 2010, **49**, 1976-1980.

4.6 Appendix I: Characterization Data of Synthesized Compounds

Designation	Description	Page
Compound 17	^{1}H, ^{13}C, HRMS	94-95
Compound 18	^{1}H, ^{13}C, HRMS	96-97

1. NMR Spectras of FITC conjugated linker

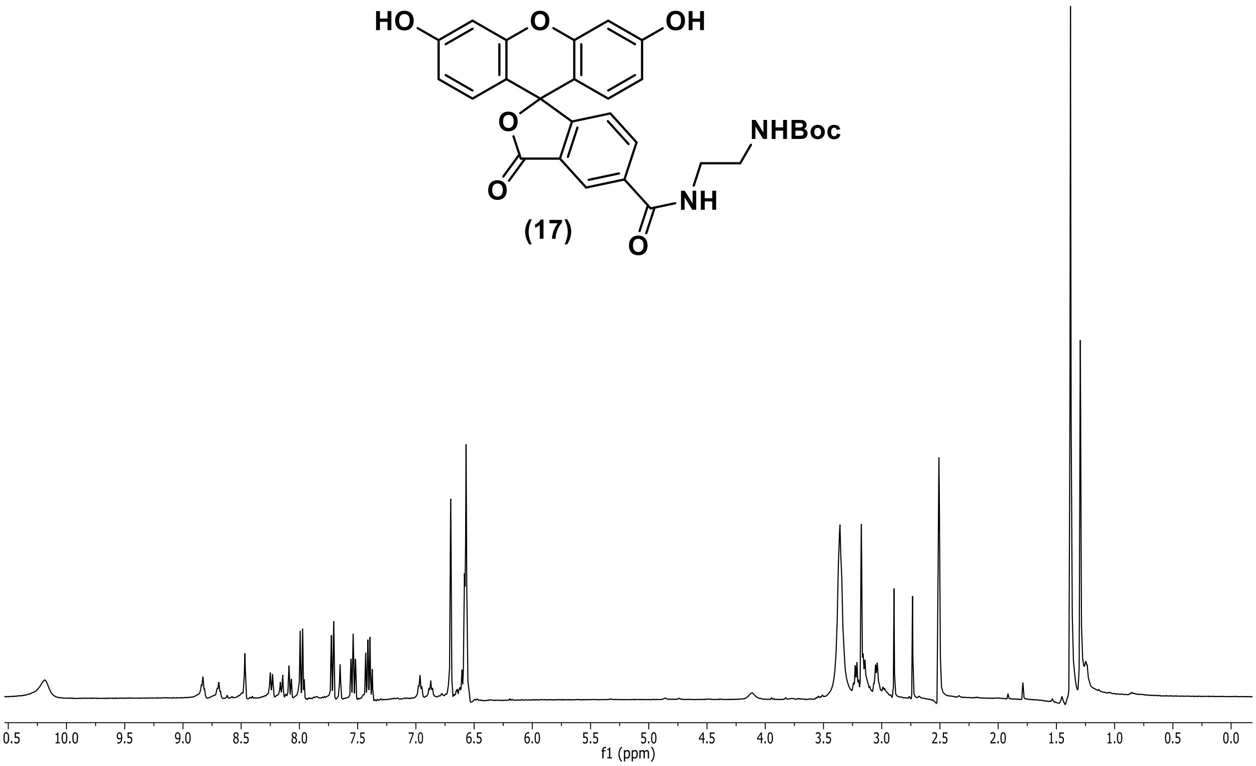
(17)

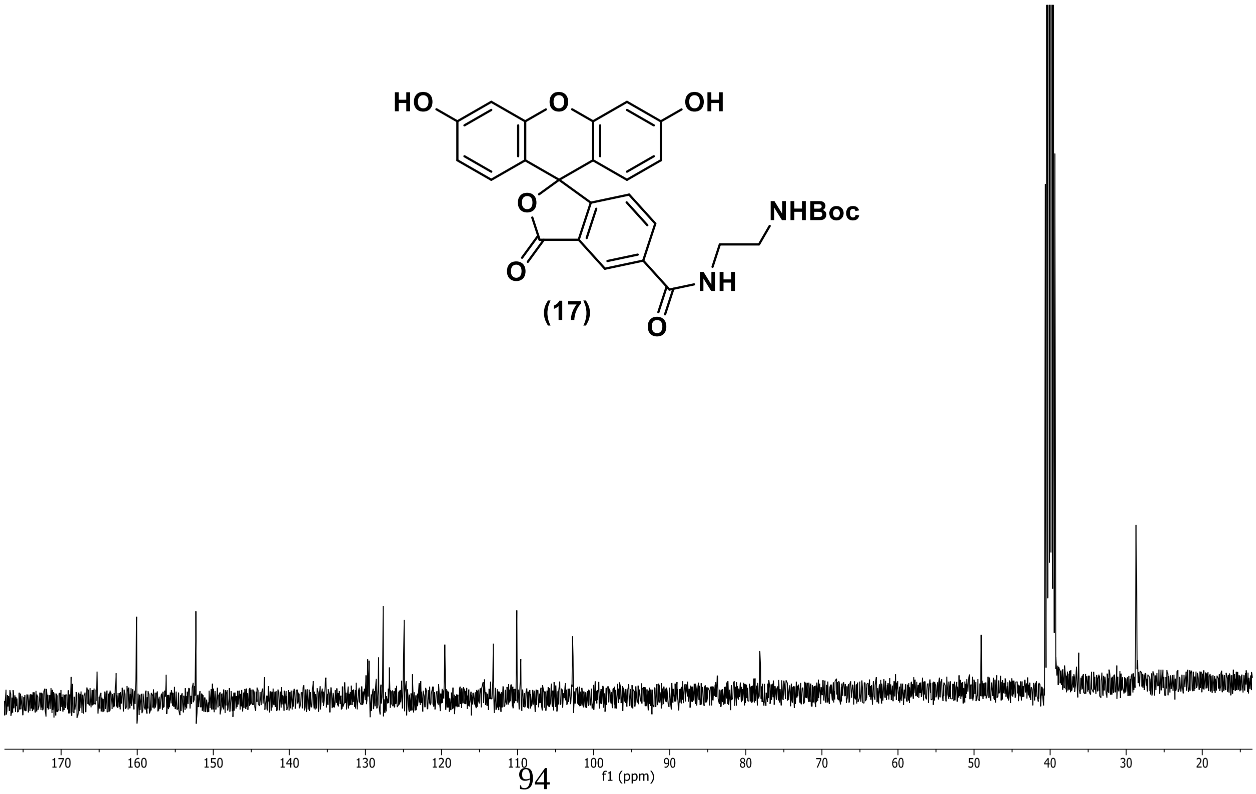
(17)

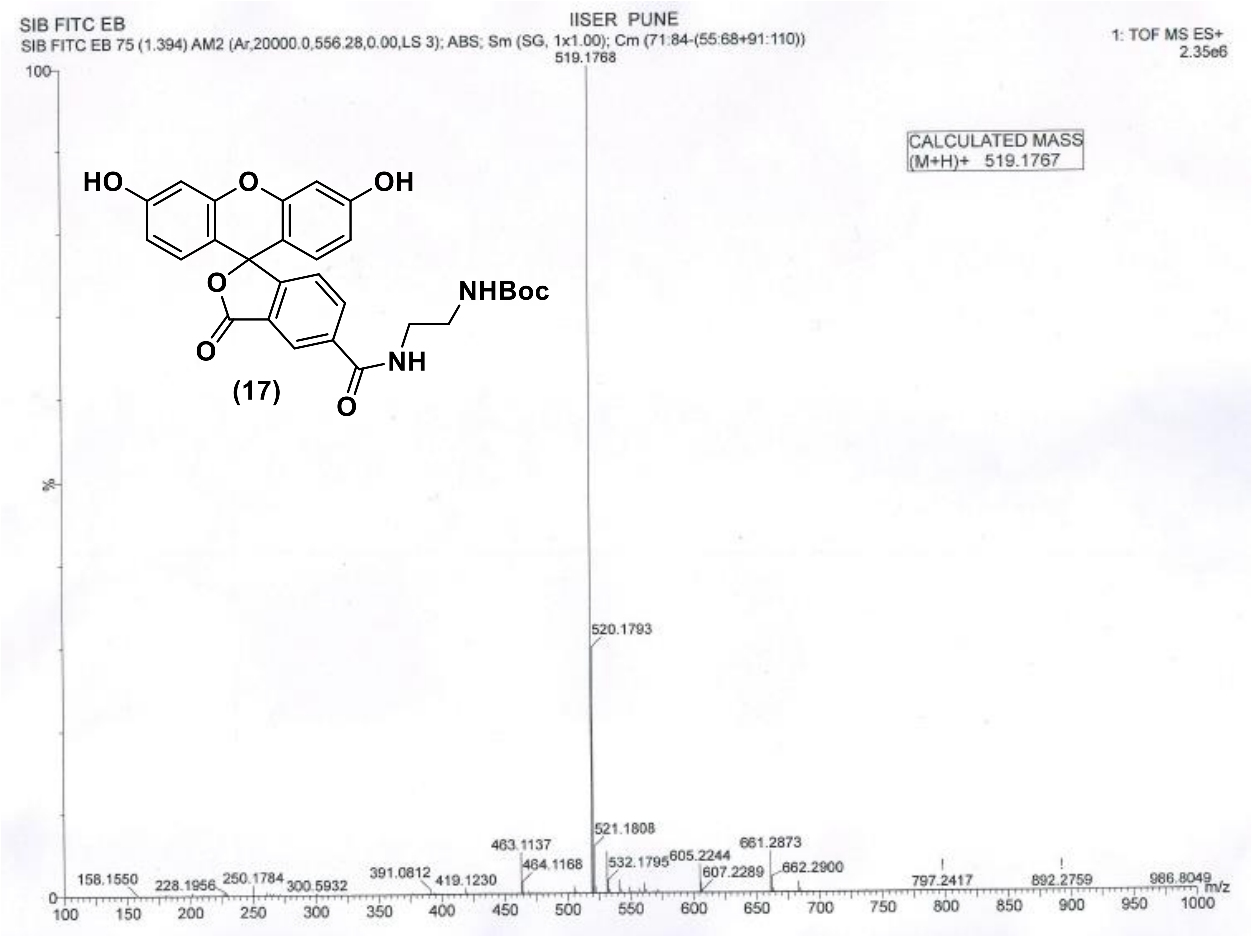
SIB FITC EB
IISER PUNE
SIB FITC EB 75 (1.394) AM2 (Ar,20000.0,556.28,0.00,LS 3); ABS; Sm (SG, 1x1.00); Cm (71:84-(55:68+91:110))
1: TOF MS ES+
2.35e6
519.1768
CALCULATED MASS
(M+H)+ 519.1767
HO
O
OH
O
NHBoc
O
NH
(17)
O
100
%
0
520.1793
521.1808
463.1137
464.1168
532.1795
605.2244
607.2289
661.2873
662.2900
158.1550
228.1956
250.1784
300.5932
391.0812
419.1230
797.2417
892.2759
986.8049
m/z
100
150
200
250
300
350
400
450
500
550
600
650
700
750
800
850
900
950
1000

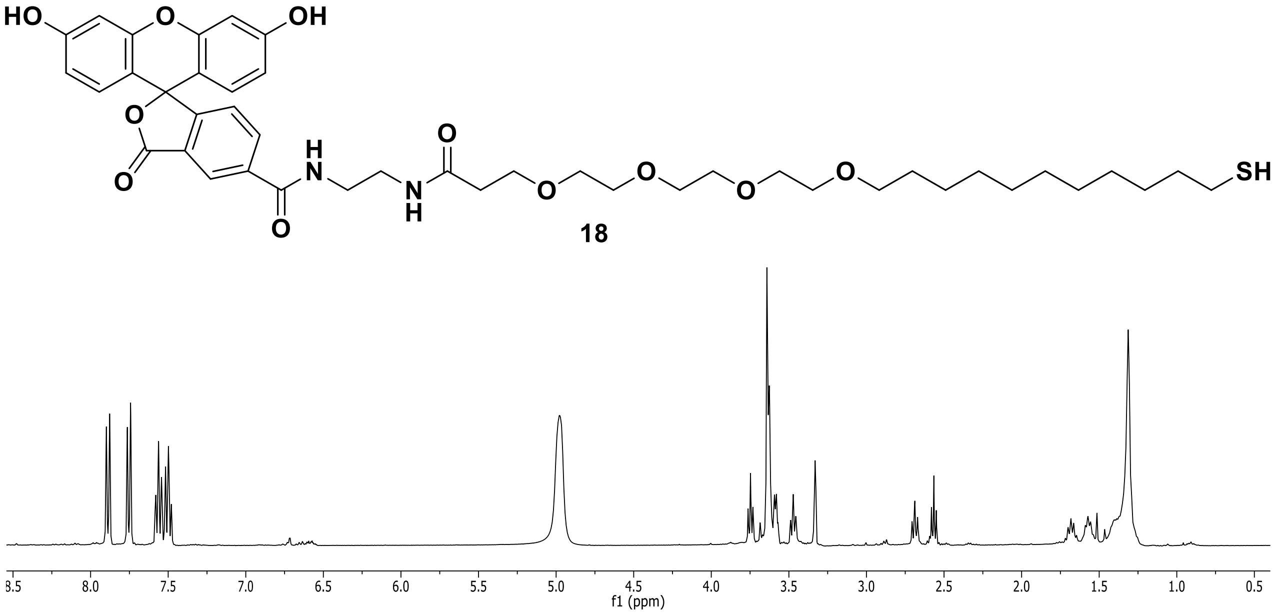

18

HO
O
OH
O
O
H
N
O
N
H
O
O
O
SH
8.5
8.0
7.5
7.0
6.5
6.0
5.5
5.0
4.5
4.0
3.5
3.0
2.5
2.0
1.5
1.0
0.5
f1 (ppm)

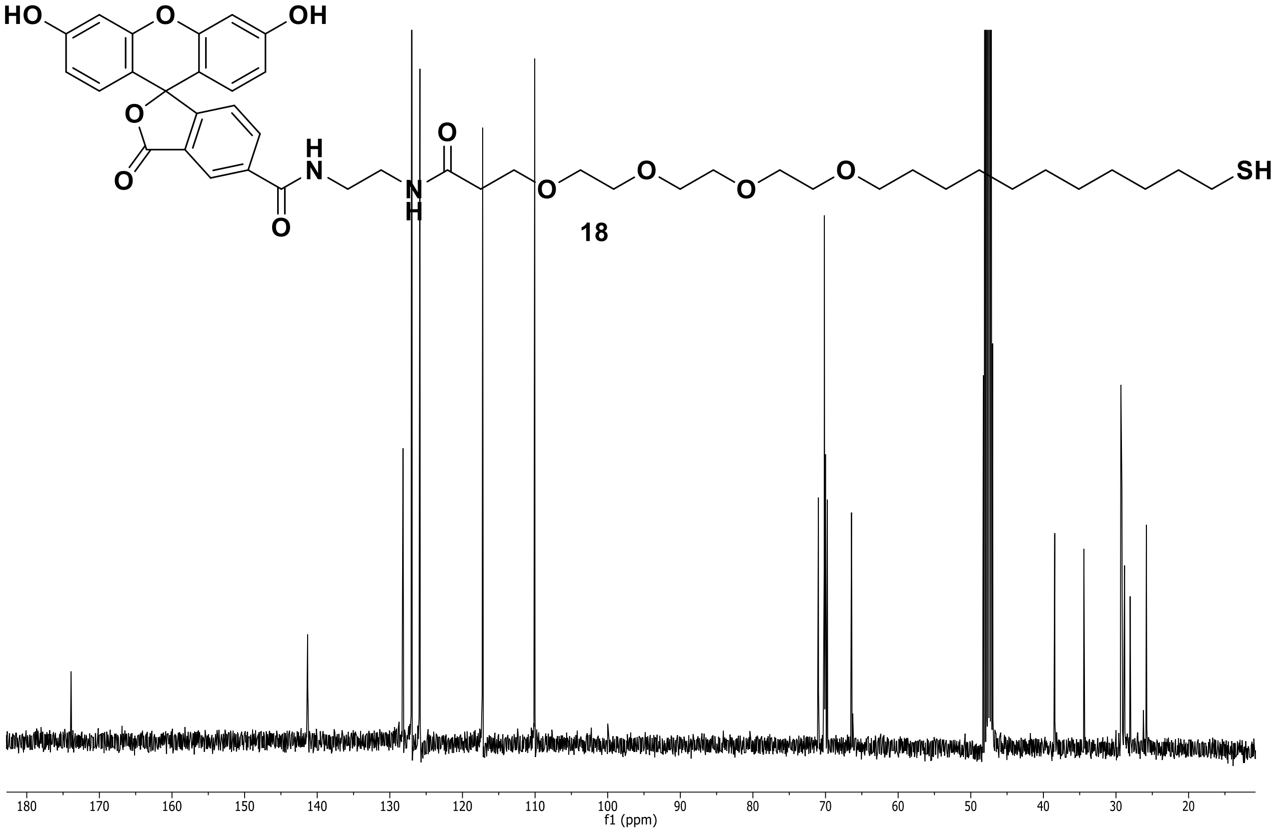

18

HO
O
OH
O
O
H
N
O
N
H
O
O
O
SH
180
170
160
150
140
130
120
110
100
90
80
70
60
50
40
30
20
f1 (ppm)

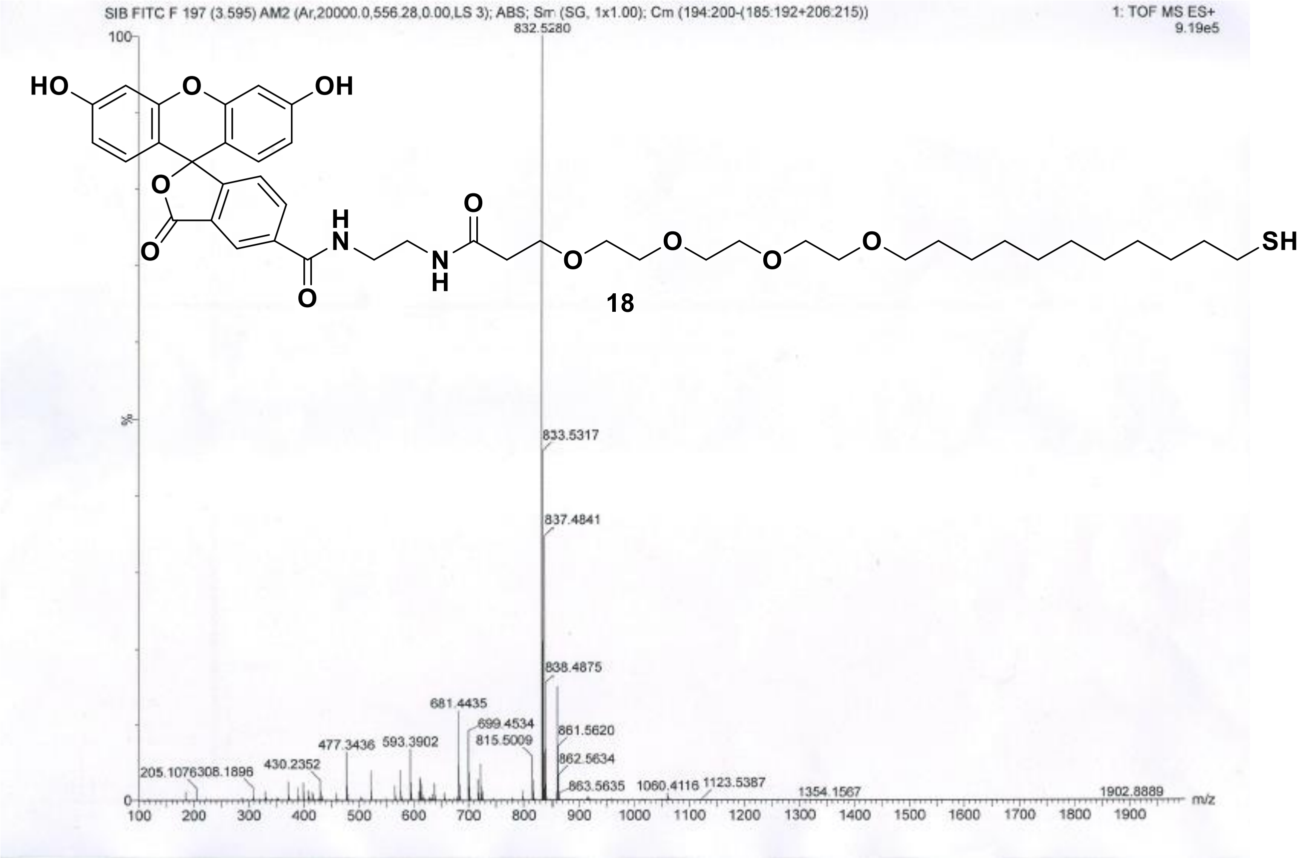

18

SIB FITC F 197 (3.595) AM2 (Ar,20000.0,556.28,0.00,LS 3); ABS; Sm (SG, 1x1.00); Cm (194:200-(185:192+206:215))
1: TOF MS ES+
9.19e5
832.5280
100
%
0
833.5317
837.4841
838.4875
681.4435
699.4534
815.5009
861.5620
862.5634
477.3436
593.3902
430.2352
205.1076
308.1896
863.5635
1060.4116
1123.5387
1354.1567
1902.8889
100
200
300
400
500
600
700
800
900
1000
1100
1200
1300
1400
1500
1600
1700
1800
1900
m/z
HO
OH
O
O
O
O
H
N
N
H
O
O
O
O
O
SH

Chapter 5

(Miscellaneous)

Self-Assembly of Collagen Glycopeptides to Profile Cell Migration and In Vivo Wound Healing

5.1 Introduction

Protein glycosylation is a post-translational process responsible for more than 50% of protein modifications in nature. Attaching glycans to proteins results in a dramatic increase in the bioavailability, stability and solubility of proteins.[1-5] However, the primary roadblock in the application of glycopeptides or glycoproteins to delineate the biology of disease pathways is the limited availability of robust, affordable and accessible synthetic platforms that are useful to decipher the biochemical basis of glycoprotein interactions. Recently, signature-based profiling of glycopeptides has provided a powerful strategy for mimicking the protein structure to understand the functions of post-translational modifications.[6-10] Such synthetic approaches have been used to prepare tumour-associated MUC-1 conjugates, collagen,[11] coiled-coils and anti-freezing glycopeptides for the study of structure-function relationships of native proteins.[12-14]

The synthesis of glycopeptides is normally carried out by incorporating glycosylated amino acid residues into the peptide skeleton in a step-wise process[15] or *via* convergent synthesis, where functionalization is achieved at the final step.[14,16-17] Host-guest interaction between sugar functionalized β-cyclodextrin (β-CD) and adamantyl scaffolds has recently emerged for the convergent assembly of multivalent glycodendrimers.[18-19] In comparison to step-wise process, the host-guest strategy allows high-throughput process to obtain a dynamic combinatorial library in a short span. Taken such advantages, we established host-guest strategy between 4-adamantyl-capped peptides and sugar-appended β-cyclodextrin to create a versatile combinatorial library of glycopeptides. We combine solid phase peptide synthesis, high-throughput phenotypic-cells migration assay, molecular biology and murine wound healing model to identify specific glyco-peptides involvement in cell migration. Briefly, we designed a library of collagen modified glycopeptides (CMGs), which is one of the most abundant fibrous structural proteins in the extracellular matrix and extensively involved in cell migration process.[20-24] We modified the collagen peptide (CPs) with 4-adamantyl derivatives, such that the triple helicity of the collagen remain intact and also undergo host-guest interactions with β-cyclodextrin derivatives. We subsequently performed high-throughput cell migration assay using primary and secondary cell lines, followed by mechanistic studies to identify specific combination that can evidently be involved in murine wound healing process. Thus, our convergent method of screening the cell migration is highly scalable to identify different targets and also represent exciting new venue for drug discovery and inhibitors.

5.2 Results and discussions

5.2.1 Construction of glyco-collagen library: Previous studies on functionalization of collagen have revealed that the middle site (Y-position) of proline-hydroxyproline-glycine triad is ideal for bio-conjugations without hampering the collagen triple helix structure.[14] To monitor the glyco-collagen mediated biological responses, we synthesized two control CPs (**C-1** and **C-2**) and adamantyl-CP (**C-3**) (Fig. 1 and Scheme 1-2) using a solid phase peptide synthesizer by following the standard protocol. The CPs was purified by reverse phase semi-preparative high-performance liquid chromatography (HPLC) (Fig. 5) and characterized by MALDI-TOF (Table. 2).

The binding events between specific glycans and their complementary receptors occur in a multivalent and cooperative manner.[25-26] Hence the *β*-cyclodextrin (*β*-CD) conjugates of common mono/disaccharide derivatives found in mammalian cell surfaces were synthesized (**G-2** to **G-7**) to mimic the collagen sugar microenvironment (Fig. 1 and Scheme 3).[27-29] Circular dichroism (CD) spectra and corresponding thermal unfolding curves of peptides **C-1** to **C-3** and their *β*-CD complexes were used to verify the successful triple-helix formation of the CPs (Fig. 10 and Table 3). Further the morphological nature of peptide **C-1** to **C-3** evaluated by Scanning Electron Microscopy (SEM). As seen in SEM images, peptides **C-1, C-2** underwent self-assembly into nano-needle structures whereas, **C-3** displayed flat nano-needles with an average size of 800 nm × 120 nm (Fig. 11).

Collagen peptide (**C-3**) was non-covalently conjugated by mixing stoichiometric amounts (1:1) of *β*-CD derivatives **(G-1** to **G-7)** yielding a combinatorial library of glyco-collagen peptides in a minute (Fig. 6). The ESI-MS (soft ionization) data for **C-3**/**G-1** of *m/z* 862 $[M+2K+2H]^+/_4$ (Fig. 8i(b)), corresponding to the host-guest complexes, validated the formation of host-guest glyco-collagen peptide (GCC) complexes. The peaks at *m/z* 768 and 1135 corresponding to individual **C-3** and **G-1** respectively, in the mass spectra arise from partial dissociation of **C-3/G-1** complex due to the collision of the analyte ions with neutral gas molecules during the ionization process. Similarly, the mass spectral data of **C-3**/**G-4** **(***m/z* 1242; $[M+K+3H]^+/_4$), **C-3**/**G-5** (*m/z* 1213; $[M+K+3H]^+/_4$), **C-3/G-10** (*m/z* 1525; $[M+K+3H]^+/_4$) and **C-3/G-6** (*m/z* 1289; $[M+K]^+/_4$) confirmed the existence of supramolecular assemblies of respective GCCs and *β*-CD derivatives (Fig. 8ii-iii). Further ^{1}H-NOESY NMR supported the anchoring of *β*-CD on adamantyl moiety as a supramolecular assembly. The overlapping of Pro-Hyp and *β*-CD peaks in the range 4.0 to 3.2 ppm, prevented unambiguous assignment of the *β*-CD peaks for identifying changes due to host-guest complex. However, the adamantyl H_a-H_c peaks revealed strong NOE interactions with the protons in *β*-CD region (Fig. 7), confirming the formation of supramolecular complex between adamantine and *β*-CD, not with phenyl group. Finally, the stability of the inclusion complex was confirmed by ITC (Fig. 9 and Table 1). The morphology of the complexes was confirmed by SEM studies (Fig. 11, Table 2). Glyco-collagen peptide **C-3/G-1** formed bi-fringe needle-like morphologies, which has slightly different topology of the host-guest complexes compared to its native form and similar morphology was observed for **C-3/G-2** complexes.

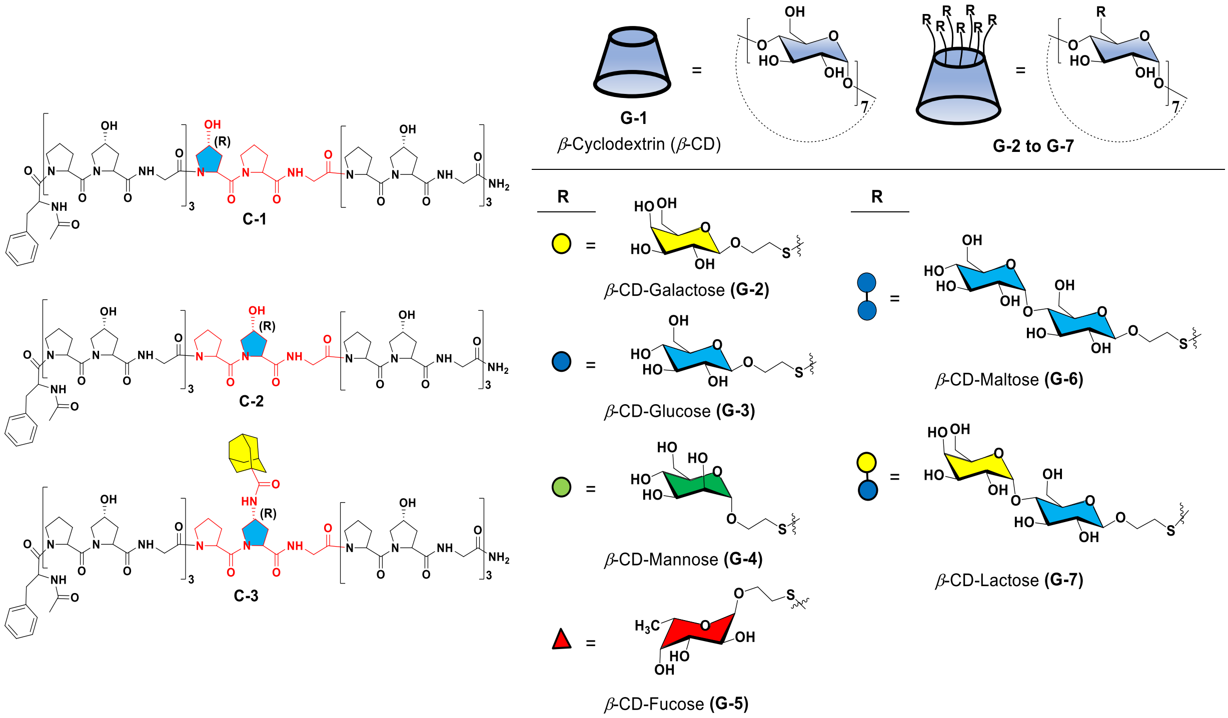

Figure 1. Molecular structures of host-guest complex of collagen related peptides (**C-1** to **C-3**) and of the sugar-capped β-cyclodextrin derivatives (**G-1** to **G-7**).

5.2.2 Identification of glyco-collagen peptides associated with wound healing. The effect of synthetic glyco-collagen conjugates on cell migration was investigated with primary fibroblast cells isolated from murine tissues (ear and tail)[30] and secondary fibroblast cell lines such as NIH-3T3 and BJ cells. Different human cancer cells, including a cervical epithelial cancer (HeLa), breast cancer (MDA-MB-231) and endothelial cells (hUVEC) were also used to investigate the cell migration. The choice of specific cell lines are based on the fact that fibroblasts and endothelial cells are directly involved in wound healing process[31] and cells isolated from primary murine tissues are often mimic *in vivo* responses. Identifying the specific glyco-collagen molecules responsible for cell-motility of cancer cells has implications in basic and translational research to target invasion and metastatic process.[32]

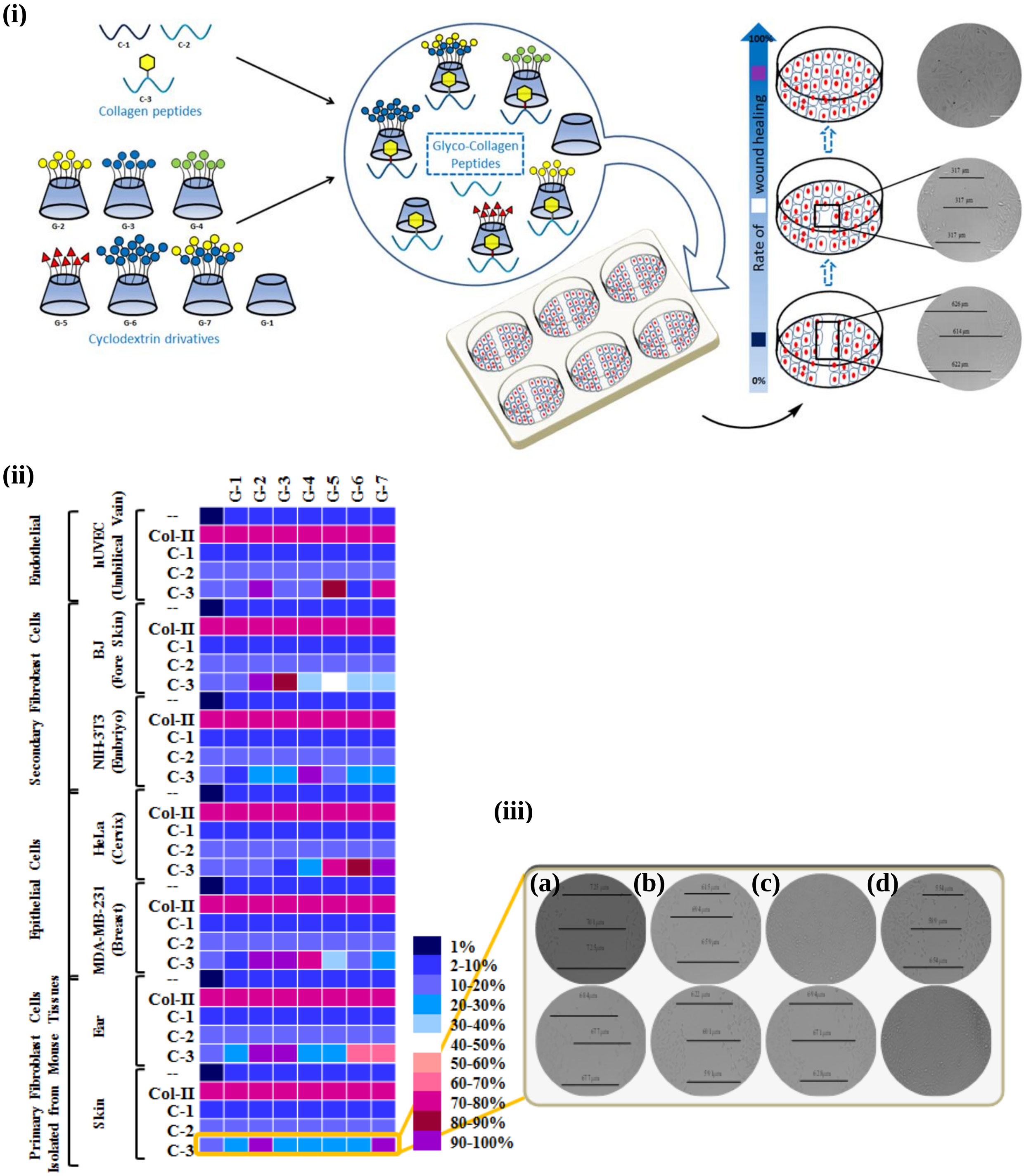

Figure 2. (i) Schematic representation of synthesis of library of collagen related peptides by host-guest method and its effect in cell migration **(ii)** Hierarchical clustering analysis (HCA) of cell migration assay with different collagen modified glycopeptides (CMG) combinations after 6 h (HeLa, MDA-MB-231), 10 h for (BJ, hUVEC, NIH-3T3), and 10 h for (skin, ear cells extracted from mouse) **(iii)** Bright field images of progressing wound healing of skin cell lines after 10 h; (a) **C-3**; (b) **C-3/G-1**; (c) **C-3/G-2**; (d) **C-3/G-3**; (e) **C-3/G-4**; (f) **C-3/G-5**; (g) **C-3/G-6**; (h) **C-3/G-7**.

Cell migration assays were carried out using standard literature protocols.[33] The phenotypic cells were seeded in 24-well plates, allowed to form monolayer by maintaining at 37°C in a CO_2 incubator (Fig. 2i). The monolayer was scratched with 1000 µl sterile tips, in each well to generate wounds followed by seven different combination of GCCs (200 µM) were added and assayed. The commercially available Collagen-II (200 µM), sugars alone (**G-1** to **G-7**) and CPs alone (**C-1** to **C-3**) were used as controls and the bright field images were recorded every one hour until any of the specific combinations of GCCs resulted in 100% wound healing with respect to untreated cells. It is hypothesized that the disparity in cell surface sugar receptors on different cells and the morphology of the GCC may influence the rate of wound healing process. The hierarchical clustering results were used to trace particular combinations of GCCs that are responsible for specific cell type wound healing and to elucidate the mechanism(s) of these processes (Fig. 2ii). For consistency, results were obtained by conducting duplicates and performed three independent times.

The hierarchical clustering analysis (HCA) responses of HeLa cell migration produced several distinct clusters. Although many combinations of the sugar-peptide complexes revealed increased cell migration during the wound healing process than the individual components, particularly the **C-3** GCC induced stronger wound healing responses compared to that of the **C-1, C-2** GCCs. Among the sugars, lactose conjugated peptide (**C-3/G-7)** showed 90-100% wound healing after 6 h compared to maltose (**C-3/G-6**) (80-90%) and fucose (**C-3/G-5**) (70-80%) during the same period. HeLa cells have been shown to express several sugar receptors and among them, lactose receptors are considered as 'Trojan horse' (Fig. 2ii, and Fig. 13iv).[34]

In order to explore cell migration of different origins (human and mouse), comparative studies of wound healing behavior of the two-fibroblast cell lines i.e., NIH-3T3 and BJ (Fig. 2ii, and Fig. 13ii-iii) were done. Both cell lines exhibited different sugar based hierarchical clusters, indicating differences in their cell surface sugar receptors. It has been shown that fibroblasts in general express growth factors, which selectively bind to heparin and glucosamine sugar moieties,[35] while NIH-3T3 cells do not contain galactose specific asialoglycoprotein receptors.[36] Thus, even though both cells are of the same phenotype, they may differ in wound healing profiles. With regard to the NIH-3T3 cell line, the combination of **C-3/G-4** exhibited 90-100% wound healing in comparison to other GCCs. In contrast **C-3/G-3** and **C-3/G-2** were effective in wound healing of BJ cells after 10 h (Fig. 13ii). The breast cancer cell lines MDA-MB-231 exhibited superior wound healing after 6 h when galactose (**C-3/G-2**), glucose (**C-3/G-3**) GCCs were administered (Fig. 13v).[37] Based on these results we can hypothesize that specific carbohydrate receptors and collagen recognizing cell-adhesive molecules demonstrate strong cell migration compared to native collagen peptides.

The experiments with the primary cell lines isolated from the different organs of murine (ear and skin) once again demonstrated that **C-3** complex with *β*-cyclodextrins modified with galactose (**G-2**) exhibited 90-100% wound healing in both primary cell lines (Fig. 2ii-iii and Fig. 13vi-vii). While, glucose (**G-3**) and lactose (**G-7**) displayed variable cell migration. The endothelial hUVEC cells also displayed 90-100% wound healing with the complexes of galactose (**C-3**/**G-2**). Complexes with fucose (**C-3**/**G-5**) and lactose (**C-3**/**G-7**) exhibited 70-80% wound healing (Fig. 13i).[38] Significantly, all these values are superior to control collagen-II, suggesting that the specific sugar-peptide combinations fine-tune the microenvironment essential for the cell migration as compared to the full-length collagen peptide.

To examine the mechanism of wound healing, fluorescent imaging experiments were performed with FITC conjugated **C-3** peptide (**C-3-F**) (Scheme 2) possessing four distinct combinations of sugars (**G-1**, **G-2, G-5** and **G-7**). The data from confocal images with two secondary cell lines (HeLa and BJ) and primary cell line isolated from skin expressing different rates of migration with **C-3-F** GCCs were generated (Fig. 3i). After incubation of **C-3-F** and GCC combination for 6 hours, fluorescence was observed on the cell surfaces and inside the cells. Among them, **C-3-F** and **C-3-F/G-1** did not bind to all the three cell lines, while BJ cells express **C-3-F/G-2, C-3-F/G-7** glycopeptides on their cell surface in a much pronounced manner compared to that of other glycopeptides. These findings suggest that **C-3-F** GCC derivatives might bind to the cell adhesive molecules through specific sugar-peptide combination. Thus the sugar and collagen sequence of glycopeptides seem to be crucial factors for cell specific interactions and uptake. We hypothesize that the glyco-peptides bind to cell surface receptors such as integrins to regulate cell migration processes while, weak fluorescence intensity indicates less impact of GCCs on cell migration. Similar trend was also observed in the skin primary cell line and HeLa cells. To support this hypothesis, the level of integrins on the cell surfaces were examined in the presence of specific GCC combinations.

5.2.3 Exploring of Integrin binding. Integrins are major class of cell adhesion molecules mediating cell-cell and cell-extracellular matrix interactions.[39] During wound healing process, collagen-integrin interactions mediate reorganization of matrix through collagen construction. X-ray crystal structure analysis has shown that triple helical structure of collagen and presence of 4-hydroxyproline is essential for the binding of integrins.[40-42] Integrins (α1β1) are collagen receptors, involved in cell migration and metastatic processes found in fibroblast, endothelial and epithelial cells.[43] All collagens are expected to bind specific integrin receptors and up-regulate the expression levels, causing the production of matrix metalloproteinases (MMPs). Using multiple antibodies for FACS analysis, we distinguished the level of integrin expression in the presence of specific glyco-CPs in primary (ear) and secondary fibroblast cells (BJ cells) (Fig. 3ii and Table 7). In case of BJ cells, the **C-3/G-1 and C-3/G-5** complexes had a small effect on integrin expression (7 % and 11 %) in BJ cells whereas, **C-3/G-2** expressed high levels (70.5%) of integrin compared to **C-3/G-7** combination (43.3%). In contrast, **C-3/G-2** expressed 7 % of integrins in HeLa and 81 % in primary skin fibroblast cells, demonstrating that the cell surface binding of glyco-CPs results in up regulation of integrins, which may influence MMPs production and promote wound healing process.

To examine the mechanism by which integrin induces cell migrations, the ERK/FAK pathways known to induce integrin-mediated cell migration during cell migration were examined in BJ and skin fibroblast cells.[44] Elevated expression levels of these proteins are considered as a general marker of cell migration. To test, if the GCCs inducing integrin elevate the ERK and FAK, protein extracts of glycol-CPs (**C-3/G-2** and **C-3/G-7**) treated cells at 6 h were analyzed for the expression level of of ERK and FAK. Western blot analysis of FAK and ERK showed that BJ cell treated with **C-3/G-2** expresed high level of ERK and FAK compared to **C-3/G-7**. In contrast, skin fibroblast cells express strong ERK and FAK in presence of both **C-3/G-2** and **C-3/G-7** conjugates (Fig. 3iii). Overall, these results suggest that the cell adhesion molecules (integrins) and sugar receptors synergistically work together to influence cell migration.

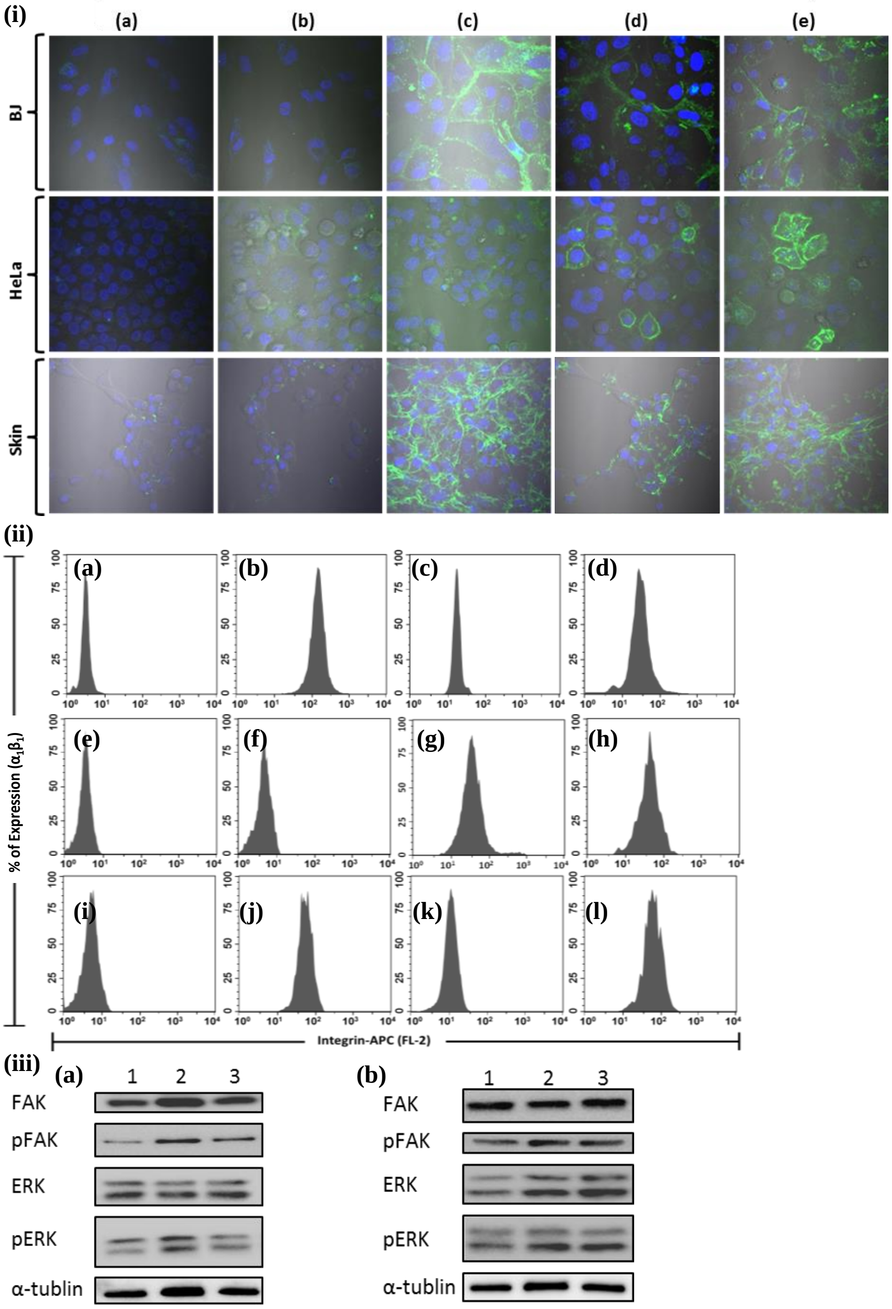

Figure 3. **(i)** Fluorescence images of different cells incubated BJ for 10 h, Hela for 6 h, and skin for 10 h with (a) **C-3-F**; (b) **C-3-F/G-1**; (c) **C-3-F/G-2**, (d) **C-3-F/G-5** and (f) **C-3-F/G-7** respectively **(ii)** Flow cytometry of integrin $(\alpha_1\beta_1)$ expression in BJ cell line after treated with (a) **C-3/G-1**, (b) **C-3/G-2**, (c) **C-3/G-5** and (d) **C-3/G-7;** integrin expression in HeLa celline after treated with (e) **C-3/G-1**, (f) **C-3/G-2**, (g) **C-3/G-5** and (h) **C-3/G-7;** integrin expression in skin cell line (i) **C-3/G-1**, (j) **C-3/G-2**, (k) **C-3/G-5** and (l) **C-3/G-7** **(iii)** The expressions of FAK, pFAK, ERK, pERK, α-tublin in (a) BJ cell lines and (b) skin cell lines(35 μg whole-cell lysate of proteins) with (1) control; (2) **C-3/G-2** and (3) **C-3/G-7** were analysed by western blotting. Protein loading was assessed by probing the blots with anti- α-tublin.

Based on the in vitro screening experiments, we investigated the wound healing effect of **C-3/G-7** in wild-type mice model.[45] Determination of wound healing rate and histology of the wound is a useful method for studying the real time application of these GCC.[46] Hence, 5 mm excisional wound was created on the dorsal surface of the mice and **C-3/G-7** and collagen-II was applied on top of the wound and the decrease in the wound area was monitored for next 15 days (Fig. 4ii). As shown in the figure 4i, ii, the wound area of **C-3/G-7** treated mice was significantly reduced compared to that of collagen-II treated and control mice at postwounding days 3, 5, 8 respectively. Complete wound closure was observed in **C-3/G-7** on day ~11 whereas natural collagen and control showed similar wound healing on day ~12, ~14 (Fig. 4i, and Fig. 14). To further confirm the progress of the wound healing, histomorphometric analysis was performed at the wound biopsies on day 8 of postwounding. Histology images of mouse shows that substantial growth of epidermis layer was observed in **C-3/G-7** treated mouse compared with control and natural collagen treated mouse, suggesting the faster wound healing rate with **C-3/G-7** peptide (Fig. 4iii). Overall, our study shows that the developments of supramolecular strategy represents an important step forward in identify specific biomarker for physiological and pathological processes.

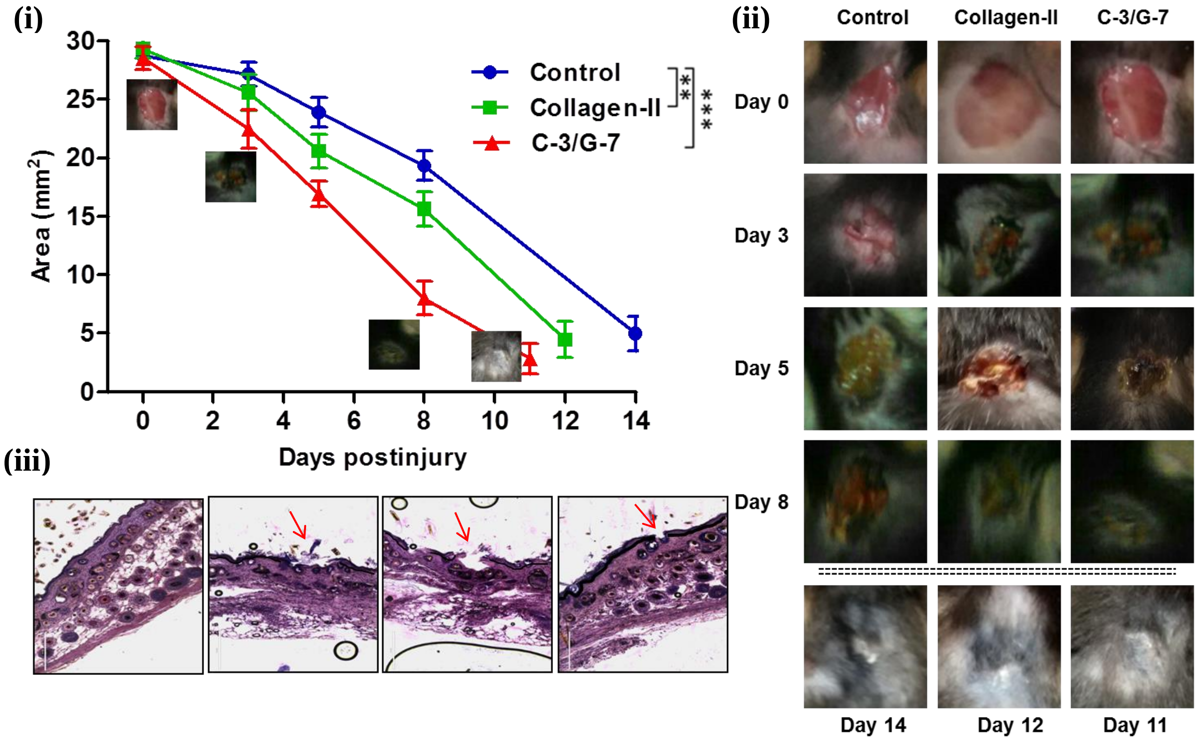

Figure 4. **(i)** Box and whisker plot map for the change in total wound size with respect to time from day 0 to day 14 in mice **(ii)** Respective pictures of wound taken from mice by treatment of collagen II (Col-II) and **C-3/G-7** at different days **(iii)** Histological analysis of wounds after treatment with (a) Normal (without wound); (b) Control; (c) collagen II; (d) **C-3/G-7** after 8 days (arrow indicates the

wound healing process, scale bar = 200 μm, n = 6, Data shown as mean ± SD, Two way ANOVA post test for significance *p<0.05, **p<0.01, ***p<0.01).

5.3 Conclusion

A new approach based on host-guest interaction to prepare glyco-peptides has been developed to understand high-throughput responses of cell migration for different cell lines. Validated through a series of biophysical and imaging techniques, it is shown that the cell adhesion molecules (integrin) and sugar receptors synergistically work together to influence cell migration. The simplicity and effectiveness of the system underscore its potential in accelerating glycopeptide research and greatly facilitates the development of new therapeutic approaches. Expanding the scope of this platform and the synthesis of new libraries is envisioned to open up a new direction in exploring and understanding the role of sugar-peptide combinations in various physiological and pathological processes for which no data are still available.

5.4 Experimental section

5.4.1 General information: All chemicals were reagent grade and used as supplied except where noted. Analytical thin layer chromatography (TLC) was performed on Merck silica gel 60 F254 plates (0.25 mmol). Compounds were visualized by UV irradiation or dipping the plate in CAM/ninhydrin solution followed by heating. Column chromatography was carried out using force flow of the indicated solvent on Fluka Kieselgel 60 (230–400 mesh). ^{1}H and ^{13}C NMR spectra were recorded on Jeol 400 MHz, Bruker 600 MHz with cryo probe using residual solvents signals as an internal reference ($CDCl_3$ δH, 7.26 ppm, δC 77.3 ppm and CD_3OD δH 3.31 ppm, δC 49.0 ppm). The chemical shifts (δ) are reported in ppm and coupling constants (J) in Hz. UV-visible measurements were performed with Evolution 300 UV-visible spectrophotometer (Thermo Fisher Scientific, USA). Analytical HPLC was performed using a LiChrospher 100 RP-18e 5 μm (250 mm x 4 mm) column from Merck. Preparative HPLC was carried out on a LiChrospher RP-18e 5 μm (250 mm x 10 mm) column from Merck. Circular Dichroism measurements were performed with J-815 CD spectro-polarimeter (Jasco, Japan). Each CD profile is an average of five independent scans of the same sample collected at a scan speed of 30 nm min^{-1}. Fluorescence spectra were recorded in FluoroMax-4 spectrofluorimeter (Horiba Scientific, U.S.A.), 8 well microscopic plates were subjected to fluroscence imaging using CLSM (Zeiss LSM 710).

5.4.2 Synthesis of 4(R)-amino-adamantylproline derivatives

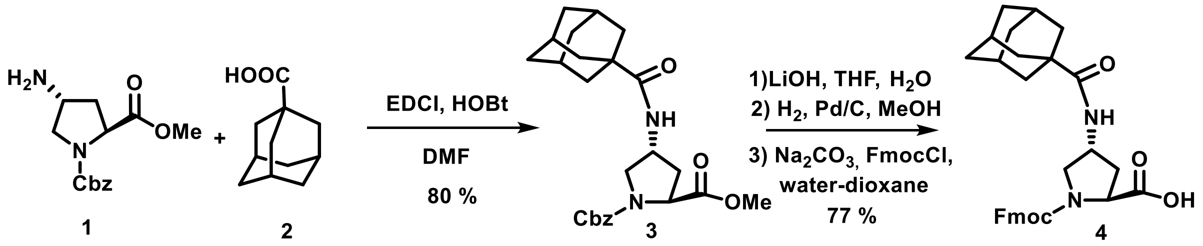

Scheme 1. Synthesis of 4(R)-amnio-adamantylproline derivatives.

(2*S*, 4*R*)-N^1-(benzyloxycarbonyl)-4-(Amino-adamantyl) proline methyl ester (3): Adamantane carboxylic acid **2** (3.25 g, 18.0 mmol), HOBt (2.4 g, 17.6 mmol) and EDCI (5.0 g, 26 mmol) were stirred in anhydrous DMF at ice cold condition for 15 min. To this solution (2*S*, 4*R*)-N^1-(benzyloxycarbonyl)-4-amino proline methyl ester **1** (5.0 g, 17.9 mmol), dissolved in anhydrous DMF was slowly added. The corresponding reaction mixture was allowed to stir for 12 h. After completion of reaction (monitored by TLC) water (100 mL) was added and the aqueous layer was extracted with ethyl acetate (3 x 80 mL) followed by brine wash. The organic layer was dried over anhydrous Na_2SO_4 and concentrated under vacuum. The crude product obtained was purified by silica gel chromatography (50 % ethyl acetate/petroleum ether) to afford compound **3** as a thick liquid. Yield: 6.4 g, (80 %). ^{1}H NMR ($CDCl_3$, 400 MHz) δ_H: 7.29-7.36 (m, 5H), 5.63 (dd, *J* = 19.9, 8 Hz, 1H), 5.03-5.22 (m, 2H), 4.54 (quint, *J* = 6.1 Hz, 1H), 4.34-4.46 (m, 1H), 3.89 (td, *J* = 10.3, 6.6 Hz, 1H), 3.57 3.75 (d, 3H), 3.36 (ddd, *J* = 36.8, 11.1, 4.7 Hz, 1H), 2.30 (dt, *J* = 11.6, 5.8 Hz, 1H), 2.11–2.23 (m, 1H), 2.04 (d, 3H), 1.80 (d, 6H), 1.71 (q, 6H). ^{13}C NMR (100 MHz, $CDCl_3$) δ_C: 178.1, 172.5, 172.3, 154.9, 154.2, 136.3, 136.2, 128.5, 128.3, 128.2, 128.1, 128.0, 67.4, 57.9, 57.7, 52.6, 52.4, 52.1, 51.9, 48.3, 47.6, 40.6, 39.2, 37.0, 36.4, 35.8, 28.0. ESI-HRMS: for $C_{25}H_{32}N_2O_5$, $[M + H]^+$ calc'd 441.2389, found 441.2397.

(2*S*, 4*R*)-N^1-(fluorenylmethyloxycarbonyl)-4-(Amino-adamantyl) proline (4): The methyl ester **3**, (5.20 g, 11.8 mmol) was subjected to hydrolysis by using LiOH (3 eq. in THF:H_2O, 1:1, 15 mL) for 1 h. THF was removed under vacuum and the aqueous layer was washed with ethyl acetate (3 x 50 mL) to remove THF and unreacted organic compound. The aqueous layer was neutralized with $KHSO_4$ and extracted with ethyl acetate (3 x 50 mL). The combine organic layer was concentrated to offered white solid, to which dry methanol (15 mL) and 10 % Pd/C (0.5 g) was added. The reaction mixture was subjected to hydrogenation for 6 h. After completion of reaction (monitored by TLC) the mixture was filtered through Whatman filter paper and the filtrate was concentrated under reduced pressure. The product obtained as a white solid powder was dissolved in water : dioxane, 1:1 (60 mL). The pH of reaction mixture was maintained at 10 by addition of 10% Na_2CO_3. The reaction mixture was stirred at 0^oC for 15 minutes to which Fmoc-Cl (5.326 g, 20 mmol) was added in portion wise during 45 minutes. The temperature of reaction was maintained at 0^oC for first 4 h and then allowed to come at room temperature and stirred for 18 h. After completion of reaction dioxane was removed under vacuum and the aqueous layer was washed with ethyl acetate (3 x 80 mL). The aqueous layer was acidified with $KHSO_4$ to pH 2 followed by extraction with ethyl acetate (3 x 70 mL). Concentration of organic layer gave crude product which was purified by silica gel chromatography (70% ethyl acetate/petroleum ether) to afford compound **4** as white solid. Yield: 5.1 g, (77 %). ^{1}H NMR (CD_3OD, 400 MHz) δ_H: 7.73 (t, 2H), 7.55–7.62 (m, 2H), 7.33 (dd, J = 12.1, 7.3 Hz, 2H), 7.26 (t, 2H), 4.27-4.47 (m, 3H), 4.14–4.23 (m, 2H), 3.78 (td, J = 7.1, 3.5 Hz, 1H), 3.28–3.33 (m, 1H), 2.23 (dt, J = 6.3 Hz, 2H), 1.95 (d, 3H), 1.81 (s, 6H), 1.67-1.75 (m, 6H).^{13}C NMR (100 MHz, CD_3OD) δ_C: 179.7, 155.3, 155.2, 144.0, 143.9, 143.8, 143.7,141.3, 141.2, 141.1, 127.5, 126.9, 126.8, 125.1, 125.0, 124.7, 119.6, 119.5, 67.8, 67.5, 59.4, 51.1, 50.9, 40.4, 38.7, 36.2, 35.8, 34.7, 28.2. ESI-HRMS: for $C_{31}H_{34}N_2O_5$, $[M + H]^+$ calc'd 515.2546, found 515.2540.

5.4.3 General procedure for synthesis of collagen model peptides: The readily available Rink amide resin with loading value 0.5-0.6 mmol/g was used and standard Fmoc chemistry was employed. The resin bound Fmoc group was first deprotected with 20% piperidine in DMF and the coupling reactions were carried out using *in situ* active ester method, using HBTU as a coupling reagent and HOBt as a recemization suppresser and DIPEA as a catalyst. All the materials used were of peptide synthesis grade (Sigma-Aldrich) and was used without further purification. Analytical grade DMF was purchased from Merck (India) and was distilled over P_2O_5 under vacuum at 45^oC, stored over 4Å molecular sieves for 2 days before using for peptide synthesis.

(a) Synthesis protocol for solid phase synthesis: The resin was pre-swollen overnight and the following steps were performed for each cycle.

- Wash with DMF 4 x 5 mL.
- 20 % piperidine in DMF 2 x 5 mL (15 min for each) for deprotection of Fmoc group.
- Wash with DMF 3 x 5 mL, MeOH 3 x 5 mL and DCM with 3 x 5 mL.
- Test for complete deprotection(chloranil test).[i]
- Coupling reaction with amino acid, DIPEA, HOBt and HBTU (3 eq.) in DMF (1 mL).

- Repeat of the coupling reaction in N-Methyl pyrrolidinone (NMP) for better yield.
- Test for completion of coupling reaction (chloranil test).

This cycle was repeated for every amino acid.

(b) General procedure for Fmoc deprotection: 20% piperidine in DMF was added to the resin and the reaction mixture was kept for 15 min, drained and the piperidine treatment was repeated 3 times. Finally the resin was washed with DMF (3x), MeOH (3x) and DCM (3x).

(c) General procedure for peptide couplings on Rink Amide Resin: Fmoc-Xxx-OH (3 eq), HBTU (3 eq) and HOBT (3 eq) dissolved in DMF/NMP followed by $i\mathrm{Pr}_2\mathrm{NEt}$ (7-8 eq) were added to the amino-functionalized resin in DMF. The mixture was kept for 2 h and last 5 min bubbled with N_2 and washed with DMF (3x), MeOH (3x) and DCM (3x). The loading value for peptide synthesis is taken as 0.5~0.6. The coupling reaction was repeated in NMP for better yield.

(d) General procedure for acetylation: Triethylamine (20 eq) and acetic anhydride (20 eq) were added to the resin in DMF (≈ 100 mM). The mixture was kept for 1 h followed by bubbled with N_2 for 5 min and washed with DMF (3x), MeOH (3x) and DCM (3x).

(e) General procedure for cleavage of peptides from the solid support: The dry peptide-resin (20 mg) was taken in round-bottomed flask to which of 20% TFA in DCM (10 mL) and Triisopropylsilane (as scavengers) (2-3 drops) were added. The resulting mixture was kept for 2 h by gentle shaking. The mixture was filtered through a sintered funnel and the resin was washed with 3 x 5 mL of above solution. The filtrate was collected in pear shape round-bottom flak and evaporated under reduced pressure. The resin was washed with MeOH (3 X 5 mL) and the washings were evaporated to dryness. The residue obtained was dissolved in anhydrous methanol (0.1 mL) and to it anhydrous diethyl ether (4 x 1.5 mL) was added. The off-white precipitate obtained was centrifuged. The precipitation procedure was repeated twice to obtained peptide as a colourless powder.

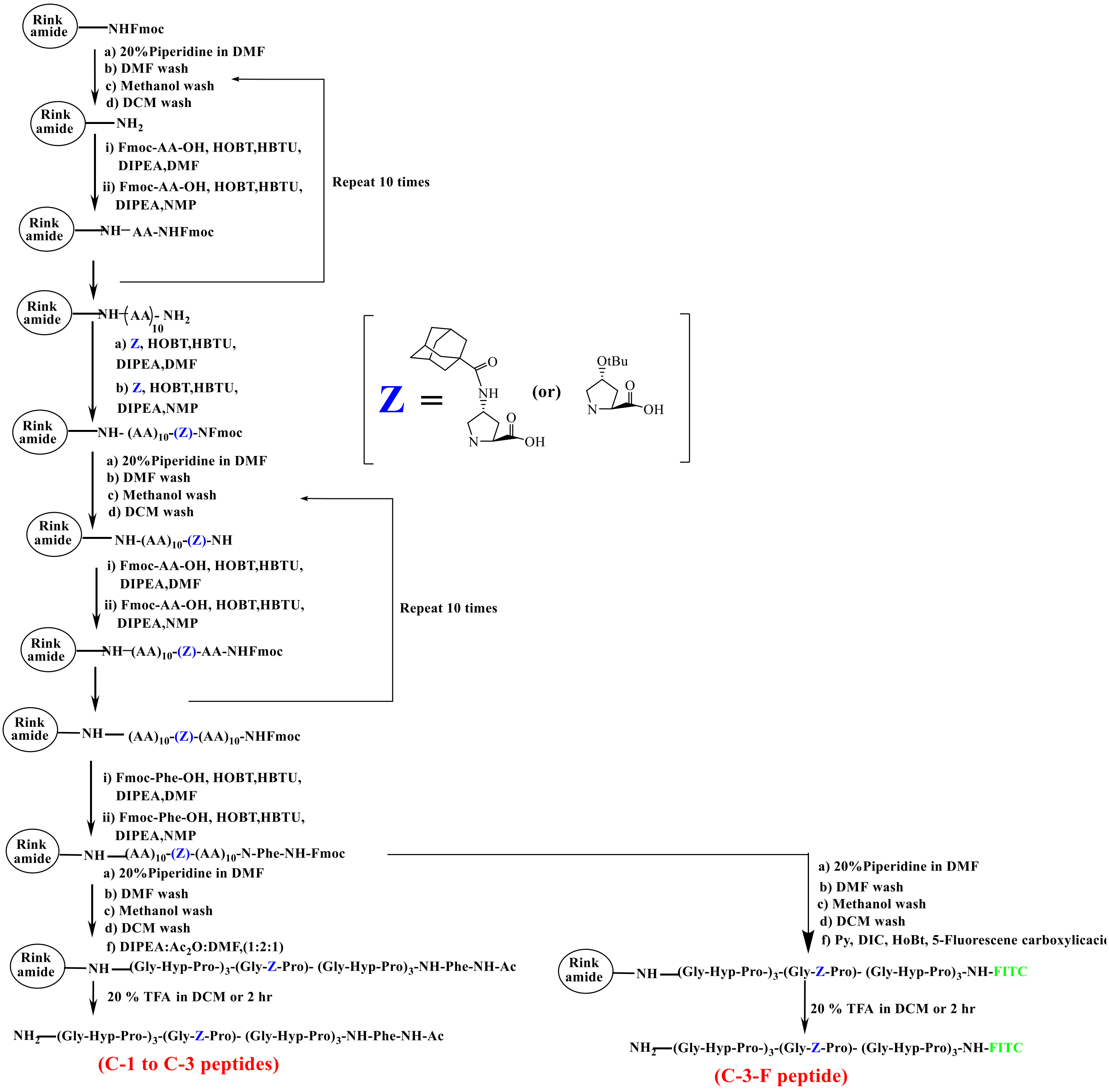

Scheme 2. Synthesis of **C-1** to **C-3** and **C-3-F** peptides.

5.4.4 Synthesis of *β*-cyclodextrin derivatives: Galactose, mannose, fucose, maltose, and lactose β-cyclodextrin derivatives (**G-2, G-4, G-5, G-6** and **G-7**) were synthesized according to published procedures.[8,27-28]

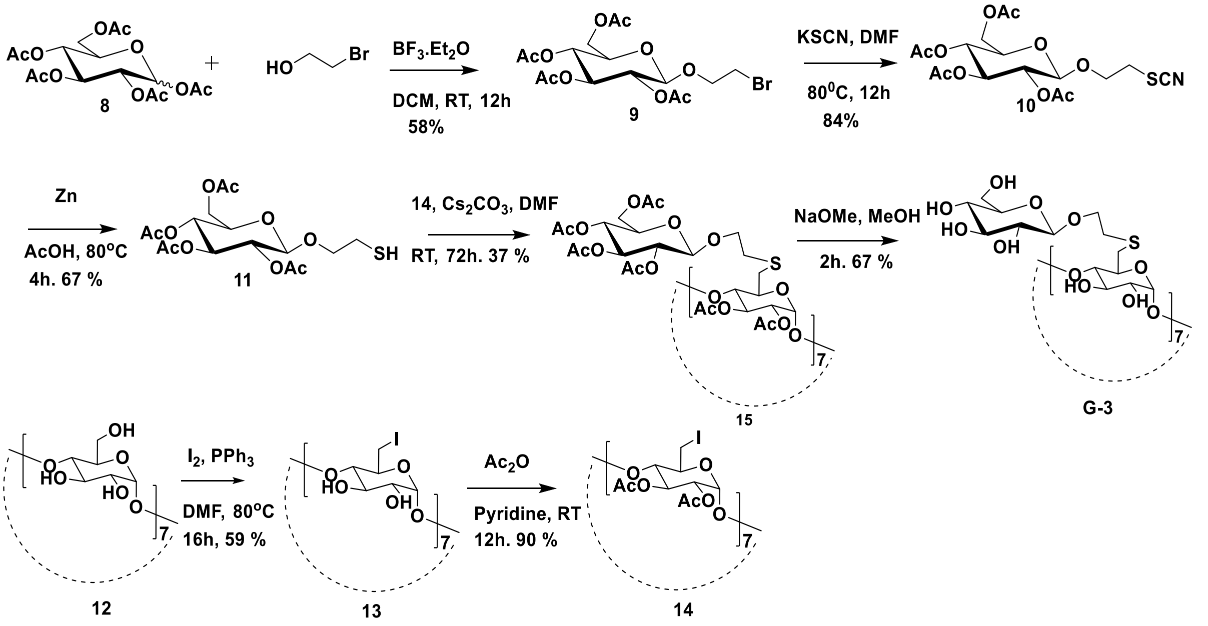

Scheme 3. Synthesis of glucose-*β*-cyclodextrin (**G-3**).

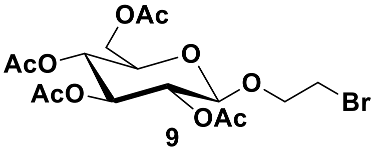

9

Per-acetylated sugar **8** (0.7 g, 1.79 mmole) was dissolved in DCM (10 mL). Then $BF_3.Et_2O$ (0.62 ml, 7.17mmol) and bromoethanol (0.50 ml, 7.17mmol) were added at 0 °C for 30 min and the reaction mixture was allowed to stir at room temperature for 12 h. Completion of reaction was monitored by TLC. After completion, the reaction mixture was neutralized with triethylamine, followed by extraction with DCM and water (1:1) mixture. Organic layer was dried over anhydrous Na_2SO_4 and concentrated under reduced pressure to give crude product, which was further purified on silica gel column chromatography using EtOAc/Pet-ether to get pure bromoethanol sugar derivative **9**. ^1H NMR (400 MHz, $CDCl_3$): δ 5.19 (t, J = 9.62, 1H), 5.08-4.97 (m, 2H), 4.56 (d, J = 7.78, 1H), 4.24-4.21 (m, 1H), 4.15-4.10 (m, 2H), 3.82-3.76 (m, 1H), 3.71-3.66 (m, 1H), 3.45-3.42 (m, 2H), 2.07 (s, 3H), 2.05 (s, 3H), 2.00 (s, 3H), 1.99 (s, 3H). ^{13}C NMR (100 MHz, $CDCl_3$): δ 170.70, 170.31, 169.46, 101.07, 72.65, 71.98, 71.08, 69.85, 68.37, 61.90, 29.98, 29.94, 20.80, 20.67. ESI-HRMS: for $C_{16}H_{23}BrO_{10}$, [M + Na]$^+$ calc'd 477.0372, found: 477.0369.

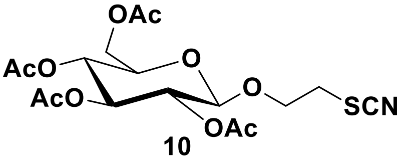

10

Compound **9** (0.2 g, 0.44 mmol) was dissolved in DMF (10 mL). Then potassium thiocyanate (0.17 g, 1.76 mmol) was added and stirred at 80 °C for 12 hr. The reaction mixture was diluted with 100 ml ethyl acetate and washed several times with water. The organic layer was dried over anhydrous Na_2SO_4 and concentrated under reduced pressure to give crude product, which was further purified by flash column using petroleum ether: ethylacetate (75:25). ^{1}H NMR (400 MHz, $CDCl_3$): δ 5.19 (t, *J* = 9.62, 1H), 5.08-4.97 (m, 2H), 4.58 (d, *J* = 7.78, 1H), 4.25-4.12 (m, 3H), 3.85-3.79 (m, 1H), 3.72-3.68 (m, 1H), 3.20-3.05 (m, 2H), 2.07 (s, 3H), 2.04 (s, 3H), 2.01 (s, 3H), 1.98 (s, 3H). ^{13}C NMR (100 MHz, $CDCl_3$): δ 170.70, 170.27, 169.47, 169.45, 111.69, 100.93, 72.61, 72.11, 71.00, 68.25, 67.36, 61.80, 33.66, 29.74, 20.80, 20.76, 20.65. ESI-HRMS: for $C_{17}H_{23}O_{10}S$, [M+Na]$^+$ calc'd 456.0940, found: 456.0944.

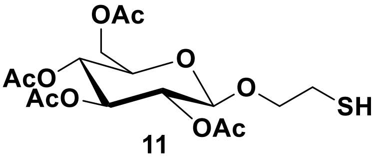

11

Compound **11** (0.23 g, 0.53 mmol) was dissolved in glacial acetic acid (30 mL). Then Zn dust (0.20 g, 3. 18 mmol) was added and refluxed at 80 °C for 4 h. The compound was filtered to remove zinc dust. The organic layer was quenched with water (50 mL). Then product was extracted with DCM (3 X 50 mL) and dried over anhydrous Na_2SO_4. Organic layer was concentrated under reduced pressure to give product, which was further used for next reaction without purification. ^{1}H NMR (400 MHz, $CDCl_3$): δ5.26-5.21 (m, 1H), 5.13-4.99 (m, 2H), 4.58 (d, *J* = 7.83, 1H), 4.30-4.27 (m, 1H), 4.18-4.10 (m, 2H), 4.05-4.01 (m, 2H), 3.74-3.72 (m, 1H), 3.66-3.62 (m, 1H), 2.77-2.67 (m, 1H), 2.12 (s, 3H), 2.08 (s, 3H), 2.05 (s, 3H), 2.03 (s, 3H); ^{13}C NMR (100 MHz, $CDCl_3$): δ 170.67, 170.28, 169.40, 169.39, 100.90, 72.71, 71.89, 71.22, 68.37, 67.90, 61.90, 29.69, 20.75, 20.61. HRMS for $C_{16}H_{24}NaO_{10}S$, [M+Na]$^+$ calc'd 431.0988; found: 431.0984.

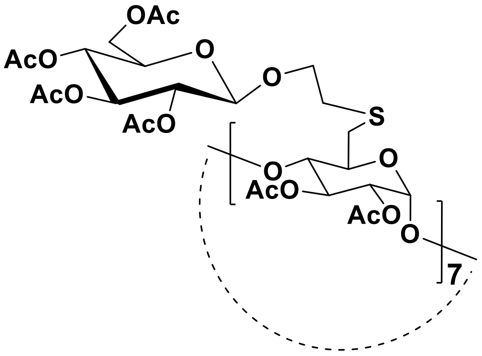

15

Compound **11** (0.21 g, 0.52 mmol) was dissolved in DMF (10 mL) then added per-acetylated 6’-Iodo-β-cyclodextrin **14** (0.1 g, 0.04mmol) and Cs_2CO_3 (0.17 g, 0.52mmol) and reaction mixture stirred at room temperature for 72 h.The reaction mixture was diluted with 100 ml ethyl acetate and washed several times with water. The organic layer was dried over anhydrous Na_2SO_4 and concentrated under reduced pressure to give crude product, which was further purified by flash column using DCM : MeOH (5-7%). ^{1}H NMR (400 MHz, $CDCl_3$): *δ* 5.24-5.17 (m, 7H), 5.11-5.05 (m, 14H), 5.00-4.95 (m, 7H), 4.59-4.44 (m, 14 H), 4.31-4.16 (m, 14H), 4.16-3.98 (m, 28H), 3.79- 3.58 (m, 28H), 2.87-2.78 (m, 14H), 2.15- 1.99 (m, 126H);^{13}C NMR (100 MHz, $CDCl_3$): *δ* 170.86, 170.72, 170.69, 170.61, 170.43, 170.38, 170.22, 170.13, 169.71, 169.59, 169.50, 169.41, 106.28, 100.69, 99.80, 96.56, 71.91, 70.90, 70.45, 69.15, 68.71, 67.06, 62.81, 61.27, 61.15, 61.02, 60.96, 60.41, 53.33, 29.77, 20.92, 20.82, 20.76, 20.69. HRMS for $C_{182}H_{252}O_{112}S_7$, $[M+2Na]^{+2}/2$ calc’d 2249.5932; found: 2249.5967.

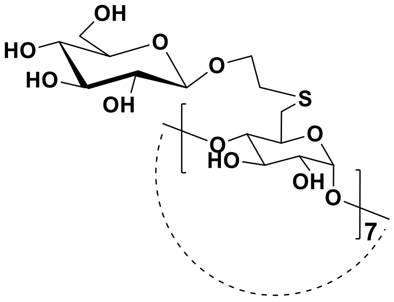

G-3

Compound **15** (0.05 g, 0.01 mmol) was dissolved in methanol (5 mL). Then sodium methoxide (29 mg, 0.55 mmol) was added and stirred for 2 h at RT. The mixture was neutralized with amberlite–IR120H$^+$resins, filtered and concentrated in vacuum afford the final compound. **S-3**. ^{1}H NMR (400 MHz, CD_3OD): *δ* 5.02 (bs, 7H), 4.81 (bs, 7H), 3.88-3.71

(m, 49H), 3.65-3.56 (m, 28H) 3.47-3.43 (m, 7H) 3.26-3.22 (m, 7H), 2.96-2.84 (m, 21H); ^{13}C NMR (100 MHz, CD$_3$OD): δ100.00, 72.93, 72.82, 72.61, 72.02, 71.96, 70.91, 70.85, 70.79, 70.75, 70.29, 70.19, 67.23, 67.18, 66.62, 60.94, 32.53.HRMS m/z calc'd for $C_{98}H_{168}O_{70}S_7$, $[M+2Na]^{+2}/2$ calc'd 1367.3713; found: 1367.3787.

5.4.5. Purification of the peptides using semi-quantitative HPLC: The synhetic peptides **C-1** to C-**3** were purified by HPLC (Waters 600 equipped with 2998-Photodiode array detector, PDA) using a semi-preperative C18 phenomenex column (250 × 10 mm) and the following method: Solvent- 0.1% TFA in MeCN: Water (5:95) (solution A), and 0.1% TFA in MeCN: Water (50:50) (solution B), gradient; 100%A to 50%B in 15 min, then 50%B to 100%A in 30 min, 100%A in 35 min. Flow rate - 3 mL/min monitored at λ = 220 nm. The fractions with the eluted peptide were collected, and concentrated using speed-Vacuum. The purity of the final peptides were further corroboraed by analytic HPLC using Merck LiChrospher 100 RP-18 (250 x 4 mm, 5 μM) column,and eluted with solutions A and B using a flow rate of 1.5 mL/min and gradient from 0 to 100% B in 20 minutes, washed 10 minutes column with B, 100% to A, 0% with the flow rate of 1.5 ml/min.

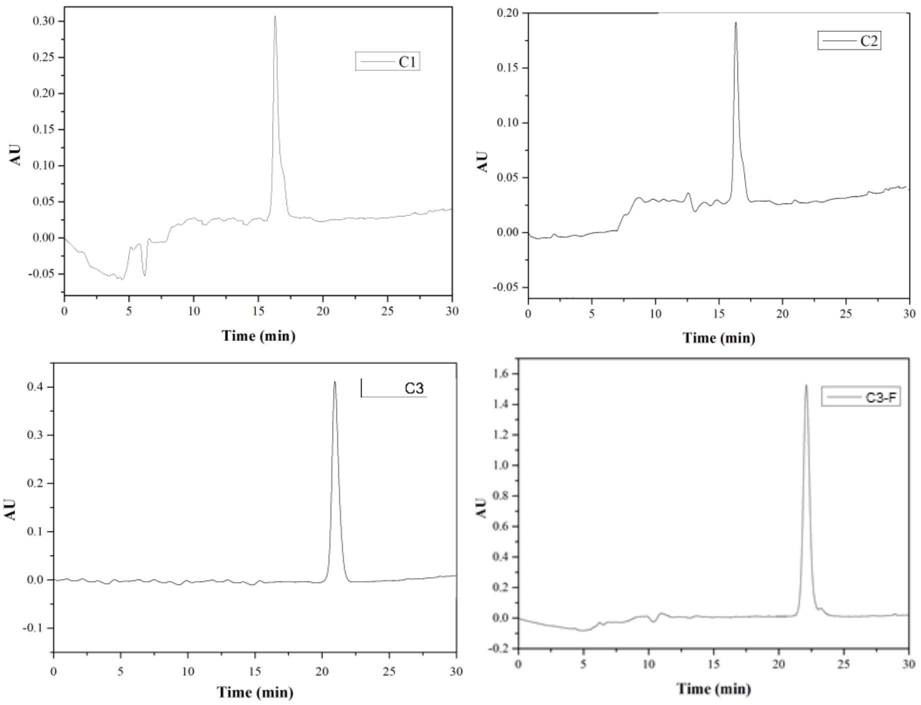

Figure 5. HPLC profiles of collagen peptides. The name of the peptide is written in the right up corner of each chromatogram.

5.4.6. Formation of host-guest complexes between modified *β*-cyclodextrin and the peptides.

Host-guest complexes were prepared by mixing equimolar concentrations of adamantyl modified peptides (**C-1** to **C-3**) with *β*-cyclodextrin (**G-1**) or *β*-cyclodextrin substituted with sugar molecules (**G-2** to **G-7,** Fig 1) followed by vortexing for 2 minutes.

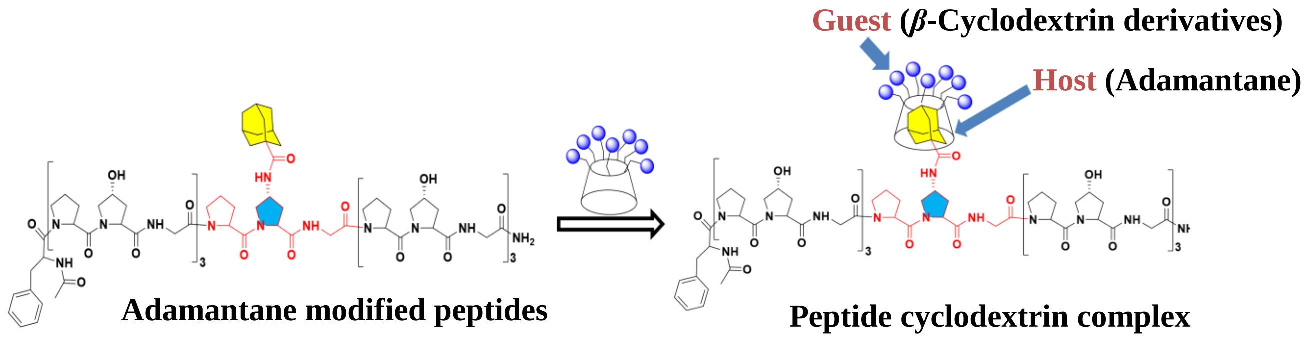

Figure 6. Molecular structures of the peptides and schematic presentation of the *β*-cyclodextrin complexes.

5.4.7. Corroboration of the complex structure by NMR: ^{1}H-NMR NOESY spectra were recorded to probe the intermolecular interactions of adamantyl protons with the *β*-cyclodextrin skeleton. These interactions indicate the incorporation of the adamantyl residue in the cavity as a result of complex formation and the cross peaks indicate which are protons that are in close proximity to the protons of the cyclodextrin host molecule. Peptide **C-3** and **G-1** were used to study host-guest complex formation as guest peptide as a host, respectively. We prepared the complex **C-3 /G-1** using the protocol mentioned above and recorded the NOESY spectrum of the complex and that of the peptide alone (**C-3**). We have focused on the peaks of the adamantyl, labelled **a, b, c** **(**Figure **7).** The cross peaks corresponds the adamantyl peaks in the complex **C-3/G-1** complex which are absent in **C-3.** NMR absorptions confirm the formation of a host-guest complex between **C-3** and **G-1**.

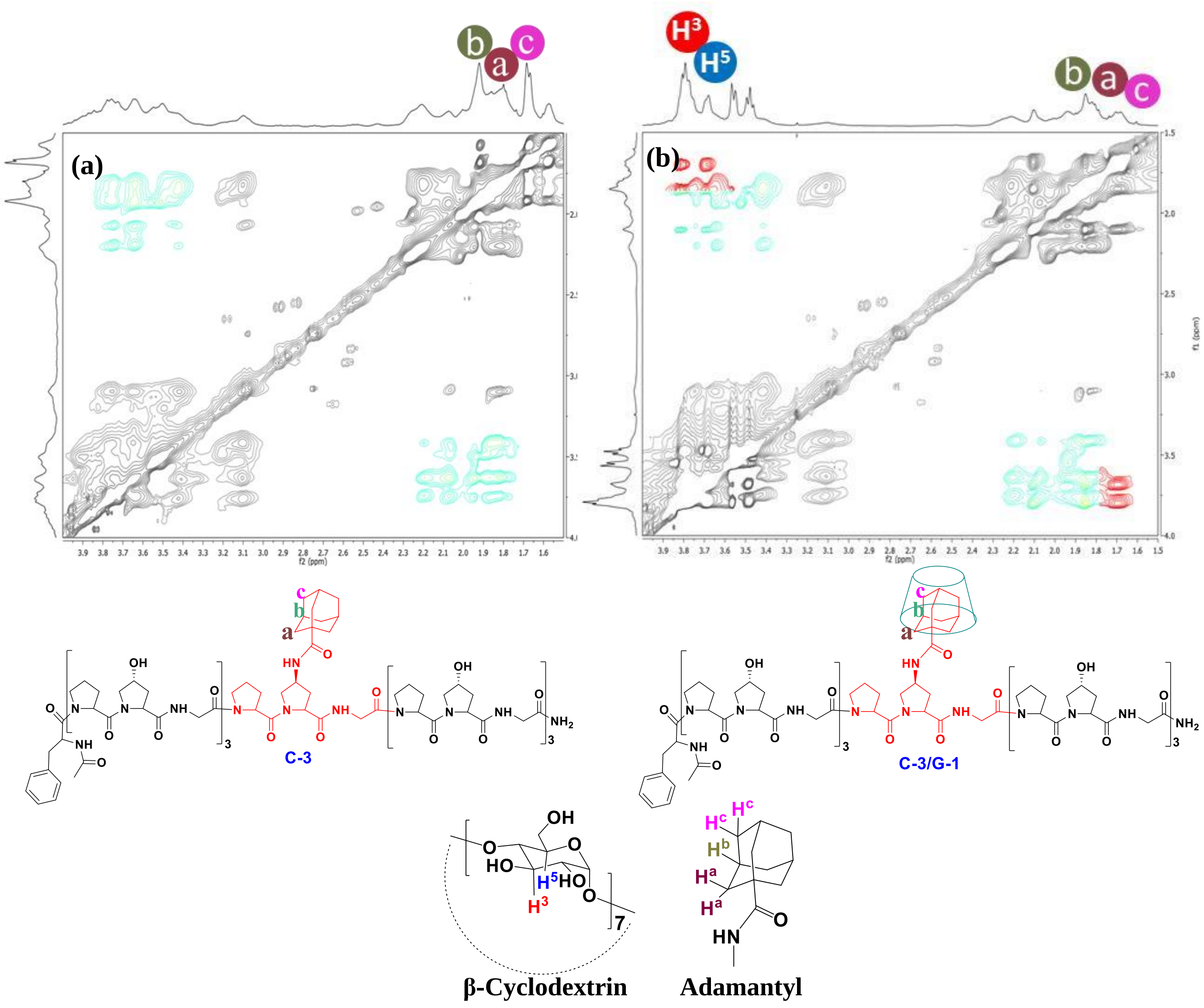

Figure 7. (a) NOE spectra of **C-3**; (b) NOE spectra of **C-3/G-1**.

5.4.8. Corroboration of the complexes structure by Mass spectrometry: The formation of host-guest inclusion complexes were analysed by mass spectrometry and also used to determine their molecular mass and the stoichiometry of the host and guest in the supramolecular assemblies. In order to keep the non-covalent complexes intact during the ionization process a native nano-ESI technique was employed. In Figure 8 the full scan of the **C-3/G-1** sample is depicted. The positive ion mass spectrum of the fully assembled complex clearly indicates the presence of a tetra charged ion $[C\text{-}3/G\text{-}1+2K+2H]^{4+}$ with m/z = 862. The peaks m/z = 768, 1135, corresponding to $[C\text{-}3 +3Na]^{3+}$ and $[G\text{-}1]^{1+}$ions were also detected. These peaks indicated partial dissociation of the complex **C-3/G-1**. Similarly, the peak with m/z = 1242 corresponds to [C-3/G-2+K+3H]$^{4+}$, the peak at m/z = 1525 correspond to [C-3/G-7+ K+ 3H]$^{4+}$, the peak m/z = 1213 correspond to [C-3/G-5+K+ 3H]$^{4+}$ respectively.

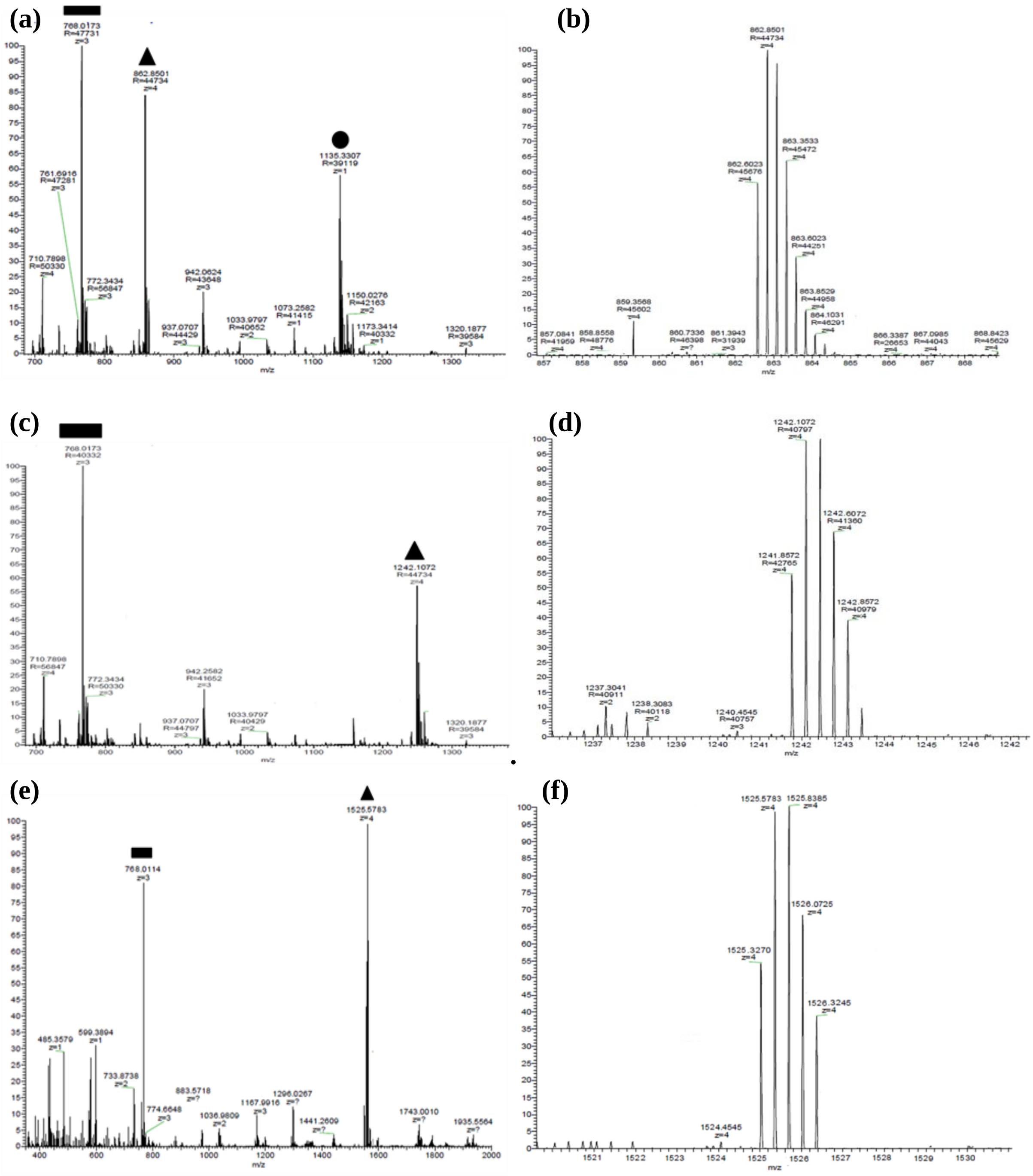

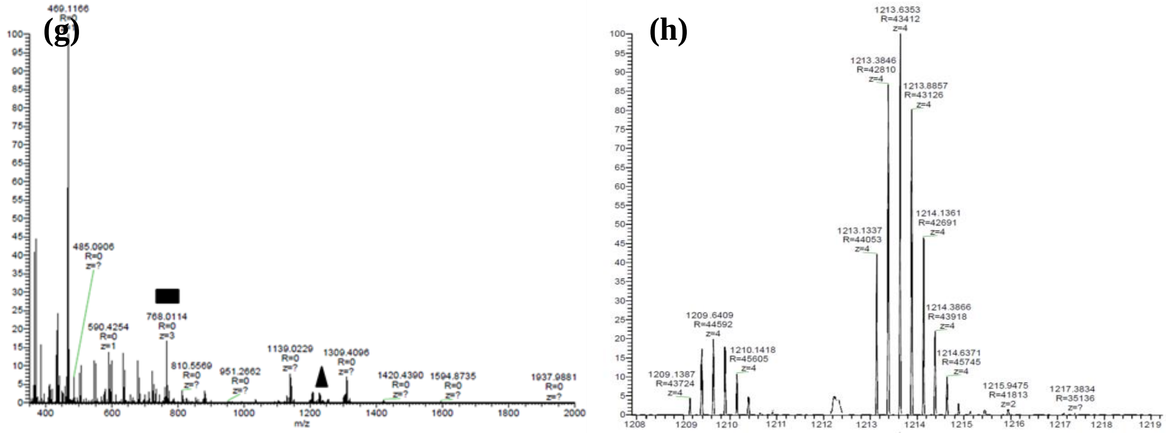

Figure 8. (a) Mass spectrum of the complex C-3/G-1, marked peaks corresponds to $[C\text{-}3+3Na]^{3+}$ (square), $[G\text{-}1]^{+}$ (circle), $[C\text{-}3/G\text{-}1+2K+2H]^{4+}$ (triangle); (b) Isotopic pattern of $[C\text{-}3/G\text{-}1+2K+2H]^{4+}$ ions; (c) Mass spectrum of the complex C-3/G-4, marked peaks corresponds to $[C\text{-}3+3Na]^{3+}$ (square) and $[C\text{-}3/G\text{-}2+K+3H]^{4+}$ (triangle) ions; (d) Isotopic pattern of $[C\text{-}3/G\text{-}2+K+3H]^{4+}$ ion; (e) Mass spectrum of C-3/G-7 complex, marked peaks corresponds to $[C\text{-}3+3Na]^{3+}$ (square) and $[C\text{-}3/G\text{-}7+K+3H]^{4+}$ (triangle); (f) Isotopic pattern of $[C\text{-}3/G\text{-}7+K+3H]^{4+}$ ion; (g) Mass spectrum of C-3/G-5 complex, marked peaks correspond to $[C\text{-}3+3Na]^{3+}$ (square) and $[C\text{-}3/G\text{-}5+K+3H]^{4+}$ (triangle) ions; (h) Isotopic pattern of $[C\text{-}3/G\text{-}5+K+3H]^{4+}$ ion.

Figure 9a. MALDI-TOF of collagen modified peptides from C-1 to C-3 and C-3-F.

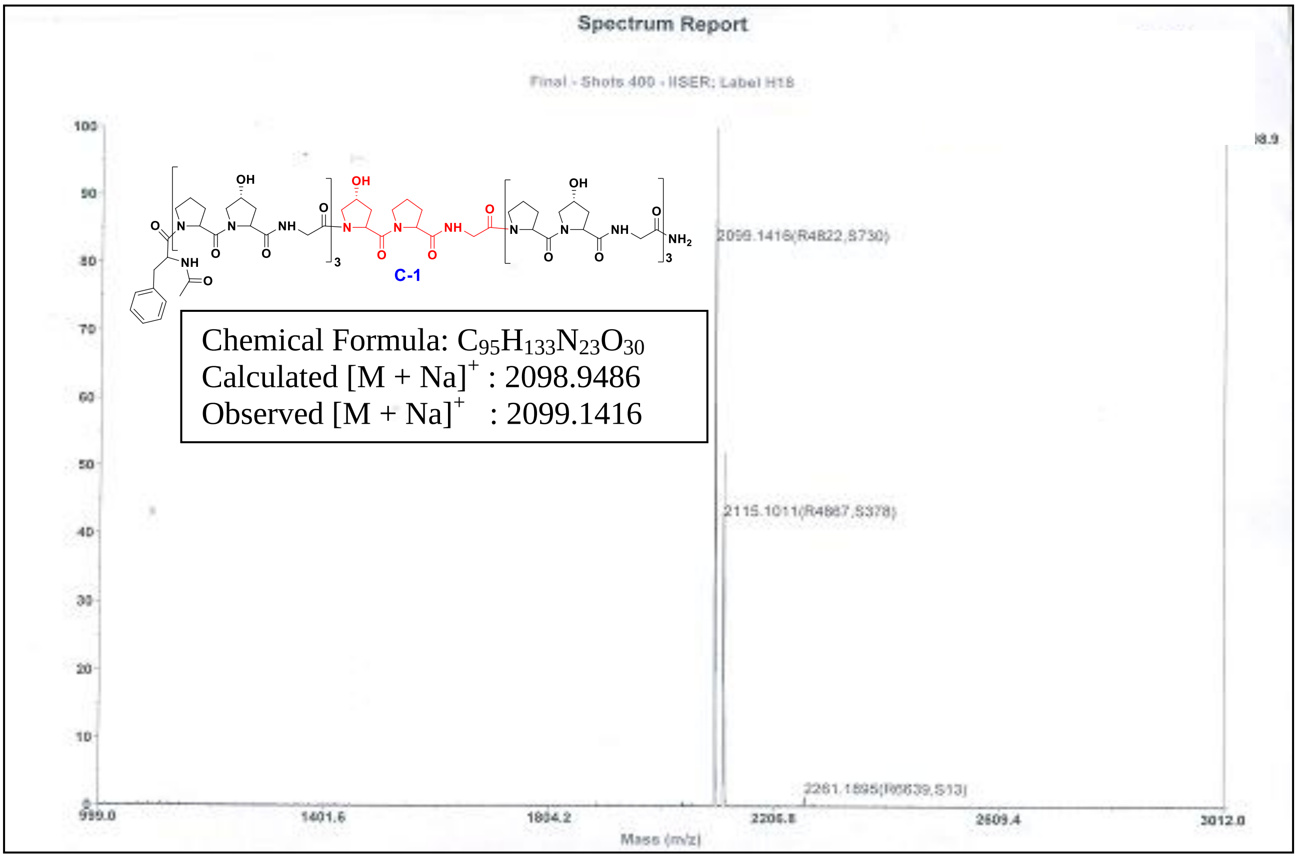

Chemical Formula: $C_{95}H_{133}N_{23}O_{30}$
Calculated $[M + Na]^{+}$: 2098.9486
Observed $[M + Na]^{+}$: 2099.1416

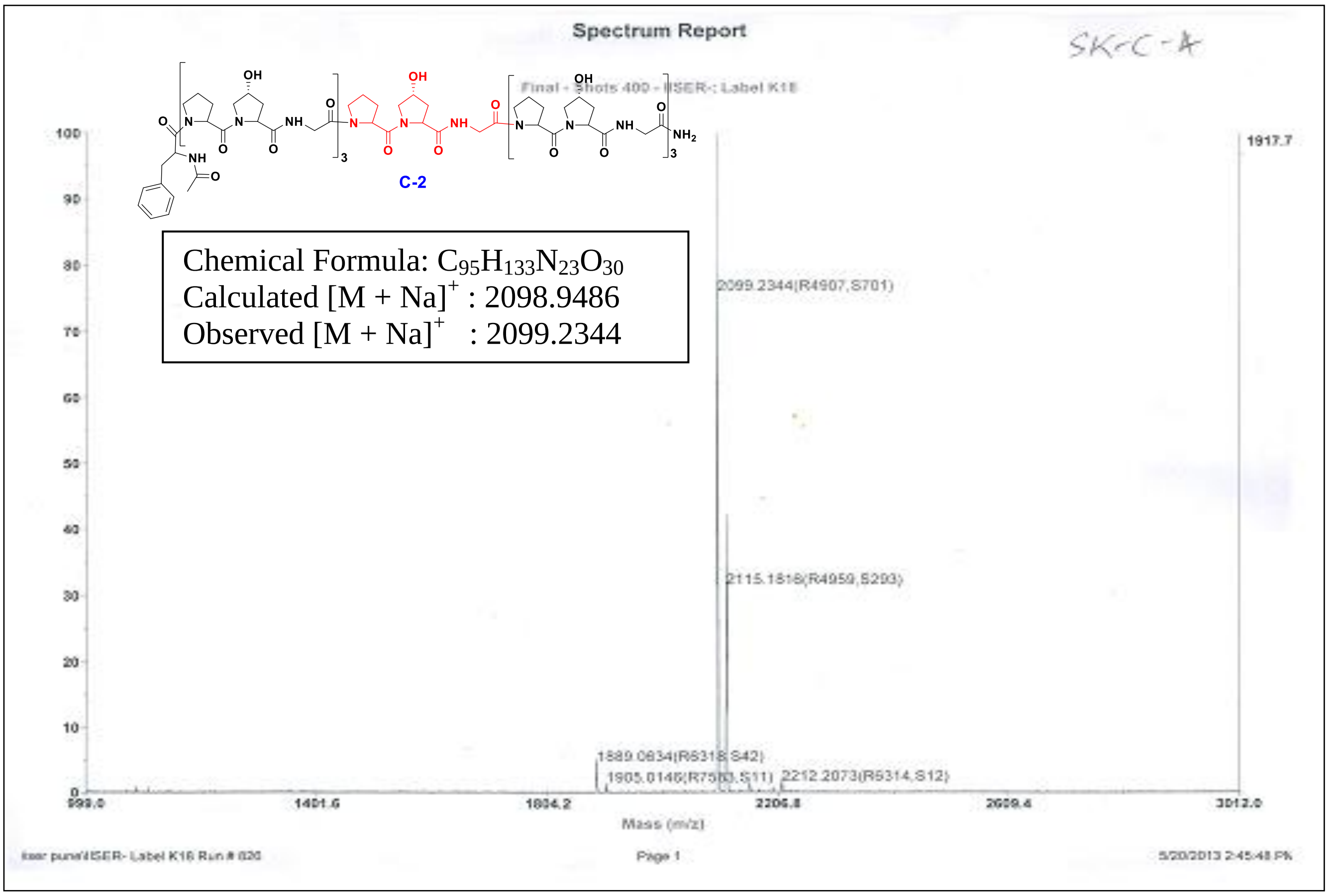

Chemical Formula: $C_{95}H_{133}N_{23}O_{30}$
Calculated $[M + Na]^+$: 2098.9486
Observed $[M + Na]^+$: 2099.2344

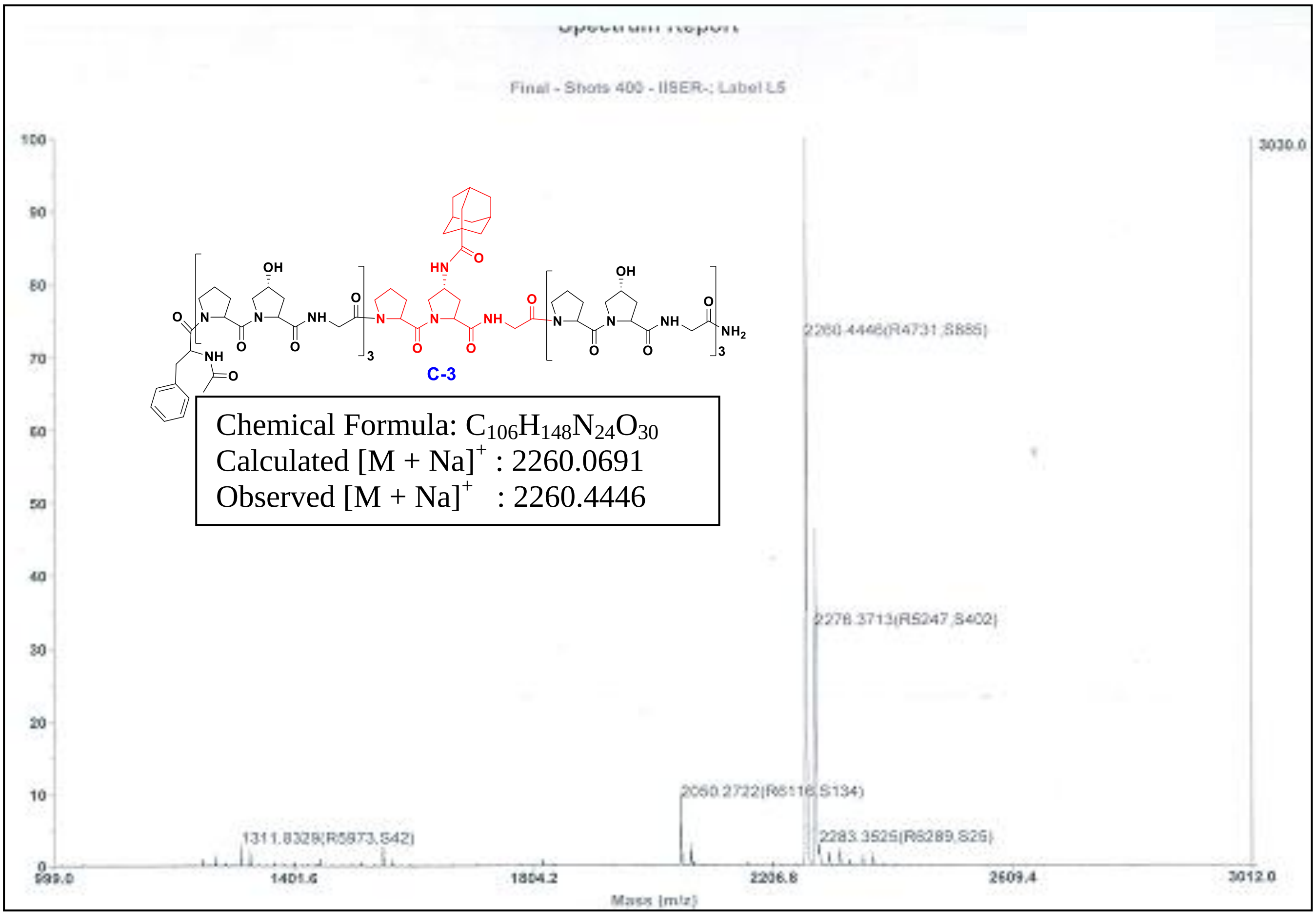

Chemical Formula: $C_{106}H_{148}N_{24}O_{30}$
Calculated $[M + Na]^+$: 2260.0691
Observed $[M + Na]^+$: 2260.4446

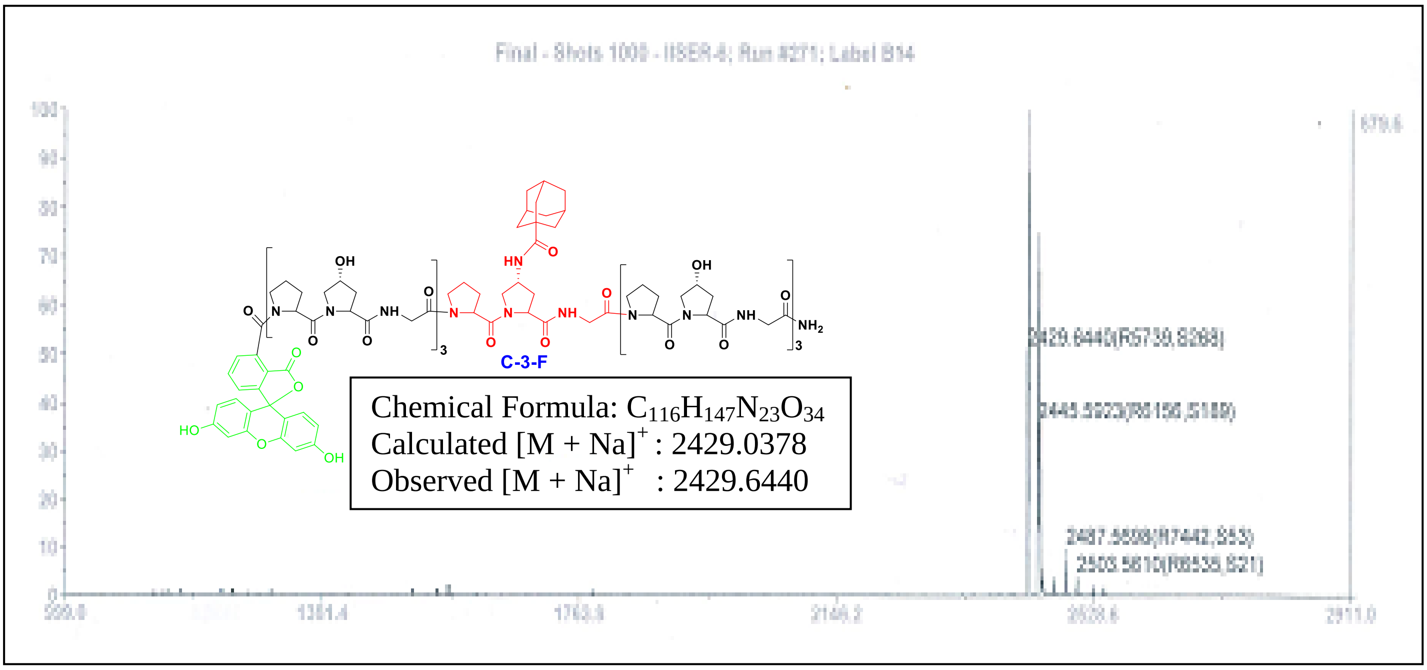

Chemical Formula: $C_{116}H_{147}N_{23}O_{34}$
Calculated $[M + Na]^+$: 2429.0378
Observed $[M + Na]^+$: 2429.6440

5.4.9 ITC binding studies

The host guest complexation further studied by isothermal titration calorimetr (ITC 200, USA) of **C-3** peptide with *β*-cyclodextrine (**G-1**) and **G-2**. Compound **G-1** or **G-2** stock solution (0.03 mM) was kept in the titration cell and was titrated by collagen peptide (**C-3**) of 0.02 mM in PBS buffer. Each experiment consisted of 18 injections with a successive time gap of 100 s between two injections. For proper mixing of the solutions the stirring speed was maintained at 1000 rotations/min. Cell temperature was kept fixed at 298 K and nearly three successive titrations were averaged out to give the ITC curves.

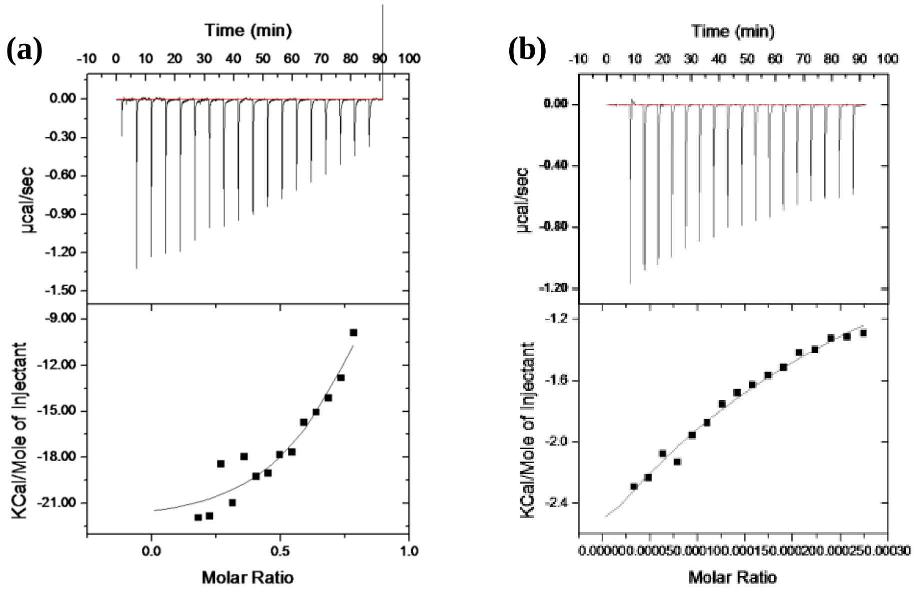

Figure 9. ITC profile for C-3/G-1 and C-3/G-2 in PBS buffer at 298K. Top panels represent the energy (μcal s^{-1}) required to maintain isothermal conditions with respect to the reference cells. Lower panels represent the heat evolved from each injection per mole of C-6 peptide versus the molar ratio of (a) conc of G-1= 0.03 mM; (b) conc of G-2 = 0.03 mM and in phosphate buffer pH 7.4.

Table 1. Binding constants of host-guest complexes.

ligand	n	Binding constant (M^{-1})	ΔH (cal/mol)	ΔS (cal/mol/deg)
C-6/G-1	0.812 ± 0.03	4.1 ± 2.2 X 10^3	-2.24 ±0.141X 10^3	-49.4
C-6/G-2	0.901 ± 0.12	5.31 ± 0.73 X 10^3	-2.03±0.108 X 10^3	-6800

Table 2. Physical characteristics of collagen related peptides.

Entry	Peptide	Cal'cd mass (m/z)	Obse'd mass (m/z)	CD T_m (^{O}C)	Topography ((l × w) or radius)
1	C-1	$[M+Na]^+$ 2098.9486	2099.1416	34.0	NN; (530-740 nm) × (90-95 nm)
2	C-2	$[M+Na]^+$ 2098.9486	2099.1951	44.0	NN; (850-970 nm) × (67-103 nm)
3	C-3	$[M+Na]^+$ 2260.0691	2260.4446	41.0	NN; (800-890 nm) × (120-160 nm)
4	C-3/G-1	3371.4491	$[M+2K+2H]^{4+}$ 862.8501	51.0	BFN; (1250-1500 nm) × (90-180 nm)
5	C-3/G-2	4925.9127	$[M+K+3H]^{4+}$ 1242.1072	54.0	BFN; (1250-1500 nm) × (90-180 nm)
6	C-3/G-5	4813.8780	$[M+K+3H]^{4+}$ 1213.6353	ND	ND
7	C-3/G-10	6060.2122	$[M+K+3H]^{4+}$ 1525.5783	ND	ND

5.4.10 Corroboration of the complexes structure by Circular Dichroism spectroscopy.

The CD spectra of the peptides were recorded at 25°C. CD data are given as normal ellipticity from the normalisation of ellipticity [θ]. To facilitate analysis of uncertainties, each set of spectra were measured using at least three individually prepared solutions and the spectra are the result of 5 accumulations. A quartz cell with a path length of 0.2 cm was used, with ensured volume 0.2 ml (200 µM) in PBS buffer. The buffer solution was used as blank and the samples were annealed at 90°C for 5 min and allowed to cool RT and the samples were stored at 4°C for 24 h before the measurement. The parameters of the measurements are as follows:

Resolution:	1 nm	Band width:	1.0 nm
Sensitivity:	100 mdeg	Response:	1 sec
Speed:	100 nm/min	Accumulation:	5

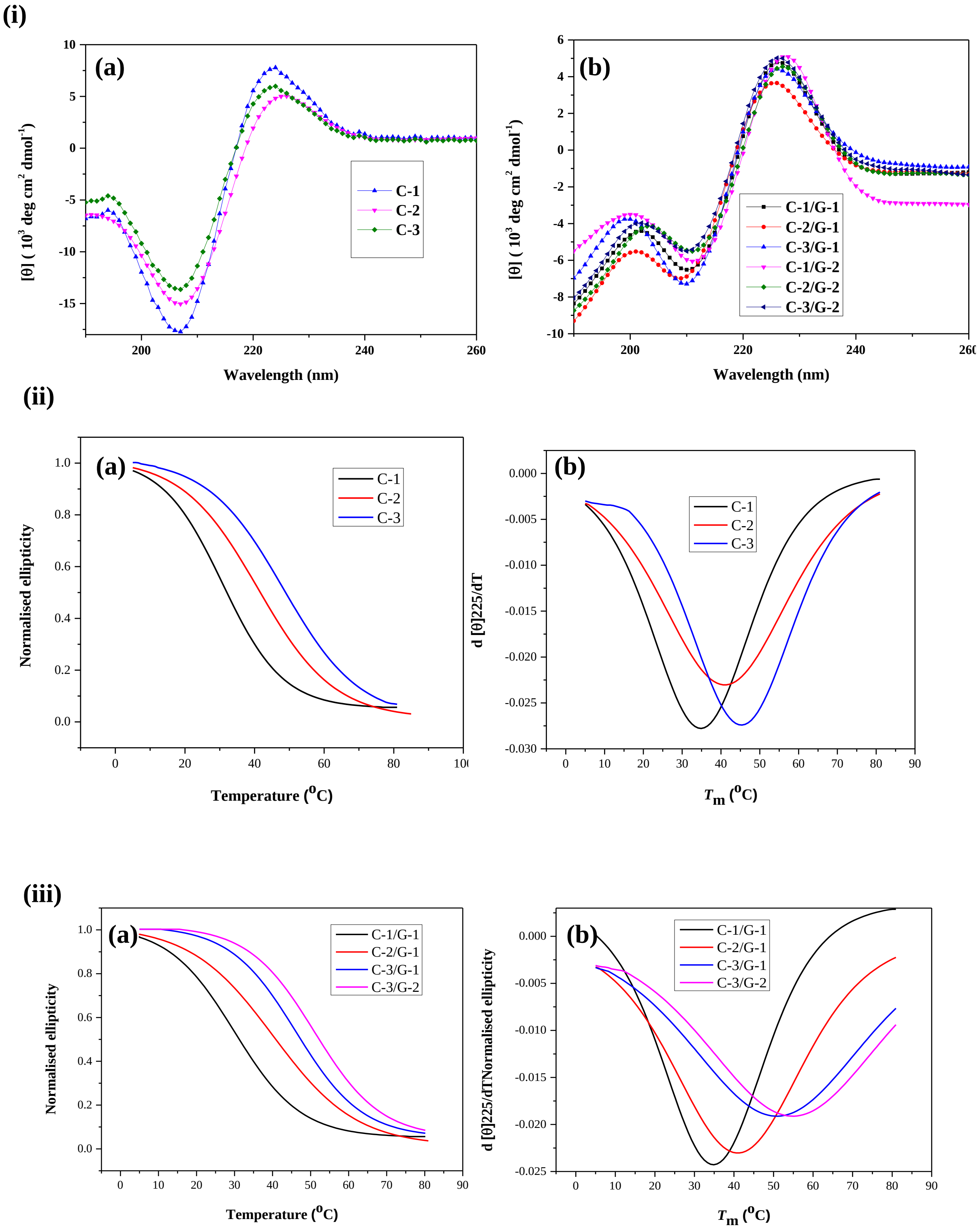

Figure 10. (i) (a) CD spectra of the CRPs from C-1 to C-3 at pH 7.2 (20mM sodium phosphate buffer), 25°C; (b) CD spectra of C-1 to C-3 complex with G-1 and G-2 respectively at pH 7.2 (20mM sodium phosphate buffer) 25°C.; (ii) (a) CD-thermal denaturation plot of C-1 to C-3 peptides and their complexes with G-1. Normal ellipticity at λ=225 nm, pH 7.2 (20 mM sodium phosphate buffer), temperature from 5°C to 85 °C; (b) First derivative cures of peptides C-1 to C-3 in complex with G-1; (iii) (a) CD-thermal denaturation plot of C-1 to C-3 peptides complex with G-1 and G-2 respectively.

Normal ellipticity at λ=225 nm, pH 7.2 (20 mM sodium phosphate buffer), temperature from 5°C to 85°C; (b) First derivative cures of peptides C-1 to C-3 complex with G-1 and G-2 respectively.

Table 3. Thermal stability (T_m) of collagen peptides and the host-guest inclusion complexes.

Peptides	T_m °C	Peptides[10]	T_m °C	Peptides[10]	T_m °C
[Hyp-Pro-Gly] (C-1)	35				
[Pro-Hyp-Gly] (C-2)	41	[Pro-Hyp-Gly]	43		
[Pro-(4R)adap-Gly] (C-3)	44	[(4R)Acp-Pro-Gly]	43	[(4R)Pvp-Pro-Gly]	44

Table 4. Thermal stability (T_m) of collagen peptides and the host-guest inclusion complexes.

Complex	T_m °C	Complex	T_m °C
C-1/G-1	34	C-1/G-2	ND
C-2/G-1	42	C-2/G-2	ND
C-3/G-1	49	C-3/G-2	54

5.4.11 Physical Properties of GCC

(a) SEM images of the peptides C-1 to **C-3 and the host-guest inclusion complexes**

Solutions of the peptides (200 µM) and host-guest complexes were drop costed on silicon wafers and were left to dry overnight in room temperature. The silicon wafer were sputter coated with gold (˜5-6 nm) and the samples were imaged using CARL ZEISS’S ULTRA PLUS Field Emission Scanning Electron Microscope (FESEM) operating at 3.0 kV. Percentage compositions of the elements in the C-3, C-3/G-1 and C-3/G-2 compounds were measured at 10 kV by EDS analysis (Table S4).

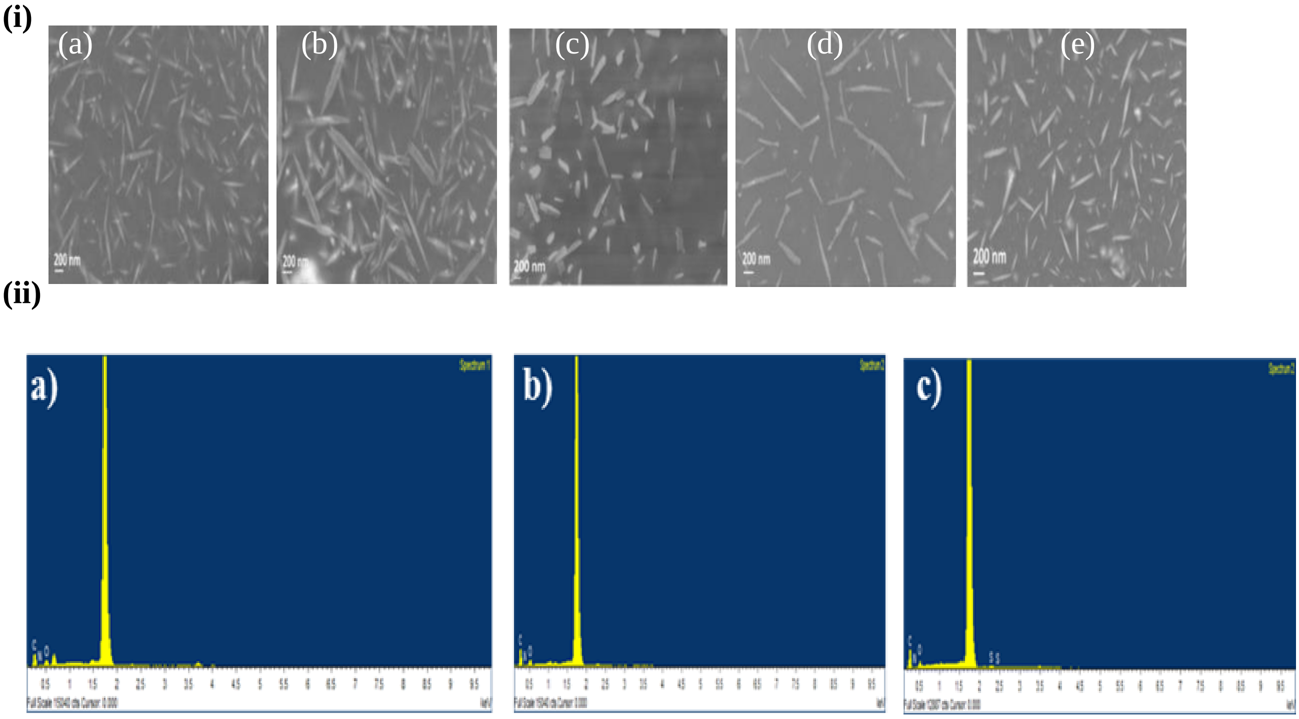

Figure 11. (i) SEM images of CRPs and its host-guest complexes (a) C-1; (b) C-2; (c) C-3; (d) C-3/G-1; (e) C-3/G-2; (ii) Energy-dispersive X-ray (EDS) spectra of C-3 (left) and the complexes C-3/G-1 (middle) and C-3/G-2 (right).

Table 5. Elemental analysis for C-3 and its glyco-collagen conjugates (GCC) G-1 and G-2, as calculated from EDS spectra.

Element	Weight% (C-3)	Weight% (C-3/G-1)	Weight% (C-3/G-2)
C K	45.39	46.01	50.91
N K	17.07	15.11	14.84
O K	37.54	38.88	32.07
S K	-	-	2.18
Total	100.00	100.00	100.00

(b) UV and Fluorescence properties of the peptides and complexes

UV-vis spectra of **C-3-F** in water displayed an absorption peak at λ_{max} = 492 nm (Figure **S10**) and emission at λ = 415 nm upon excitation with light of λ = 489 nm. The quantum yield of the **C-3-F** peptide was calculated to be 0.677 (Table S3). The relative fluorescence quantum yields can also be determined by measuring the fluorescence of a reference fluorophore, FITC derivative, of known quantum yield Φ.

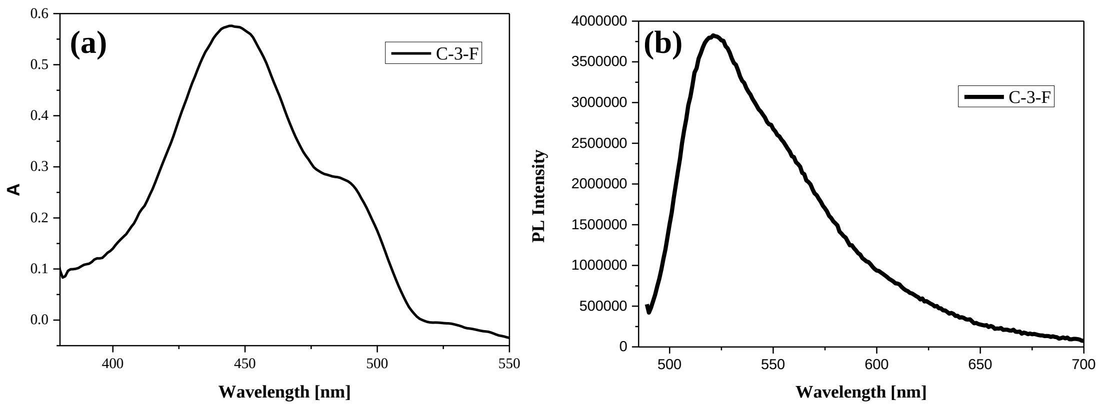

Figure 12. UV-Vis absorption (left) and fluorescence emission (λ_{ex} at 489 nm) spectra (right) of C-3-F (FITC labelled C-3 peptide).

Table 6. The photophysical properties of C-3-F peptide (FITC labelled C-3 peptide).

Peptide	λ_{max}^{abs}	$A_{\max}$	λ_{max}^{em}	φ
C-3-F	492	0.10184	517	0.677

5.4.12 Wound healing assay

Cell line	Growth Media
HeLa/NIH-3T3/MDA-MB-231/ BJ	Cells were grown at 37 °C in 5% CO_2 atmosphere in DMEM medium containing 10% fetal bovine serum and 0.1% streptomycin
hUVEC	Cells were grown at 37 °C in 5% CO_2 atmosphere in EGM-2 medium containing 1% fatal calf serum and other additives, including growth factors.

i) Procedure for isolation of fibroblast cells from mouse skin and ear. We followed according to literature procedure for isolating skin fibroblast cells from mouse[4]. In detail, prior to collection, mouse skin was cleaned with 70% ethanol followed by shave the area with scalpel blade, incision cut was made by sterilized scalpel blade. After cut of mouse skin, tissues were washed with 70% ethanol, PBS for 3-4 min and immediately transferred into DMEM medium. Tissue sections were further cut into tiny pieces and kept it for digestion for 90 min then cells were collected by centrifugation. Collected cells were cultured in DMEM medium containing 10% fetal bovine serum and 0.1% streptomycin. Similar procedure followed for ear fibroblast cells from mouse.

Cells were seeded into 24-well tissue culture plates to form a monolayer. Details about the cell types, medium and other conditions are summarized in above table. The monolayer was gently scratched across the center of the well using 1000 µl pipette tips and the wells were gently washed with PBS followed by medium to remove detached cells. Different combinations of glyco-collagen conjugates (GCC) (200 µM) were added to different wells and after incubation of one hours, bright field microscopic images were recorded. The gap distance and area were quantitatively evaluated using ImageJ software. The measurements were done in triplicates. The results have shown that since each cell line has a different growth rate, it also corresponded to the wound healing process. For HeLa, MDA-MB-231, we have observed complete wound healing after 6-7 hours, whereas with BJ, hUVEC and NIH-3T3 wound healing was observed after 9-10 hours and for skin, ear cells wound healing was observed after 10-11 h.

$$\text{Percentage of wound healing} = \frac{(d_o-d_1)\ X100}{d_0}$$

(i)

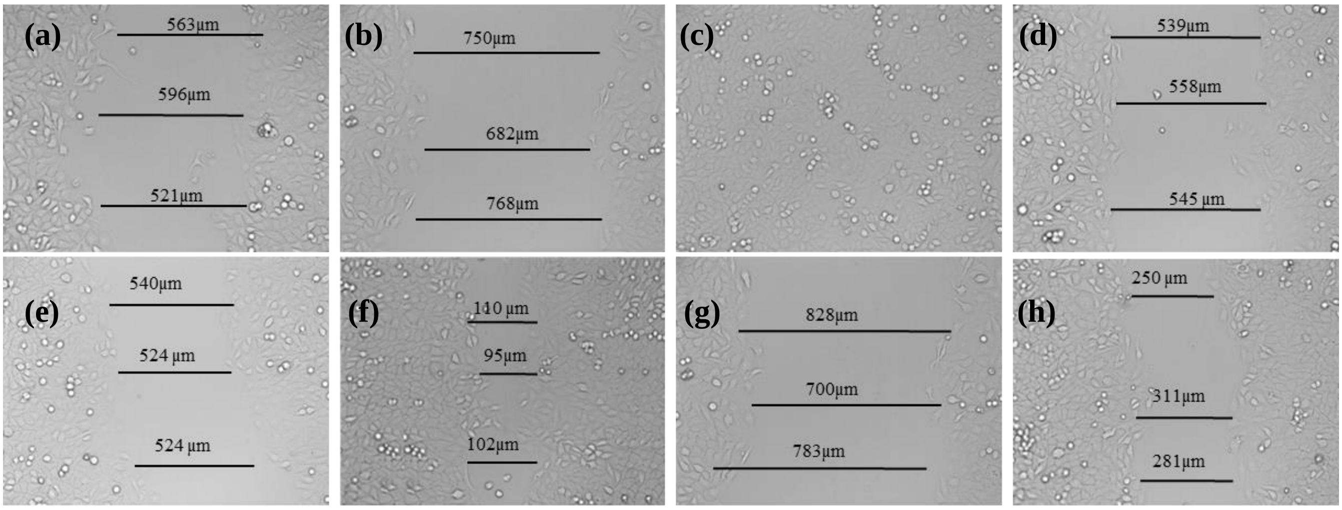

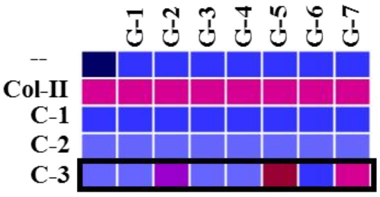

(ii)

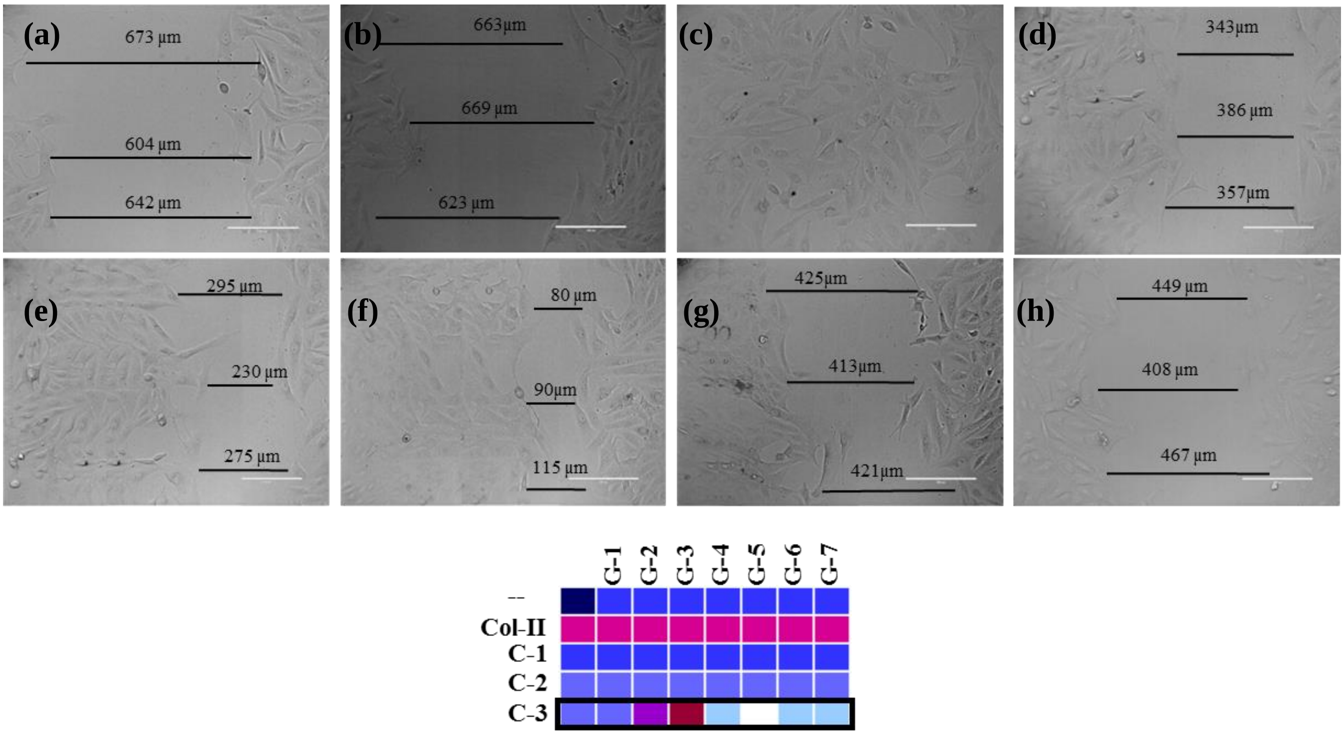
(a)
673 µm
604 µm
642 µm
(b)
663µm
669 µm
623 µm
(c)
(d)
343µm
386 µm
357µm
(e)
295 µm
230 µm
275 µm
(f)
80 µm
90µm
115 µm
(g)
425µm
413µm
421µm
(h)
449 µm
408 µm
467 µm
G-1
G-2
G-3
G-4
G-5
G-6
G-7
--
Col-II
C-1
C-2
C-3

(iii)

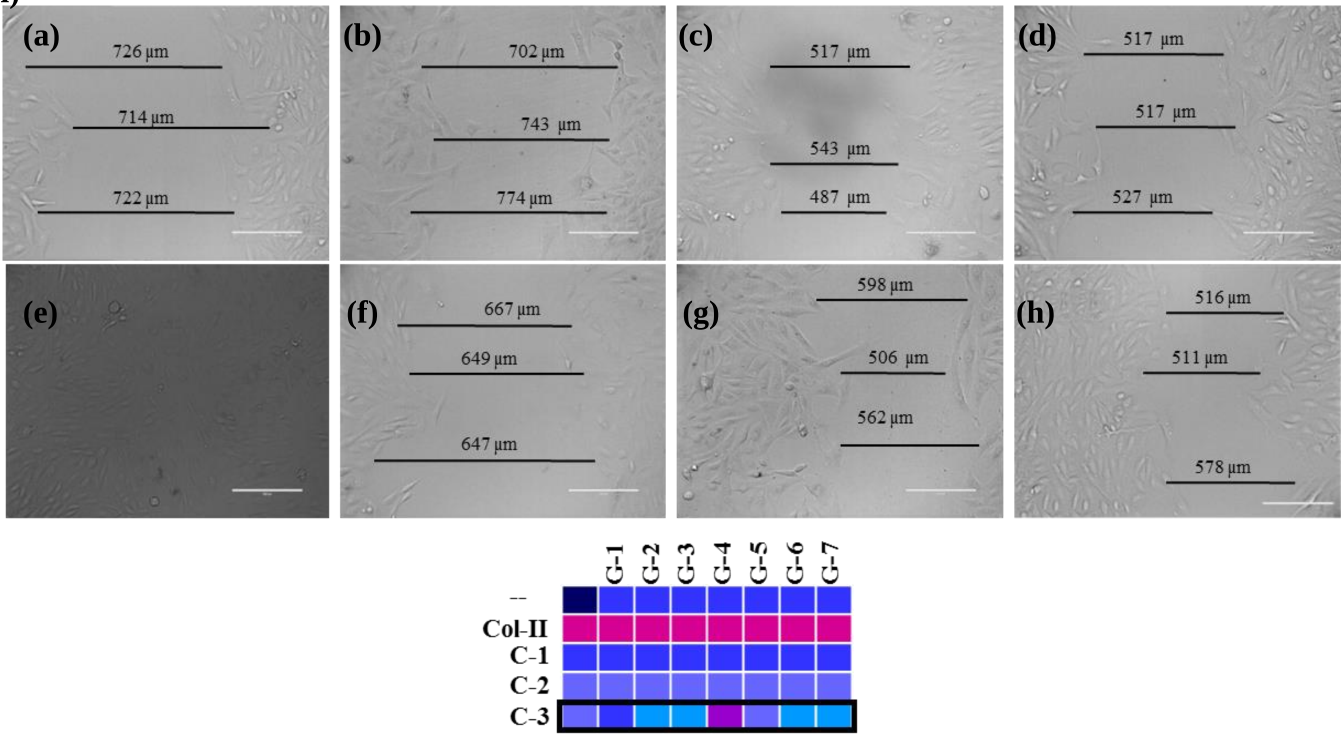
(a)
726 µm
714 µm
722 µm
(b)
702 µm
743 µm
774 µm
(c)
517 µm
543 µm
487 µm
(d)
517 µm
517 µm
527 µm
(e)
(f)
667 µm
649 µm
647 µm
(g)
598 µm
506 µm
562 µm
(h)
516 µm
511 µm
578 µm
G-1
G-2
G-3
G-4
G-5
G-6
G-7
--
Col-II
C-1
C-2
C-3

(iv)

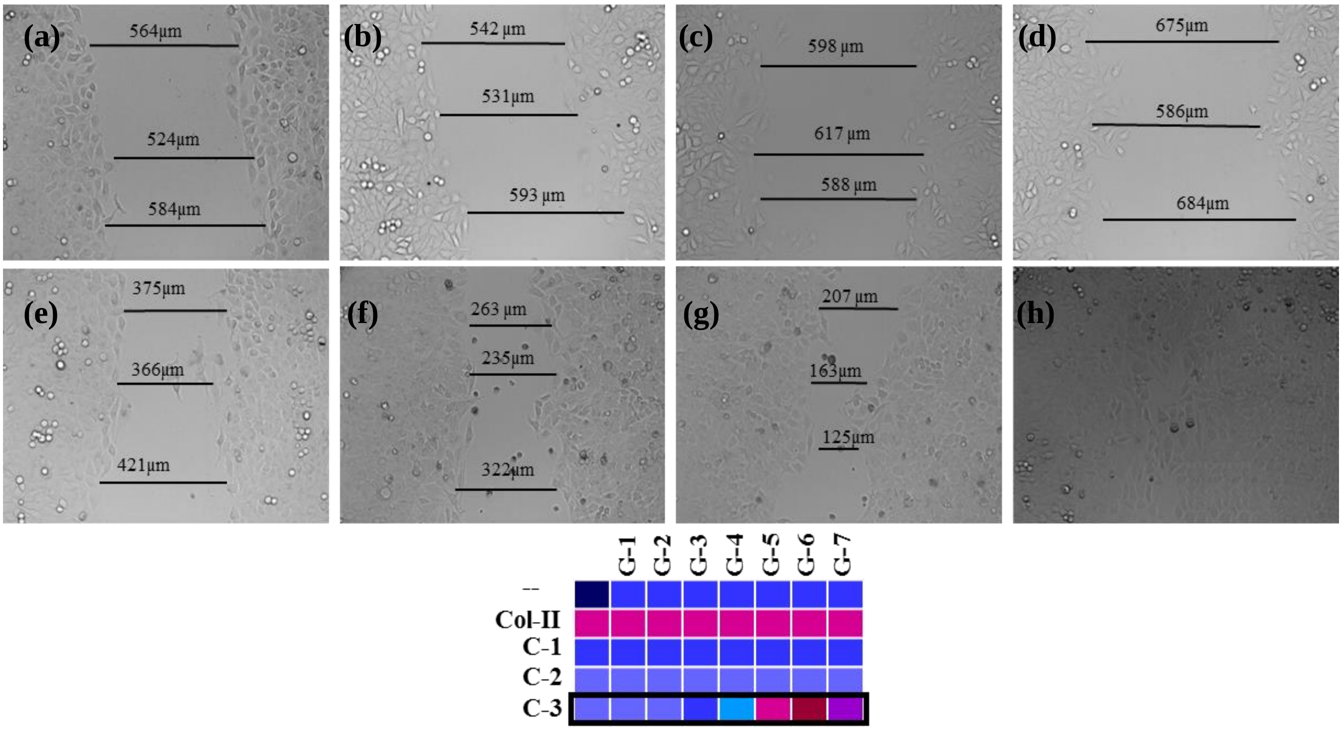
(a)
564µm
524µm
584µm
(b)
542 µm
531µm
593 µm
(c)
598 µm
617 µm
588 µm
(d)
675µm
586µm
684µm
(e)
375µm
366µm
421µm
(f)
263 µm
235µm
322µm
(g)
207 µm
163µm
125µm
(h)
G-1
G-2
G-3
G-4
G-5
G-6
G-7
--
Col-II
C-1
C-2
C-3

(v)

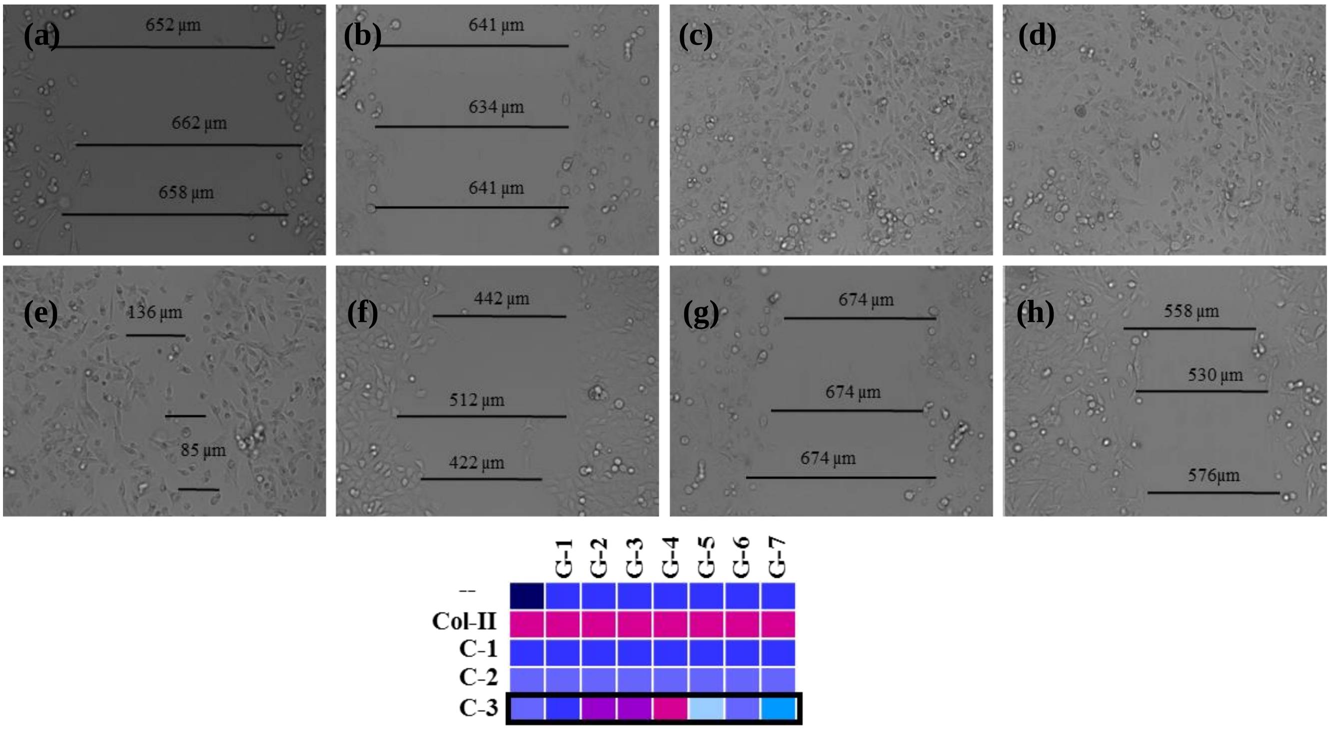
(a)
652 µm
662 µm
658 µm
(b)
641 µm
634 µm
641 µm
(c)
(d)
(e)
136 µm
85 µm
(f)
442 µm
512 µm
422 µm
(g)
674 µm
674 µm
674 µm
(h)
558 µm
530 µm
576µm
G-1
G-2
G-3
G-4
G-5
G-6
G-7
--
Col-II
C-1
C-2
C-3

(vi)

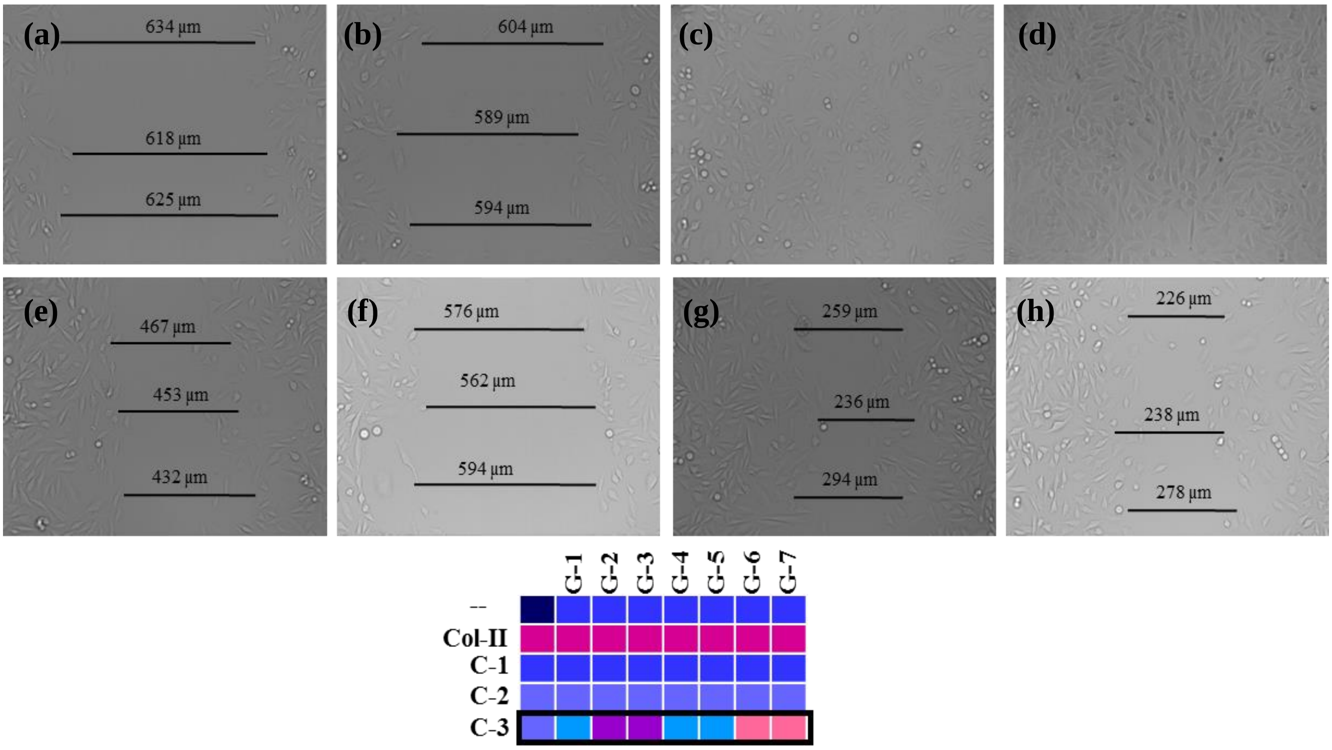

(vii)

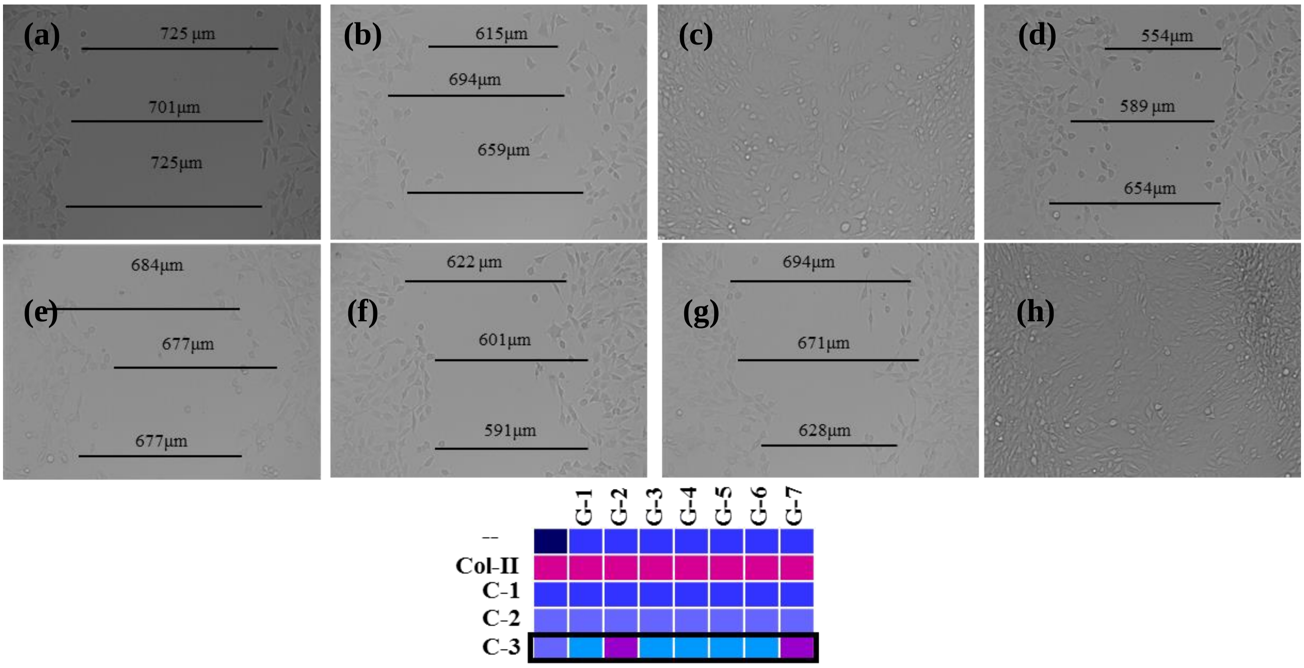

Figure 13. (i) Influence of C-3 and its complexes on wound healing processes with hHUVEC cells after 6 hours. (a) C-3; (b) C-3/G-1; (c) C-3/G-2; (d) C-3/G-3; (e) C-3/G-4; (f) C-3/G-5; (g) C-3/G-6; (h) C-3/G-7; (ii) Influence of C-3 and its complexes on wound healing processes with BJ cells after 10 hours. (a) C-3; (b) C-3/G-1; (c) C-3/G-2; (d) C-3/G-3; (e) C-3/G-4; (f) C-3/G-5; (g) C-3/G-6; (h) C-3/G-7; (iii) Influence of C-3 and its complexes on wound healing processes with NIH3T3 cell lines after 10 hours. (a) C-3; (b) C-3/G-1; (c) C-3/G-2; (d) C-3/G-3; (e) C-3/G-4; (f) C-3/G-5; (g) C-3/G-6;

(h) C-3/G-7; (iv) Influence of C-3 and its complexes on wound healing processes with HeLa cell lines after 6 hours. (a) C-3; (b) C-3/G-1; (c) C-3/G-2; (d) C-3/G-3; (e) C-3/G-4; (f) C-3/G-5; (g) C-3/G-6; (h) C-3/G-7; (v) Influence of C-3 and its complexes on wound healing processes with MDA – MB 231 cells after 6 hours. (a) C-3; (b) C-3/G-1; (c) C-3/G-2; (d) C-3/G-3; (e) C-3/G-4; (f) C-3/G-5; (g) C-3/G-6; (h) C-3/G-7; (vi) Influence of C-3 and its complexes on wound healing processes with ear cells after 10 hours. (a) C-3; (b) C-3/G-1; (c) C-3/G-2; (d) C-3/G-3; (e) C-3/G-4; (f) C-3/G-5; (g) C-3/G-6; (h) C-3/G-7; (vii) Influence of C-3 and its complexes on wound healing processes with skin cells after 10 hours. (a) C-3; (b) C-3/G-1; (c) C-3/G-2; (d) C-3/G-3; (e) C-3/G-4; (f) C-3/G-5; (g) C-3/G-6; (h) C-3/G-7.

5.4.13 Confocal Laser Scanning Microscope (CLSM) images. HeLa/skin/BJ cells were taken in a 8 well chambered cover glass (sigma Aldrich). They were fed with FITC-conjugated **C-3-F** (200 µM) for 6 hours, washed twice with PBS and dissolved in DMEM media. The cells were treated with Hoechst 33342 (10 µL of 2 µg/mL solution) to stain nuclei for 30 mins, washed 3 times with PBS buffer. The fluorescence of Hoechst 33342 and FITC complexes were excited with an argon laser at 405 nm and 450 nm respectively, and the emission was collected through 403–452 nm and 500-530 nm filters, respectively.

5.4.14 Western blot analysis. BJ and skin cells were grown on a 100 mm petri dish and treated with 200 µM of **C-3/G-1**, **C-3/G-2, C-3/G-5, C-3/G-7** for 6 h respectively. Cells were pelleted, and washed with PBS buffer and treated with protease inhibitors before treating with lysis buffer containing 150 mM NaCl, 1% NP-40, 0.25% SDS, 1 mM EDTA, 1 mM PMSF in 50 mM Tris-Cl (pH 7.4). After 1 hour, the supernatant was collected by centrifugation at 14000 rpm for 15 min and stored in aliquots. Protein content was quantified using Bradford method. 35 µg of protein was loaded on SDS-polyacrylamide gel electrophoresis (10%) and transferred onto a PVDF membrane. The membrane was incubated for 2 hours with specific antibodies corresponding to FAK, phospho FAK (Tyr397), ERK1/2, and phospho ERK (Thr202/Tyr204). Thereafter, the membranes were incubated with an HRP-conjugated secondary antibody for 1 hour at room temperature. Band visualization was performed using the Immobilon Western Chemiluminescent HRP substrate kit (Millipore Corporation, MA, USA). α-tubulin was used as an internal standard. Biorad Protein Ladder (Thermo, EU) was used to determine the molecular weights of the protein bands.

5.4.15 Fluorescence-activated cell sorting assay (FACS)

HeLa/skin/BJ cells were cultured as described above and treated with **C-3** host-guest complexes (**G-1**, **G-2**, **G-5**, **G-7**) (200 µM) for 6 hours respectively, at 37^0C. The cells washed with PBS and were detached and transferred to FACS tubes. Integrin α1β1 mouse antibody (Santa Cruz biotechnology) were added and incubated for 1 hour followed by a secondary antibody. The fluorescent channel FL-2 was used to detect integrin levels. All data were analysed with the FlowJo software.

Table 7. FACS analyses of HeLa, skin and BJ cell lines.

Cellines	Level of integrin expression in %			
	C-3/G-1	C-3/G-2	C-3/G-5	C-3/G-7
BJ (α1β1)	5.8	65.8	31.7	41.3
HeLa (α1β1)	4.1	7.4	51.7	58.3
Skin (α1β1)	7.8	60.4	12.8	61.7

5.4.16 *In vivo* wound healing experiment: Male C57BL mice (7-8 weeks old) were collected from Reliance Biotech, Bombay. Prior to experiment the mices were maintiained in animal house for 48 h in 12 h/12 h light/dark cycle, with proper food and water. All mouse experiments were performed in accordance with the relevant guidelines and regulations of Institutional Animal Ethical Committee regulation, set up by CPCSEA, Govt. of India. Mice (n =6) were anesthetized by ketamine and the dorsal flank was shaved and sterilized with 70% ethanol. Excisional wound was generated using 6 mm biopsy punch excision (surface area 28.27 mm^2) and treated with native collagen II and **C-3/G-7** (500 µM). Progress of wound healing was observed by imaging and histology, over 3, 5, 8, 11, 12, 14 days. Histology images were taken by cutting the tissue section of wound and fixed in bouins fixative, followed by dehydration with ethanol and xylene. The tissues were embeded in paraflast, and 10 µM sections were cut using microtome. The tissue sections were fixed on a PLL coated glass plates followed by treatment with hematoxylin and eosin stain and morphology of the section were observed under EOS microscopy.

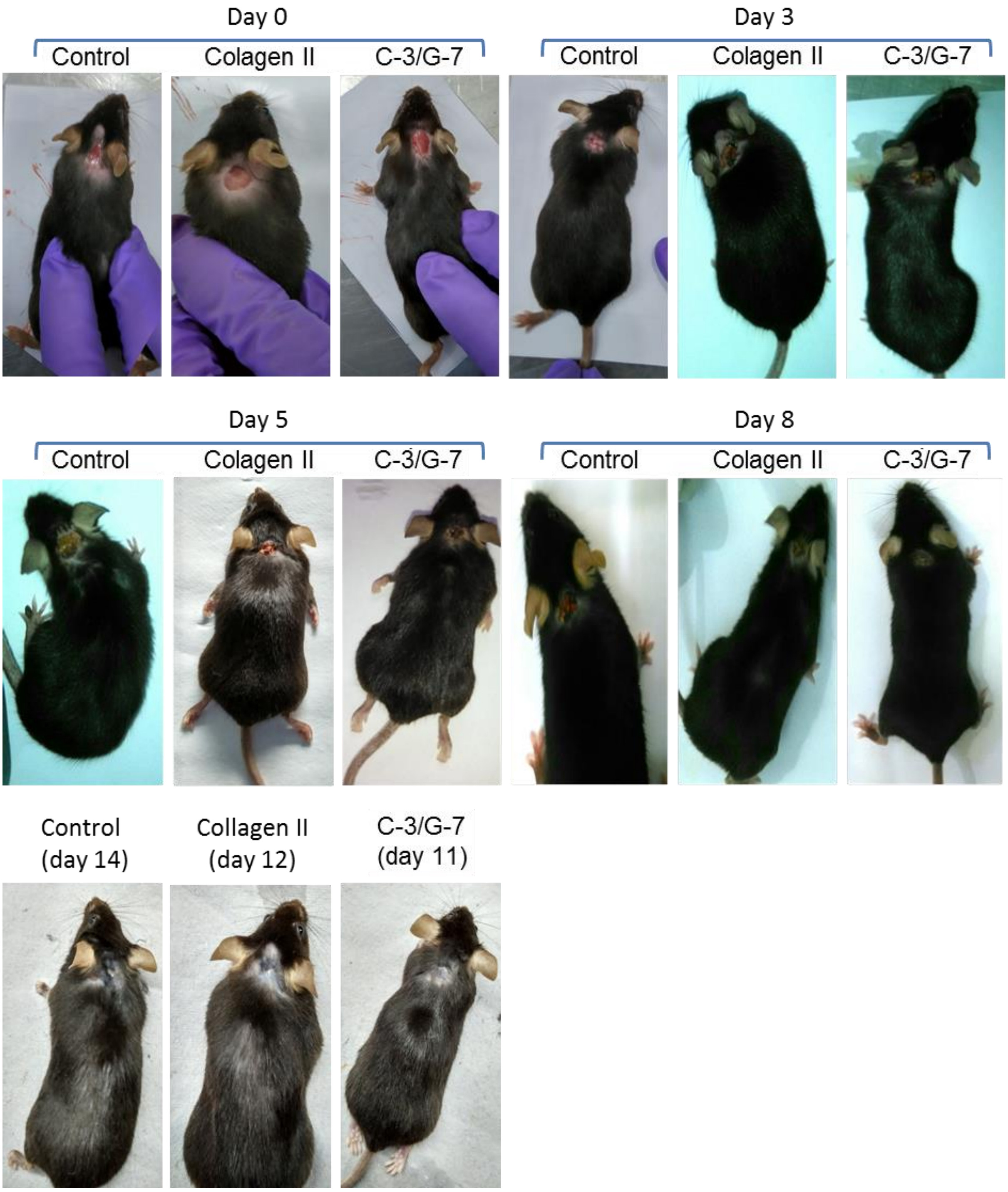

Figure 14. Progress of wound healing of mouse, over the days from (0 to 14) by treatment with collagen-II and **C-3/G-7**. Compound treated with **C-3/G-7** showed more wound healing rate compare to collagen II and control.

5.5 References

1. R. A. Dwek, *Chem. Rev.*, 1996, **96**, 683-720.
2. T. Buskas, S. Ingale and G. J. Boons, *Glycobiology*, 2006, **16**, 113R-136R.
3. J. Roth, *Chem. Rev.*, 2002, **102**, 285-303.
4. M. A. Wolfert and G. J. Boons, *Nat. Chem. Biol.*, 2013, **9**, 776-784.
5. K. Harrison, J. Hallett, T. S. Burcham, R. E. Feeney, W. L. Kerr and Y. Yeh, *Nature*, 1987, **328**, 241-243.
6. F. W. Kotch, I. A. Guzei and R. T. Raines, *J. Am. Chem. Soc.*, 2008, **130**, 2952-2953.
7. C. M. Yamazaki, I. Nakase, H. Endo, S. Kishimoto, Y. Mashiyama, R. Masuda, S. Futaki and T. Koide, *Angew. Chem. Int. Ed. Engl.*, 2013, **52**, 5497-5500.
8. J. K. Kim, Y. Xu, X. Xu, D. R. Keene, S. Gurusiddappa, X. Liang, K. K. Wary and M. Hook, *J. Biol. Chem.*, 2005, **280**, 32512-32520.
9. P. Wang, J. Zhu, Y. Yuan and S. J. Danishefsky, *J. Am. Chem. Soc.*, 2009, **131**, 16669-16671.
10. I. E. Andersson, C. D. Andersson, T. Batsalova, B. Dzhambazov, R. Holmdahl, J. Kihlberg and A. Linusson, *PloS one*, 2011, **6**, e17881.
11. N. Gaidzik, U. Westerlind and H. Kunz, *Chem. Soc. Rev.*, 2013, **42**, 4421-4442.
12. J. A. Falenski, U. I. Gerling and B. Koksch, *Bioorg. Med. Chem.*, 2010, **18**, 3703-3706.
13. L. Nagel, C. Budke, A. Dreyer, T. Koop and N. Sewald, *Beilstein journal of organic chemistry,* 2012, **8**, 1657-1667.
14. R. S. Erdmann and H. Wennemers, *J. Am. Chem. Soc.*, 2010, **132**, 13957-13959.
15. U. Westerlind, *Beilstein journal of organic chemistry*, 2012, **8**, 804-818.
16. L. Russo, A. Sgambato, M. Lecchi, V. Pastori, M. Raspanti, A. Natalello, S. M. Doglia, F. Nicotra and L. Cipolla, *ACS chemical neuroscience*, 2014, **5**, 261-265.
17. D. Bini, L. Russo, C. Battocchio, A. Natalello, G. Polzonetti, S. M. Doglia, F. Nicotra and L. Cipolla, *Org. Lett.*, 2014, **16**, 1298-1301.
18. D. Grunstein, M. Maglinao, R. Kikkeri, M. Collot, K. Barylyuk, B. Lepenies, F. Kamena, R. Zenobi and P. H. Seeberger, *J. Am. Chem. Soc.*, 2011, **133**, 13957-13966.
19. H. Bavireddi, R. Vasudeva Murthy, M. Gade, S. Sangabathuni, P. M. Choudhary, C. Alex, B. Lepenies and R. Kikkeri, *Nanoscale,* 2016, **8**, 19696-19702.
20. M. D. Shoulders and R. T. Raines, *Annu. Rev. Biochem*, 2009, **78**, 929-958.
21. B. Brodsky, G. Thiagarajan, B. Madhan and K. Kar, *Biopolymers*, 2008, **89**, 345-353.

22. D. J. Prockop and K. I. Kivirikko, *Annu. Rev. Biochem*, 1995, **64**, 403-434.

23. S. T. Nillesen, P. J. Geutjes, R. Wismans, J. Schalkwijk, W. F. Daamen and T. H. van Kuppevelt, *Biomaterials*, 2007, **28**, 1123-1131.

24. W. Wang, M. Zhang, W. Lu, X. Zhang, D. Ma, X. Rong, C. Yu and Y. Jin, *Tissue engineering. Part C, Methods*, 2010, **16**, 269-279.

25. C. R. Bertozzi and L. L. Kiessling, *Science*, 2001, **291**, 2357-2364.

26. R. G. Spiro, *J. Biol. Chem.*, 1967, **242**, 4813-4823.

27. H. Bavireddi, P. Bharate and R. Kikkeri, *Chem Commun (Camb)*, 2013, **49**, 3988-3990.

28. M. Gade, A. Paul, C. Alex, D. Choudhury, H. V. Thulasiram and R. Kikkeri, *Chem Commun (Camb)*, 2015, **51**, 6346-6349.

29. A. Garcia-Barrientos, J. J. Garcia-Lopez, J. Isac-Garcia, F. Ortega-Caballero, C. Uriel, A. Vargas-Berenguel and F. Santoyo-Gonzalez, *Synthesis-Stuttgart*, 2001, 1057-1064.

30. A. Seluanov, A. Vaidya and V. Gorbunova, *J. Vis. Exp*., 2010, **44**, 2033

31. J. C. Tam, K. M. Lau, C. L. Liu, M. H. To, H. F. Kwok, K. K. Lai, C. P. Lau, C. H. Ko, P. C. Leung, K. P. Fung and C. B. Lau, *J. Ethnopharmacol.*, 2011, **134**, 831-838.

32. A. Wells, J. Grahovac, S. Wheeler, B. Ma and D. Lauffenburger, *Trends Pharmacol. Sci.*, 2013, **34**, 283-289.

33. C. C. Liang, A. Y. Park and J. L. Guan, *Nat Protoc*, 2007, **2**, 329-333.

34. D. Benito-Alifonso, S. Tremel, B. Hou, H. Lockyear, J. Mantell, D. J. Fermin, P. Verkade, M. Berry and M. C. Galan, *Angew. Chem. Int. Ed. Engl.*, 2014, **53**, 810-814.

35. T. Sletten, M. Kostas, J. Bober, V. Sorensen, M. Yadollahi, S. Olsnes, J. Tomala, J. Otlewski, M. Zakrzewska and A. Wiedlocha, *PloS one*, 2014, **9**, e90687.

36. G. Quan, X. Pan, Z. Wang, Q. Wu, G. Li, L. Dian, B. Chen and C. Wu, *Journal of nanobiotechnology*, 2015, **13**, 7.

37. Y. Ma, H. Chen, S. Su, T. Wang, C. Zhang, G. Fida, S. Cui, J. Zhao and Y. Gu, *Journal of Cancer*, 2015, **6**, 658-670.

38. Y. Yang, M. Yu, T. T. Yan, Z. H. Zhao, Y. L. Sha and Z. J. Li, *Bioorg. Med. Chem.*, 2010, **18**, 5234-5240.

39. R. O. Hynes, *Cell*, 1992, **69**, 11-25.

40. J. Emsley, C. G. Knight, R. W. Farndale, M. J. Barnes and R. C. Liddington, *Cell*, 2000, **101**, 47-56.

41. C. F. Tiger, F. Fougerousse, G. Grundstrom, T. Velling and D. Gullberg, *Dev. Biol.*, 2001, **237**, 116-129.
42. J. K. Kim, Y. Xu, X. Xu, D. R. Keene, S. Gurusiddappa, X. Liang, K. K. Wary and M. Hook, *J. Biol. Chem.*, 2005, **280**, 32512-32520.
43. G. Szulgit, R. Rudolph, A. Wandel, M. Tenenhaus, R. Panos and H. Gardner, *The Journal of investigative dermatology*, 2002, **118**, 409-415.
44. S. Saleem, J. Li, S. P. Yee, G. F. Fellows, C. G. Goodyer and R. Wang, J. Pathol, 2009, 219, 182-192.
45. D. M. Ansell, L. Campbell, H. A. Thomason, A. Brass and M. J. Hardman, *Wound Repair Regen*., 2014, **22**, 281-287.
46. A. Sindrilaru, T. Peters, J. Schymeinsky, T. Oreshkova, H. Wang, A. Gompf, F. Mannella, M. Wlaschek, C. Sunderkotter, K. L. Rudolph, B. Walzog, X. R. Bustelo and K. D. Fischer, *Blood*, 2009, **113**, 5266-5276.
